

**Mechanical Integration
of the
Micro Vertex Detector
for the
CBM experiment**

Dissertation
zur Erlangung des Doktorgrades
der Naturwissenschaften

vorgelegt beim Fachbereich Physik
der Johann Wolfgang Goethe-Universität
in Frankfurt am Main

von

Tobias Tischler
aus Hagen

2015
(D 30)

vom Fachbereich Physik der
Johann Wolfgang Goethe-Universität als Dissertation angenommen.

Dekan: Prof. Dr. R. Reifarth

Gutachter: Prof. Dr. J. Stroth

Prof. Dr. P. Senger

Datum der Disputation: 13.11.2015

Abstract

Within this thesis, the mechanical integration of the Micro Vertex Detector (MVD) of the Compressed Baryonic Matter (CBM) experiment is developed. The CBM experiment, which is being set up at the future FAIR facility, aims to investigate the phase diagram of strongly interacting matter in the regime of high net-baryon densities and moderate temperatures. Heavy-ion collisions at beam energies in the range of 2 to 45 AGeV, complemented by results from elementary reactions, will allow access to these conditions. The experiments conducted at LHC (CERN, Switzerland) and at RHIC (BNL, USA/does not apply within the Beam Energy Scan program) so far focus on the investigation of the phase diagram in the regime of high temperatures and vanishing net-baryon densities.

The high beam intensities provided by FAIR will enable CBM to focus its experimental program on systematic studies of rare particles. Among other particle species, open charm-carrying particles are one of the most promising observables to investigate the medium created in heavy-ion collisions since their charm quarks are exposed to the medium and traverse its whole evolution. The fact that the decay particles of these rare observables are also produced abundantly in direct processes in heavy-ion collisions results in a huge combinatorial background which attributes specific requirements to the detector systems. The call for a high interaction rate leads to a cutting-edge detector system which provides an excellent spatial resolution, thin detector stations and the capability to cope with the induced radiation as well as the high rate of traversing particles and the resulting track density.

The required demands are to be implemented by the MVD which will be equipped with four planar stations positioned at 50, 100, 150 and 200 mm downstream the target. The geometrical acceptance, which has to be covered with charge-sensitive material, is defined according to the requirements of CBM in the polar angle range of $[2.5^\circ, 25^\circ]$. The MVD stations have to contribute as little as possible to the overall material budget. The expected beam intensity and the vicinity close to the target require silicon detectors that provide a hardness against non-ionizing radiation of more than 10^{13} n_{eq}/cm² and against ionizing radiation of more than 1 Mrad. In addition, the read-out time of the sensors has to be as short as possible to avoid potential ambiguities in the particle tracking caused by the pile-up of hits having emerged from different collisions.

For the time being, Monolithic Active Pixel Sensors (MAPS) offer the optimal choice of technology required to address the physics program of CBM with respect to the spectroscopy of open charm and di-electrons. The geometrical properties of these sensors define the layout of the detector. To limit the multiple scattering of the produced particles inside the geometrical acceptance, the sensors and the MVD have to operate in a moderate vacuum.

The sensors are thinned down to a thickness of 50 μm and, to achieve a maximum polar angle coverage, they are glued onto both sides of dedicated thin carriers. These carriers, which are made of highly thermally conductive materials such as CVD diamond or encapsulated TPG, allow efficient extraction of the power produced in the sensors. This enables their operation at temperatures well below 0 $^{\circ}\text{C}$ as suggested by corresponding radiation hardness studies. Dedicated actively cooled aluminum-based heat sinks are positioned outside of the acceptance to dissipate the heat produced by the sensors and the front-end electronics. The design of the MVD, including the realistic thicknesses of the integrated materials, has been developed and refined in the context of this thesis. It has been transformed into a unique software model which is used to simulate and further optimize the mechanical and thermal properties of the MVD, as well as in sophisticated physics simulations. The model allowed evaluation of the material budget of each individual MVD station in its geometrical acceptance. The calculated averaged material budget values stay well below the material budget target values demanded by the physics cases. The thermal management of the MVD has been simulated on the level of a quadrant of each MVD station – four identically constructed quadrants are forming an MVD station – taking into account material properties of the sensors, the glue and the sensor carrier. The temperature gradients across the pixels of a given sensor area in the direction of the rows and columns were found to be in an acceptable range of below 5 K. A temperature difference between the thermal interface area and the maximum sensor temperature of $\Delta T \approx 5$ K on the first and a value of $\Delta T \approx 40$ K on the fourth MVD station has been thermally simulated assuming a sensor power dissipation of 0.35 W/cm², highlighting the need to optimize the thermal interface between the involved materials as well as the power dissipation of the sensors.

The feasibility of several key aspects required for the construction phase of the MVD has been investigated within the MVD Prototype project. The construction of the MVD Prototype allowed evaluation, testing and validation of the handling and the double-sided integration of ultra-thin sensors – the required working steps for their integration have been specified, evaluated and successfully established – as well as their operation in the laboratory and during a concluding in-beam test using high-energetic pions provided by the CERN-SPS. The thermal characterization of the MVD Prototype during its operation – in a temperature range from [5 $^{\circ}\text{C}$, 25 $^{\circ}\text{C}$], not in vacuum – confirmed the corresponding thermal simulations conducted during its design phase and substantiated the results of the thermal simulations for the design of the MVD. The aim of a material budget value of only $x/X_0 \sim 0.3\%$ for the MVD Prototype has been accomplished. Analyzing the in-beam data, the nominal sensor performance parameters were successfully reproduced, demonstrating that the proposed integration process does not impair the sensors' performance. Moreover, no evidence of potential impact on the sensors' performance arising from mechanical weaknesses of the MVD Prototype mechanics has been found within the analyzed data.

Based on the MVD Prototype and the simulations of the material budget as well as the thermal management, this thesis evaluated the work packages, procedures and quality assurance parameters needed to set up the starting version of the MVD and addressed open questions as well as critical procedures to be studied prior to the production phase of the detector, emphasizing the evaluation of the cooling concept in vacuum and the integration of sensors in ladder structures on both sides of the quadrants of the MVD stations.

Kurzfassung

Im Rahmen der vorliegenden Arbeit wurde die mechanische Integration des Mikrovertexdetektors (MVD) des *Compressed Baryonic Matter* (CBM)-Experimentes entwickelt. Das CBM-Experiment, welches an der zukünftigen Beschleuniger-Anlage FAIR aufgebaut wird, bezweckt das Phasendiagramm stark wechselwirkender Materie in der Region eines hohen baryo-chemischen Potentials bei zeitgleichen moderaten Temperaturen zu erforschen. Diese Bedingungen werden mithilfe von Schwerionenkollisionen, die gleichzeitig durch elementare Reaktionen unterstützt werden sollen, in einem Strahl-Energiebereich von 2 bis zu 45 AGeV erreicht. Die Messungen, die am LHC (CERN) und am RHIC (BNL/nicht innerhalb des *Beam Energy Scan*-Programms) mit Schwerionenexperimenten durchgeführt werden, zielen darauf ab, die Eigenschaften des Phasendiagrammes bei minimalem baryo-chemischem Potential und hohen Temperaturen zu untersuchen. Die hohen Strahlintensitäten an FAIR werden es dem CBM-Experiment erstmalig ermöglichen systematische Untersuchungen von seltenen Teilchen vorzunehmen. Neben anderen Teilchensorten, sollen hauptsächlich Teilchen mit schweren (charm-)Quarks verwendet werden, da diese bis zu ihrem Zerfall den vorherrschenden Bedingungen ausgesetzt sind und somit eine vielversprechende Observable des erzeugten Mediums darstellen. Spezielle Anforderungen werden dadurch an den Detektor gestellt, dass die Zerfallsteilchen dieser seltenen Observable infolge einer jeden Nukleon-Nukleon-Kollision in einer hohen Anzahl sowohl durch Teilchenzerfälle entstehen als auch direkt erzeugt werden und somit zu einem hohen Signaluntergrund beitragen. Die notwendige hohe Interaktionsrate erfordert einen innovativen Detektor mit einer ausgezeichneten Ortsauflösung, möglichst dünnen Detektorstationen, einer hohen Strahlenhärte und einer hohen Ratenfestigkeit.

Diese Anforderungen sollen mit dem MVD umgesetzt werden, der aus vier planaren Stationen bestehen wird, die in Abständen von 50, 100, 150 und 200 mm zum *Target* positioniert werden. Die geometrische Akzeptanz, die von jeder MVD-Station mit dem aktiven Bereich der Sensoren überdeckt werden muss, ist von CBM mit einem Polarwinkelbereich von $[2, 5^\circ, 25^\circ]$ vorgegeben; hierbei müssen die MVD-Stationen gleichzeitig ein minimales Material-Budget aufweisen. Die erwartete Strahlintensität in der Nähe zum *Target* erfordert eine Sensortechnologie, die über eine Strahlenhärte von mehr als 1 Mrad gegenüber ionisierender und 10^{13} n_{eq}/cm² gegenüber nicht-ionisierender Strahlung sowie über eine hohe Auslesegeschwindigkeit verfügt; diese Eigenschaften werden aktuell hauptsächlich von *Monolithic Active Pixel Sensors* bereitgestellt. Die Dimensionen der zukünftigen Sensoren definieren das Layout des Detektors, welche zur Reduzierung der Vielfachstreuung der produzierten Teilchen innerhalb der geometrischen Akzeptanz in einem moderaten Vakuum

betrieben werden müssen. Die maximale Abdeckung der Akzeptanz wird durch die doppel­seitige Integration der Sensoren auf spezialisierten und dünnen Sensoren­trägern ge­währ­leistet. Die Sensoren­träger, die aus hoch-wärmeleitfähigen Materialien, wie zum Beispiel CVD-Diamant oder eingefasstem *Thermal Pyrolytic Graphite* bestehen, ermöglichen die Ableitung der von den Sensoren erzeugten Verlustleistung aus der Akzeptanz des Detek­tors und deren Operation bei Temperaturen von unter 0 °C. Die außerhalb der Akzeptanz positionierten aktiv gekühlten Aluminium-Kühl­senken gestatten das Abführen der von den Sensoren und der in deren Nähe positionierten Auslese­elektronik erzeugten Verlustleistung. Anhand dieser Anforderungen wurde in der vorliegenden Arbeit eine detaillierte Geometrie des MVDs entwickelt. Diese Geometrie wurde in eine Darstellung übertragen, die es ermög­licht, das mechanische und thermische Verhalten des MVDs zu simulieren und zu optimie­ren, und die in differenzierten Physiksimulationen eingesetzt werden kann. Mit dieser Dar­stellung konnte das Material-Budget der einzelnen MVD-Stationen untersucht werden und die extrahierten und über die definierte Akzeptanz gemittelten Werte des Material-Budgets zeigen, dass die festgelegten Zielwerte für die jeweiligen MVD-Stationen unterboten werden konnten. Das thermische Verhalten der durch die Sensoren, den Kleber und die Senso­ren­träger gebildeten Einheit wurde für jede MVD-Station simuliert. Dabei konnten die Tem­peraturgradienten entlang der Pixel­spalten und Pixel­zeilen der Sensoren zu je weniger als 5 K bestimmt werden; diese liegen in einem akzeptablen Bereich. Die Differenz zwischen der maximalen Sensortemperatur und der an der thermischen Kontaktfläche gemessenen Tem­peratur (−20 °C) betrug auf der ersten MVD Station 5 K und auf der vierten Station 40 K; die Notwendigkeit zur Optimierung der Temperaturübergänge zwischen den Materialien sowie der Verlustleistung der Sensoren ist somit gegeben. Die Realisierung von wichtigen Kriterien für die Konstruktionsphase des MVDs wurde im Rahmen des MVD Prototyp-Projektes untersucht. Die Konstruktion des MVD Prototypen ermöglichte die Erprobung der Handhabung und der doppel­seitigen Integration von dünnen Sensoren, deren Verklebung sowie deren Betrieb im Labor und während einer Teststrahlzeit mit minimal ionisierenden Teilchen (Pionen) am CERN-SPS. Die thermische Charakterisierung des MVD Prototypen während dessen Betriebs – in einem Temperaturbereich von [5 °C, 25 °C], nicht im Vakuum – bestätigte die durchgeführten thermischen Simulationen während der Planungsphase und bekräftigte die Ergebnisse der thermischen Simulationen für das Design des MVDs. Das Material-Budget-Ziel des MVD Prototypen von nur maximal $x/X_0 = 0,3\%$ konnte erreicht werden. Die Analyse der in der Teststrahlzeit gewonnenen Daten zeigte, dass die intrin­sische Auflösung der Sensoren reproduziert werden konnte. Dabei konnte kein Einfluss des angewendeten Integrationsprozesses auf die Funktionstüchtigkeit der Sensoren festgestellt und die mechanische Stabilität der Halterung der Sensoren bestätigt werden.

Basierend auf dem MVD Prototypen und den durchgeführten Simulationen des ther­mischen Managements und des Material-Budgets wurden in dieser Arbeit wichtige Arbeits­schritte, Prozeduren und Qualitätssicherungsaspekte, die für die Konstruktion des MVDs am SIS100 von entscheidender Bedeutung sind, diskutiert und wichtige Fragen wie zum Bei­spiel die notwendige Evaluierung des Kühlkonzeptes im Vakuum sowie der Integrationspro­zess von Sensoren in Leiterstrukturen auf beiden Seiten der Quadranten der MVD-Stationen beleuchtet.

Contents

Abstract	III
Kurzfassung	V
Contents	V
List of Figures	VIII
List of Tables	XII
1 Introduction	1
2 Heavy-Ion Collisions and the Strong Interaction	4
2.1 Heavy-Ion Collisions	4
2.2 The QCD Phase Diagram	5
2.2.1 Rare Observables	9
2.2.2 Demands on the Tracking and Vertexing Detectors	14
2.3 The CBM Experiment	15
2.3.1 The Dipole Magnet	17
2.3.2 The Micro Vertex Detector	17
2.3.3 The Silicon Tracking System	17
2.3.4 The Ring Imaging Cherenkov Detector	18
2.3.5 The Transition Radiation Detector	18
2.3.6 The Muon Chamber System	18
2.3.7 The Timing Multi-Gap Resistive Plate Chambers	19
2.3.8 The Electromagnetic Calorimeter	19
2.3.9 The Projectile Spectator Detector	19
2.3.10 The Online Event Selection and Data Acquisition	19
3 Requirements for the MVD Design	21
3.1 Requirements Derived from the Physics Cases	21
3.1.1 Acceptance Coverage	22
3.1.2 Vertex Resolution, Material Budget and Spatial Resolution	25
3.1.3 Radiation Hardness Demands on the MVD	30
3.1.4 Track matching across STS and MVD	31

3.1.5	Read-Out Speed and Granularity	31
3.2	The MVD Sensor Technology	33
3.3	Requirements Derived from Operation Conditions	37
3.3.1	Requirements from the Vacuum Operation	37
3.3.2	Requirements from the Configuration of the MVD	37
3.3.3	Requirements from Spatial Restrictions	38
3.4	Summary	39
4	Design Proposal of the MVD	41
4.1	Design Approach	41
4.1.1	Sensor Geometry	44
4.1.2	Sensor Arrangement	45
4.1.3	Sensor Support and Thermal Management	51
4.1.4	Mechanical Properties of the Flex Print Cable	66
4.1.5	Support Structures inside the Vacuum Vessel	67
4.1.6	The MVD Vacuum Vessel	70
4.2	The MVD in Physics Simulation	71
4.2.1	CAD to ROOT-Transformation	71
4.2.2	Examination of the Transformation Process	75
4.3	Summary	83
5	The MVD Prototype Project	85
5.1	The Components of the MVD Prototype and the Reference Planes	88
5.1.1	The Sensor: MIMOSA-26 AHR	90
5.1.2	The Sensor Carriers	92
5.1.3	The Glue	92
5.1.4	The Heat Sink	95
5.1.5	The Flex Print Cable	95
5.2	Thermal and Material Budget Simulations of the MVD Prototype	96
5.2.1	Thermal Simulations Using the Example of the MVD Prototype	96
5.2.2	Material Budget of the MVD Prototype	100
5.3	The Construction of the MVD Prototype and the Reference Planes	101
5.3.1	The Mechanical Handling of Ultra-Thin CMOS Sensors	101
5.3.2	Integration Process of the MVD Prototype and the Reference Planes	104
5.3.3	Evaluation of the Sensor Distances in the “Core Modules”	114
5.3.4	The Grounding Concept of the MVD Prototype and the Reference Planes	116
5.4	Evaluation in the Laboratory	117
5.4.1	Thermal Measurements Using the MVD Prototype	117
5.4.2	Commissioning of the MVD Prototype in the Laboratory	124
5.5	In-Beam Test	126
5.5.1	In-Beam Set-Up	126
5.5.2	In-Beam Running Conditions	132
5.5.3	Data Analysis	132

5.5.4	Sensor In-Beam Performance	134
5.6	Summary and Discussion	147
6	Towards the MVD at SIS100 - Discussion	149
7	Summary and Outlook	156
	Zusammenfassung	159
A	Physics Case	168
A.1	Observables	168
B	Requirements for the MVD Design	172
C	Design Proposal of the MVD	183
D	MVD Prototype Project	206
D.1	Estimation of the Air Pocket Pressure Resulting on the Sensor	206
D.2	Estimation of the Heat Extracted from a Single Sensor via Thermal Radiation and Convection	207
D.3	Thermal Simulations of the MVD Prototype	209
D.4	Material Budget of the MVD Prototype	211
D.5	The Sensor Carriers of the Reference Planes	211
D.6	The Mechanical Handling of the Ultra-Thin CMOS Sensors	212
D.7	The Two-Sensor Positioning-Tool	213
D.8	Impact of Wrongly Diced Sensors on their Edge-to-Edge Positioning	214
D.9	Construction Steps of the Reference Planes	215
D.10	Evaluation of the Sensor Distances in the “Core Modules”	217
D.11	Temperature Measurements on the MVD Prototype Sensors and the Reference Plane Sensors	218
D.12	In-Beam Set-Up	222
D.13	Data Analysis	226
E	Towards the MVD at SIS100	236
	Bibliography	237

List of Figures

2.1	Sketch of the QCD phase diagram	6
2.2	D -meson decay trajectories	10
2.3	Simulated invariant mass spectrum for D^+	11
2.4	Simulated invariant mass spectrum for e^+e^-	13
2.5	Simulated decay length distribution for D^0 and D^+	15
2.6	CBM detector configurations	16
3.1	P_T - y -distributions of accepted D^0 decay products assuming a thermal source with the properties of $T = 120$ MeV and $E_{\text{beam}} = 25$ AGeV	24
3.2	Sketch of the parameters contributing to the secondary vertex resolution	26
3.3	Evaluation of the geometrical and the multiple scattering contribution of the position resolution	27
3.4	Momentum distribution of the accepted D -meson decay particles	28
3.5	Dependency of the secondary vertex resolution as a function of the spatial resolution and the thickness of the first two MVD stations	30
3.6	Occupancy distribution on the first MVD station	32
3.7	Working principle of MAPS	34
3.8	Sketch of the electronic working scheme of MAPS	35
3.9	Selected dependencies within the MVD	40
4.1	Design Proposal of the MVD - overview	43
4.2	The sensor of the MVD: MIMOSIS-1	45
4.3	Simulated incident angles of particles on the MVD stations	47
4.4	Sensor arrangement on the first MVD station	48
4.5	The first MVD station	49
4.6	Properties of materials used for the sensor carriers: Thermal conductivity versus Young's modulus	53
4.7	Components of the thermal management of the first MVD station	58
4.8	Sketch of the heat flow	59
4.9	Thermal simulation: Arrangement of the components	61
4.10	Thermal simulation: Results for the first MVD station	64
4.11	Thermal simulation: An overview of the results	65
4.12	Half-station support structure of the first MVD station	68
4.13	Design Proposal of the MVD	69

4.14	MVD positioned in the CBM Magnet	70
4.15	Naming convention and transformation of the MVD from CAD to ROOT	73
4.16	MVD within the simulation framework	74
4.17	Simulated particle hits on the first and the third MVD station	76
4.18	Simulated material budget of the first and the third MVD station in the small φ -range	81
4.19	Simulated material budget of the first and the third MVD station in the complete φ -range	82
5.1	Sketch of the MVD Prototype and the reference planes	87
5.2	Sketch of the components of the “core module”	89
5.3	The MIMOSA-26 sensor	91
5.4	Glue dispensing techniques	93
5.5	Glue dispensing results	94
5.6	Arrangement of the double-sided module within the thermal simulation framework	97
5.7	Thermal simulation of the double-sided module for an interface area temperature of 19 °C	99
5.8	Tool for the positioning of a single sensor	102
5.9	Final tool for the positioning and gluing of two sensors at once	103
5.10	Integration steps for the “core module”	104
5.11	Double-sided positioning- and gluing-tool	105
5.12	Integration of the FPC into the “core module”	107
5.13	The double-sided module of the MVD Prototype	107
5.14	The heat sink of the MVD Prototype	109
5.15	The completed assembly of the MVD Prototype	110
5.16	The MVD Prototype	112
5.17	Sketch of the reference planes at different stages during the sensor integration process	113
5.18	The set-up of a reference plane	113
5.19	Evaluated distances between the sensors in a “core module”	115
5.20	Block diagram of the distribution of the grounding	117
5.21	Extraction of the calibration parameter for the temperature measurements on the MVD Prototype sensors	119
5.22	MVD Prototype sensors: Infrared versus real	120
5.23	MVD Prototype sensors: Temperature gradients across the surface of the sensors	121
5.24	MVD Prototype sensors: Absolute temperatures on the sensors	121
5.25	MVD Prototype sensors: Correlated response to electrons emitted by a strontium source	125
5.26	Sketch of the in-beam test set-up	127
5.27	Sketch of sensor arrangement in the in-beam test	128
5.28	Sketch of the read-out scheme for the sensor data	129
5.29	In-beam test set-up: Installed MVD Prototype and reference planes	131

5.30	Temperature dependence of the efficiency of the MVD Prototype sensors . . .	136
5.31	Efficiency of the MVD Prototype sensors as function of the applied threshold settings	137
5.32	Residuals of the MVD Prototype sensors	140
5.33	Fake hit rate of the MVD Prototype sensors as function of the temperature .	141
5.34	Shift of the Prototype sensors within a data set	144
5.35	Possible vibration frequencies	146
A.1	Particle multiplicity as function of the energy (HSD approach)	168
A.2	Track definition for the e^+e^- -pairs	170
B.1	P_t - y -distributions of accepted D^- decay products assuming a thermal source with the properties of $T = 120$ MeV and $E_{\text{beam}} = 25$ AGeV	173
B.2	P_t - y -distributions of accepted D^+ decay products assuming a thermal source with the properties of $T = 120$ MeV and $E_{\text{beam}} = 25$ AGeV	174
B.3	P_t - y -distributions of accepted D^0 decay products assuming a thermal source with the properties of $T = 100$ MeV and $E_{\text{beam}} = 17$ AGeV	175
B.4	P_t - y -distributions of accepted D^- decay products assuming a thermal source with the properties of $T = 100$ MeV and $E_{\text{beam}} = 17$ AGeV	176
B.5	P_t - y -distributions of accepted D^+ decay products assuming a thermal source with the properties of $T = 100$ MeV and $E_{\text{beam}} = 17$ AGeV	177
B.6	P_t - y -distributions of D^0 s for which the decay particles have been accepted assuming a thermal source with the properties of $E_{\text{beam}} = 25$ AGeV, $T = 120$ MeV and $E_{\text{beam}} = 17$ AGeV, $T = 100$ MeV	178
B.7	P_t - y -distributions of D^- for which the decay particles have been accepted assuming a thermal source with the properties of $E_{\text{beam}} = 25$ AGeV, $T = 120$ MeV and $E_{\text{beam}} = 17$ AGeV, $T = 100$ MeV	179
B.8	P_t - y -distributions of D^+ for which the decay particles have been accepted assuming a thermal source with the properties of $E_{\text{beam}} = 25$ AGeV, $T = 120$ MeV and $E_{\text{beam}} = 17$ AGeV, $T = 100$ MeV	180
B.9	Occupancy distribution on the MVD stations 1, 2 and 3	181
B.10	Creation of the ionizing radiation damage	182
B.11	Available space for the MVD inside the CBM magnet	182
C.1	Sensor arrangement on the first MVD Station - vertical arrangement	184
C.2	The first MVD station - vertical arrangement	185
C.3	Sensor arrangement on the second MVD station	186
C.4	Sensor arrangement on the third MVD station	187
C.5	Sensor arrangement on the fourth MVD station	188
C.6	Calculation of the thickness of the CVD diamond sensor carriers	189
C.7	Thermal conductivities of the materials in the thermal simulation framework	190
C.8	Heat sinks of the MVD stations 1, 2 and 3	191
C.9	Thermal simulation: Results for the second MVD station	193
C.10	Thermal simulation: Results for the third MVD station	194

C.11	Thermal simulation: Results for the fourth MVD station	195
C.12	Half-station support structure of the MVD stations 1, 2 and 3	196
C.13	Base plates for the positioning of the MVD half-stations	197
C.14	Simulated particle hits on all MVD stations	198
C.15	Simulated particle hits on the second and the fourth MVD station	199
C.16	Simulated material budget for the second and the fourth MVD station in the small φ -range	200
C.17	Simulated material budget for the second and the fourth MVD station in the complete φ -range	201
C.18	Cross-sectional view of the material budget of the first and the third MVD station	202
C.19	Cross-sectional view of the material budget for the second and the fourth MVD station	203
D.1	Thermal simulation of the double-sided module for an interface area temperature of 10 °C	209
D.2	Thermal simulation of the double-sided module for an interface area temperature of 0 °C	210
D.3	Contributions to the material budget of the MVD Prototype	211
D.4	Sensor carriers of the reference planes	211
D.5	Tools for the positioning of two sensors	213
D.6	Positioning of wrongly diced sensors	214
D.7	Construction of the references planes: Step 1 - 6	215
D.8	Construction of the references planes: Step 7 - 11	216
D.9	Reference planes: Absolute temperature on the sensors	219
D.10	Reference planes: Infrared picture of the sensors	220
D.11	MVD Prototype sensors: Simulated and measured temperature gradients across the sensor's surface for different power dissipation values of the on-chip electronics	221
D.12	In-beam test set-up: The base plate	222
D.13	In-beam test set-up: The cooling distribution system of the reference planes (sketched)	223
D.14	In-beam test set-up: The cooling system of the reference plane	224
D.15	In-beam test set-up	225
D.16	Data analysis: Degrees of freedom and tracking method	227
D.17	Temperature dependence of the average cluster multiplicity	228
D.18	Temperature dependence of the residuals of the MVD Prototype sensors	230
D.19	Vibration evaluation: Distance distribution reference plane tracks to MVD Prototype hits	231
D.20	Vibration evaluation: Possible frequencies	232
D.21	Vibration evaluation: ProfileX distribution and fast Fourier transform	233
E.1	The geometry of the MVD: 1 : 1 mock-up	236

List of Tables

2.1	Heavy-ion experiments investigating the QCD phase diagram	8
2.2	Properties of the D -mesons	9
2.3	Properties of the mesons	12
3.1	Acceptance coverage	23
3.2	Yield of D -mesons accepted with the MVD, STS and TOF normalized to the yield of D -mesons accepted with the STS and TOF only	23
3.3	Material budget target values	30
3.4	Radiation hardness demands	31
4.1	Envisioned performance of the MIMOSIS-1 sensor	44
4.2	Number of required MIMOSIS-1 sensors	50
4.3	Dimensions of the sensor carriers	52
4.4	Physical properties of materials used for the sensor carriers	54
4.5	Calculation of the thickness of the CVD diamond sensor carriers	56
4.6	Parameters for the simulation of the thermal management of the individual quadrants	62
4.7	Number of required FPCs	67
4.8	Naming convention of the MVD sensors	72
4.9	Contributions of the integrated materials to the material budget of the MVD	77
4.10	Average material budget values of the individual MVD stations	80
5.1	Properties of the “core module” components	89
5.2	Properties of the investigated glues	93
5.3	Parameters for the simulation of the thermal management of the double-sided module	97
5.4	MVD Prototype sensors: Overview of the simulated temperatures	98
5.5	Material budget of the MVD Prototype	100
5.6	MVD Prototype sensors: Comparison of the measured and simulated absolute temperatures on the sensors	122
5.7	Applied sensor running conditions for the evaluation of the sensor in-beam performance	134
A.1	Simulated data sample for D -mesons: Selection of signal candidates	169
A.2	Simulated data sample for D -mesons: Background suppression	169

A.3	Simulated data sample for mesons decaying in e^+e^- : Background suppression	171
C.1	Dimensions of the heat sinks of the MVD	189
C.2	Thermal simulation: An overview of the results	192
C.3	Dimensions of the half-station support structures of the MVD	192
C.4	The material budget of the first MVD station as a function of the distance to the beam axis for both φ -intervals	198
C.5	The material budget of the third MVD station as a function of the distance to the beam axis for the small φ -interval	198
C.6	The material budget of the third MVD station as a function of the distance to the beam axis for the outer areas of the quadrants for the complete φ -interval	204
C.7	The material budget of the second MVD station as a function of the distance to the beam axis for both φ -intervals	204
C.8	The material budget of the fourth MVD station as a function of the distance to the beam axis for the small φ -interval	204
C.9	The material budget of the fourth MVD station as a function of the distance to the beam axis for the outer areas of the quadrants for the complete φ -interval	205
D.1	Properties of nitrogen	208
D.2	Evaluated sensor distances in a “core module”	217
D.3	Evaluated pixel-to-pixel-distances in a “core module”	217
D.4	MVD Prototype sensors: Absolute temperatures on the sensors	218
D.5	Reference planes: Absolute temperatures on the sensors	219
D.6	Sensitivity of the alignment parameters	227
D.7	Sensitivity of residuals and the pointing resolution	228
D.8	Contribution of the multiple scattering to the sensor pointing resolution	229
D.9	Vibration evaluation: Extracted frequencies	234
D.10	Thermal expansion of the “core module” components	235

Chapter 1

Introduction

The subject of this thesis is part of the development of the Micro Vertex Detector for the Compressed Baryonic Matter (CBM) experiment. The CBM experiment is one of the major experiments being set up at the future Facility for Antiproton and Ion Research (FAIR), which is under construction at the GSI Helmholtzzentrum für Schwerionenforschung in Darmstadt, Germany.

The CBM experiment aims at the investigation of the phase diagram of strongly interacting matter in the region of high net-baryon densities and moderate temperatures. Heavy-ion collisions at beam energies in the range of 2 to 45 AGeV provided by the SIS100/300 accelerators will be used to facilitate this investigation. The CBM research program comprises the search for the onset of the phase transition between hadronic and partonic matter, the search for the possible critical endpoint of the first-order phase transition and the study of in-medium effects in dense baryonic matter [1].

The studies require two different kinds of observables in terms of produced particles. In this thesis, the discussion of observables is limited to the ones of interest in context of the operation of the MVD. First, since charm quarks – their production is understood to occur in first-chance (hard) collisions in the early phase of a heavy-ion collision – traverse the whole evolution of the medium, the hadronized charm carrying particles are promising observables for the study of the created medium. Second, particles like electron-positron-pairs which can leave – after their “creation” from a vector meson decay in the medium – the strongly-coupled medium without being further distorted due to their electromagnetic coupling. These particles offer a clean signal of the properties of their mother particle. The measurements of both observables, open charm and di-electrons, attribute highly specific requirements to the experiment which aims to study their properties in nucleus-nucleus collisions. In the di-electron case, the branching ratios of the vector mesons into e^+e^- -pairs are of about 10^{-5} and below. The corresponding ratios for open charm particles are in the order of 10^{-2} . These two facts call for a high interaction rate. The accelerators (SIS100/300) at FAIR will provide beams with an intensity of 10^9 ions per second and more for Au-ions, thus requiring new detector systems which are capable of coping with the induced radiation as well as the high flux of traversing particles.

Due to their short lifetime, e.g., D^0 -mesons are decaying after $c\tau = 123 \mu\text{m}$ in the center-of-mass system, the reconstruction of open charm particles can only be accomplished by identifying their decay particles. The decay into pions and kaons is the dominant decay channel of open charm particles. At the same time, such particles can also be produced in direct processes which occur several orders of magnitude more frequently. The combinatorial background which arises by combining all charged particles in a decay channel of open charm of one collision can be reduced by the identification of the decay vertex of the open charm particles which is a clear signature of this process. The short lifetime of the open charm particles as well as the high track density of more than 700 charged particles per Au+Au-collision at 25 AGeV calls for a vertex detector capable of providing excellent spatial resolution to distinguish the decay vertex of the open charm particles, the secondary vertex, from the primary collision vertex.

The vertex detector in the CBM experiment, the Micro Vertex Detector (MVD), has to provide this excellent spatial resolution as well as high granularity. A high radiation hardness of the sensor technology integrated into the MVD is mandatory to position the first detector station as close as possible to the target to ensure the reconstruction of the secondary decay vertex with an excellent resolution. The MVD stations have to be as thin as possible with respect to the material budget to limit the multiple scattering of the particles in the MVD stations so as not to deteriorate the precision of the secondary vertex measurement. The multiple scattering of the particles will be further reduced by the in-vacuum operation of the MVD. The MVD will be equipped with Monolithic Active Pixel Sensors (MAPS) which offer the best compatibility with the above-mentioned requirements as well as an excellent perspective to improve the technology in aspects in which compatibility has not been achieved yet.

This thesis is a contribution to the design and the development of the Micro Vertex Detector of the CBM experiment. It elaborates on the mechanical integration of the MVD. It can be divided into two main parts: The first presents a design and design aspects developed to meet the requirements imposed by the performance criteria outlined above by the open charm and the di-electron physics cases. The second part is devoted to testing the feasibility of several key design aspects by means of simulations, prototyping as well as laboratory and in-beam tests.

The thesis is structured as follows:

In Chapter 2, the phase diagram of strongly interacting matter is introduced and the possibilities to investigate this phase diagram using heavy-ion collisions in the laboratory are presented. In discussing the CBM experiment, particular emphasis is placed on the open charm and the di-electron physics cases in which the MVD is contributing to the measurements.

In Chapter 3, the requirements attributed to the Micro Vertex Detector from the open charm and the di-electron physics cases as well as from the operation conditions are introduced. In addition, the above-mentioned sensor technology used to equip the MVD stations will be presented.

In Chapter 4, the design proposal of the MVD is presented. Furthermore, the design proposal

is converted to a format compatible with the physics simulation framework of CBM, thus allowing for further studies focusing on the material budget of the MVD.

The MVD Prototype project, presented in Chapter 5, concentrates on the development, the integration and the construction of the MVD Prototype. The construction of this detector calls for various strategies for the mechanical handling and integration of the ultra-thin MAPS, as well as the required thermal management of the materials involved. The MVD Prototype has subsequently been tested in the laboratory and an in-beam test at the CERN-SPS. At the end of Chapter 5, the data recorded during this in-beam test is analyzed and the performance of the MVD Prototype is evaluated.

The thesis concludes with a detailed discussion of the steps that have already been taken and those steps remaining to be taken in the near future for the construction of the MVD as being operated at SIS100.

Chapter 2

Heavy-Ion Collisions and the Strong Interaction

The interaction of the constituents of matter is governed by the strong force described by the theory of Quantum Chromo Dynamics (QCD). The charge of the strong interaction is called color, carried by quarks, the smallest known constituents of matter, and by gluons, representing the force carriers of the strong interaction. Only color neutral objects are realized in nature. These color neutral states are formed by combining three quarks carrying different color, or by the combination of a quark and an antiquark which carry color and anticolor, respectively. Gluons carry the strong charge themselves which allows them to interact also among each other. In QCD, observables cannot be calculated exactly for all energies since the coupling strength α_s strongly depends on the momentum transfer. For a large momentum transfer, α_s becomes small and can be described using the perturbation theory. On the other hand, for small momentum transfers, α_s becomes large so that the description of the interactions can only be approximated using effective models and lattice QCD.

2.1 Heavy-Ion Collisions

The investigation of strongly interacting systems can be conducted in the laboratory using heavy-ion collisions. During a heavy-ion collision, the created system passes through different evolution stages. The first two can be named with first-chance collisions and the transition to a hot and dense phase, provided the energy of the colliding ions is high enough. The system is expanding continuously as different evolution stages are reached. In the chemical freeze-out stage, the particle identity is being defined and in the kinetic freeze-out stage, the momenta of the particles are determined.

The particle production in heavy-ion collisions at various energies can be described using a hadro-chemical model which allows calculation of particle densities based on chemical freeze-out temperatures T and (baryo-)chemical potentials μ . A sharp rise of the determined temperature with increasing beam energy has been observed while for higher collision ener-

gies ($\sqrt{s_{NN}} > 10$ GeV), a constant temperature value of around 160 MeV is found [2]. Such a limiting temperature is also predicted by lattice QCD calculations [3]. At the same time, the baryo-chemical potential is decreasing smoothly as a function of the energy [2].

2.2 The QCD Phase Diagram

Our current knowledge of strongly interacting matter can be summarized in the QCD phase diagram presented in Figure 2.1. The matter under study is characterized using two thermodynamical variables, the temperature T and the baryo-chemical potential μ_B . The phase diagram can be roughly divided into two regimes, namely, the hadronic regime and the Quark-Gluon Plasma (QGP) regime [4]. In the hadronic regime, located in the lower left-hand corner of the QCD phase diagram, matter is confined to hadrons. For the ground state at $T = 0$, the matter is bound to nucleons and is forming atomic nuclei. In the regime of the Quark-Gluon Plasma, the constituents of the hadrons, quarks and gluons, are no longer confined and can move freely.

In principle, two different paths are possible for the transition between the hadronic and the Quark-Gluon Plasma regime. For the first path, only the temperature T of the matter under study is raised to high values and the baryo-chemical potential μ_B is kept small and constant. The second path is characterized by a variation of both thermodynamical variables resulting in a moderate temperature T as well as a high baryo-chemical potential μ_B . For both paths, the transition from the hadronic to the QGP regime is predicted to be indicated by a large increase of the number of degrees of freedom [5]. The path for which the baryo-chemical potential μ_B is fixed to a small value and the temperature is increased, the transition between the two regimes is predicted to be a rapid crossover which is expected to be located in a temperature range of 150 – 200 MeV [3]. For the second path, a first-order phase transition is predicted. The rapid crossover between the QGP phase and the hadronic phase and the first-order phase transition are expected to converge in the predicted so-called critical point [6, 7].

Recently, the possible existence of an additional regime within the QCD phase diagram, the Quarkyonic regime, has been predicted [5]. This regime is expected to be located in the region of moderate temperature T and high baryo-chemical potential μ_B . The properties of matter after its transition from the hadronic regime to the Quarkyonic one are still under debate nowadays [5].

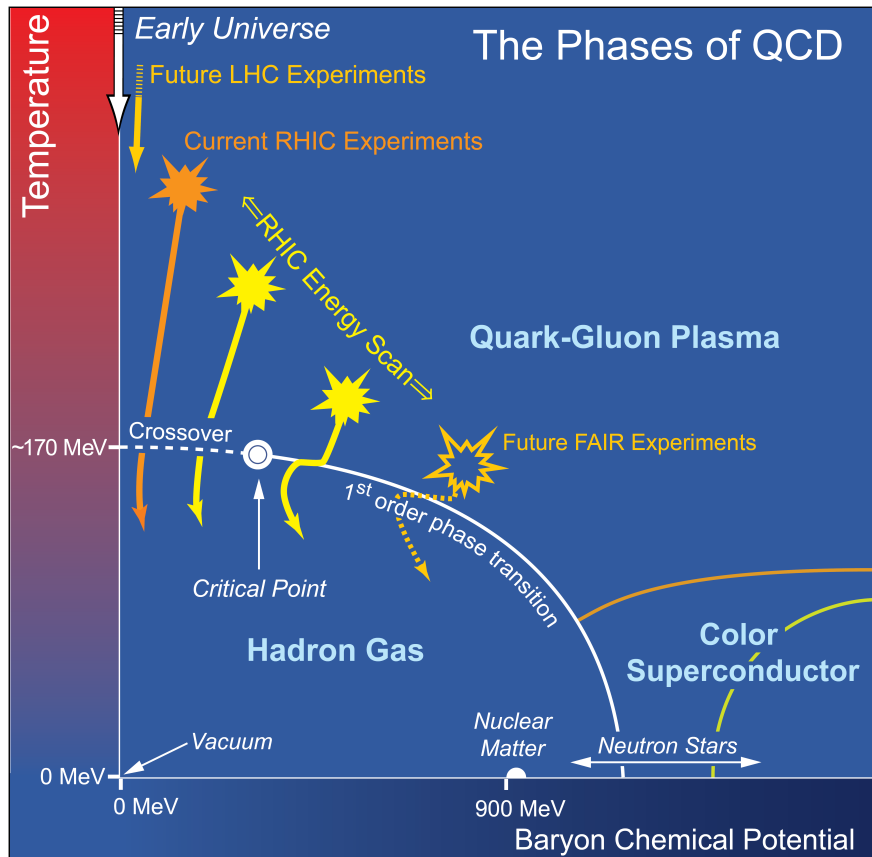


Figure 2.1: The sketch of the QCD phase diagram of strongly interacting matter is shown qualitatively as a function of the baryon chemical potential and the temperature. The dashed line represents the crossover phase transition from the confined hadronic matter to the deconfined Quark-Gluon Plasma. The solid line represents a first-order phase transition. The mutual convergence of the different types of phase transitions defines the critical point. The figure is taken from [4].

The Experimental Investigation of the QCD Phase Diagram

The experimental investigation of the QCD phase diagram is conducted by use of heavy-ion collisions at the facilities LHC¹, SPS², RHIC³, SIS18⁴ and in the future at FAIR⁵. At AGS⁶, the experimental program has been completed. The beam energies available at the different experimental facilities are listed in Table 2.1.

At LHC, the QCD phase diagram is investigated in the regime of vanishing baryo-chemical potential and high temperatures. The matter is formed at very high temperatures, cools down, and crosses the cross-over region from the QGP regime to the hadronic regime. The experimental apparatuses ATLAS [8], CMS [9] and ALICE [10] are investigating this matter.

The STAR detector [11] is using collision energies of up to 200 GeV⁷ per nucleon, which are provided by RHIC, for investigations in the same temperature-baryo-chemical-potential region as the physics program at LHC. In addition, within the RHIC Beam Energy Scan program ranging from 200 GeV down to 7.7 GeV [12], the QCD phase diagram is investigated in the region of higher baryo-chemical potential. Given the collider set-up at RHIC being optimized for high injection energies of the beam particles, the beam luminosity which can be provided for experiments in the low energy regime (below 7.7 GeV) is limited. As a result of this, the collection of the required statistics to allow for detailed investigations of rare observables at low beam energies appears to be challenging.

The NA61/SHINE detector [13] studies the QCD phase diagram in the lower regions of the Beam Energy Scan program using various collision energies from 5.3 to 16.9 GeV at SPS. The region of lower beam energies and high baryo-chemical potential has been explored with heavy-ion experiments at the AGS using collision energies of 2.7 to 4.9 GeV [14]. At this facility, due to limited statistics only bulk observables (e.g., pions, protons and kaons) have been investigated.

The HADES experiment studies the QCD phase diagram in the region of lower temperatures and high baryo-chemical potential using beam energies of 2.4 to 3.2 GeV provided by SIS18.

The accelerators at the future FAIR facility will provide high beam intensities and beam energies⁸ from 2.7 to 13.1 GeV sufficient to study the produced medium using rare ob-

¹Large Hadron Collider (LHC) at CERN, Geneva, Switzerland.

²Super Proton Synchrotron (SPS) at CERN, Geneva, Switzerland.

³Relativistic Heavy Ion Collider (RHIC) at Brookhaven, USA.

⁴Schwerionensynchrotron (SIS) 18 at GSI, Darmstadt, Germany.

⁵Facility for Antiproton and Ion Research (FAIR) at GSI, Darmstadt, Germany.

⁶Alternating Gradient Synchrotron (AGS) at Brookhaven, USA

⁷The beam energies available at the different facilities depend on the collision system chosen and are presented in the center-of-mass-system unless stated otherwise.

⁸At FAIR, the maximal accelerator energies available will differ depending on the point in time. Using SIS100 which will be built first, energies of up to 4.9 GeV for Au, 5.5 GeV for Ca, and 7.6 GeV for protons will be delivered. After the completion of SIS300, energies of 8.3 GeV for Au and 13.1 GeV for protons will be provided. The numbers are taken from [7] and transformed into the center of mass system. They are valid for symmetric collision systems.

Accelerator facility	Beam energy in the center of mass system $\sqrt{s_{NN}}$ [GeV]	Experiments	HIC physic program
LHC	450 – 7000	ATLAS, CMS, ALICE	ongoing
RHIC	200	STAR, PHENIX	ongoing
RHIC-BES	7.7 – 200	STAR, PHENIX	ongoing
SPS	5.3 – 16.9	NA61/SHINE, NA60, CERES	ongoing/completed
AGS	2.7 – 4.9	E802,...	completed
SIS18	2.4 – 3.2	HADES, FOPI	ongoing
SIS100(300)	2.7 – 13.1	CBM	under construction

Table 2.1: Heavy-ion experiments investigating the QCD phase diagram using different beam energies.

servables. The Compressed Baryonic Matter (CBM) experiment will allow for systematic investigations of the QCD phase diagram in the region of moderate temperature and moderate to higher baryo-chemical potential with the required statistics. The CBM experiment is optimized with respect to the detection of rare observables like open charm and di-electrons which both feature very low production cross-sections in the channels of interest.

2.2.1 Rare Observables

Open Charm

The production of charm quarks is understood to occur in first-chance (hard) collisions in the early phase of a heavy-ion collision where the energy density is highest [15]. Since charm quarks traverse the whole evolution of the medium, the hadronized charm carrying particles are promising observables for the study of the created medium. Given the low production cross-section of the D -mesons and their branching ratios listed in Table 2.2, a high interaction rate is required to accumulate high statistics achieving a sufficient measurement accuracy. Calculations with the HSD⁹ transport model result in D -meson multiplicities of about $10^{-5} - 10^{-6}$ in central Au+Au-collisions at a beam energy of 25 AGeV, see Figure A.1 in the Appendix and [15]. However, due to their short life times, D -mesons cannot be detected directly. Assuming a beam collision energy of 25 AGeV Au+Au, the decay length of the D^\pm -mesons can be estimated to $c \tau \gamma \beta = 312 \mu\text{m} \times 3.8 \approx 1200 \mu\text{m}$, whereby in this special case $\gamma \beta = 3.8$ [16]. For the D^0 -meson and $\overline{D^0}$ -meson, the decay length can be calculated to a value of $c \tau \gamma \beta \approx 500 \mu\text{m}$. Therefore, the first MVD station will not be able to detect D -mesons but their decay particles which are (a) pion(s) and a kaon. The fact that these decay particles are also produced abundantly in direct processes in each heavy-ion collision, resulting in a huge combinatorial background in the signal, requires the identification of the decay vertex of the D -mesons, the secondary vertex. To achieve this, an excellent vertex resolution of the MVD is mandatory to separate the pion and kaon tracks coming from the primary vertex from those pion and kaon tracks which are decay particles of the D -mesons and which originate from the secondary vertex. This situation is exemplarily shown in Figure 2.2 for the decay of $D^+ \rightarrow \pi^+ \pi^+ K^-$. The identification of the secondary vertex is the main task of the MVD in the open charm physics case.

A recent simulation of the capability of the CBM detector to reconstruct and identify D -

⁹HSD is the acronym for Hadron-String Dynamics transport approach, developed at the Justus Liebig University Gießen and Goethe University Frankfurt.

	Quark content	Mass [MeV/c ²]	Lifetime $c \times \tau$ [μm]	Branching ratio	
				Channel	[%]
D^+	$c \bar{d}$	1869.62	312	$K^- \pi^+ \pi^+$	9.13 ± 0.19
D^-	$\bar{c} d$			$K^+ \pi^- \pi^-$	
D^0	$c \bar{u}$	1864.86	123	$K^- \pi^+$	3.88 ± 0.05
$\overline{D^0}$	$\bar{c} u$			$K^+ \pi^-$	

Table 2.2: The properties of the most common D -mesons to be studied with the CBM detector. The numbers are taken from [17].

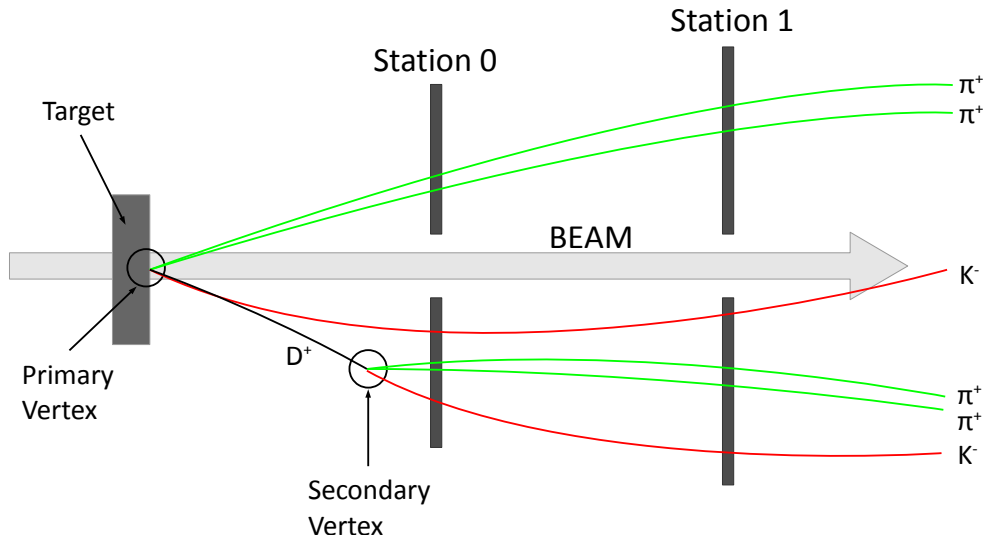


Figure 2.2: Sketch of the trajectories of kaons and pions originating from the primary vertex and from the D^+ -meson decay (secondary vertex) which are detected exemplarily by the MVD stations 0 and 1.

mesons is presented in [16]. The extracted invariant mass spectrum for a measurement of two months “beam on target” is depicted in Figure 2.3. The description of the simulation procedure and details on the rejection of the combinatorial background, which dominates the signal by 8 – 9 orders of magnitude, can be found in [16]. After the selection of the signal candidates (see Table A.1 in the Appendix), the background has been reduced by 99.82% while, at the same time, the signal is lowered by 27.6%, (see Table A.2 in the Appendix). The strategy to extract this signal from the recorded data leads to several requirements, see Chapter 3, which have to be complied with respect to the design of the MVD, see Chapter 4.

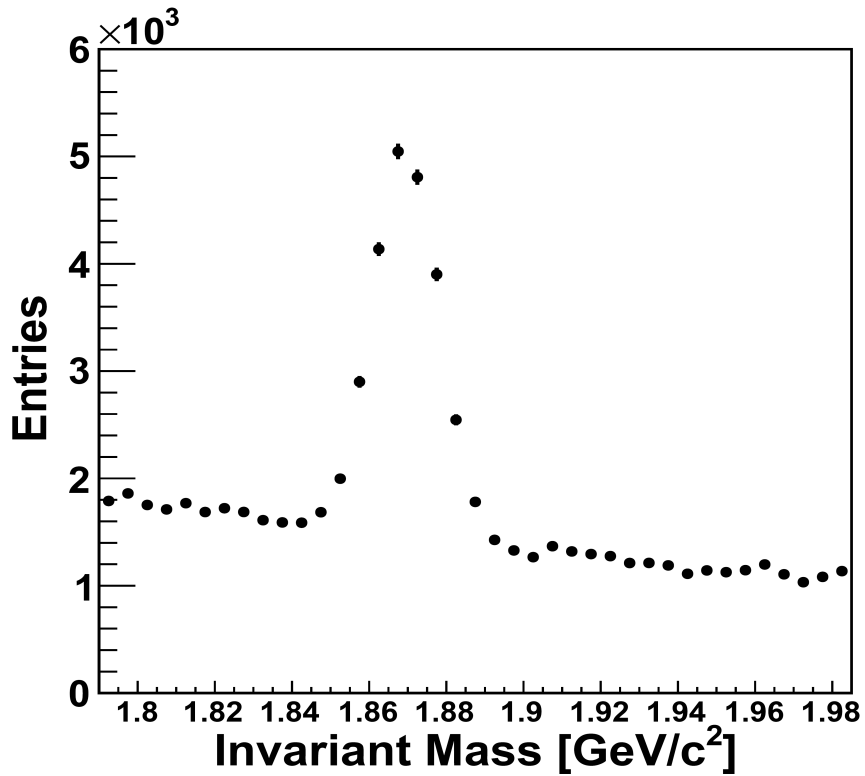


Figure 2.3: The invariant mass spectrum for the decay channel of $D^+ \rightarrow K^- \pi^+ \pi^+$ after applying all required cuts. Based on the multiplicity assumptions of the HSD model, the signal-to-noise-ratio of the spectrum is 1.5, including a significance of the signal of 95. The invariant mass resolution is stated to be $8.56 \pm 0.22 \text{ MeV}/c^2$. The spectrum is taken from [16].

Di-Electrons

Short-lived vector mesons have a lifetime comparable to the lifetime of the medium created in heavy-ion collisions. Therefore, the decay of the vector mesons into, e.g., e^+e^- (see Table 2.3), can take place inside the medium. To identify and reconstruct a clean vector meson signal, their decay products should not be affected by final state interactions while propagating to the detectors. Penetrating particles such as di-electrons are promising observables since they do not participate in the strong interaction in the collision zone and are only affected by electromagnetic interactions. The branching ratios for different mesons decaying into e^+e^- are shown in Table 2.3. Comparing the branching ratio of, e.g., the ω into e^+e^- with a probability of conversion to occur, it is obvious that the measurement of di-electrons originating from vector mesons will be dominated by a large combinatorial background. The conversion probability depends on the material budget contributed by the detector systems in the acceptance as well as in its close vicinity and has been extracted from simulations to be, on an average, of a value of 6.5% for the first 70 cm downstream the CBM target [18]. Therefore, to identify, separate and reconstruct the e^+e^- -pairs originating from the rare observables from those produced in conversion, a sophisticated strategy is required to suppress the background and extract the e^+e^- -signal. A similar strategy is mandatory to deal with the background contribution of the π^0 -Dalitz decay electrons. At the same time, special attention has to be devoted to the fact that the acceptance and the efficiency of the detector will be limited.

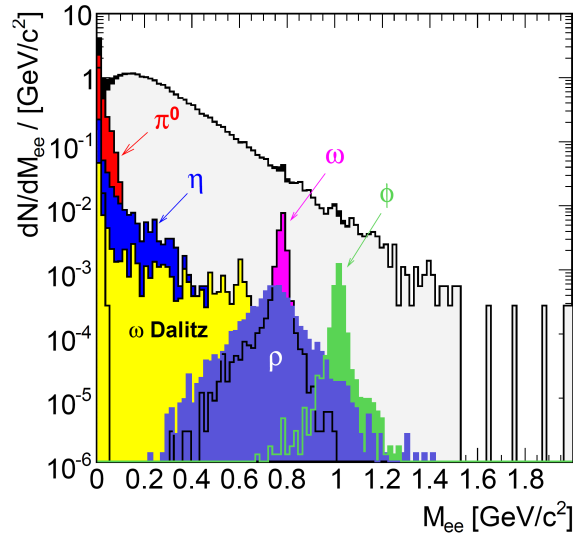
A recent simulation for the identification and the reconstruction of di-electrons with the CBM detector is presented in [19], the extracted spectrum is shown in Figure 2.4(b). A detailed description of the simulation procedure and the steps which have been taken into account to reject the combinatorial background¹⁰ and to extract the signal can be found in

¹⁰The cuts applied to the simulated data sample are presented in Table A.3 in the Appendix. A selection of decay modes resulting in e^+e^- -pairs and their possible tracks in the MVD and the Silicon Tracking System of the CBM experiment are sketched in Figure A.2.

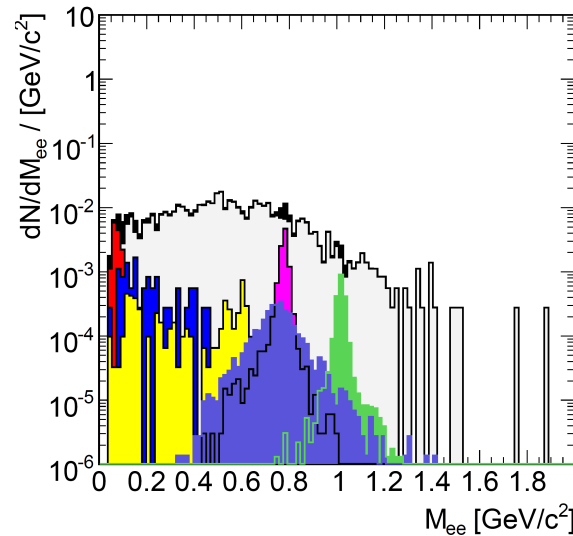
Branching ratio				
	Channel (interesting)	[%]	Channel (preferred)	[%]
π^0	γe^+e^-	1.174 ± 0.035	$\gamma\gamma$	98.823 ± 0.034
η	γe^+e^-	$(6.9 \pm 0.4) \times 10^{-3}$	charged modes	28.10 ± 0.34
ρ^0	e^+e^-	$(4.72 \pm 0.05) \times 10^{-5}$	$\pi^+\pi^-$	~ 100
ω	e^+e^-	$(7.28 \pm 0.14) \times 10^{-5}$	$\pi^+\pi^-\pi^0$	89.2 ± 0.7
ϕ	$l^+l^- \rightarrow e^+e^-$	$(2.954 \pm 0.03) \times 10^{-4}$	K^+K^-	48.9 ± 0.5

Table 2.3: The properties of the most common meson-di-electron sources to be studied with the CBM detector. The numbers are taken from [17].

[19]. The strategy to extract this signal from the recorded data leads to several requirements, see Chapter 3, which have to be complied with respect to the design of the MVD, see Chapter 4.



(a) Invariant mass spectrum without any cuts.



(b) Invariant mass spectrum with all cuts.

Figure 2.4: The invariant mass spectra for the e^+e^- -pairs before (a) and after (b) applying all required cuts for a simulation of 2×10^5 central Au + Au collisions at 25 AGeV. The contributions to the spectrum are: π^0 Dalitz in red; γ in dark green; η Dalitz in dark blue; ω Dalitz in blue; ω in magenta; ρ^0 in green; ϕ in violet; all e^+e^- pairs in black fill; combinatorial background in grey fill. The spectrum is taken from [19].

2.2.2 Demands on the Tracking and Vertexing Detectors

The reconstruction of open charm carrying particles and di-electrons requires an enormous effort in both, software and hardware. To achieve the simulated and extracted spectra found for both observables in the experiment, detectors featuring unprecedented properties with respect to tracking and vertexing of the produced particles have to be incorporated into the CBM experiment.

The tasks of particle tracking and secondary vertex identification are shared between the Micro Vertex Detector (see Section 2.3.2 and Chapter 3 for details) and the Silicon Tracking System (STS, see Section 2.3.3)¹¹. The MVD features a high spatial resolution required for an excellent secondary vertex resolution, a low material budget and high hardness to non-ionizing and ionizing radiation allowing for the positioning of the MVD stations in close vicinity of the target. The STS has to provide a low material budget and a fast read-out of the silicon strip sensors to reconstruct the particle tracks and to determine the momenta of charged particles.

The identification of the secondary decay vertex is a task dedicated to the MVD, since the STS is not capable of resolving displaced vertices on the scale of the decay length of the D -mesons [22]. Their decay lengths in the laboratory frame are of the order of magnitude of 1 mm. For the D -mesons decay distributions, which are exemplarily depicted in Figure 2.5 for D^+ and D^0 , a thermal source with a temperature T and a beam energy E_{beam} emitting these particles has been used.

The identification of the low-momentum di-electrons has to be achieved before one of the electrons is bent out of the polar angles of the detector as a result of the magnetic field. Their identification is required to reduce the background generated by the reconstruction of only one partner of the e^+e^- -pairs. A schematic track topology of low-momentum di-electrons is shown in Figure A.2 in the Appendix. Di-electrons originating from conversion in the target are emitted as close pairs with a small opening angle between them. In the physics simulations, an opening angle cut of $\theta_{1,2} \leq 2^\circ$ [19] is used to reject these di-electrons. Since the MVD is positioned between the target and the first station of the STS at 300 mm downstream the target [22], the identification as well as the reconstruction of the low-momentum di-electrons have to be facilitated by the MVD.

¹¹The concept to use two different highly specialized tracking detectors based on pixel sensors and silicon strip sensors is widely used in heavy-ion experiments, e.g., in the STAR Heavy Flavor Tracker [20] and the ALICE Inner Tracking System [21].

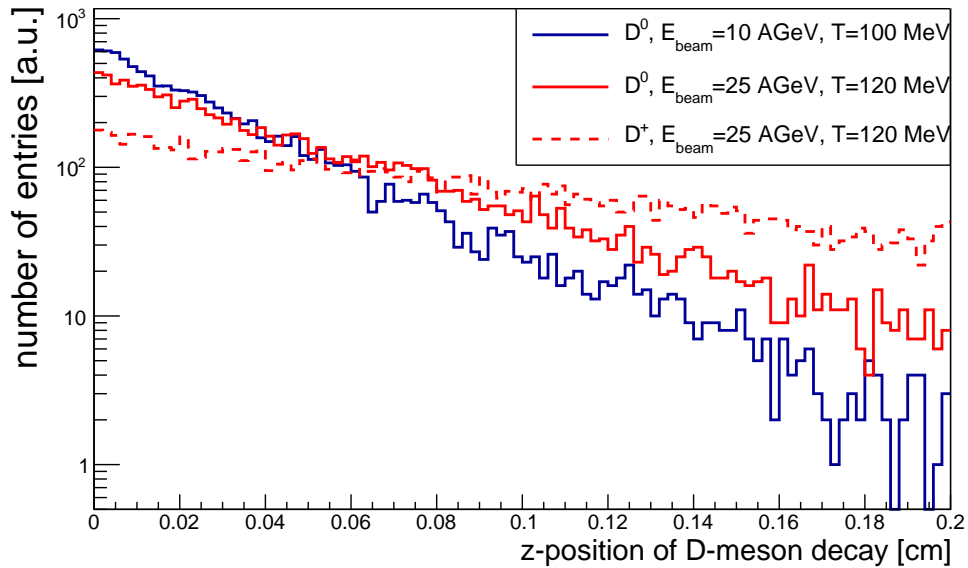


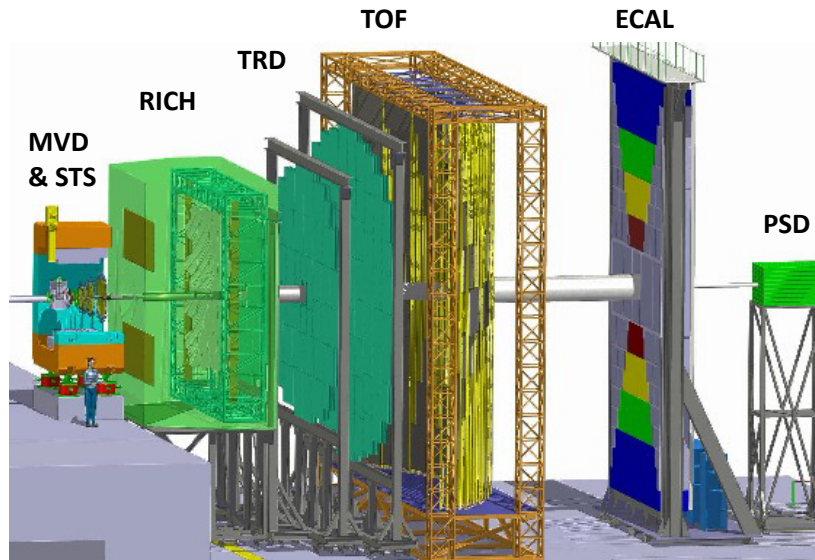
Figure 2.5: Simulated decay length distribution for D^0 and D^+ . The continuous lines represent the decay lengths of D^0 s for a temperature of $T = 100$ MeV of the thermal source and a beam collision energy of $E_{beam} = 10$ AGeV (in blue) and a temperature of $T = 120$ MeV and a beam collision energy of $E_{beam} = 25$ AGeV (in red). The dashed line depicts the decay length of D^+ s applying the conditions of the red D^0 decay distribution.

2.3 The CBM Experiment

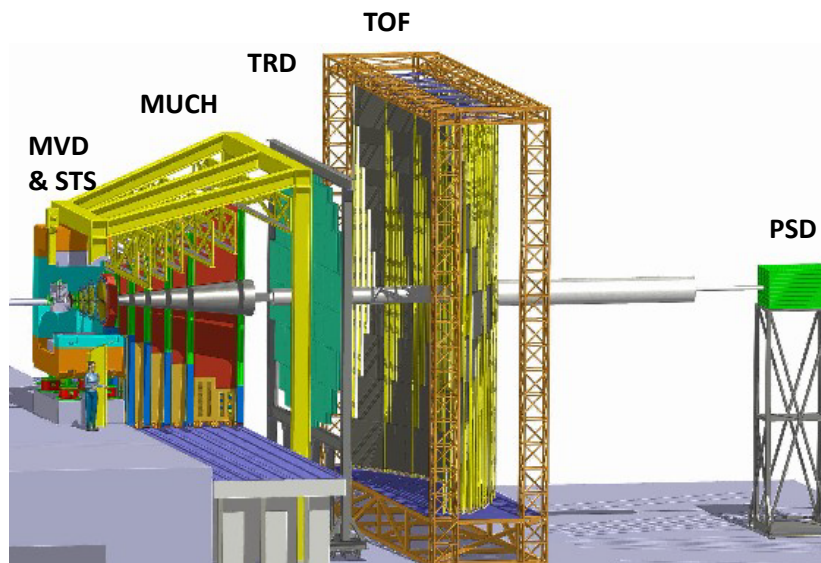
The CBM experiment is shown in a schematic overview in Figure 2.6. Two different detector configurations will be used to measure the particles produced in the heavy-ion collisions in the target using hadronic, leptonic and photonic observables. One configuration is dedicated to the measurement of di-electrons, while the other one has been developed to detect muons. Both configurations comprise several sub-detectors required to track, identify and reconstruct the produced particles.

The CBM detector comprises a Micro Vertex Detector providing a high resolution to determine the secondary decay vertices, a low-mass Silicon Tracking System (STS), a Transition Radiation Detector (TRD), a Time-Of-Flight (TOF) wall and a Projectile Spectator Detector (PSD). In the electron configuration of the CBM experiment, a Ring Imaging Cherenkov Detector (RICH) and an Electromagnetic Calorimeter (ECAL) will be used additionally to conduct the measurements. For the measurements in the muon channel, the RICH and the ECAL have to be removed from the detector set-up and a Muon Chamber (MUCH) system, consisting of segmented iron-absorbers in which all particles except muons can be absorbed, will be placed at the measuring position of the RICH.

The following description of the CBM detectors in the order of their positions downstream the target is presented in analogy to [7, 22].



(a) The electron configuration of the CBM experiment.



(b) The muon configuration of the CBM experiment.

Figure 2.6: *The CBM detector configurations. The two set-ups differ in the use of the Ring Imaging Cherenkov Detector (RICH) and several Transition Radiation Detector (TRD) planes in the electron set-up. In the muon set-up, a Muon Chamber system (MUCH) will replace the RICH. The figures are taken from [7].*

2.3.1 The Dipole Magnet

The superconducting dipole magnet is providing the magnetic field required to allow the momentum measurements via the bending of the charged particle tracks in the STS. The magnetic field integral in the vicinity of the CBM target will be of the order of magnitude of 1 Tm. The aperture of the magnet is defined to be larger than $\pm 25^\circ$, which allows to position the MVD and the STS inside the magnet [23].

2.3.2 The Micro Vertex Detector

The Micro Vertex Detector has to supplement the measurements of the STS providing a high spatial resolution to identify the secondary decay vertex of short-lived particles.

The mechanical integration of the MVD is the main subject of this thesis. The requirements of the detector, which have to be complied with respect to the design of the MVD, can be derived from the physics cases as well as its resulting operation conditions and are discussed in detail in Chapter 3, including a description of the chosen sensor technology CMOS¹² Monolithic Active Pixel Sensors (MAPS).

2.3.3 The Silicon Tracking System

The Silicon Tracking System (STS) is the central tracking detector of the CBM experiment [22]. The STS aims at the reconstruction of charged particle¹³ tracks as well as the determination of their momentum. The STS consists of 8 tracking layers of silicon detectors located at distances between 30 and 100 cm downstream the target inside the magnetic dipole field. The required momentum resolution is of the order of $\Delta p/p = 1\%$. To achieve this performance, detector stations featuring an ultra-low material budget are required, and, in particular, the location of power-dissipating front-end electronics has to be restricted to the volume outside of the acceptance of the STS stations. The STS is built of silicon microstrip sensors mounted onto light-weight mechanical support ladders. The microstrip sensors will be double-sided with a stereo angle of 7.5° , a strip pitch of $58 \mu\text{m}$, strip lengths between 20 and 60 mm and a thickness of $300 \mu\text{m}$ of silicon. The sensors will be read out through multi-line micro-cables with fast electronics which are positioned in the periphery of the stations, where cooling lines and other infrastructure can be placed without any impact on the material budget of the individual station in the acceptance. A detailed description of the Silicon Tracking System can be found in [22].

¹²CMOS is the acronym for Complementary Metal Oxide Semiconductor.

¹³The multiplicity of charged particles is up to 700 per event within the detector acceptance for an Au+Au-collision at 25 AGeV.

2.3.4 The Ring Imaging Cherenkov Detector

The Ring Imaging Cherenkov (RICH) detector is designed to provide the identification of electrons and to suppress pions in the momentum range below 10 GeV/c. The RICH comprises a radiator, an array of mirrors and a plane of photo detectors. If a charged particle is traversing the radiator with a velocity higher than the speed of light in this particular material, Cherenkov light is produced. The Cherenkov light is emitted with a constant angle ϑ relative to the track of the particle. The angle is defined with the relation $\cos(\vartheta) = 1/(\beta \times n)$ in which β is the velocity of the particle and n the refractive index of the radiator material. The emitted light cone is reflected by the mirror plane on the array of photo detectors positioned in the focal plane of the mirrors, producing rings of the collected photons. The detector will be positioned behind the dipole magnet and will consist of a 1.7 m long gas radiator, made of CO₂. The mirror system will consist of 72 individual glass mirrors. The photo detector plane which is shielded against the magnetic field is based on MAPMTs (MultiAnode Photomultiplier Tubes) providing a high granularity, a high geometrical acceptance as well as a high detection efficiency of photons, also in the near UV region. The high granularity (approximately 55000 channels) and a high number of photons per ring allow to expect a pion suppression in the order of 500 according to previously conducted simulations [24]. A detailed description of the RICH detector can be found in [24].

2.3.5 The Transition Radiation Detector

The Transition Radiation Detector (TRD) will consist of three individual stations comprising three detector layers each. Each layer consists of a radiator in which the traversing charged particles are producing the transition radiation and a gaseous detector measuring the energy deposited by charged particles and their produced transition radiation. The TRD will contribute to the tracking of particles and the identification of electrons and positrons with $p > 1.5$ GeV/c and a Lorentz boost γ higher than 1000. Using this information, the electrons can be further distinguished from pions. The pion suppression factor obtained with 9 TRD layers is estimated to be well above 100 at an electron efficiency of 90%. The detector stations will be located between 5 and 10 m downstream the target, whereas the total active detector area amounts to about 600 m². A more detailed description of the TRD is given in [25].

2.3.6 The Muon Chamber System

The Muon Chamber System (MUCH) has to identify low-momentum muons in an environment of high particle densities. The MUCH system relies on the concept to track the particles through a hadron absorber system and to perform momentum-dependent muon identification. This task will be achieved using a segmented hadron absorber and placing triplets of tracking detector planes in the gaps between the absorber layers. The absorber and detector system is placed downstream of the Silicon Tracking System (STS) which will

determine the momentum of the particles. In order to reduce the amount of mesons decaying into muons, the absorber and detector system have to be as compact as possible. The actual design of the muon detector system consists of six hadron absorber layers built from iron plates with different thicknesses and 18 gaseous tracking chambers. The identification of a muon depends on its momentum which varies with the mass of the vector mesons it originates from as well as the beam energy. Fast and highly granular detector planes might be built from gaseous detectors based on GEM technology and straw tubes. A detailed description of the Muon Chamber System is given in [25].

2.3.7 The Timing Multi-Gap Resistive Plate Chambers

The Timing Multi-Gap Resistive Plate Chambers (RPC) will be used for hadron identification via Time-Of-Flight (TOF) measurements. The Time-Of-Flight will be measured in between a start detector close to the target and the TOF wall. The required time resolution of the RPCs is in the order of 80 ps. The RPCs will be arranged in a large array of more than 150 m² comprising a large number of 60000 individual measuring cells. A detailed description of the TOF system can be found in [25].

2.3.8 The Electromagnetic Calorimeter

The Electromagnetic Calorimeter (ECAL) will be used in a “shashlik”-type configuration to measure direct photons and neutral mesons decaying into photons. The ECAL is composed of modules which consist of 140 layers of lead and scintillator material allowing a flexible positioning with respect to the target.

2.3.9 The Projectile Spectator Detector

The Projectile Spectator Detector (PSD) will be used to determine the collision centrality and the orientation of the reaction plane. The measurement of the energy carried by the spectator projectile nucleons (which do not participate in a heavy-ion collision) allows to determine the amount of participating nucleons in a collision and with this, the collision centrality. The participants of a collision are defined as those impinging beam nucleons which overlap with the target nucleons. These measurements have to be carried out event-wise to allow for the analysis of event-by-event observables. The PSD is a modular lead-scintillator calorimeter which provides sufficient and uniform energy resolution.

2.3.10 The Online Event Selection and Data Acquisition

To study the properties of particles with a small production cross-section in the CBM experiment, high beam interaction rates are required to provide the mandatory high statistics. The online event selection systems and the data acquisition of the CBM experiment will

be designed for Au+Au-collisions with an event rate of up to 10 MHz. These event rates require dedicated online event selection algorithms (and hardware) which reject the background events (that contain no signal). The event selection system will be based on a fast online event reconstruction running on a high-performance computer farm equipped with many-core CPUs and graphic cards. Track reconstruction, which is the most time consuming combinatorial stage of the event reconstruction, will be based on parallel track finding and fitting algorithms. A detailed description of the online event selection and data acquisition system can be found in [25].

Chapter 3

Requirements for the MVD Design

The MVD will mainly contribute to the measurements of the open charm and the di-electron physics cases introduced in the previous chapter. Both observables demand several highly specific requirements for the MVD. The required characteristics by which the MVD must comply will be introduced and worked out in this chapter in detail. Their introduction is divided into two parts. The first part deals with the required detector characteristics which can be derived from the physics cases, the second part evaluates the requirements derived from the operation conditions of the MVD. The derived requirements are used to guide the design of the MVD presented in Chapter 4. The technological feasibility of the components, which have to be integrated into the MVD, is examined in detail in Chapter 5 in the context of the MVD Prototype project.

3.1 Requirements Derived from the Physics Cases

The main requirements for the design of the MVD which can be derived from the open charm physics case are a high resolution and a low material budget. For the di-electron physics case, the main requirements are granularity, a low material budget and an enlarged polar angle coverage. These physics case specific requirements on the design of the MVD have to be combined with the request for a high read-out speed and a sufficient radiation hardness.

For the MVD discussed in the context of this thesis, the number of the stations as well as their positions in the proximity to the target will not be discussed on the basis of latest physics simulations¹. Furthermore, it is assumed that the detection of particles carrying open charm at SIS300(/100) drives the selection of the sensors as well as the detector layout. The design and layout of the MVD assumes an equidistant arrangement of four MVD stations between the target and the first STS station, see Chapter 4.

¹The MVD as being operated at SIS100 is presently the subject of new, ongoing simulations.

3.1.1 Acceptance Coverage

The size of the individual detector station integrated into CBM is determined by the polar angle coverage in order to detect the forward-booster particles produced in a heavy-ion collision in a fixed-target configuration. The polar angle which marks the inner radii of the detector stations is defined as 2.5° , leaving space for the beam particles to pass through. The outer radii of the detector stations are determined by a larger polar angle of 25° [26].

The acceptance coverage of the MVD stations has been adjusted on the basis of two reasons: The magnetic dipole field with a field integral of up to 1 Tm provided by the CBM magnet results in a deflection of low-momentum particles in horizontal direction beyond polar angles of 25° [19]. These low-momentum particles provide valuable information for the di-electron physics case, especially for the background suppression. Therefore, to track these low-momentum particles the geometrical acceptance of the three last MVD stations has been enlarged with respect to the outer radii of 25° in the horizontal plane, see Table 3.1, as it is also being planned for the detector stations of the STS [22].

The expected radiation dose on the first MVD station, located 50 mm downstream the target, at a polar angle of 2.5° - close to the beam - required the enlargement of the beam hole of this station to ensure a reasonable operation time of the sensors.

A detailed list of the polar angles of the MVD stations which have to be covered with charge-sensitive sensor area is presented in Table 3.1.

The impact of the geometrical acceptance of the proposed design of the MVD, which will in detail be presented in chapter 4, on the number of D -meson decay particles geometrically accepted in the STS and in the TOF has been simulated. A set of 10000 D^0 s, D^- s and D^+ s has been simulated in the framework of the Pluto event generator [27] assuming a thermal source with constant temperature T and a center-of-mass velocity of E_{beam} . Four collision systems have been considered. The branching ratios of the D -mesons into the decay channels of interest have been set to 100% and the full magnetic field has been used. It has to be emphasized that detector and reconstruction efficiencies have not been considered here. To be accepted in the analysis, all D -meson decay products to be detected have to leave more than 4 hits in the STS and minimum 1 hit in the TOF. The p_T - y -distribution of the decay particles of the D^0 -mesons are depicted in color in Figure 3.1. The D^0 -meson decay particles which are additionally geometrically accepted by the proposed design of the MVD applying the criterion of more than 1 hit in any 2 MVD stations are display in black. For the simulated collision system ($T = 120$ MeV and $E_{\text{beam}} = 25$ AGeV, D^0 -meson decay) depicted in this figure, the geometrical acceptance criterion applied on the MVD decreases the number of accepted pions and kaons from 4173 to 3974 which is at the level of 5%. This percentage level and the limited number of 10000 simulated D^0 s do not permit a qualitative discussion of the differences of the y -distributions depicted in the inlay of Figure 3.1. The difference of both y -distributions for y -values of $y > 3$ results from the mandatory larger inner radii of the MVD stations to guarantee a sufficient operation time of the sensors in the expected high radiation environment. The difference of the y -distributions for values of $y < 1.2$ occurs due to the large horizontal acceptance of the first 5 STS stations. The decrease of the accepted decay particles of D^+ s and D^- s in the STS and in the TOF applying

3.1. Requirements Derived from the Physics Cases

Station number ^a	Distance to the target [mm]	Radius [mm]		Polar angle coverage [°]	
		Inner	Outer	Inner	Outer
0	50	5.5	25	6.3	26.6
1	100	5.5	50	3.1	26.6
2	150	8.3	75	3.2	26.6
3	200	10.5	100	3.1	26.6

Table 3.1: The dimensions of the MVD stations which have to be covered with charge-sensitive detector material acceptance resulting from the required polar angles. The required polar angle coverage is taken from [1]. The corresponding dimensions of the MVD stations are taken from [29]. The adjustment of the polar angle coverage is motivated in the text.

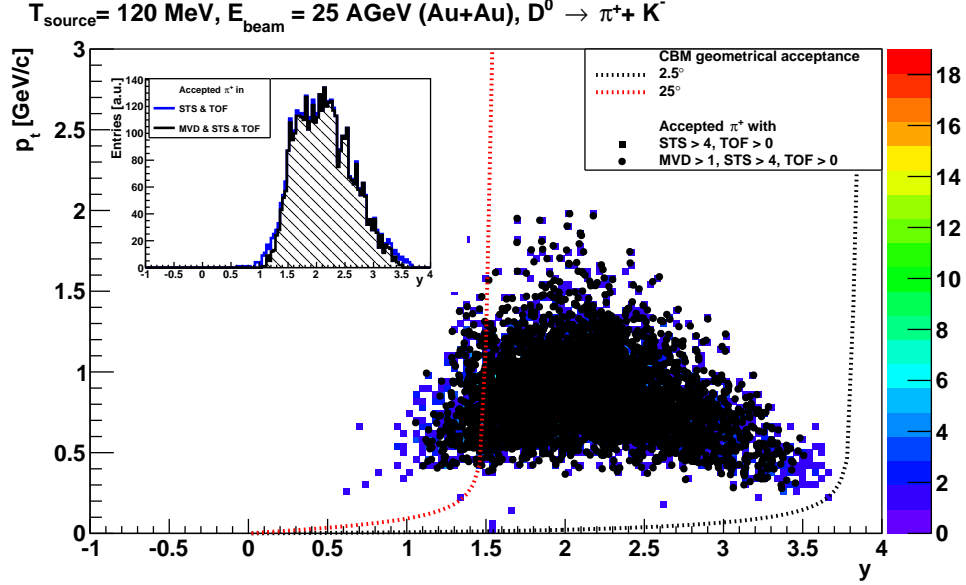
^aIn this thesis, the MVD stations are numbered starting from 0 to guarantee the required consistency with the CBM numbering rules laid down in [28].

<i>D</i> -meson decay channel	Properties of the thermal source					
	25 AGeV / 120 MeV		17 AGeV / 100 MeV		14 AGeV / 100 MeV	10 AGeV / 100 MeV
		Figure		Figure		
$D^0 \rightarrow \pi^+ K^-$	95.2%	3.1	95.0%	B.3	93.5%	90.5%
$D^- \rightarrow \pi^- \pi^- K^+$	87.2%	B.1	87.3%	B.4	87.1%	84.4%
$D^+ \rightarrow \pi^+ \pi^+ K^-$	88.7%	B.2	89.3%	B.5	86.8%	85.6%

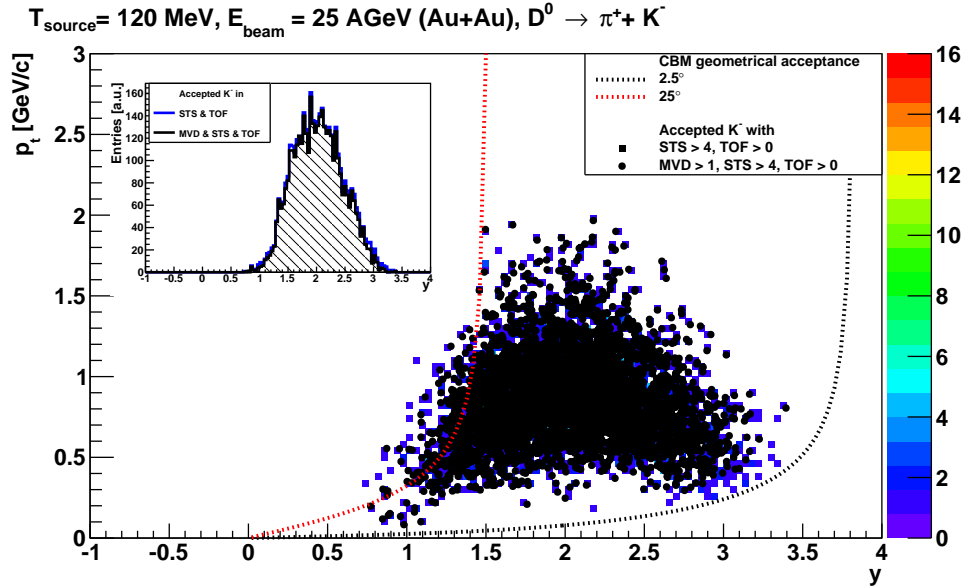
Table 3.2: Yield of *D*-mesons accepted with the MVD, STS and TOF normalized to the yield of *D*-mesons accepted with STS and TOF only. The criterion required for the decay particles to be accepted is defined as more than 4 hits in the STS and minimum 1 hit in the TOF and additionally more than 1 hits in any 2 MVD stations. The standard magnetic field has been applied but no particle tracking.

the geometrical acceptance criterion of the MVD is determined to be of about 11 – 13% for a simulated collision system of $T = 120$ MeV and $E_{\text{beam}} = 25$ AGeV. A detailed compilation of the results is listed in Table 3.2.

The distributions of the *D*-mesons for which the decay particles have been accepted are shown in the rapidity- p_t -plane in Figures B.6, B.7 and B.8 in the Appendix.



(a) P_t - y -distributions of π^+ decaying from 10.000 D^0 -mesons. Colored: 4173 pions which are geometrically accepted in STS (more than 4 hits) and TOF (minimum 1 hit). Black: 3974 pions requiring additionally more than 1 hit in any 2 MVD stations. To be accepted, the same criteria have to be fulfilled for the K^- . The inlay depicts the corresponding y -distributions.



(b) P_t - y -distributions of K^- decaying from 10.000 D^0 -mesons. Colored: 4173 kaons which are geometrically accepted in STS (more than 4 hits) and TOF (minimum 1 hit). Black: 3974 kaons requiring additionally more than 1 hit in any 2 MVD stations. To be accepted, the same criteria have to be fulfilled for the π^+ . The inlay depicts the corresponding y -distributions.

Figure 3.1: P_t - y -distributions of accepted π^+ (a) and K^- (b) originating from D^0 decays assuming a thermal source with $T = 120 \text{ MeV}$, at $E_{\text{beam}} = 25 \text{ AGeV}$.

3.1.2 Vertex Resolution, Material Budget and Spatial Resolution

An excellent vertex resolution of the MVD is mandatory to reconstruct the secondary decay vertex of the open charm mesons with the required accuracy. This requires the optimization of the interplay in between the position resolution of the sensor technology chosen to equip the MVD and its read-out speed, see Section 3.1.5. At the same time, the material budget of the individual MVD stations causing the multiple scattering the particles impinging on the detector stations are affected by has to be optimized while examining its impact on the thermal management of the MVD stations.

The basic design parameters guiding the configuration of the detector stations with respect to the impact of the multiple scattering and the position resolution can be derived from a simplified model calculation [30]. It assumes that the location of a secondary vertex is determined by means of straight tracks reconstructed from two hits in two detector stations produced by the decay particles of the D -mesons (e.g., pion(s) or kaon) as sketched in Figure 3.2. The individual track is reconstructed assuming a position resolution as well as a certain multiple scattering. The model has been specifically deduced from a particle collider geometry and without the presence of a magnetic field:

$$\sigma_{SV}^2 = \frac{\sigma_1^2 r_2^2 + \sigma_2^2 r_1^2}{(r_2 - r_1)^2} + \frac{\theta_{ms}^2 r_1^2}{\cos^4 \theta}. \quad (3.1)$$

The errors in the position measurements in the first and the second detector station are given by σ_1 and σ_2 , respectively. The impact angle of the particle on the first MVD station is defined by θ . It can be read off from the formula that the first detector station has to be positioned as close as possible to the target and that the resolution provided by the sensor technology positioned on the first station is of paramount importance. In addition to this, the material budget measured in units of the radiation length x/X_0 has to be as low as possible due to the dependence of $\theta_{ms} \sim 1/p \times \sqrt{x/X_0}$, whereas θ_{ms} itself² is defined as

$$\theta_{ms} = \frac{13.6 \text{ MeV}}{\beta pc} z \sqrt{x/X_0} [1 + 0.038 \ln(x/X_0)]. \quad (3.2)$$

The contributions of the geometrical and the multiple scattering parts of Equation (3.1) have been evaluated with respect to the momentum of the particles impinging on the MVD station and the material budget value of the first detector station. Both parts of Equation (3.1) have been equalized and evaluated with respect to the momentum of the particles impinging³ on the MVD station and the material budget value of the first detector station. The result is shown in Figure 3.3. It can be read off from the graph that for a material budget value of the first detector station of $x/X_0 = 0.3\%$, the multiple scattering and the geometrical contribution are equal for a particle momentum of $p = 2.67 \text{ GeV}/c$. For a material budget value of the first detector station of $x/X_0 = 0.5\%$, both parts of the equation are equal for a

²The formula is taken from [17].

³The data set simulated for the study of the incident angles on the MVD stations, compare to Figure 4.3a, has been used in this study.

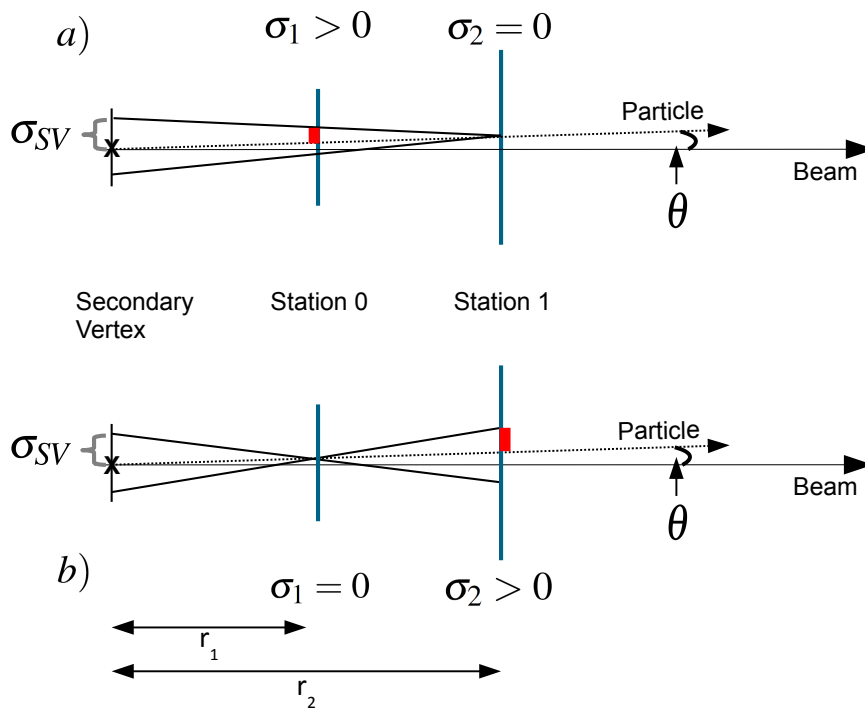


Figure 3.2: The parameters contributing to the secondary vertex resolution. The secondary decay vertex is represented with X. σ_{SV} is the extrapolated secondary decay vertex of the primary particle produced in the heavy-ion collision. Case a) assumes a perfect resolution of the second station; case b) assumes a perfect resolution of the first station. The resolution of the other MVD station providing a resolution value different from 0 is indicated with a red bar. θ marks the incident angle of the particle on the first detector station.

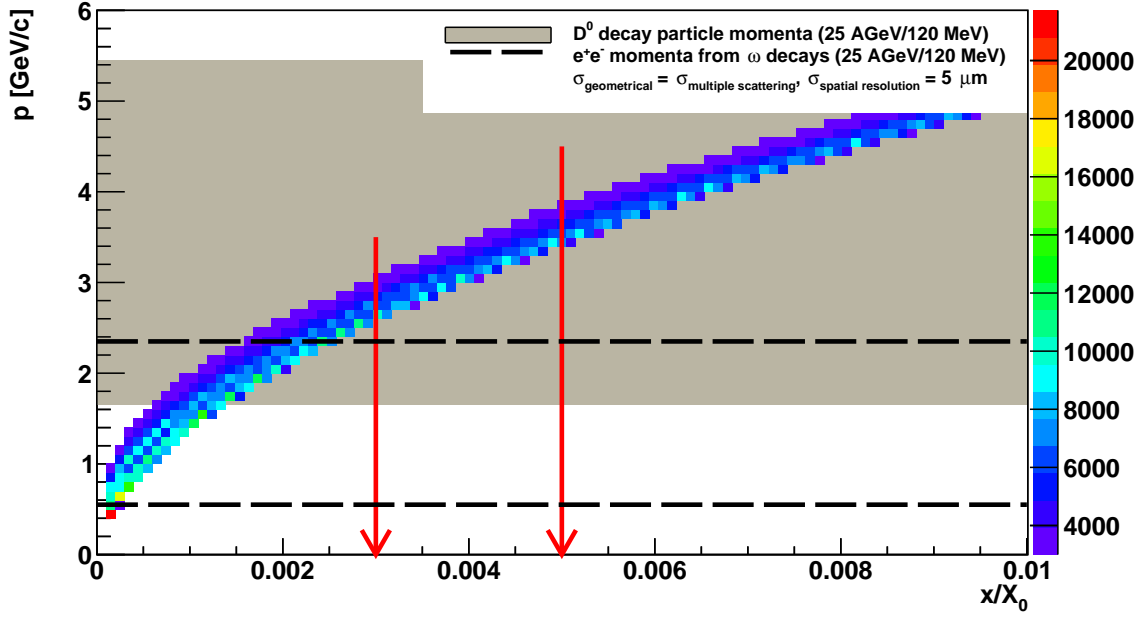
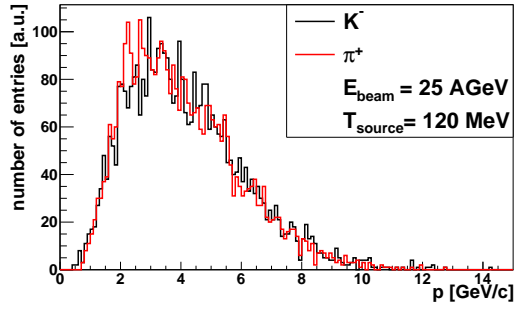


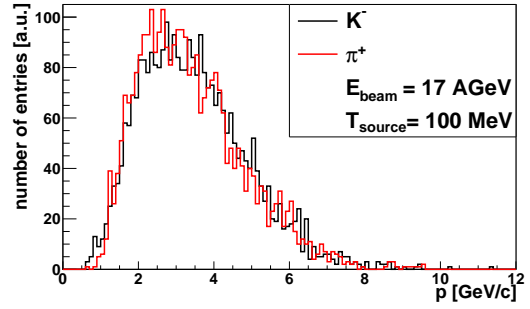
Figure 3.3: Evaluation of the geometrical and the multiple scattering contribution of the position resolution of Equation (3.1) with respect to the momentum of the particles impinging on the MVD station and the material budget value of the first detector station. The width of the distribution results from the different incident angles of the particles on the detector, compare to Figure 4.3a. A minimum of 3000 entries in each shown bin has been required.

particle momentum of $p = 3.54$ GeV/c. The filled area indicates the range of the momenta of the D^0 decay particles assuming a thermal source with $T = 120$ MeV, at $E_{\text{beam}} = 25$ AGeV. The dashed lines represent the upper and the lower momentum of e^+ and e^- originated from ω decays [31] assuming the same thermal source properties which have been applied in the case of the D^0 s. The width of the distribution results from the different incident angles of the particles on the detector, compare to Figure 4.3a.

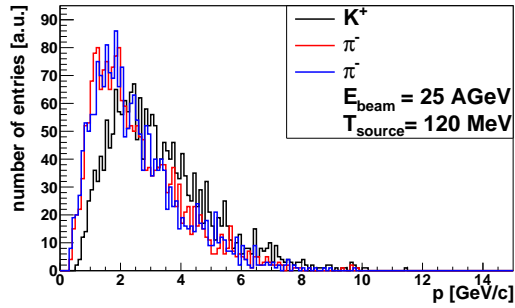
The momentum distributions of the accepted D -meson decay particles have been extracted from the simulated data. The distributions are displayed in Figure 3.4 for the thermal source properties of $E_{\text{beam}} = 25$ AGeV and $T = 120$ MeV showing a full width at half maximum momentum value of about 4.2 GeV/c for accepted decay particles originating from D^0 s and of about 3.3 GeV/c for those originating from D^- s and D^+ s. For the properties of the thermal source of $E_{\text{beam}} = 17$ AGeV and $T = 100$ MeV, the full width at half maximum momentum values are reduced to a value of about 3.5 GeV/c for accepted decay particles from D^0 s and of about 2.7 GeV/c for those originating from D^- s and D^+ s. Therefore, the momenta of the D -meson decay particles are in the order of the momentum which has been extracted from the evaluation of formula (3.1).



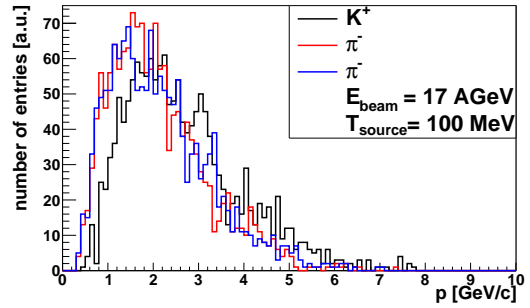
(a) Momentum distribution of π^+ and K^- originating from D^0 decays assuming a thermal source with $T = 120$ MeV, at $E_{\text{beam}} = 25$ AGeV.



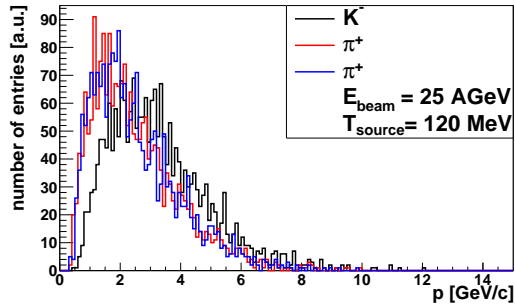
(b) Momentum distribution of π^+ and K^- originating from D^0 decays assuming a thermal source with $T = 100$ MeV, at $E_{\text{beam}} = 17$ AGeV.



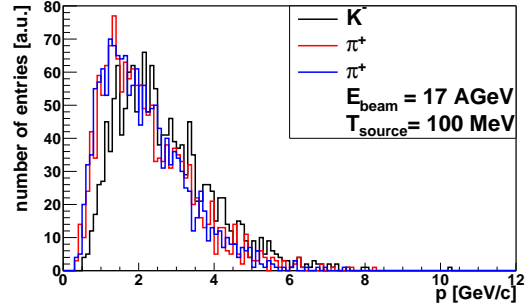
(c) Momentum distribution of π^- , π^- and K^+ originating from D^- decays assuming a thermal source with $T = 120$ MeV, at $E_{\text{beam}} = 25$ AGeV.



(d) Momentum distribution of π^- , π^- and K^+ originating from D^- decays assuming a thermal source with $T = 100$ MeV, at $E_{\text{beam}} = 17$ AGeV.



(e) Momentum distribution of π^+ , π^+ and K^- originating from D^+ decays assuming a thermal source with $T = 120$ MeV, at $E_{\text{beam}} = 25$ AGeV.



(f) Momentum distribution of π^+ , π^+ and K^- originating from D^+ decays assuming a thermal source with $T = 100$ MeV, at $E_{\text{beam}} = 17$ AGeV.

Figure 3.4: Momentum distribution of the accepted D -meson decay particles assuming a thermal source with $T = 120$ MeV, at $E_{\text{beam}} = 25$ AGeV as well as $T = 100$ MeV, at $E_{\text{beam}} = 17$ AGeV. The acceptance criterion required a minimum of 2 hits in the MVD, 5 hits in the STS and 1 hit in the TOF for a particle track to be accepted. The standard magnetic field has been applied but no particle tracking.

A determination of the secondary vertex resolution which has to be provided by the MVD can be obtained from physics simulations. In Figure 3.5, the position resolution of the secondary vertex along the beam axis is presented as a function of the spatial resolution and the thickness of the MVD stations [16]. The decay vertex of a D^+ -meson is identified by use of the decay particles $\pi^+\pi^+K^-$. The MVD is assumed to consist of two stations positioned at 100 and 200 mm downstream the target, featuring a thickness of 150 μm silicon equivalent. In this simulation, a spatial resolution of the sensor technology employed in the MVD of below 5 μm and a thickness of the two MVD stations of a maximum of 300 μm silicon equivalent are needed to achieve a secondary vertex resolution below 100 μm .

To achieve the required resolution of the secondary vertex, a target value for the material budget of the individual MVD station has to be defined as an upper limit based on the results shown in Figure 3.3 and 3.5. For the first MVD station, positioned in a distance of 50 mm to the target, the importance of the material budget for the precision of the vertex resolution can be read off from the formula (3.1) in which the contribution of the material budget is the dominant factor. Therefore, the material budget target value for the first MVD station has been set to a value of $x/X_0 = 0.3\%$. The target value of the material budget for the other MVD stations has been defined to be $x/X_0 = 0.5\%$, since the material budget is not the dominant factor for these stations. The material budget target values for the individual MVD stations are listed in Table 3.3. As not to disturb the resolution of the secondary decay vertex and preventing the produced particles from multiple scattering before they will be detected in the first MVD station, the operation of the MVD in vacuum is essential.

The mechanical stability of the detector, its positioning accuracy and the related reproducibility impact the position resolution of the secondary vertex as well. The mechanical stability of the individual detector stations has to be stable over a dedicated measurement period. The mechanical stability of a prototype of the first MVD station has been evaluated in the context of this thesis, compare to Section 5.5. The positioning accuracy of the sensors and the MVD stations with respect to the beam axis as well as its reproducibility are discussed in Section 3.3.

The nominal spatial resolution σ_{sp} of the sensors to be integrated in the MVD stations depends on the chosen sensor technology. For example, the spatial resolution of any pixel sensor can be stated to be

$$\sigma_{sp} = \text{pitch}/\sqrt{12} \quad (3.3)$$

based on geometrical estimations, disregarding however any charge-sharing between the pixels integrated in the sensor as well as the potential presence of noise.

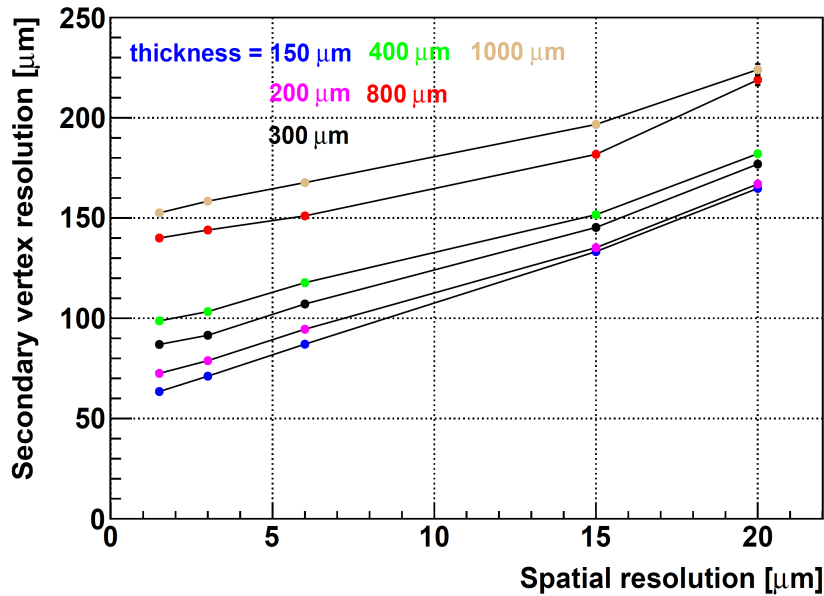


Figure 3.5: The dependency of the secondary vertex resolution (cf. Figure 2.2) for the decay channel $D^+ \rightarrow \pi^+ \pi^+ K^-$ as function of the spatial resolution and the thickness of the first two MVD stations presented in silicon equivalent. The figure is taken from [16].

Station number	Material budget target value x/X_0 [%]
0	≤ 0.3
1	≤ 0.5
2	≤ 0.5
3	≤ 0.5

Table 3.3: The envisioned material budget target values for all MVD stations. The material budget target values are taken from [32].

3.1.3 Radiation Hardness Demands on the MVD

The first MVD station is positioned as close as possible to the target to resolve the secondary decay vertex with a minimal perturbation. The proximity to the target⁴ of this station is limited by the dose of the ionizing and non-ionizing radiation which the chosen sensor technology for the MVD is able to withstand while remaining operational. Since the accumulated

⁴The integrated particle flux (resulting in a high radiation dose) through a given area of a station positioned close to the target is larger than the one for the same area on a station at some distance away from the target.

Distance to the target [mm]	Radiation type	
	Non-ionizing [$10^{12} \frac{n_{eq}}{cm^2}$]	Ionizing [krad]
50	8.0	400
100	4.0	550

Table 3.4: *The calculated radiation doses against which the chosen sensor technology has to be radiation hard. The numbers for the ionizing and the non-ionizing radiation per collision (Au + Au, 35 AGeV) have been extracted from Fluka simulations [33] and have been scaled with the collision rate and the CBM running period to estimate the radiation dose per running year.*

radiation doses decrease with increasing distance from the target, the radiation hardness demands for the other MVD stations are less stringent.

The radiation dose, both for the ionizing and the non-ionizing radiation, is estimated at the expected positions of the MVD stations in order to ensure that the sensors of the MVD remain functional for one CBM running period. One CBM running period is defined as two months (5×10^6 seconds) with a beam interaction rate in the order of magnitude of 10^5 collisions per second [16]. The expected radiation doses are listed in Table 3.4.

3.1.4 Track matching across STS and MVD

In the track reconstruction software of the CBM simulation and analysis framework [34], the detected particle tracks are reconstructed in the STS and afterward extrapolated from the first STS station to the last MVD station. These extrapolated tracks have to pass through a vacuum window which is separating the STS and the MVD. To avoid potential ambiguities with respect to the connection of the hits reconstructed in the MVD and the potentially scattered tracks, the two most downstream stations of the MVD have to be positioned as close as possible to the vacuum window [29]. The third MVD station is reducing possible ambiguities which might arise using the Cellular Automaton tracking algorithm [35] to match the hits reconstructed in the MVD with the reconstructed tracks in the STS, compare to Figure 4.7 in [29]. The fourth MVD station supports the particle tracking through the whole CBM experiment, as it has been demonstrated in open charm simulations carried out in [29].

3.1.5 Read-Out Speed and Granularity

The read-out speed of the sensor technology chosen to equip the MVD has to be such that the probability of the occurrence of potential event pile-ups is minimized. An event pile-up is defined as the occasion of more than one interaction of the beam with the target during one single read-out cycle of the MVD sensors. If the number of event pile-ups taking place

during one single read-out cycle of the sensors is close to ten, the performance of the track reconstruction software will be deteriorated significantly (as it is noted in [29, 36]).

The granularity of the sensor technology of the MVD is mainly determined by the secondary vertex resolution, as discussed above. In addition, the hit occupancy of the pixel sensors should not exceed a value of 1%, which has been assumed to be the occupancy limit defined by the bandwidth of the read-out system [16]. A maximal hit density of 3.5 hits/mm²/collision close to the beam axis for central Au+Au-collisions with a beam collision energy of 25 AGeV (including δ -electrons) has been found in [37]. With a possible pixel pitch⁵ of the MVD sensors of 18 μ m, which translates to about 3000 pixels per mm², this can be converted into an occupancy of about 0.2% in a hotspot located close to the beam pipe on the first MVD station. This value is significantly smaller than the occupancy limit of 1% [16]. The occupancy distribution on the first MVD station using the proposed design of the MVD, see Chapter 4, as well as the current versions of the hit-finder and digitizer in the CBM simulation framework is exemplarily shown in Figure 3.6. The distribution depicts the situation for which 100 events with a beam collision energy of 25 AGeV have been averaged including an event pile-up of 3 and a number of 100 δ -electrons per pile-up [38]. The occupancy distributions for the other MVD stations are displayed in Figure B.9a, B.9b and B.9c in the Appendix.

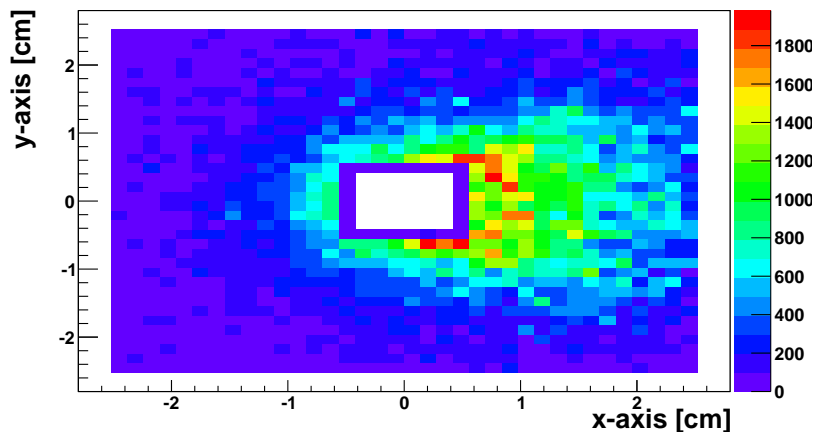


Figure 3.6: Occupancy distribution on the first MVD station. For the distribution, 100 events with a beam collision energy of 25 AGeV have been averaged together with a pile-up of 3 and a number of 100 δ -electrons per pile-up.

⁵The pixel pitch is defined as the distance between two collecting diodes implemented in CMOS sensors.

3.2 The MVD Sensor Technology

CMOS Monolithic Active Pixel Sensors (MAPS) have been chosen to equip the stations of the MVD. The silicon sensors, named MIMOSA⁶, are developed at the IPHC⁷ in Strasbourg.

The decision to use MAPS as pixel sensor technology for the MVD has been made several years ago after comprehensive studies had been conducted to examine the available sensor technologies, their working principles [39, 40] and their compatibility with the requirements derived from the physics cases [41]. The studied sensor technologies are strip sensors, Hybrid Active Pixel Sensors (HAPS), Charge-Coupled Devices (CCD), Depleted Field Effect Transistor (DEPFET), Silicon On Insulator (SOI) and MAPS. MAPS offer the best compatibility with respect to the required radiation hardness, read-out time and spatial resolution. At the same time, after being thinned in a standardized process [42], the sensors thickness of 50 μm amounts to an ultra-low material budget which is equivalent to a value of $x/X_0 = 0.053\%$. In addition, MAPS offered a clear path to improve the technology in those cases in which the compatibility has not yet been achieved at the time the decision had been made.

The CMOS process allows to integrate sensing detector elements and processing electronics onto the same silicon substrate [43]. The working principle of conventional MAPS, which are based on an epitaxial layer providing a resistivity of a few Ωcm , is sketched in Figure 3.7 and will be discussed as follows⁸.

The charge-sensitive volume of MAPS is a not fully depleted epitaxial layer (P–). This sensitive volume is surrounded by two layers made of highly-doped silicon (P++), see Figure 3.7. When a charged particle is traversing the sensor, electron-hole pairs are created along the particle trajectory in the whole sensor volume. Those created in the P-doped epitaxial layer participate in the creation of the signal. The “holes” are attracted by the P++-substrate, while the electrons will be reflected by the P++-substrate. The electrons diffuse thermally within the epitaxial layer until they reach the depleted region in front of the N-Well (which forms the collecting diode inside the P-Well), or recombine in the crystal, or are lost due to radiation-induced defects.

The thickness of the sensors is typically several hundreds of micrometers. Since the epitaxial layer of the MAPS which is forming the active volume is only 14 to 20 μm thick [43, 44], the substrate of the sensors can be thinned down to a thickness of about 50 μm by using a back thinning process. The thinning process can be conducted without any performance loss of the sensor [42]. Nevertheless, the thinning of the sensor results in a reduction of the production yield. For the PXL⁹ detector which is part of the Heavy Flavor Tracker (HFT) of the STAR experiment, the sensor yield has been determined to be 50 – 60% after the functionalities of the sensors have been evaluated electrically by the use of probe tests [45].

The electronic working principle of MAPS is exemplarily sketched for the MIMOSA-26

⁶MIMOSA is the acronym for Minimum Ionizing Particle MOS Active Pixel.

⁷Institut Pluridisciplinaire Hubert Curien, Strasbourg, France.

⁸The explanation is given in analogy to [39].

⁹PXL stands for the part of the HFT which is equipped with MAPS developed at the IPHC.

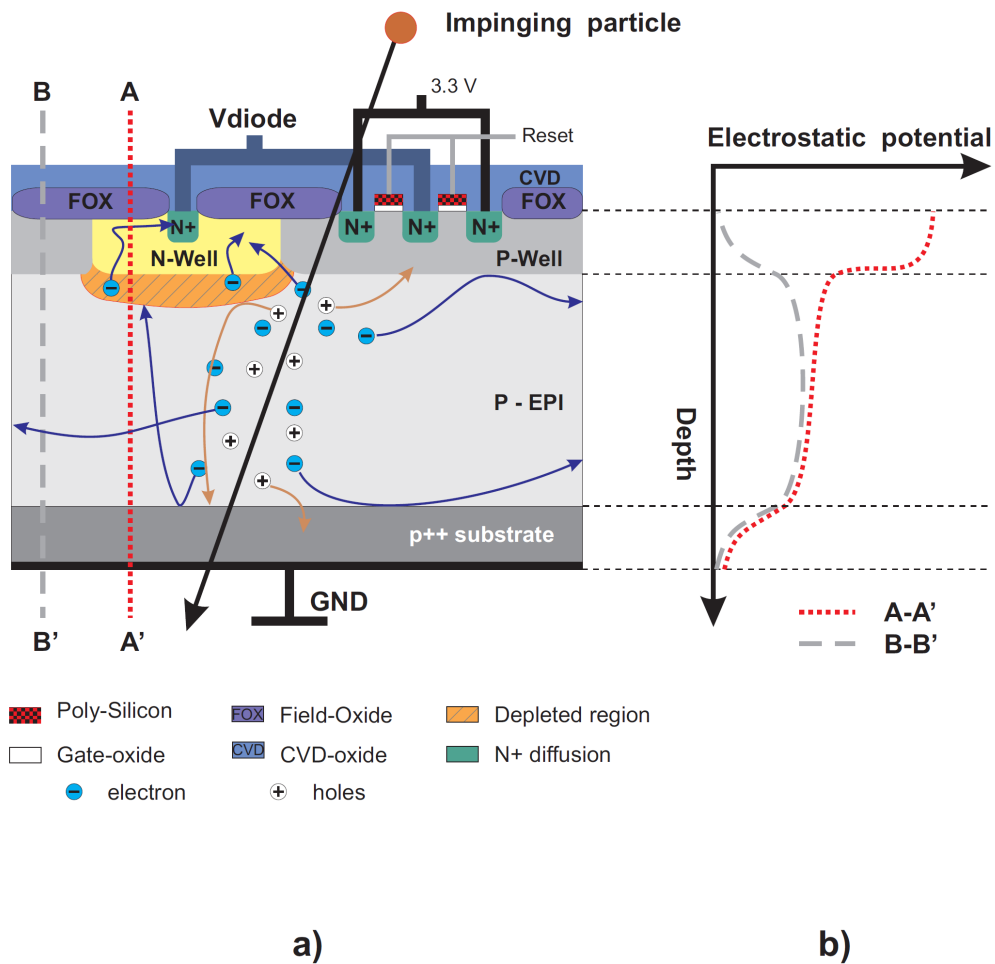


Figure 3.7: The working principle of MAPS using the example of a low-resistivity MI-MOSA. Figure a) shows the situation when a charged particle is traversing the sensor. Despite that the electron-hole pairs are generated in the whole silicon, they are shown in the epitaxial layer only. Figure b) shows the electrostatic potential as a function of depth through the sensor in a cross-sectional view. The lines indicate two different cuts: the red dotted one the path (A–A’), whereas the grey dashed line indicates the path (B–B’). The figures are taken from [39].

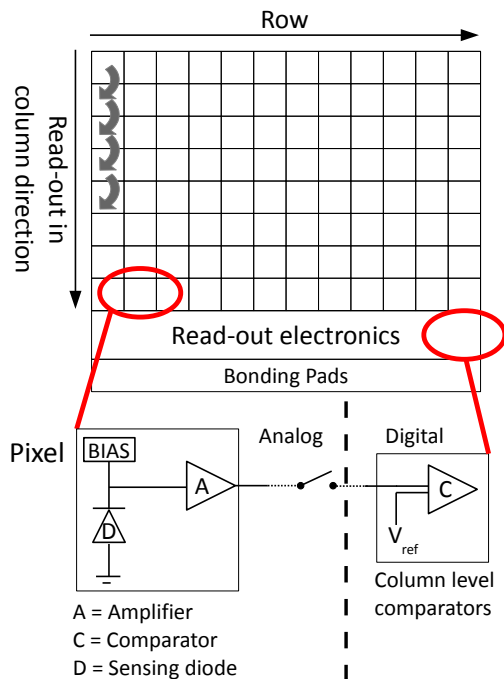


Figure 3.8: The electronic working scheme of MAPS.

sensor¹⁰ in Figure 3.8. The sensor is sub-divided into pixels, read-out electronics and bonding pads.

The pixels¹¹ are arranged in rows and columns with a typical distance of 10 to 30 μm to each other. The read-out of the pixels is carried out row-by-row in the column direction in a so-called rolling shutter mode [46]. At the end of each column, a column-level comparator, indicated with (C), is implemented. The pixels themselves comprise a reverse biased sensing diode (D) and a signal amplifier (A). In case of MIMOSA-26, they are equipped with a comparator. The output of the pixels is analog, whereas the data format has been converted into a digital one after passing the comparator stage.

The implementation of processing electronics such as column-wise discriminators, zero-suppression logic [46] and memory onto the same substrate requests a distinguished area on the sensor. In this part of the sensor, no particle transitions will be detected which requires an arrangement of the sensors on both sides of a support material to maximize the station's acceptance, see below, Section 4.1.2.

The read-out time of the sensor correlates with the number of pixels in a column. Less pixels per column lead to a faster read-out of the “pixel array”. The reduction of the read-out time of the sensors can be achieved by using shorter pixel columns and/or elongated pixels (instead of quadratic ones) in the column direction which is currently being discussed [16, 47]. This offers a promising solution to reach the short read-out time demanded for the future MVD sensors, named MIMOSIS-1¹².

¹⁰MIMOSA-26 sensors will be used in the MVD Prototype project which will be discussed in detail in Chapter 5.

¹¹Typically, a sensor features more than 500000 pixels depending on the sensor generation.

¹²MIMOSIS-1 is the acronym for MIMOSA for SIS100.

In addition, a newly available fabrication process which allows to integrate sensor components with a smaller feature size is currently under investigation at the IPHC. This process could allow to implement parts of the read-out circuits directly in each pixel (e.g., discriminators) and could result in a read-out time in the order of several μs [47].

The hardness of the MIMOSA sensors with respect to non-ionizing and ionizing radiation has been improved continuously.

The maximal radiation dose after which a standard MIMOSA-26 sensor – fabricated in a CMOS process providing a feature size of $0.35\ \mu\text{m}$ and a non-depleted volume in the epitaxial layer – still remains functional, has been determined to be about 300 krad and a few $10^{12}\ \text{n}_{\text{eq}}/\text{cm}^2$ at an operating temperature of $20\ ^\circ\text{C}$ [48].

Comparing these numbers to the calculated radiation doses expected at the positions of the first and the second MVD station listed in Table 3.4, it is obvious that the achieved radiation hardness of this sensor is insufficient in order to remain functional during a CBM year.

The hardness of the MIMOSA sensors with respect to the non-ionizing radiation has recently overcome this level by use of high-resistivity epitaxial layers as the basis of the sensors [49]. MIMOSA-18 AHR¹³ is an example of such a sensor which remained operational after its irradiation to a dose of $3 \cdot 10^{13}\ \text{n}_{\text{eq}}/\text{cm}^2$ at an operating temperature of $0\ ^\circ\text{C}$ [50].

The hardness against the ionizing radiation has been obtained after realizing MIMOSA-32 in the $0.18\ \mu\text{m}$ Tower/Jazz CMOS process allowing the use of smaller feature sizes for the production of MAPS [47]. MIMOSA-32 has been proven to be operational at a temperature of $20\ ^\circ\text{C}$ after its irradiation to 10 Mrad [51].

The MIMOSA sensors used to equip the MVD still have to be functional after they have been exposed to the combined dose of ionizing and non-ionizing radiation. Therefore, the combination of both, a feature size of $0.18\ \mu\text{m}$ and the high-resistivity epitaxial layer, is required, which is being realized in MIMOSA-32. This sensor proved its functionality at a temperature of $15\ ^\circ\text{C}$, after being irradiated to 1 Mrad as well as to $1 \cdot 10^{13}\ \text{n}_{\text{eq}}/\text{cm}^2$ [52].

¹³The abbreviation AHR comprises the $0.35\ \mu\text{m}$ -sensor production process of AustriaMicroSystems (A) and the used high resistivity epitaxial layer (HR).

3.3 Requirements Derived from Operation Conditions

The positioning of the MVD inside vacuum, inside the CBM magnet and its operation inside an area of limited access due to radiation safety regulations defines additional requirements for the MVD.

3.3.1 Requirements from the Vacuum Operation

The positioning of the MVD inside vacuum to not deteriorate the resolution of the secondary vertex due to the multiple scattering of the D -meson decay particles in air, see Section 3.1.2, requires a dedicated cooling concept for the MVD, in particular, for the sensors. Their dissipated power has to be evacuated efficiently to provide the best possible sensor operation conditions. These are defined by the need to keep a constant operation temperature well below 0° [49] which is also required to reduce radiation-induced defects. At the same time, it has to be ensured that the optimization of the operation temperature towards lower temperature values does not negate the advantages of the in-vacuum operation of the MVD in terms of multiple scattering within the individual stations. The optimization of the set-up of the MVD with respect to its operation in a moderate vacuum is presently studied [53]. These studies comprise the selection of materials, glues and gluing techniques with respect to potential outgassing. In addition, the thermal management and connectivity issues (vacuum feedthroughs for signals, power supplies and the cooling medium) are studied.

3.3.2 Requirements from the Configuration of the MVD

The configuration of the MVD inside the mentioned environmental conditions requires additional studies related to

- the operation in a magnetic field,
- the need to remotely move the MVD stations away from the beam during beam tuning and focusing into a “save position” in order to prevent the sensors from being hit by beam particles [32],
- the maximum precision in the positioning and the aligning of the MVD stations,
- the need to ensure the mechanical stability of the MVD stations over a dedicated period of measuring time,
- the need to minimize the displacement and stress resulting on all integrated materials resulting from thermal cycles and
- the need to minimize stress on the stations due to connected read-out cables and cooling pipes.

The required remote positioning system¹⁴ is mandatory to ensure that the MVD is positioned in a “save position” in order to prevent the sensors from being hit by beam particles during the time in which the beam is tuned and focused. After this, the remote positioning system has to guarantee that the MVD is positioned in its “measuring position” in order not to deteriorate the secondary vertex resolution. A value based on experimental measurements for the distance which is required in between the MVD sensors and the unfocused beam as well as for the achievable precision in re-positioning the MVD in its “measuring position” is not yet available. For the former, a value of up to 50 mm is currently envisaged [54]. For the latter, a precision in the order of 50 μm is intended to be achieved using dedicated mechanical stops to determine the “measuring position” of the MVD. These mechanical stops would also allow to obtain a reproducibility in the same order of magnitude. Dedicated routines providing these actions need to be worked out.

In case of a malfunction of several sensors integrated onto one of the quadrants or an MVD half-station (for definitions see Chapter 4), a modular design and construction of the detector is required to ease their exchange. A detailed plan for servicing of the MVD has to be established as a result of limited and restricted access to the detector during the running period of the CBM experiment. In addition, a strategy for fully disassembling the detector has to be developed in case the MVD is not participating in the measurements of a special physics case.

3.3.3 Requirements from Spatial Restrictions

As laid down in Section 3.1, the MVD stations will be placed inside a vacuum vessel which is situated inside the CBM magnet [23], positioned between the target and the Silicon Tracking System [22]. In addition, the MVD will be surrounded by the thermal enclosure of the STS from five sides (see Figure B.11). Access to the detector will only be possible from the front. In front of the MVD, the target and the beam pipe will be positioned. In between the fourth MVD station and the first STS station at 300 mm downstream the target, a curved vacuum window – which is presently extending to $z \geq 220$ mm [55], in close vicinity to the MVD – has to be positioned to allow the STS to operate in a cooled atmosphere. Within the vacuum vessel, the space available for the MVD is limited to a volume of $660 \times 660 \times 285$ mm³, see Figure B.11.

Additional space might be required below and above the MVD for the installation of correction coils for the magnetic field. For the di-electron physics case, a magnetic-field-free region between the target and the first MVD station is being suggested to limit the possibility that the tracks of the e^+e^- -pairs are bent apart from each other before being tracked in the first MVD station [19].

¹⁴The development of a remote positioning system for the MVD is not part of this thesis.

3.4 Summary

The requirements for the detector characteristics derived from the physics cases hint at a Micro Vertex Detector which is equipped with four stations featuring an excellent pointing and secondary vertex resolution combined with the above-mentioned hardness against ionizing and non-ionizing radiation. Due to the required minimal material budget of the MVD, the MVD stations must be thin to achieve the necessary precision in pointing and vertexing. The read-out of the pixel sensors has to be fast in order to reduce the potential event pile-up in the detector to a minimum. As a result of these requirements, Monolithic Active Pixel Sensors are chosen as sensor technology to equip the individual MVD stations. The MAPS-based MIMOSA-“generations” developed at the IPHC demonstrate the best compatibility with the requested demands. The requirements for the detector characteristics derived from the operation conditions are the operation in vacuum including all subsequent challenges to achieve the best sensor operation conditions, the operation in the magnetic field, the remote positioning of the MVD stations as well as their servicing.

The four main topics derived from the physics cases include radiation hardness, material budget, granularity and read-out speed. In order to guarantee the optimal operation conditions for the sensors, these features have to be optimized focusing on the cooling of the sensors in vacuum. During this optimization process, the impact on the other three topics has to be studied in detail as a result of their strong dependencies.

In Figure 3.9, the above-mentioned topics are depicted indicating their direct connection to the physics case of measuring open charm. Focusing on the issue of “material budget”, which is one of the important ones in the context of the mechanical integration of the MVD and this thesis, the dependencies are discussed.

The low material budget required to reduce the deterioration of the secondary vertex resolution which is necessary to identify the decay products of the D -mesons (see above, Section 3.1.2) to a minimum can be achieved by use of thin detector stations. To allow for the definition of a precise pointing vector on the secondary vertex and to reduce the multiple scattering of the particles traversing the MVD, the MVD stations will be positioned inside vacuum, see Section 3.1.2 above. The positioning inside vacuum requires a dedicated cooling concept and cooling system to guarantee the best possible sensor operation parameters, see Section 3.3.1. Besides the fact that the cooling of the sensors is beneficial in terms of reducing the noise of the pixels while being operated and exposed to a high amount of radiation, the material needed to evacuate the power dissipated by the sensors inside vacuum is contributing to the material budget in the polar angles of the MVD. An optimal balance between the required cooling and the material budget has to be achieved in order to provide optimal operation conditions for the sensors and, at the same time, not to exceed the material budget demanded by the physics cases.

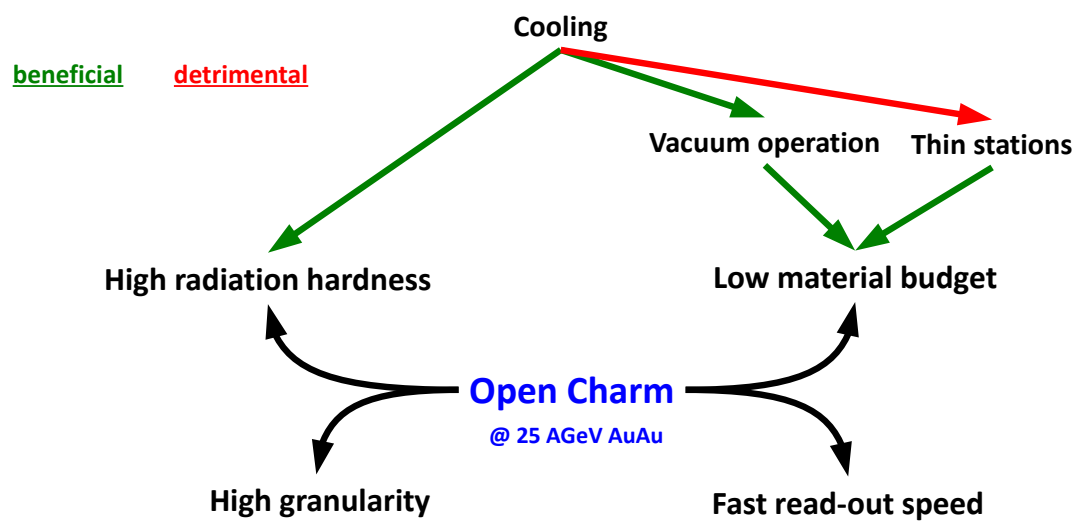


Figure 3.9: Selected dependencies within the MVD to illustrate their complexity. The above shown four topics are directly connected to the open charm physics case.

Chapter 4

Design Proposal of the MVD

The design of the Micro Vertex Detector is guided by the requirements on the detector characteristics derived from the physics cases and from the operation conditions presented in Chapter 3. The design proposal of the MVD addresses these technical challenges. The experience and the knowledge gained from the MVD Demonstrator project [40, 56] and the MVD Prototype project, which is subject of Chapter 5 of this thesis, are incorporated into the design proposal of the MVD. The transformation of the proposed MVD from an engineering model to a model which can be used in physics simulations is conducted to allow further studies relating to the material budget of the detector.

4.1 Design Approach

The design approach¹ of the MVD is based on four stations, as mentioned above in Section 3.1. The sensors are arranged on the individual MVD stations to cover the required polar angles given for the dedicated MVD station. The sensors are positioned in a double-sided arrangement on dedicated sensor carriers used for their support and cooling. The sensor carriers have to provide an excellent thermal conductivity and a high radiation length. Aluminum-based heat sinks are positioned in close vicinity to the acceptance of the MVD to limit the length of the cooling paths spanned between the sensors and the dedicated areas in which the heat dissipated by the sensors can be evacuated from the sensor carriers.

The design of the MVD is set up modular to ease its construction and to allow a fast exchange of malfunctioning components. Hence, the symmetry of the arranged sensors in the required polar angles is used to identify repetitive components and to define the smallest building block in the construction of the MVD.

A naming convention [58] has been defined to guarantee a unique encoding of all integrated components. The smallest building block in the MVD consists of the sensors and their dedicated sensor carriers as well as the sensor read-out cables. They are forming a quadrant. Four quadrants are mandatory to cover the required polar angles of each individual MVD

¹The software used to design the MVD is called Autodesk Inventor [57].

station. A quadrant is the functional element which might be exchanged after the occurrence of potential malfunctions of a not yet defined number of sensors on it. The number of sensors positioned on a quadrant is increasing with the distance of the MVD station to the target due to the larger polar angle coverage required. Within the design approach of the MVD, it is assumed that only one sensor type as well as one sensor geometry is used to cover the polar angles.

The next building block, a half-station, is made up of two quadrants which are mechanically linked to a common heat sink. Two half-stations are forming a single MVD station. The four individual MVD stations positioned at 50, 100, 150 and 200 mm downstream the target constitute the MVD, which itself is a sub-detector of the CBM experiment.

The MVD is depicted in Figure 4.1 displaying an overview of the components which will be discussed below.

The sensors, their read-out cables (FPC) and the support carriers are indicated with (1) forming the inner-most area of the MVD stations. The heat sink of a half-station is marked with (2). The half-station support structure is indicated with (3) and the base plate of a group of half-stations is labeled with (4).

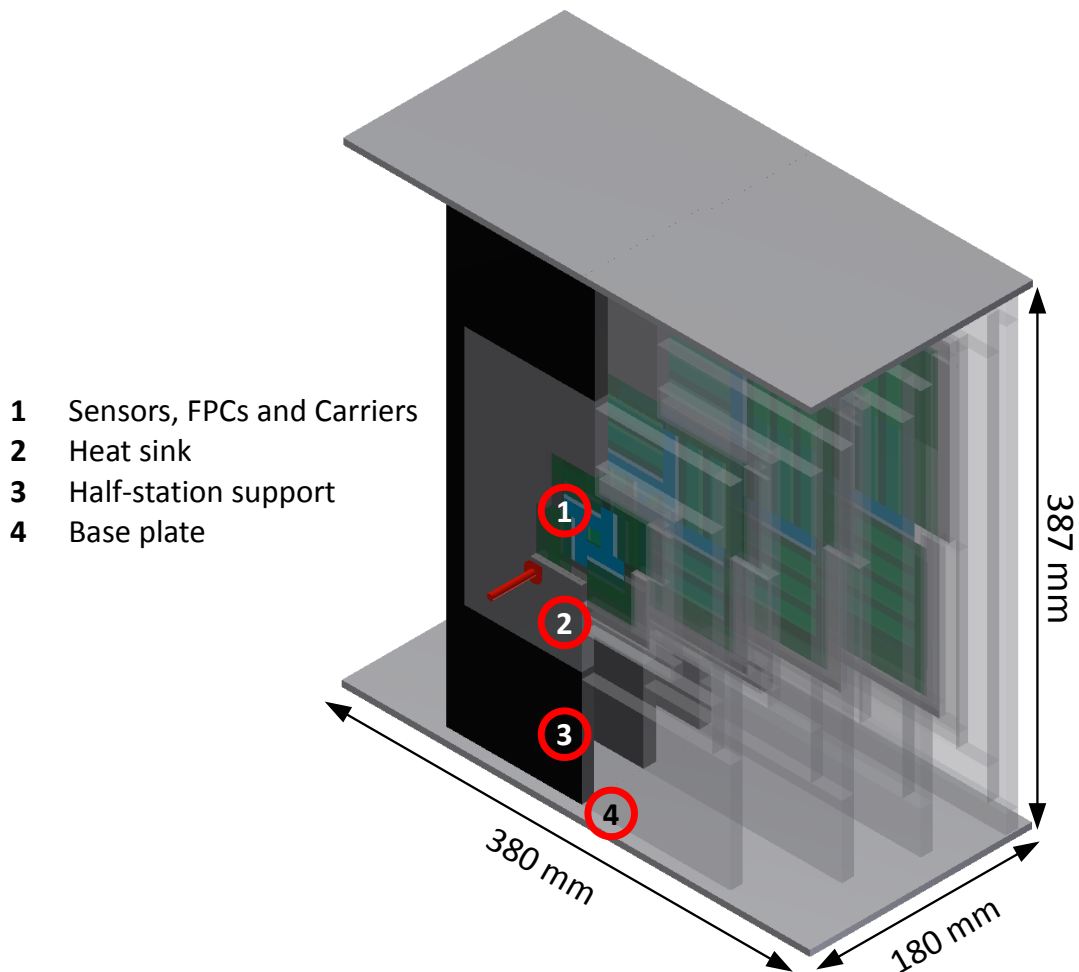


Figure 4.1: The design proposal of the MVD is exemplarily shown in an up-right frontal view on the CAD model of the MVD, the half-stations being in their measuring position. The direction of the beam is indicated with the red arrow. The target which is not shown in this figure will be positioned at the tip of the arrow. To visualize all stations and their sensors, the half-station support structures and the heat sinks of the "right downstream side"-group of the half-stations have been set transparent.

4.1.1 Sensor Geometry

The sensor, named MIMOSIS-1, which will be integrated into the MVD has not yet been developed. Therefore, its final dimensions are not yet available. For the design proposal of the MVD introduced as follows, the sensor dimensions will be extracted and extrapolated from known facts. Using the envisioned performance of MIMOSIS-1 listed in Table 4.1, an educated guess can be made related to the possible dimensions of the sensors. The sensor is depicted in Figure 4.2.

The read-out time of the sensor can be adjusted and tuned with the number of pixels which are arranged in one single sensor column, as described in Section 3.2. The envisioned sensor read-out time of $30 \mu\text{s}$ and the planned pixel clock of 10 MHz can be combined to calculate the number of pixels per column which leads to $10 \times 10^6 / \text{s} \times 30 \times 10^{-6} \text{ s} = 300$ pixels. Assuming a pixel pitch of $33 \mu\text{m}$ in the column direction, these 300 pixels result in a charge-sensitive column length of $300 \times 33 \mu\text{m} \approx 10000 \mu\text{m} \approx 10 \text{ mm}$. The width of the MIMOSIS-1 can be assumed to be 30 mm , as stated in [47], resulting in a charge-sensitive sensor area of $30 \times 10 \text{ mm}^2$. An area of 3 mm times the width of the sensor has to be reserved for the on-chip electronics [59]. The dimensions of the individual sensors² used in the design proposal of the MVD are assumed to be $30 \times 13 \text{ mm}^2$. For the power dissipation of the individual sensor, a maximal value of 0.35 W/cm^2 [47] and a minimal value of 0.185 W/cm^2 [60] can be considered to be reasonable.

²The sensor geometry corresponds with the form factor of the sensors under investigation planned to be used in the ALICE Inner Tracking System at the LHC [21, 47].

Read-out time	$30 \mu\text{s}$
Operating clock	80 MHz
Pixel clock	$2 \times 5 \text{ MHz}$
Pitch pixel	$33 \times 20 \mu\text{m}^2$
Pixels per column	300
Length per column	10 mm
Sensor width	30 mm
Area of the on-chip electronics	$3 \text{ mm} \times \text{sensor width}$
Power dissipation	0.35 W/cm^2 (max.) 0.185 W/cm^2 (min.)
Sensor dimension	$30 \times 13 \times 0.05 \text{ mm}^3$

Table 4.1: The envisioned performance of MIMOSIS-1. The numbers are taken from [47].

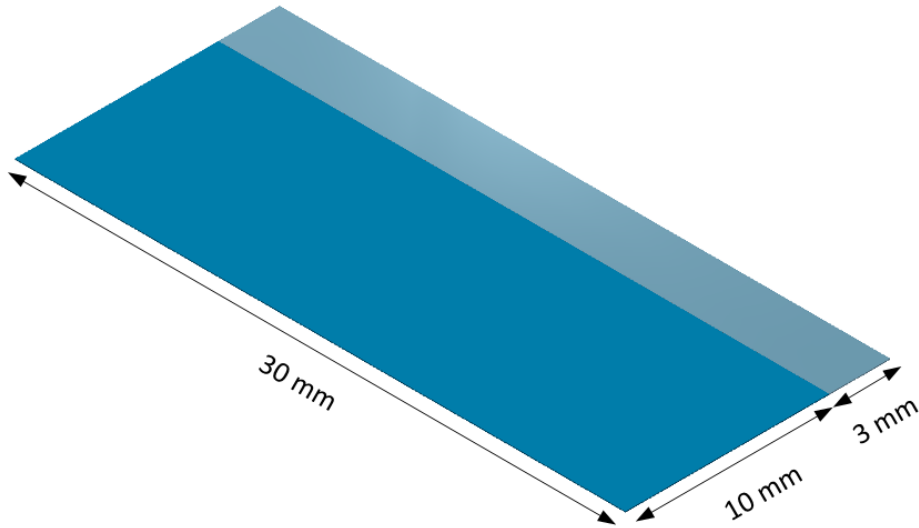


Figure 4.2: *MIMOSIS-1.* The charge-sensitive sensor area is represented by the $30 \times 10 \text{ mm}^2$ dark blue area, while the light blue area symbolizes the on-chip electronics which covers an area of $30 \times 3 \text{ mm}^2$.

4.1.2 Sensor Arrangement

The arrangement of the sensors inside the MVD is guided by two parameters, the coverage of the required polar angle interval with charge-sensitive sensor area, which itself has to account for the on-chip electronics in terms of a non-sensitive area with respect to particle transitions and the incident angles of the particles on the MVD stations as well as the distance between two adjacent sensors, and the positioning of the sensors to maximize the distance between the on-chip electronics and the beam to limit the possible occurrence of latch-ups and single event upsets [61].

Due to the non-sensitive area of the sensors hosting the on-chip electronics, a double-sided arrangement of the sensors on their support and cooling material is required. The finite thickness of the sensor carrier is causing a gap through which inclined particles might pass without their detection on the individual MVD station. The number of possibly not detected particles has to be minimized without inducing an excessively large overlap area between the sensors positioned on both sides of the sensor carrier. Thus, the incident angles of the particles on the MVD stations have been simulated. In the CbmRoot framework [34], UrQMD³ has been used to generate 50 Au+Au-collisions with a beam collision energy of 25 AGeV. Two different magnetic field configurations have been accounted for: a full magnetic field and a magnetic field reduced to 70% of the full one. The produced particles have been transported through the geometry of the MVD worked out in this chapter. The results shown in Figure 4.3a have been normalized to one Au+Au collision. A cut on the minimum momen-

³UrQMD is the abbreviation for Ultrarelativistic Quantum Molecular Dynamics model which is a microscopic model used to simulate (ultra-)relativistic heavy ion collisions, developed at the Goethe University Frankfurt.

tum of the particles has not been applied. In the scenario accounting for the full magnetic field, 99.9% of the particles (depicted in black) impinge on the MVD stations with an angle of maximal 68° (indicated with the vertical dashed black line) and for the reduced magnetic field, a value of 99.7% of the produced particles (shown in red). The sensor arrangement accounts for this maximal incident angle. The coverage of this incident angle results in a shift of the sensors on the opposite sides of the sensor carriers towards each other in such a way that their charge-sensitive areas are overlapping by the amount of $500\ \mu\text{m}$, as sketched in Figure 4.3b. The overlap of the charge-sensitive areas will ease the relative alignment of the sensors given that some of the particle tracks will be detected twice in an individual MVD station.

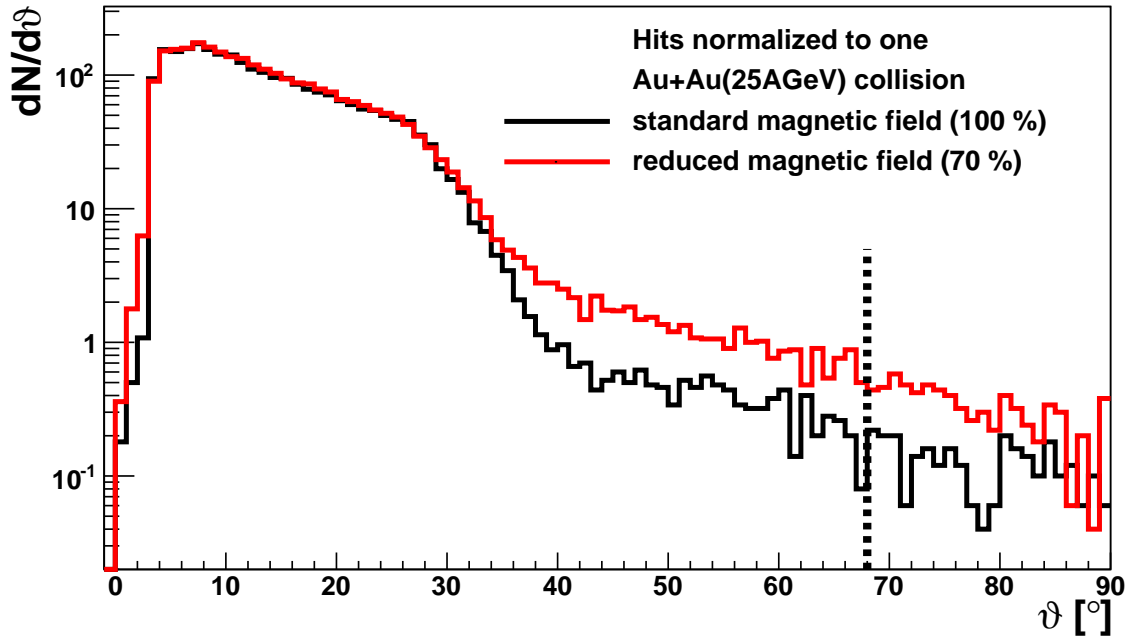
The distance between two adjacent sensors has to be as small as possible to avoid dead, non-sensitive areas. An edge-to-edge positioning of the sensors would be the preferred setting; however, the positioning accuracy depends on the accuracy of the positioning tools used and the accuracy of the sensor dicing. An evaluation of the positioning accuracy of the sensors integrated within the MVD Prototype project is presented in Section 5.3.3.

The sensor arrangement will be exemplarily discussed for the first station positioned at 50 mm downstream the target. Its required polar angles which have to be covered are shown as dashed circles in Figure 4.4(a), their specifications are listed in Table 3.1. The polar angle interval can be divided into four equal parts which will be covered by the individual quadrants hosting a station-dependent number of MIMOSIS-1 sensors. The first sensor is positioned horizontally on the sensor carrier, its charge-sensitive sensor area is indicated in dark blue in Figure 4.4(a). The need to position an additional sensor to cover the full polar angle interval can be clearly seen in this figure. The second sensor will be positioned on the other side of the sensor carrier accounting for the required shift of the charge-sensitive areas towards each other. The relating figure is depicted in 4.4(b). In order to complete the first MVD station, three additional quadrants are required. The arrangement of the sensors for this first MVD station is shown separately for the front side, see Figure 4.4(c), and for the back side, see Figure 4.4(d). A black frame has been added on top of the sensors to visualize their dimensions. The individual quadrants are indicated with dashed lines. The sensors on the back side of the carrier are coded in darker colors. In Figure 4.5, the complete first MVD station is shown for the horizontal sensor arrangement.

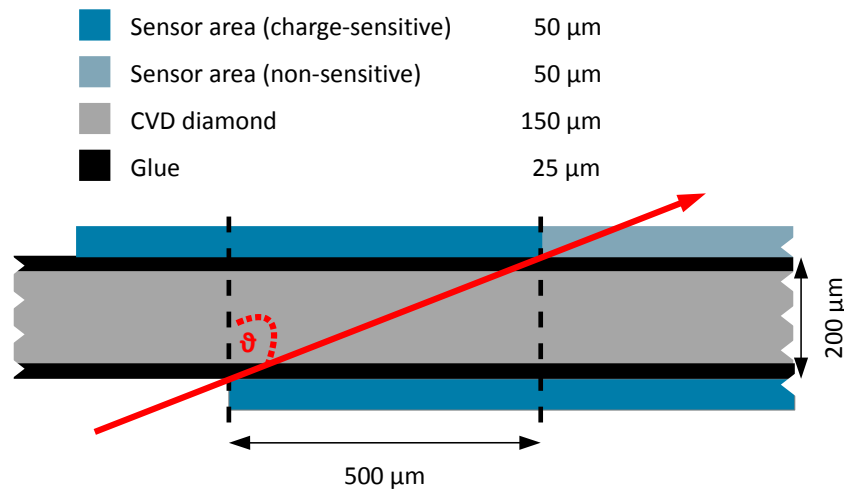
A second sensor arrangement is studied using a vertical arrangement of the sensors, defined by the orientation of the sensors in the lower right quadrant, shown in Figure C.1 in the Appendix.

Comparing both sensor arrangements with each other, the distance of the on-chip electronics to the beam is smaller for the vertical sensor arrangement than for the horizontal one. This could result in an increased probability of a direct beam-ion hit in the on-chip electronics inducing Single-Event Upsets and Latch-Ups [61]. As a result, the horizontal sensor arrangement is chosen to serve as the baseline for the sensor arrangement in the design proposal of the MVD.

The arrangement of the sensors in the polar angle interval of the other MVD stations is executed accordingly. The minimum total number of sensors needed to cover these intervals of all four MVD stations with charge-sensitive sensor material amounts to 248, as listed



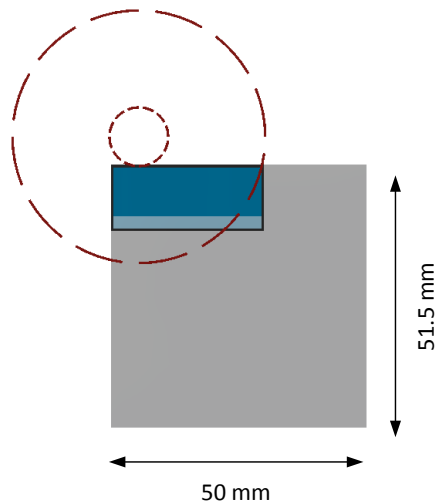
(a) Simulation of the particle incident angles on the MVD stations.



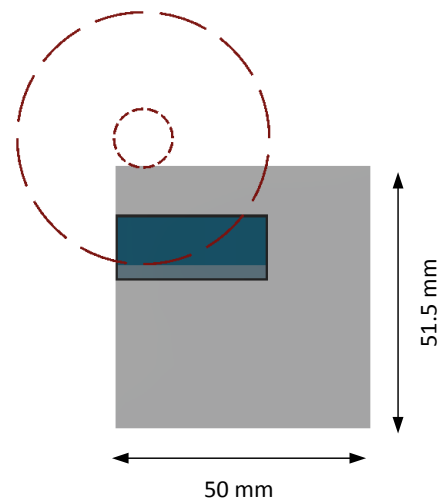
(b) Sketch of the maximal particle incident angle.

Figure 4.3: The incident angles of the particles on the MVD stations (simulated and sketched). The incident angle ϑ is defined as the angle spanned between the particle track from the target to the MVD station on which the particle is detected and the beam axis.

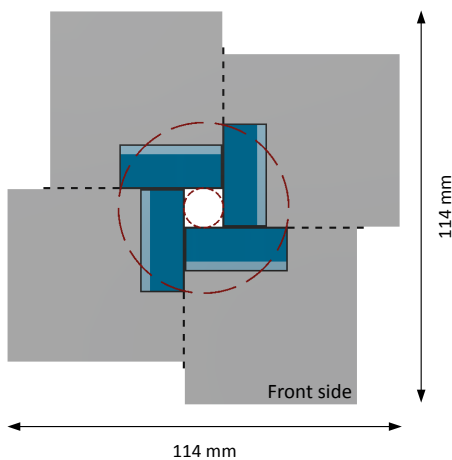
in Table 4.2. For the MVD stations positioned at 100, 150 and 200 mm downstream the target, the dimensions of the sensor carriers offer the option to position additional sensors, and with this, to extend the polar angle coverage in the horizontal direction as it has been requested by the di-electron physics case [19]. This extended option is chosen as baseline



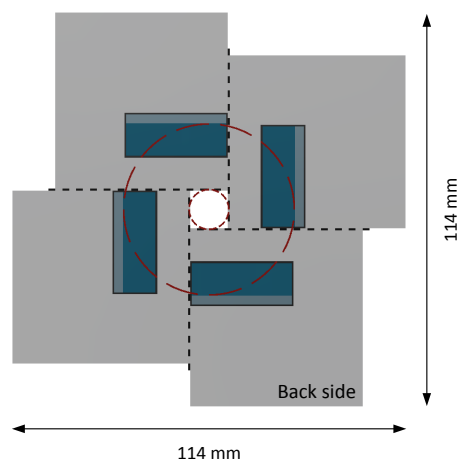
(a) Polar angle interval (dashed circles) of the first MVD station and the first MIMOSIS-1 sensor positioned on the front side of the quadrant.



(b) The second MIMOSIS-1 sensor positioned on the back side of the quadrant.



(c) All sensors on the front side of the first MVD station.



(d) All sensors on the back side of the first MVD station.

Figure 4.4: The sensor arrangement on the first MVD station. The sensors are depicted in dark blue for the charge-sensitive and light blue for the non-sensitive sensor area on the front side. From the sensors on the back side of the station, the charge-sensitive area is visible in a darker blue. The polar angle interval to be covered is indicated with red dashed circles, while the sensor carrier is indicated with light grey. To visualize the dimensions of the sensors, a black frame has been applied to them. The dashed lines indicate the dimensions of the quadrants and the sensor carriers.

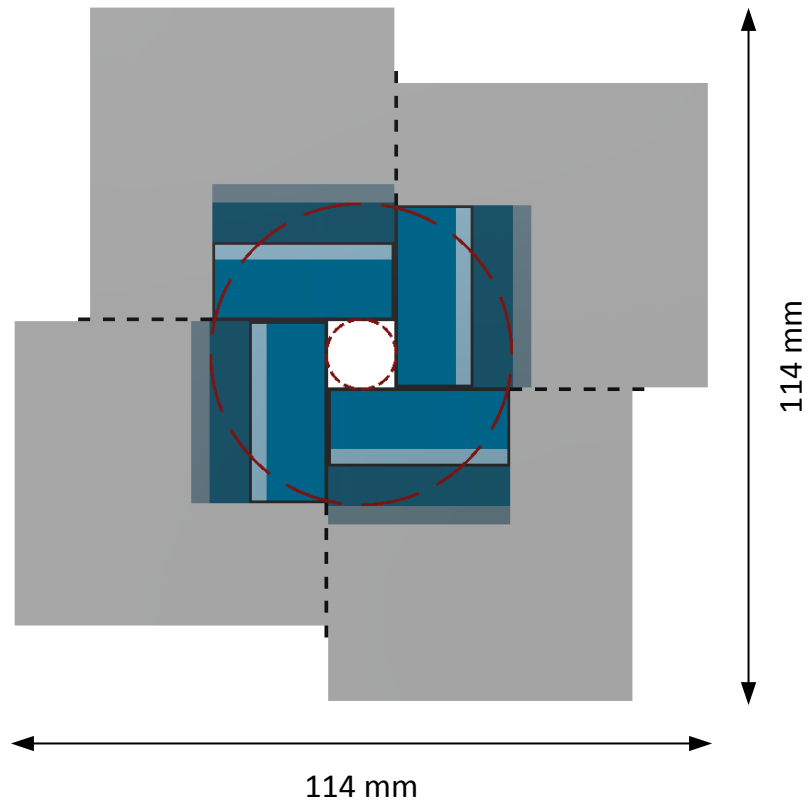


Figure 4.5: The first MVD station positioned at 50 mm downstream the target. The sensors are depicted in dark blue for the charge-sensitive and light blue for the non-sensitive sensor area on the front side. From the sensors on the back side of the station, the charge-sensitive area is visible in a darker blue. The polar angle interval to be covered is indicated with red dashed circles, while the sensor carrier is indicated with light grey. To visualize the dimensions of the sensors, a black frame has been applied to them. The dashed lines indicate the dimensions of the quadrants and the sensor carriers.

Station	Minimum		Extended		Figure
	per Quadrant	Total	per Quadrant	Total	
0	2	8	2	8	4.5
1	9	36	10	40	C.3
2	19	76	21	84	C.4
3	32	128	40	160	C.5
Total		248		292	

Table 4.2: *The number of MIMOSIS-1 sensors needed to equip the individual MVD stations for the sensor arrangements featuring the minimum number of sensors and the extended number.*

for the sensor arrangement of the MVD. The required number of sensors can be determined to be 292, as listed in Table 4.2.

4.1.3 Sensor Support and Thermal Management

The sensors have to be supported, held and cooled in the polar angle interval of the detector without exceeding the material budget target values defined for the individual MVD station. The cooling concept has to guarantee the optimal detection properties of the sensors and to provide constant temperature profiles across their surfaces, both in vacuum. The cooling of the MVD sensors to a temperature below 0 °C is mandatory to decrease the radiation-induced noise and keeping the signal-to-noise ratio at a level required for an efficient particle detection [51]. At the same time, it has to be ensured that the optimization of the cooling system does not negate the advantages of the operation in vacuum in terms of the multiple scattering in the MVD stations, see below, Section 4.2.2.

For the cooling concept of the MVD, two possible methods have been under consideration, namely an active cooling method and a heat conduction-based one.

In a cooling concept based on active cooling, the materials on which the sensors are glued and which are used to position the sensors in the polar angles of the detector are directly cooled by dedicated cooling pipes. The cooling pipes are used to evacuate the heat dissipated by the sensors to ensure the best possible sensor operation conditions and as such, need to be positioned inside the polar angles, as it is foreseen in the ALICE Inner Tracking System Upgrade [21]. The cooling pipes and the circulating cooling liquid contribute to the overall material budget of the dedicated detector station in a significant manner and the material budget averaged over the polar angles is increased substantially [21].

For a cooling concept which is based on heat conduction within the polar angles of the detector as it will be used in the MVD, materials which, at the same time, feature an excellent thermal conductivity and a high radiation length are required. Due to the operation of the MVD in vacuum, these materials provide the only path to evacuate the heat dissipated by the sensors, but simultaneously their contribution to the material budget of the individual detector station has to be as small as possible. Outside of the acceptance of the detector, the constraints due to minimizing the material budget and the resulting multiple scattering are less stringent allowing the positioning of actively cooled heat sinks.

The properties and dimensions of the sensor carriers as well as the heat sinks are discussed below. In addition, the thermal management of the interplay between the sensors, the glue and the sensor carriers will be evaluated in terms of thermal simulations.

The Sensor Carriers

The carriers serving as support and cooling material for the sensors within the polar angle interval of the MVD stations have to combine the above-mentioned requirements. Furthermore, the different coefficients of thermal expansion of the bonded materials have to be studied.

Station number	Dimensions per quadrant [mm ³]
0	50 × 51.5 × 0.15
1	80 × 80 × 0.15
2	110 × 99 × 0.5
3	140 × 127.5 × 0.5

Table 4.3: *The respective dimensions of the sensor carriers for the individual quadrant of each MVD station.*

Dimensions of the Sensor Carriers

The dimensions of the sensor carriers in terms of their length and width are adjusted to the number of the sensors which are required to cover the polar angles and, therefore, which they have to support. Additional areas have to be included to account for the positioning of the read-out cables (see Section 4.1.4 below) and for the thermal interface areas of the sensor carriers with the aluminum heat sinks.

Sensor Carrier Materials

The materials which are commonly used to evacuate the heat dissipated by electrical components out of confined volumes are metals. The high thermal conductivity provided by materials like copper with a value of ~ 400 W/mK and aluminum with a value of ~ 235 W/mK contrasts with the small radiation length of both materials. Due to their radiation length values (listed in Table 4.4), these materials are not feasible sensor carriers.

In Figure 4.6, the thermal properties of different relevant as well as reference materials are displayed as a function of the corresponding mechanical stiffness. In this figure, special emphasis is placed on the radiation length of the materials, while several important aspects, like the costs of the materials, their properties relating to machining, surface properties as well as producibility have not been taken into account. The x-axis represents the thermal conductivity and the y-axis shows the Young's modulus of the individual material, both multiplied by the corresponding radiation length of the individual material. The materials that show large values in λX_0 and EX_0 are best suited for their integration into the MVD.

Carbon fiber composite (CFC) provides a higher radiation length (a factor of two compared to aluminum) but its heat conductivity of 12 to 17 W/mK, depending on the orientation of the fiber, is lower by a factor of almost 20 compared to aluminum, see Table 4.4. Using CFC as sensor carrier material, an active cooling system with circulating cooling liquid within dedicated pipes in the polar angles of the detector would be required to evacuate the power dissipated by the sensors, as planned for the upgrade of the ALICE Inner Tracking System [21]. Applying this approach to the mandatory double-sided sensor arrangement of the MVD, the material budget target value of the first MVD station would be exceeded, as demonstrated in [62].

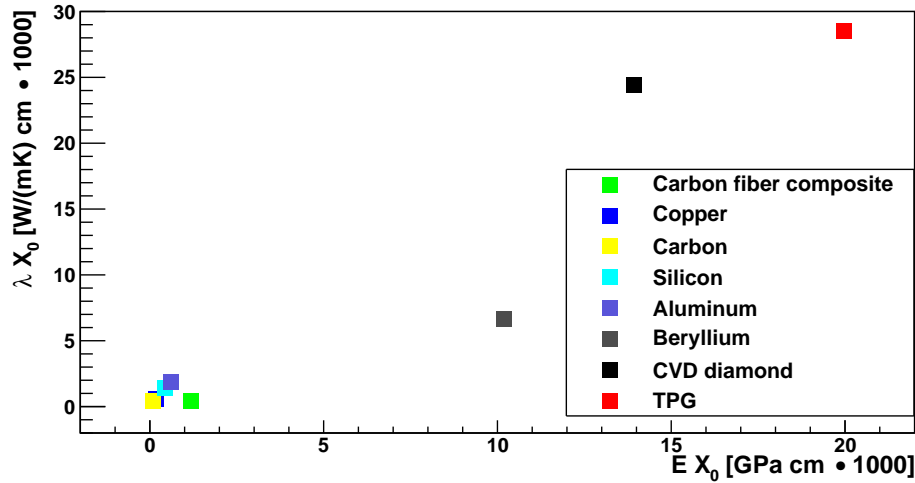


Figure 4.6: The thermal conductivity versus the Young's modulus of materials considered as sensor carriers. Optimal materials are characterized by large values in λX_0 and $E X_0$. For TPG, only the properties in the x-y-direction are shown. The figure is taken from [40].

CVD diamond⁴ [63] and Thermal Pyrolytic Graphite (TPG [64]) demonstrate the highest values of the material properties in both combinations displayed in Figure 4.6. Their physical material properties and their applicability in the MVD will be discussed in detail below.

Additionally, the different coefficients of thermal expansion (CTE) of the materials employed to cool the sensors have to be taken into account, especially in order to avoid potential bi-metal effects. For the possible sensor carriers based on advanced carbon materials, like TPG and CVD diamond, the CTEs are listed in Table 4.4. The values for bare silicon and SiO₂ are also shown. For the glue, the values of E501 which is utilized within the MVD Prototype project are listed.

The coefficients of thermal expansion of bare silicon and SiO₂ in comparison to the CTE of the sensor carrier made of CVD diamond and TPG differ by a factor of three and two, respectively. The CTE of the glue is higher by a factor of 50 than the one of the sensor carrier materials. Comparing the CTE of silicon with the one of the glue, the difference amounts to a factor of 100.

When the sensors are glued onto their carriers at room temperature and subsequently operated at about -20 °C, this temperature difference results in a change of the lateral dimension of the glue along the width of the sensor by 50 μm . At the same time, the dimensions of the sensors and the CVD diamond might vary by 0.5 μm and 0.8 μm , respectively. To prevent the sensors from breaking while their operation temperature is lowered, the glue chosen to hold the sensors on the sensor carriers has to remain soft after curing to absorb the effects of the different coefficients of thermal expansion most effectively.

⁴CVD is the abbreviation for Chemical Vapor Deposition.

Material	Heat conductivity [W/mK]	Radiation length (Dahl form) [cm]	CTE [10^{-6}K^{-1}]	Young's modulus E [GPa]
CVD diamond	> 1800	12.22	1.0	1140
TPG	$1500_{xy}/20_z$	19.03	$1_{xy}/25_z$	$1050_{xy}/36_z$
Si (bare)	150	9.48	3.0	47
SiO ₂	1.38	12.3	0.59	68
Glue	0.05	35	50 – 60	
CFC	$17_{xy}/12_z$	25.11	$0.6_{xy}/5.7_z$	47
Aluminum	235	8.99	23	68
Copper	400	1.47	17	115

Table 4.4: The physical material properties of different materials. The values are valid under standard conditions.

Thermal Pyrolytic Graphite

Thermal Pyrolytic Graphite (TPG) provides a high thermal conductivity as well as a high radiation length resulting in a low material budget, see Table 4.4. TPG has been evaluated with respect to its applicability for the MVD within the MVD Demonstrator project [40, 56] in which TPG has been employed as sensor carrier. In the course of this project, its mechanical properties have been surveyed in detail using mechanical static load tests. TPG is built out of highly oriented crystals in a layered structure. The material properties, e.g., heat conductivity and stiffness, are highly anisotropic and significantly depend on the orientation, i.e., in-plane (defined by the TPG layers) and perpendicular to that plane, see Table 4.4. It has been found that TPG provides a poor surface quality which can be seen, for instance, in cavities and grooves in the top layer of the material. In addition, the possibility to machine TPG in a reproducible and precise process is limited due to its slaty properties, see [56]. As a result of these aspects, the use of bare TPG as material for the sensor carriers within the MVD has been put last.

CVD Diamond

Polycrystalline CVD diamond is an advanced carbon-based material providing, at the same time, a high thermal conductivity (more than 1800 W/mK), a sufficient stiffness (Young's modulus of 1050 GPa) as well as a mandatory high radiation length (12.22 cm). The coefficient of thermal expansion is $1.0 \times 10^{-6}/\text{K}$ for an ambient temperature of 300 K. All these material properties have been taken from [63].

The required thickness of the CVD diamond sensor carrier can be calculated using the following equation

$$\tau_V = \frac{1}{2} \frac{\dot{q} \cdot L^2}{\lambda \cdot \Delta T} \quad (4.1)$$

in which \dot{q} represents the heat flux per unit area, ΔT the temperature gradient across the sensor surface for a given distance L and λ the heat conductivity of the CVD diamond carrier, compare [41]. For this calculation it has been assumed that the material is cooled from one side only, and the material is contributing to the heat conduction by its thermal conductivity. In addition, it is assumed that the heat flux is constant over the area. In this context, L represents the maximum distance which has to be covered with the charge-sensitive sensor area for the first MVD station, e.g., about 3 cm, across the polar angle interval of the detector station. The temperature gradient ΔT across the surface of the sensor has to be kept small to exclude potential temperature driven nonuniformity in the response of the pixels, which could turn into an unwanted fixed pattern noise, see [65].

The resulting CVD diamond thickness which is mandatory to handle the power dissipation of two different sensors, e.g., the sensor used for prototyping MIMOSA-26 (see Section 5.1.1) with a power dissipation of about 1 W/cm^2 , and the anticipated sensor for the MVD MIMOSIS-1 with an expected maximal power dissipation of 0.35 W/cm^2 , has been calculated using Equation 4.1. The used values for the calculation are listed in Table 4.5 as well as the results, which are also shown in Figure C.6 in the Appendix.

Since the minimum thickness of CVD diamond serving as qualified mechanical support providing a sufficient rigidity has been evaluated to be about $120 \text{ }\mu\text{m}$ [66], the thickness of CVD diamond used as material for the sensor carriers of the first and the second MVD station is chosen to be $150 \text{ }\mu\text{m}$. The attempt to reach the lowest technologically possible thickness of the CVD diamond sensor carrier is, in particular, important for the first MVD station since its material budget value and the resulting multiple scattering directly impacts the vertex resolution, see Section 3.1.2.

For the third and fourth MVD station, a different material can be considered to serve as sensor carrier since the target values for the material budget have been increased to $x/X_0 = 0.5\%$. In addition, the dimensions of their sensor carriers which are determined to have a value of $110 \times 99 \text{ mm}^2$ and $140 \times 127.5 \text{ mm}^2$ respectively, exceed what is technologically feasible in the production process of CVD diamond [66]. As a result of polishing and thinning the CVD diamond carrier to its desired thickness, external forces as well as internal mechanical stress are the main reasons for the limitation of the production process of thin CVD diamond carriers featuring larger dimensions. In addition, due to the costs of CVD diamond reaching up to 30 € per mm^3 , it is not affordable to equip the third and the fourth MVD stations with CVD diamond carriers.

Carbon-Fiber Encapsulated TPG

Carbon-fiber encapsulated TPG (CF-TPG-CF [67]) is a promising material to serve as sensor carrier for the third and the fourth MVD stations.

The carbon-fiber encapsulant of the TPG provides an additional stiffness to the TPG combined with only a small amount of additional material and with this an additional contribution to the material budget. The rigidity of the carbon-fiber encapsulated TPG is increased by use of vias with a diameter of $200 \text{ }\mu\text{m}$ which are arranged in a quadratic pitch of 3 mm over the surface of the TPG and which have been perforated into the TPG. The vias are

Variables				
\dot{q}	[W/cm ²]	1	0.35	0.35
ΔT	[K]	10	10	5
L	[cm]	3	3	3
λ	[W/mK]	2300	2300	2300
τ_V	[μm]	~ 200	~ 70	~ 150
x/X_0	[%]	0.164	0.057	0.123

Table 4.5: Calculation of the thickness of the CVD diamond applying three different scenarios using Equation 4.1. In the first column, an increased power dissipation for the MIMOSA-26 sensors is assumed; in the second column, the result assuming the expected power dissipation of MIMOSIS-1 is listed; the third column shows this result taking into account the expected power dissipation of MIMOSIS-1 combined with a lower allowed temperature gradient across the sensor's surface.

filled with glue which additionally fills up the space in between the carbon fibers, thus also avoiding that the glue leaks onto the carbon-fibers. The thickness of TPG can be assumed to be 380 μm . A value of 60 μm is expected for the carbon-fibers [68]. The properties of this material combination are subject to ongoing studies.

The Heat Sink

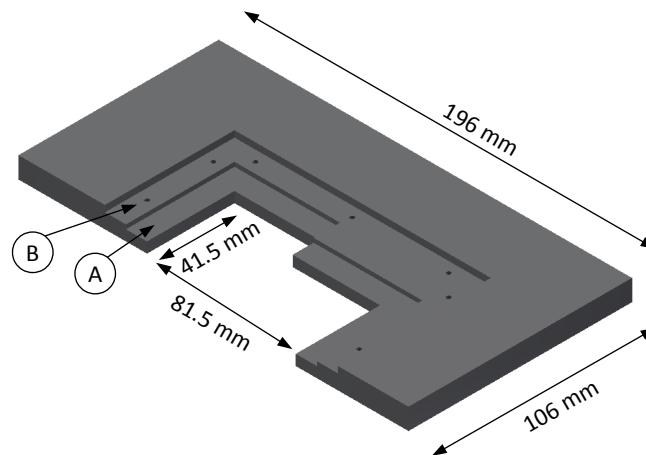
The sensor carriers are thermally coupled to their heat sinks which are positioned in close vicinity to the acceptance of the individual MVD station. This ensures that the length of the cooling paths from the sensors to the areas in which their dissipated heat can be evacuated from the sensor carriers are minimized. At the same time, the material budget inside the polar angles is kept at a minimum. An individual heat sink will be provided for each half-station serving two sensor-equipped quadrants at once. To limit the probability of being radioactively activated, the heat sinks of the MVD will be made of aluminum.

To evacuate the heat efficiently from the sensor carriers, the heat sinks are enclosing the individual sensor carrier from two sides. Therefore, a c-like shape of the heat sinks has been proposed, compare Figure 4.7(a). The individual aluminum heat sink contains a buried pipe to allow for the circulation of the cooling fluid⁵. To enlarge the area which can be used to transfer the heat from the heat sinks to the cooling liquid, two half loops are embedded in the short sides of the heat sinks. The length of the cooling pipe inside the heat sinks is station-dependent and, therefore, increasing for the MVD stations 1, 2 and 3 to maximize the heat transfer. The properties of the circulating cooling liquid have to be optimized with respect to its flow parameters and its interaction with the cooling pipes inside the heat sink in order to provide an efficient heat evacuation. To limit the heating up of the cooling liquid while being pumped from the cooling system to the vacuum vessel, the installed cooling pipes in between these two MVD components have to be insulated from the ambient temperature. The dimensions of the heat sinks of the individual MVD stations are listed in Table C.1 in the Appendix.

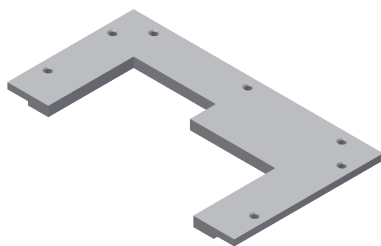
The sensor carriers are clamped onto the heat sinks from the top by dedicated cover plates providing the necessary fixation of the quadrants in the polar angles of the detector, compare Figure 4.7(b). To establish a thermal interface between the aluminum heat sinks and the sensor carriers, an area of 10 mm along two sides of the individual sensor carrier as well as on the dedicated heat sink, indicated with the letter (A) in Figure 4.7(a), is provided. The thermal interface itself has to be optimized to limit the temperature gradient from the heat sink to the sensor carrier. Here, soft heat conducting pads may be considered, optionally, in combination with a low outgassing heat conducting paste [69] in order not to deteriorate the vacuum. In Figure 4.7(d), the heat sink, a cover plate to allow for the clamping of the quadrants on the heat sink and the assembled heat sink are shown.

In the context of this thesis, a detailed test of the cooling concept of the MVD has been conducted using the example of the MVD Prototype. The results are presented in Sections 5.2.1 and 5.4.1 below.

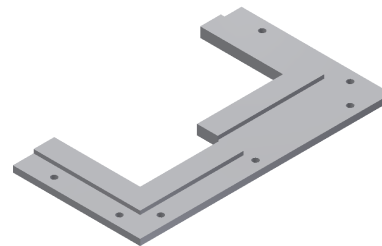
⁵The decision as to which type of the cooling fluid will be used depends on the operation temperature of the sensors.



(a) The heat sink of the first MVD station.



(b) Cover plate, front side.



(c) Cover plate, back side.



(d) Cross-sectional view of the entire heat sink including the quadrants.

Figure 4.7: At the top, the heat sink of the first MVD station is depicted. The dimensions are listed in Table C.1. The letter (A) indicates the thermal interface area on which the sensor carrier will be positioned. It will be clamped onto the heat sink from above using the cover plate which is machined in a step-like arrangement and which is then screwed onto the heat sink using the threads on the level indicated with the letter (B). Below that, the cover plate from two separate points of view and, at the bottom, the assembled heat sink is shown.

Thermal Management

Based on the proposed sensor arrangement on an individual MVD station, the thermal management between the sensors, the glue and the sensor carriers is thermally simulated focusing on two different temperature profiles on the individual sensor. The temperature gradient ΔT across the sensor's surface and the absolute sensor temperature are chosen to characterize the cooling concept of the MVD.

The different building blocks of the MVD and media involved in evacuating the heat dissipated by the sensors from the detector are sketched in Figure 4.8. In addition, the thermal interfaces defined by the contact areas of two different integrated materials are indicated. These thermal interfaces are introducing additional temperature gradients in the system. The thermal coupling between the materials involved has to be adjusted to minimize the impact of these temperature gradients on the temperature difference between the temperature set for the cooling liquid at the cooling system and the temperature measured on the sensors since the cooling power of the set-up, including the chiller and the piping, is not unlimited. The heat dissipated by the sensors is transferred through glue (1) to the sensor carrier. From there, the heat is evacuated to the aluminum heat sink, using the thermal interface indicated with (2), and the cooling liquid circulating in the cooling tubes (3), towards the cooling system (4), which finally removes the heat from the system.

The heat transfer between two materials defining a thermal interface is described with an equation formulated by Newton

$$\dot{Q} = \alpha \cdot A \cdot \Delta T_{\alpha} \quad (4.2)$$

in which \dot{Q} represents the power dissipation of the sensors, α the heat transfer coefficient, A the contact area between the materials defining the thermal interface and ΔT_{α} the temperature gradient between the materials involved.

The optimization of the heat transfer between the involved materials has to be carried out

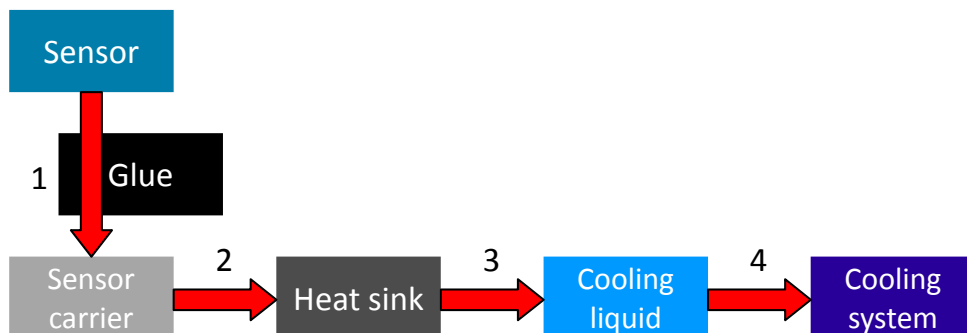


Figure 4.8: The heat flow and thermal interfaces between the involved components of the MVD.

according to the variables shown in Equation (4.2). Since the power dissipation of the sensors is determined by their design for a certain operation scenario, a potential reduction of the temperature gradient can only be achieved by optimizing the contact area A and the heat transfer coefficient α .

An increase of the dedicated contact areas which are included in the design and the dimensions of the sensor carriers as well as the heat sinks to establish their thermal interface might be cost-intensive (in particular for the CVD diamond sensor carrier).

To assist in the reduction of the temperature gradient between, e.g., the sensor carrier and the heat sink, a volume in between these materials [70] can be introduced, which can be filled with thermal conductive materials. The heat transfer coefficient is described as

$$\alpha = \lambda/s, \quad (4.3)$$

in which λ represents the thermal conductivity and s the thickness of the material. Different materials providing a sufficient thermal conductivity as well as a low outgassing rate have been studied in the context of the PANDA⁶ luminosity detector [69].

Simulation of the thermal behavior of a quadrant of the MVD stations

The thermal behavior of a quadrant of each MVD station, comprising sensors, sensor carrier and glue, is simulated using Autodesk Simulation CFD⁷ 2014 [71]. This allows to evaluate the temperature gradient across the sensor's surface as well as the absolute sensor temperatures for different sensor power dissipation values with respect to the temperature of a heat bath in which the thermal interface area of the sensor carrier has been positioned, see Figure 4.9(a).

The temperature gradients across the surface of the individual sub-matrices of the sensors have to be kept small, e.g., in the order of 10 K, to exclude potential temperature-driven nonuniformity in the response of the pixels. This applies, in particular, in case there might be only one common operation setting per matrix anticipated to handle the adjustment of the pixel threshold [72].

The sensors have to be cooled during their operation in the high radiation environment which is expected at the positions of the MVD stations. Within the silicon of the sensors, radiation-induced defects cause the occurrence of a leakage current which results in a raise of the noise. The signal generated by a traversing particle has to overcome the applied threshold level, see Section 5.1.1, which has to be set commensurately with the current amount of noise. Therefore, the signal-to-noise ratio is decreasing. The operation of the sensors at a temperature below 0 °C should limit this effect, see [49], as well as the impact of electronic noise onto the generated signals (e.g., shot noise [39]).

⁶PANDA is the abbreviation for Anti-Proton ANnihilation at DArmstadt, and one of the experiments at the future FAIR facility.

⁷Autodesk Simulation CFD 2014 provides a direct interface in Autodesk Inventor Professional 2013 [57]. The constructed 3D-model can be exchanged between these programs without additional effort.

Material	Station	Heat conductivity [W/mK]	Power dissipation [W/cm ²]	Temperature [°C]
CVD diamond	0/1	2000 _{xyz}	—	—
TPG	2/3	1500 _{xy} / 20 _z	—	—
Silicon	all	150* at 20 °C	—	—
Glue	all	0.05	—	—
Sensor	all	—	0.35	—
	all	—	0.185	—
$T_{\text{interface}}$	all	—	—	−20

Table 4.6: *The parameters used for the simulation of the thermal management of the individual quadrants of the MVD stations.*

**For the thermal conductivity of silicon, temperature-dependent values have been applied, see Figure C.7.*

For the first and the second MVD station, the properties of CVD diamond are assigned to the sensor carriers, while for the third and the fourth MVD station, the material properties of bare TPG are applied to the sensor carrier to substitute the CF-TPG-CF. The properties of the glue are assumed to be identical with those of the glue employed in the MVD Prototype project, see Section 5.1.3. All parameters used within the thermal simulations are listed in Table 4.6.

The results for the temperature gradients across the sensor's surface are extracted after a thermal equilibrium between all components has been developed. The absolute temperatures on the sensors are referenced to the temperature of the heat bath $T_{\text{interface}}$.

Results

The results⁸ of the thermal simulations for the first MVD station are shown exemplarily in Figure 4.10 (for the other stations, cf. Figures C.9, C.10 and C.11 in the Appendix).

In Figure 4.10, the dimensions of the individual plots are defined by the dimensions of the sensor carriers. The dimensions of the MIMOSIS-1 sensors positioned on the front and back side of the sensor carriers are indicated by the dashed lines. One block within these borders symbolizes the charge-sensitive area of an individual FSBB. The thermal interface area which is positioned in a heat bath with a temperature of -20 °C is indicated by the continuous line in 10 mm distance to the edges of the sensor carrier opposite to the sensors. The area located between the sensors and the sensor-free thermal interface, on which neither

⁸Given the fact that the MIMOSIS-1 sensors are not yet available, these results can only be seen as reference values until further experimental investigations which are not part of this thesis have been conducted.

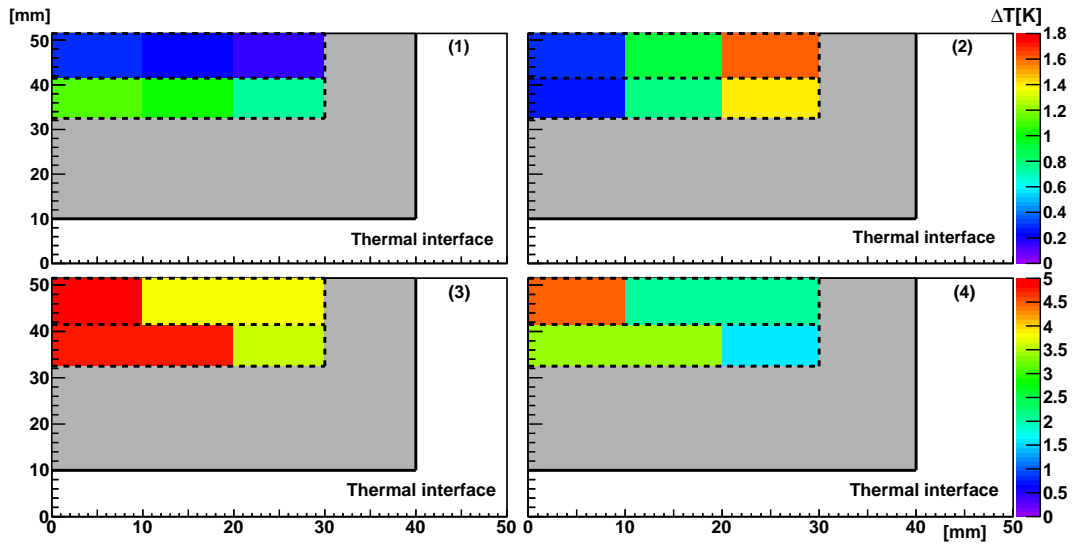
sensors are positioned nor the thermal interface to the heat sink is being formed, is depicted in grey.

The temperature gradients across the individual FSBB surface are evaluated as function of the pixel column (upper left plots, (1)) and the pixel row (upper right plots, (2)). The temperature gradients in the pixel column direction do not exceed 0.8 K for a sensor power dissipation value as heat input of 0.35 W/cm^2 and 0.4 K given a heat input of 0.185 W/cm^2 . In the direction of the pixel row, the temperature gradients found are not higher than 1.6 K and 0.6 K featuring a heat input of 0.35 W/cm^2 and 0.185 W/cm^2 , respectively. It has to be noted, though, that the temperature gradients across the FSBB surfaces are only evaluated for the positions sketched in Figure 4.9(b). For other positions across the FSBBs, the temperature gradients may vary.

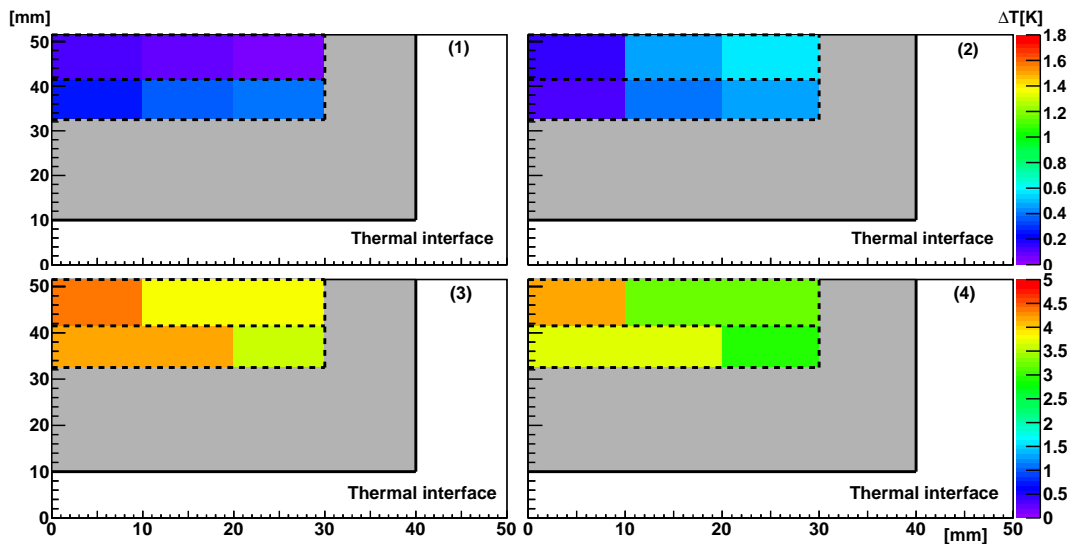
The lower left and lower right plots show the results of the evaluation of the maximum (3) and minimum (4) temperature found on an FSBB with respect to the temperature of the heat bath in which the thermal interface area has been positioned. The temperature difference between the maximum temperature found on an FSBB on the first MVD station and the temperature of the heat bath is $T_{\text{maximum}} - T_{\text{interface}} = 5 \text{ K}$ for a sensor heat input of 0.35 W/cm^2 and $T_{\text{maximum}} - T_{\text{interface}} = 4.4 \text{ K}$ for a value of 0.185 W/cm^2 .

The temperature gradients across the FSBBs positioned on the MVD stations do not exceed $\Delta T = 5 \text{ K}$, both in the pixel column as well as in the pixel row direction, which is indicated by the dashed line in Figure 4.11.

While the temperature difference between the maximum temperature and the temperature of the heat bath ($T_{\text{maximum}} - T_{\text{interface}}$) does not vary by more than 0.6 K when applying the two different sensor heat input values for the first MVD station, the situation differs for the other stations. Due to the increased number of sensors positioned on the sensor carrier, the temperature differences between the two different sensor heat input values rise from 7.2 K at the second MVD station and 7.3 K at the third station to 18.1 K at the fourth MVD station.



(a) Results for a power dissipation value of 0.35 W/cm^2 .



(b) Results for a power dissipation value of 0.185 W/cm^2 .

Figure 4.10: The results of the thermal simulations for the first MVD station. The dimensions of the sensor carriers mark the borders of each individual sub-plot. The dimensions of the MIMOSIS-1 sensors are indicated by dashed lines. Within these borders, each individual FSBB is symbolized by a single block. The thermal interface area which is positioned in a heat bath with a temperature of -20°C is indicated by the continuous line. The sensor-free area on the sensor carriers is depicted in grey. The temperature gradients across the individual FSBB surface are evaluated with respect to the pixel column (upper left plots, (1)) and the pixel row (upper right plots, (2)). The lower left and lower right plots show the results of the evaluation of the maximum (3) and minimum (4) temperature found on an FSBB with respect to the temperature applied to the thermal interface area.

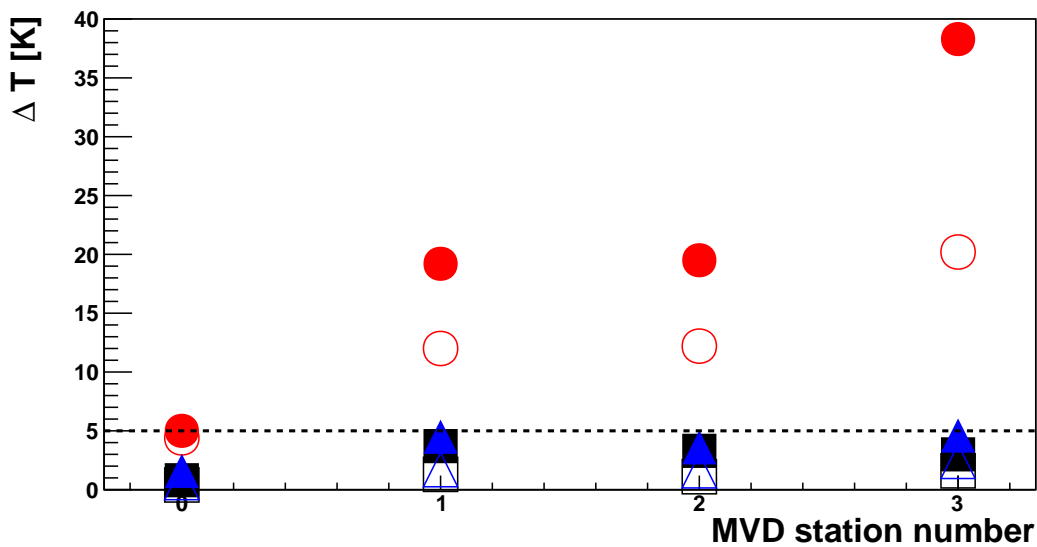


Figure 4.11: The maximum values found on the individual MVD stations in the thermal simulations. The two power dissipation values are represented by different fill factors: the full symbols correspond to the power dissipation value of 0.35 W/cm^2 , the open ones to a power dissipation value of 0.185 W/cm^2 . The blue triangles represent the maximum temperature gradient across the FSBBs of an MVD station in the direction of the pixel row and the black squares represent the maximum temperature gradient across the FSBBs in the pixel column direction. The red dots depict the difference between the maximum temperature on an FSBB of an MVD station and the temperature of the heat bath $T_{\text{maximum}} - T_{\text{interface}}$. The dashed line symbolizes a temperature gradient of 5 K which is not exceeded for both pixel directions.

4.1.4 Mechanical Properties of the Flex Print Cable

The mechanical properties of the Flex Print Cable (FPC) which is to be integrated into the MVD will be discussed in this thesis, specifically its assumed dimensions and its contribution to the material budget of each of the individual MVD stations. The electrical design and layout of the FPC is subject of ongoing studies [74]. So far, it is planned that a single FPC will provide all required electrical connections to operate two MIMOSIS-1 sensors at once.

Two different materials, aluminum and copper, are candidates for the electrical lines in the design of the FPC. From a material budget point of view, the use of an aluminum-based FPC is preferred because of the higher radiation length of aluminum compared to copper, see Table 4.4. However, the higher resistivity of aluminum compared to copper might lead to the need to integrate thicker lines compared to copper-based ones. The dependency of the thickness of the lines on the FPC and the used material is currently being investigated [74]. In addition, the production process of aluminum-based FPCs is commercially not well established yet and, therefore, the access to those cables is limited. On the other hand, the production processes of copper-based FPCs are well established; however, its use would lead to a higher contribution to the material budget of an individual MVD station compared to the aluminum option.

A conventional, copper-based FPC with an assumed homogeneous distribution of the material resulting in a material budget of $x/X_0 = 0.06\%$ [74] is included in the design proposal of the MVD.

The FPC will be positioned facing the edge of the sensors where the bonding pads and the on-chip electronics are located, see the light blue area in Figure 4.2. It will be routed parallel to the row of sensors positioned on the sensor carrier, thus it is modeled like the FPC developed for the PXL detector [75].

As a result of various constraints, such as mechanics and handling, the maximum physical dimensions of the FPCs can be determined as follows:

The length of the FPC is defined by the distance between the first bonding pad and the first stage of read-out electronics situated on top of the heat sink. This results in FPCs featuring a different length for each MVD station. It has to be taken into account that the sensors and the top of the heat sink are located in different z-positions.

The maximal width of the FPC is composed of two different numbers. First, the distance between the different sensor ladders⁹ on the sensor carriers, see exemplarily the sensor arrangement on the second MVD station in Figure C.3 in the Appendix. This distance is determined to have a value of 6 mm. Second, the length of an individual MIMOSIS-1 sensor which is assumed to be of a value of 13 mm, see Section 4.1.1.

The width of the FPC amounts to a value of 19 mm. Hence, in order to be able to read out the first row of sensors, the FPC will be covering the sensors of the second row. The width of 19 mm is a maximal working value for the time until the positions of the bonding pads of the MIMOSIS-1 sensors are specified. They have to be kept free of any other material to

⁹A sensor ladder comprises the positioning of several sensors next to each other in the same row.

Station number	FPC types	Number of FPCs	
		Type 1	Type 2
0	1	8	–
1	1	20	–
2	2	28	28
3	2	40	40

Table 4.7: *The number of FPCs required to read out the sensors to be integrated into the MVD.*

allow for the bonding of the sensors.

For the read-out of the third and the fourth sensors positioned in each sensor ladder (on the third and the fourth MVD station), another FPC has to be positioned on the sensor carrier. The additional FPCs will be positioned on top of those FPCs which read out the first two sensors.

The number of FPCs required for each MVD station is listed in Table 4.7. These numbers do not account for the fact that the design of the MVD stations requires a mirrored layout of the FPCs which will be used on the front and on the back side of each station.

4.1.5 Support Structures inside the Vacuum Vessel

The MVD will be divided into a “right downstream side” and a “left downstream side”, both made up of the MVD half-stations. The two groups of half-stations will be positioned on common base plates. The base plates fix the positions of the individual half-stations with respect to each other from the top and the bottom. In addition, this positioning allows to move the two groups of half-stations in horizontal direction perpendicular to the beam axis, and thus away from the primary beam. This feature is needed to minimize the risk of damaging the sensors as a consequence of being hit by the primary beam particles while the beam is tuned or focused. At this point in time, a distance based on experimental measurements of how far the first sensors of the MVD stations have to be moved away from a non-optimal focused beam is not yet available. The current assumption envisages a value of up to 50 mm [54].

Half-Station Support Structures

The individual MVD half-stations consist of the equipped sensor carriers and their dedicated heat sinks. Due to the different outer dimensions of the heat sinks of the individual half-stations (cf. Figure C.8), an additional half-station support structure is required to compensate for these different dimensions and to enable the mounting onto a common base

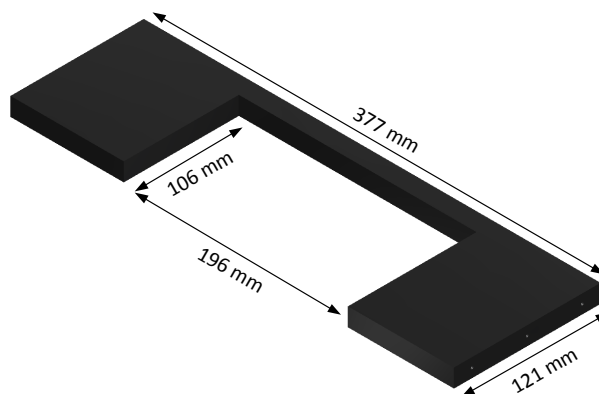


Figure 4.12: *The half-station support structure of the first MVD station positioned at 50 mm downstream the target. The cut-out in the inner part allows for the positioning of the heat sink.*

plate. The design of the half-station support structures has been chosen in such a way that a modularized construction of the MVD is permitted, as exemplarily depicted for the first MVD station in Figure 4.12. The modularized design approach of the components of the MVD eases their exchange in case of a malfunction. The dimensions of the half-station support structures are listed in Table C.3 in the Appendix.

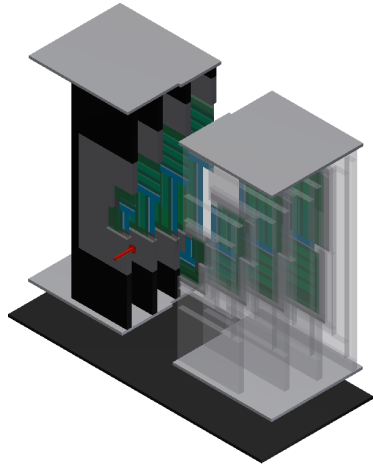
Base Plates

The base plates represent the interface between the individual MVD half-stations and the holding structure underneath them, which connects to a remotely movable sliding carriage¹⁰. A special mechanical system, which is not part of this thesis either, has to be established to position the two groups of half-stations precisely in the measuring position after moving them away from the beam axis. The precise and repetitive re-establishing of the measuring positions of the MVD stations will ease the (re-)alignment procedure of the MVD. The base plates are shown in Figure C.13 in the Appendix.

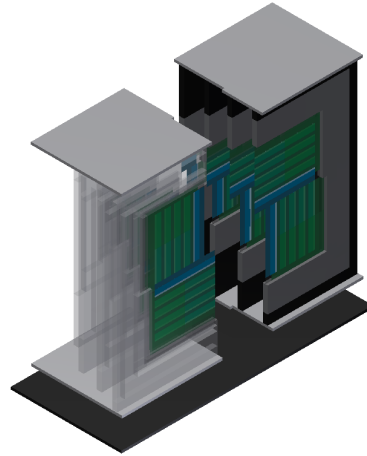
Micro Vertex Detector

The proposed design of the MVD is depicted in Figure 4.13.

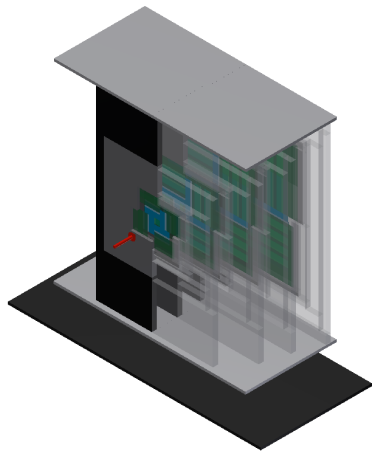
¹⁰This carriage and its mounting to the target vacuum vessel are not part of this thesis. The base plate will also provide fixture to the cables and cooling pipes.



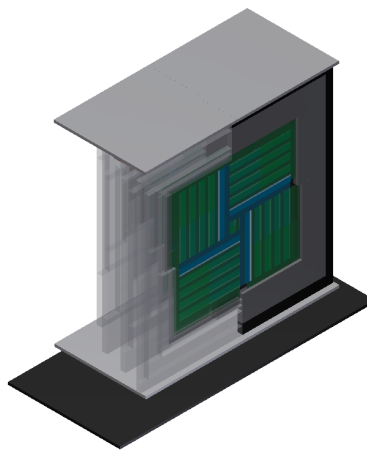
(a) Up-right frontal view on the MVD, half-stations moved apart.



(b) Up-right rear view on the MVD, half-stations moved apart.



(c) Up-right frontal view on the MVD, half-stations in measuring position.



(d) Up-right rear view on the MVD, half-stations in measuring position.

Figure 4.13: The design proposal of the MVD. To visualize all stations and their sensors, the half-station support structures and the heat sinks of the “right downstream side”-group of the half-stations are depicted transparent. The upper two figures show the two groups of MVD half-stations moved away from the beam. The common base of the MVD is represented by the black rectangular plate below the two groups of half-stations. The beam comes from the left indicated with the red arrow in figures (a) and (c). The color code corresponds to the one used in Figure 4.1.

4.1.6 The MVD Vacuum Vessel

The vacuum vessel housing the MVD has the proposed dimensions of $650 \times 540 \times 285 \text{ mm}^3$ and fits into the available volume inside the CBM magnet in front of the STS. In the vacuum vessel, a differential vacuum will be provided to reduce the multiple scattering of the produced particles to a minimum. The vacuum vessel housing the MVD is surrounded by the STS thermal enclosure [22]. The front plate of the MVD vacuum vessel supports the target chamber and connects directly to the beam pipe. The back wall of the MVD vessel has to form an interface from vacuum to normal pressure and has to feature a special light weight material with regard to the material budget.

A base table directly connected to the front flange should allow to disassemble the MVD within a limited amount of time in case the detector is not required for measurements of a physics case, see Section 3.3.

The operation in vacuum requires a yet undefined number of feedthroughs mounted on the front flange to allow the necessary supply lines of the detector, like electrical supply for the sensors, read-out cables and cooling tubes, to reach the detector inside the vacuum vessel and pipes, thus allowing for the pumping of the vacuum vessel itself.

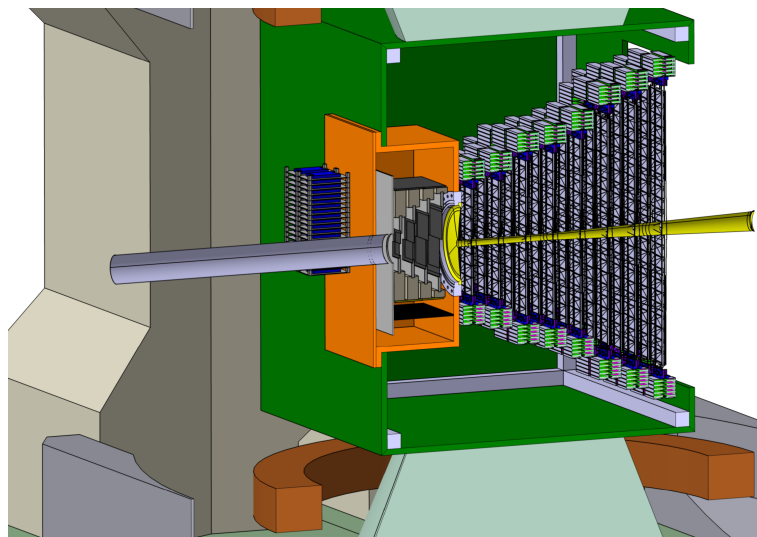


Figure 4.14: A detailed view of the MVD and the position of its vacuum vessel (orange), the beam pipe in front of the MVD and downstream the STS stations in their thermal enclosure (green). The structures outside of the STS thermal enclosure are part of the CBM Magnet. This figure is taken from [22].

4.2 The MVD in Physics Simulation

The proposed design of the MVD is used within the simulation framework of CBM, Cbm-Root [34], featuring a realistic description of the material budget of the detector as well as the implementation of segmented charge-sensitive sensor areas in the double-sided arrangement. The required steps to be taken until the geometry can be used in CbmRoot will be introduced below and initial studies employing this geometry will be presented.

4.2.1 CAD to ROOT-Transformation

The Transformation Routine

The specific transformation routine used to transform a designed engineering model into a format which can be used within the dedicated simulation framework, starting from a standardized exchange format of common CAD software, has been developed by the Micro Vertex Detector group of the PANDA experiment [76].

Two important preparation steps have to be conducted in advance to facilitate this transformation, namely the reduction of the complexity of the parts of the model to basic geometric shapes and a unique naming scheme, in particular, for the charge-sensitive sensor areas. For the transformation discussed in the context of this thesis, the transformed model is adopted from the geometric design of the detector allowing for fast changes of the layout as well as the implementation of additional detector components. In studies requiring a different focus, for example, relating to a possible misalignment of the sensors, a different sensor arrangement on the MVD stations is mandatory to prevent the sensors from overlapping each other.

Geometric Shapes

The transformation routine requires a detector model consisting of basic geometric shapes which are not too complex, e.g., rectangles, circles, or cylinders. Therefore, the model of the MVD introduced in Section 4.1, has to be revised to contain basic geometric shapes only. In particular, the heat sinks and the support structures of the MVD half-stations have to be adopted because of their structural complexity, cf. Figures 4.7 and 4.12.

Naming Convention of the Sensors

For the later use of the MVD model in the simulation framework, it is mandatory that all transformed geometric shapes are assigned a unique name or coding, depending on their position within the model. The necessity to provide a unique naming scheme is directly connected to the tracking of the particles through the sensors. If a particle is traversing several sensors positioned on consecutive MVD stations, the track reconstruction software needs to retrieve the individual and unique charge-sensitive volume on these stations to link the individual particle hit on the sensors to the particle track.

MVD-SX-QX-LX-CXX-PX	
SX	for the station [0, 1, 2, 3]
QX	for the quadrant [0, 1, 2, 3]
LX	for the layer [0, 1]
CXX	for the chip [00, ..., 40]
PX	for the chip sub-structure [0, 1] (charge-sensitive/non-sensitive)

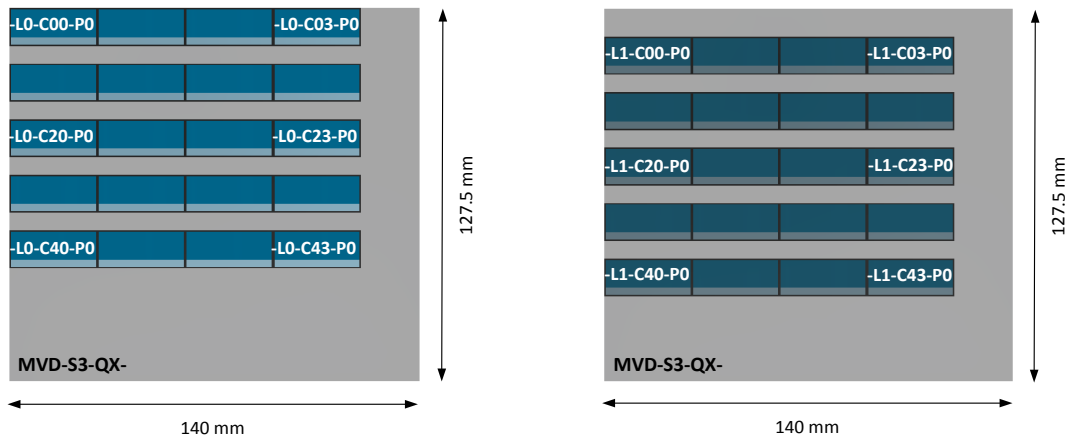
Table 4.8: *The naming convention of the sensors of the MVD.*

Mapping the naming convention introduced at the beginning of Section 4.1 to the level of the sensors, the geometrical shape of an individual sensor will be assigned with a unique identifier according to the scheme MVD-SX-QX-LX-CXX-PX as listed in Table 4.8 and exemplarily shown for one quadrant of the fourth MVD station in Figure 4.15(a).

The string SX determines the position of the sensor on the individual MVD station accounting for the numbering of the stations starting from zero. On the level of the quadrants, the counting starts with the “lower right downstream side” quadrant and continues in counter-clockwise direction using the string QX. The position of the sensor on the front side (facing the target) or on the back side (in beam direction) of the sensor carrier is represented by the string LX, featuring 0/1. In order to determine the position of the individual sensors on the sensor carrier, a two-dimensional grid is spanned over the sensors. Using this grid, the individual positions of the chips (sensors) can be numbered with CXX with respect to their position in the rows and columns. Within CXX, the first number refers to the row (also known as ladder) and the second one to the column position of the sensors, both starting from zero. For example, if the sensor is first in both coordinates, positioned closest to the beam hole, its identifier is defined to be C00. The sensor in the fifth row and first column on the fourth MVD station is addressed with the identifier C40, whereas C43 identifies the sensor in the fifth row and fourth column on the same station, compare Figure 4.15(a). The subdivision of the individual sensor into a charge-sensitive and a non-sensitive area is represented by PX. In this string, the charge-sensitive area is identified with P0 and the non-sensitive area with P1.

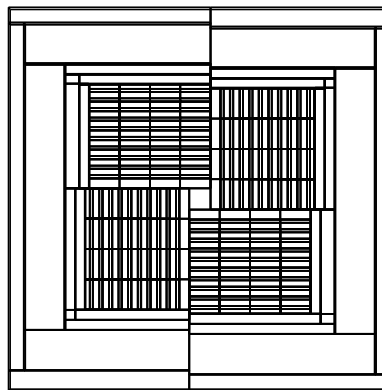
MVD within the Simulation Framework

The transformed model of the MVD can be displayed within the simulation framework. In Figure 4.16(a), the CBM magnet is depicted (in turquoise) surrounding the MVD and the STS from the top and the bottom. In Figure 4.16(b), the MVD is shown in front of the STS, for which only the sensor areas are shown (in red). In Figure 4.16(c), the MVD is



(a) The naming convention applied to the front side of the quadrant of the fourth MVD station.

(b) The naming convention applied to the back side of the quadrant of the fourth MVD station.



(c) Transformed fourth MVD station.

Figure 4.15: (a),(b) The naming convention applied to the sensors positioned on the fourth station. The sensor arrangement is identical for all four quadrants of the station. The black frames indicate the width of the sensors. (c) The outcome of the transformation process for the fourth station. Due to the limitation of using basic geometric shapes, the artificial structuring of the heat sink and the half-station support are visible.

depicted comprising all four stations, their support structures and the base plates (both in green). Figure 4.16(d) shows all four MVD stations but reduced to the components inside the detector acceptance, namely the sensor carriers made of CVD diamond and carbon-fiber encapsulated TPG (in blue) and both, the charge-sensitive and the non-sensitive, sensor areas (in red). The last picture in Figure 4.16 depicts the sensor areas of the MVD only.

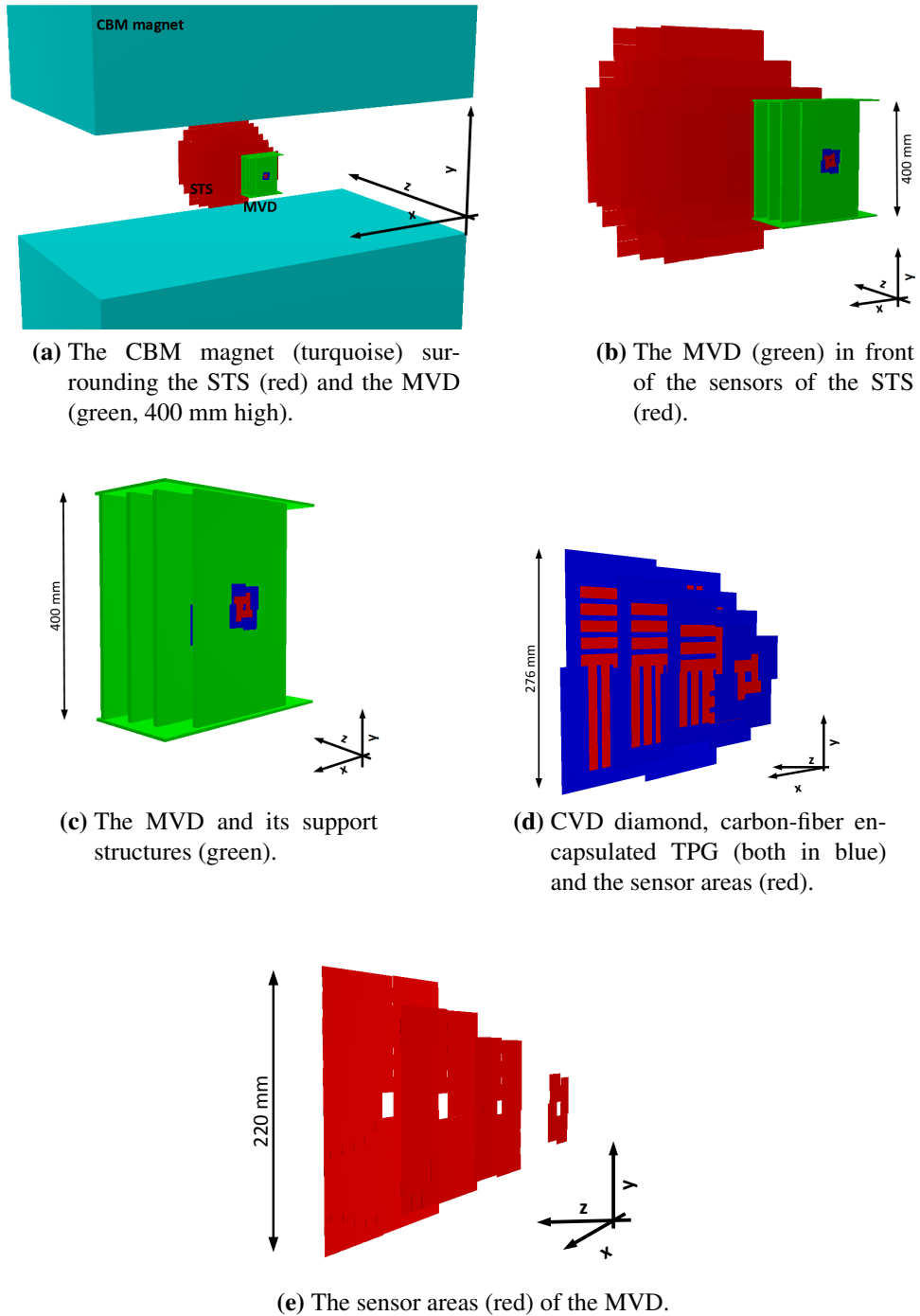


Figure 4.16: The MVD within the simulation framework.

4.2.2 Examination of the Transformation Process

The transformation process of the proposed MVD model from the engineering design to a simulation compatible design has to be examined separately for the charge-sensitive material of the sensors and the entire material of the MVD as different criteria apply.

In case of the charge-sensitive sensor shapes, it is essential that these can be retrieved from the outcome of a simulation in which the particles produced in Au+Au-collisions in the target are transported through the geometry of the MVD.

The contribution of the materials to the material budget of the detector has to be determined using the knowledge of the materials and their thicknesses which have been implemented in the design of the MVD.

Both examination methods share the same starting point in the simulation framework of CBM as the transformed geometry is assigned to be used as MVD. The origin of the coordinate system of the new MVD geometry is located at the position of the target in order to facilitate the correct transportation of particles produced in the target through the MVD including all its components.

Examination of the Transformation Process of the Charge-Sensitive Material

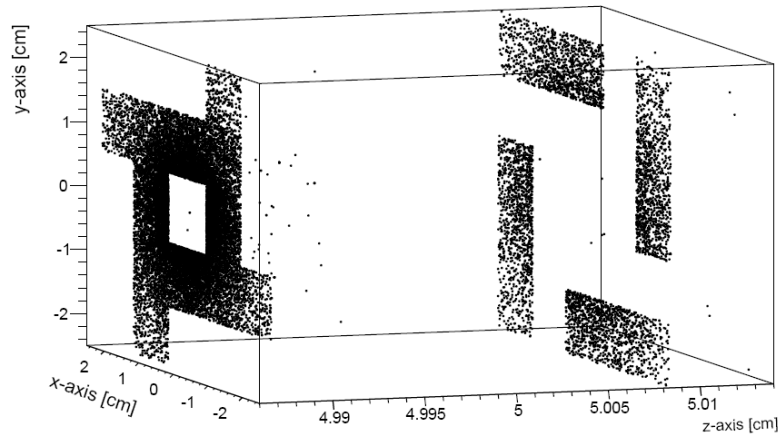
The examination of the transformation process of the charge-sensitive material is carried out by comparing the positions of these areas in the transformed model with their positions in the engineering model. In the simulation framework, a subroutine allows to set dedicated shapes as *sensitive* with respect to the crossing of particles. This option is connected to the unique identifier of the charge-sensitive sensor shape P0 which has been included in the naming convention of the geometrical shapes.

A standard routine of CbmRoot has been used to transport 50 central Au+Au UrQMD-events with an energy of 25 AGeV through the MVD geometry without applying any magnetic field. During the transportation of the particles through the detector, the hit points produced by the simulated test particles in the *sensitive*-set charge-sensitive sensor shapes are registered. The transformation process of the charge-sensitive material can be checked for its correct application by comparing the particle hit distributions on the level of the individual MVD station¹¹ with the implemented sensor arrangement on this station. The hit distributions found on the first and the third MVD station¹² are exemplarily depicted in Figure 4.17, separately for the front and the back side of the sensor carrier; the sensor arrangement of both stations is displayed in Figures 4.4 and C.4 in the Appendix, respectively. Comparing the hit distributions and the arrangement of the sensors on both MVD stations, they are found to be in accordance with each other. This means that all charge-sensitive sensor shapes implemented in the engineering model can be retrieved from the model compatible with the simulation framework.

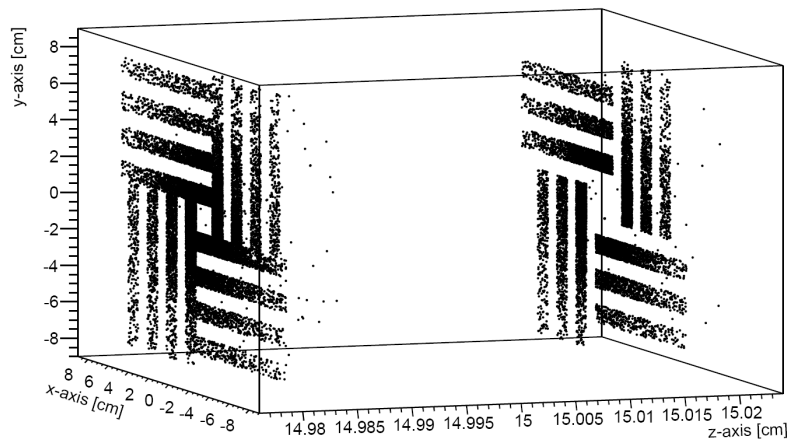
¹¹The simulated hit distributions on all MVD stations are depicted in Figure C.14 in the Appendix.

¹²The hit distributions found on the second and the fourth MVD station are depicted in Figure C.15; their individual sensor arrangement is shown in Figures C.3 and C.5, respectively. These figures can be found in the Appendix.

As a result of this observation, it can be noted that the transformation process for the charge-sensitive material has been examined successfully using the option of setting the dedicated charge-sensitive sensor shapes as *sensitive*.



(a) Simulated particle hits on the first MVD station. Note the scale of the z-axis, indicating the CVD diamond carrier thickness of $150\ \mu\text{m}$.



(b) Simulated particle hits on the third MVD station. Note the scale of the z-axis, indicating the thickness of the CF-TPG-CF sensor carrier implemented by means of the material budget contribution of CVD diamond.

Figure 4.17: Monte-Carlo hits registered on the separated sensor layers of the first and the third MVD station. The hits are generated by simulated particles (50 central Au+Au UrQMD events with an energy of 25 AGeV) transported through the detector model.

Examination of the Transformation Process of the Material of the MVD

The examination of the transformation process of the material of the MVD is carried out by determining the material budget positioned in the polar angles of the MVD by its geometry. The materials positioned inside the polar angles are listed in Table 4.9 including their individual thickness and their associated material budget contribution. In the context of this thesis, the amount of material located inside the polar angles of the detector is measured in units of the radiation length. It is essential to review the material budget of the MVD stations with respect to the material budget target values stated in Table 3.3. In particular, the material budget value of the first MVD station is of paramount importance due to its direct impact on the secondary vertex resolution of the MVD, see Chapter 3.1.2.

For the determination of the material budget of the individual MVD station, a standard routine of CbmRoot is used to generate a set of one million test particles, μ -neutrinos, which undergo almost no physical interaction with the material they are traversing due to their small cross-section. The test particles which are emitted isotropic from the target point are transported through the MVD geometry. A dedicated software code is evaluating the material budget of the materials each of the test particles passes through. For each particle found inside the geometry of the MVD, the angle ϑ of its trajectory along which it has been emitted from the target point is calculated. This track has to be sampled several times: By determining the z-position, the MVD station and layer which have been traversed are assessed. By examining the radiation length of the material, the material through which the particle has been passed is identified. The contribution of the individual traversed material to the overall material budget of each individual MVD station is calculated and saved in histograms according to the angle ϑ . For the ϑ -interval ranging from $[0^\circ, 90^\circ]$, 900 bins

Component	Material	Color	Thickness	
			[μm]	x/X_0 [%]
Sensors	Silicon	charge-sensitive / dark blue	50	0.05
		non-sensitive / light blue		
Glue	Epoxy	black	30	0.009
Support	CVD diamond	grey	150	0.123
	CF-TPG-CF	grey	500	0.247
FPC	Copper	green	200	0.06
Heat sink	Aluminum	dark grey	10^4	11.1

Table 4.9: The values of the material budget contribution of the individual components integrated into the MVD.

are reserved within the histogram. To guarantee a correct normalization process, additional counting histograms are filled simultaneously.

Comparing the contributions of the individual materials to the material budget of the dedicated MVD station depicted in the extracted histograms and the materials positioned in the geometry of the MVD listed in Table 4.9, they are found to be in accordance with each other. This means that all materials implemented in the engineering model of the MVD can be retrieved from the model compatible with the simulation framework. This observation allows to state that the transformation process of the materials has been examined successfully with the calculation of the material budget of the MVD stations using test particles traversing the MVD.

Results of the Material Budget Calculations

The extracted material budget distributions for the individual MVD stations have to be compared to the material budget target values derived from the physics cases for the MVD and are exemplarily discussed for the first and the third MVD station¹³. In addition, the discussion is subdivided for two different intervals in φ , while φ is defined as the azimuthal angle in the x-y-plane on the individual MVD station.

The set-up of the material budget plots is exemplarily discussed using the example of the one of the first MVD station which is, as function of the polar angle, depicted in Figure 4.18(a). The color coding to visualize the contribution of the individual materials to the material budget of the dedicated MVD station is adopted from the one used in the design approach of the MVD, see Section 4.1. The required polar angle coverage of the individual MVD station is given by $\vartheta = [2.5^\circ, 25^\circ]$, its end is indicated by the black dashed line. For ϑ -angles exceeding 25° and, therefore, the outer regions of the polar angle coverage, the color coding provides a lower saturation, c.f. Figure 4.18(a). The material budget target value of the individual MVD station, as defined in Table 3.3, is illustrated by the red arrow. The average material budget value calculated for each MVD station within the required polar angles is indicated by the red dashed line.

The contribution of the layer of glue to the material budget of an individual MVD station is stated in Table 4.9 and depicted in the material budget plots (in black). The contribution of the heat sink to the material budget of the individual MVD stations is also accounted for but the value of $x/X_0 \sim 11\%$ exceeds by far the maximum value displayed in the histograms. Its contribution to the material budget is visible by the dark grey area rising for ϑ -angles exceeding 30° , outside of the required polar angle coverage of the MVD stations, see Figure 4.18(a).

For the material budget as function of the polar angle in the φ -interval ranging from $[0^\circ, 2.5^\circ]$, the contributions of the individual MIMOSIS-1 sensors and the FPCs as well as their overlapping areas are clearly separated from each other as depicted in Figure 4.18(a) for the first MVD station. The material budget averaged over the polar angles is found to be $x/X_0 = 0.225\%$ for this station, which falls short of its material budget target value defined as $x/X_0 = 0.3\%$, compare Chapter 3.

¹³The corresponding figures for the second and the fourth MVD station can be found in Appendix C.

Since the sensor arrangement inside the polar angles is not only optimized with respect to their coverage with charge-sensitive material but also accounts for the detection of the inclined particle tracks by the minimization of the gap between the sensors introduced by the finite thickness of the sensor carriers and the need to position the FPCs inside the polar angle interval to read out the sensors, a local overstepping of the material budget target values cannot be avoided. This local overstepping appears in the region where the two MIMOSIS-1 sensors are overlapping and the FPC reading out the sensor on the front side of the sensor carrier is positioned, compare Figure 4.18(a). It is not apparent in the cross-sectional view of the first MVD station, see Figure C.18(a) and Table C.4, for which the contributions of the individual materials to the material budget are simply added with respect to their distance to the beam axis. The difference of the two models raises from the fact that the calculation of the material budget using simulated test particles permits to study the impact of inclined tracks with respect to the individual MVD station. Therefore, in this more realistic scenario, the test particles might traverse a larger amount of material due to their incident angle compared to a simplistic summation of the material budget contributions.

For the third MVD station, the averaged material budget calculated in the polar angle interval is determined to have a value of $x/X_0 = 0.436\%$ and, therefore, clearly below the material budget target value of $x/X_0 = 0.5\%$, cf. Table 4.10. The material budget target value is locally overstepped for the third MVD station in the outer polar angle regions for the method based on the inclined test particle tracks through the MVD stations, compare Figure 4.18(b). The values of the material budget contributions as a function of their distance to the beam axis using the simplistic summation method are found to be below the target value of $x/X_0 = 0.5\%$, as listed in Table C.5. The difference between the two methods is attributable to the different calculation methods.

For the interval in φ ranging from $[0^\circ, 360^\circ]$, the clear separation between the individual overlaps of the sensors, glue and FPCs contributing to the material budget is washed out due to the arrangement in rectangular quadrants inside the individual MVD station, see Section 4.1.2. The averaged material budget of the first MVD station can be calculated to have a value of $x/X_0 = 0.239\%$, which still falls short of the material budget target value of $x/X_0 = 0.3\%$, see Figure 4.19(a). The local overstepping of the material budget target value is slightly more pronounced compared to the φ -interval ranging from $[0^\circ, 2.5^\circ]$. In case of the third MVD station, see Figure 4.19(b), the averaged material budget is determined to have a value of $x/X_0 = 0.468\%$ and, therefore, clearly below the material budget target value of $x/X_0 = 0.5\%$ given for this station, see Table 4.10. The larger increase of the material budget in the outer polar angle regions leading to a larger local overstepping of the material budget target value can be explained by the need to position an additional FPC on each side of the sensor carriers to read out the third sensor in each of the sensor ladders, cf. Figure C.18(c) and Table C.6.

The material budget values averaged over the polar angles in ϑ of the MVD for the individual MVD stations accounting for both different φ -intervals are listed in Table 4.10.

Station	Material budget x/X_0 [%]		Target value
	Average in φ -range		
	$[0^\circ, 2.5^\circ]$	$[0^\circ, 360^\circ]$	
0	0.225	0.239	≤ 0.3
1	0.288	0.313	≤ 0.5
2	0.436	0.468	≤ 0.5
3	0.446	0.494	≤ 0.5

Table 4.10: The calculated material budget values of the individual MVD stations.

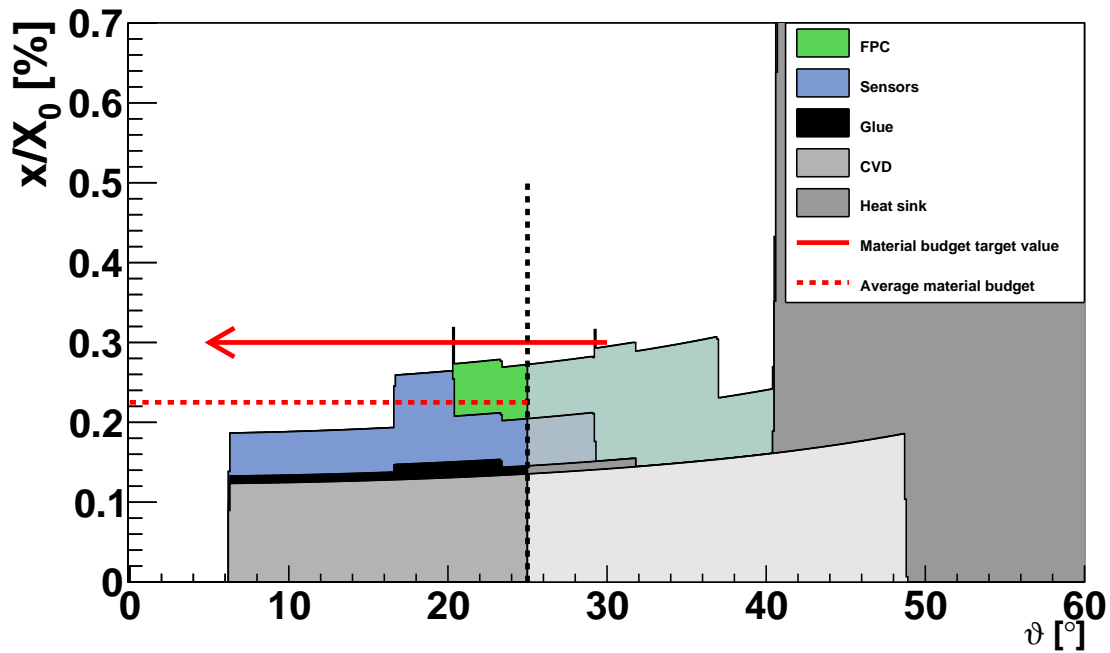
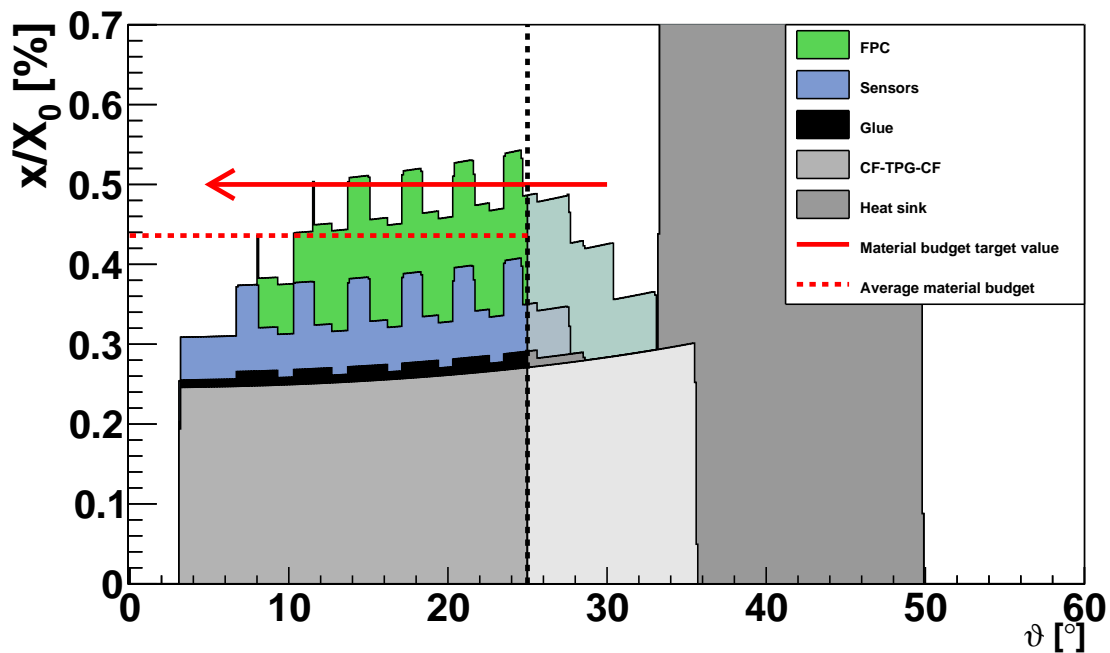
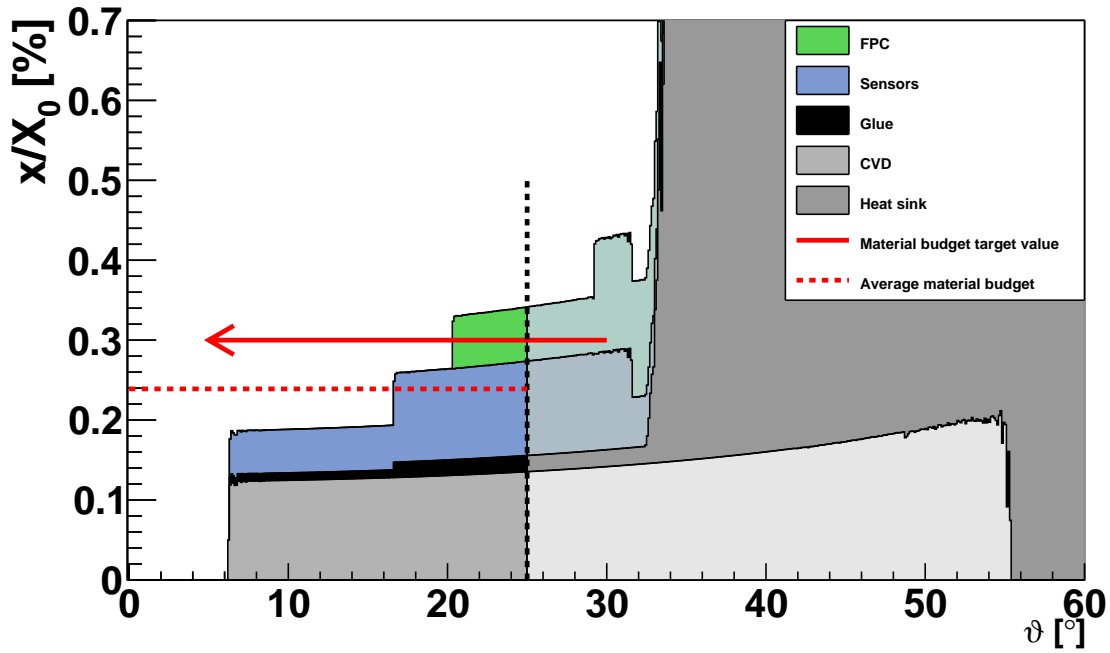
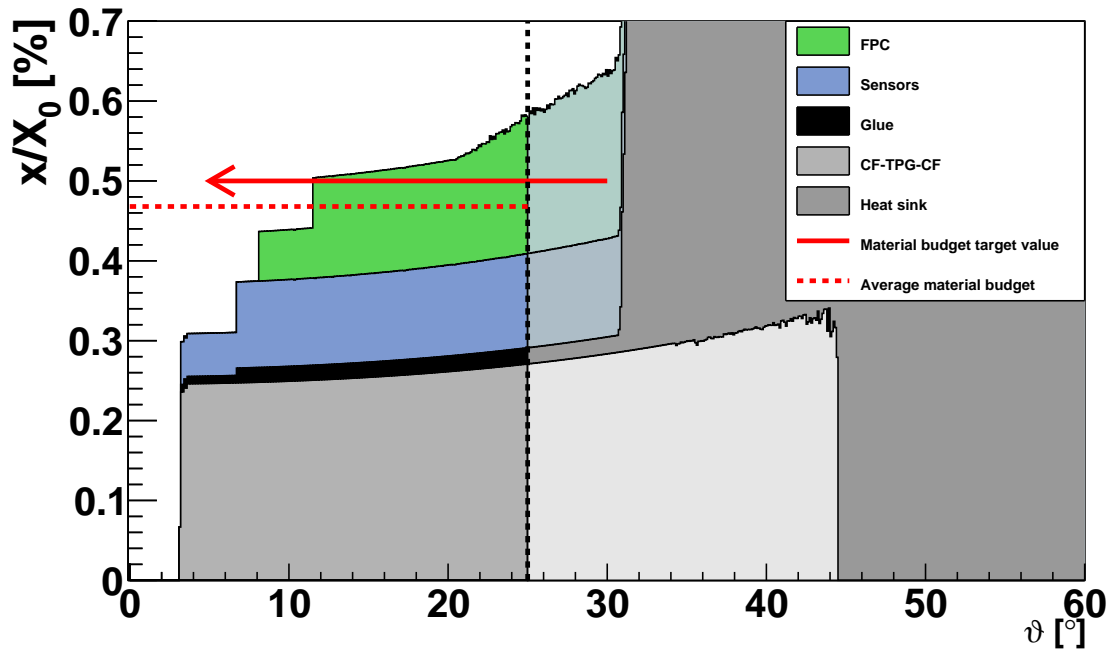
(a) Simulated material budget for the first MVD station in the **small** ϑ -interval.(b) Simulated material budget for the third MVD station in the **small** ϑ -interval.

Figure 4.18: The material budget as function of the polar angles of the first (a) and the third (b) MVD station in the ϑ -range of $[0^\circ, 2.5^\circ]$. The target value for the material budget is indicated with the red arrow at $x/X_0 \sim 0.3\%$ for the first and at $x/X_0 \sim 0.5\%$ for the third station. The required polar angle coverage reaches towards the black dashed vertical line and includes the ϑ -values featuring a color code with higher saturation.



(a) Simulated material budget for the first MVD station in the **complete** φ -interval.



(b) Simulated material budget for the third MVD station in the **complete** φ -interval.

Figure 4.19: The material budget as function of the polar angles of the first (a) and the third (b) MVD station in the φ -range of $[0^\circ, 360^\circ]$. The target value for the material budget is indicated with the red arrow at $x/X_0 \sim 0.3\%$ for the first and at $x/X_0 \sim 0.5\%$ for the third station. The required polar angle coverage reaches towards the black dashed vertical line and includes the ϑ -values featuring a color code with higher saturation.

4.3 Summary

In this chapter, a geometry of the MVD has been elaborated and examined with due consideration of the requirements on the MVD design laid down in Chapter 3. The main focus has been directed towards the coverage of the required polar angle interval of the MVD with charge-sensitive sensor material positioned on four MVD stations. Taking into account the possibility of inclined particles traversing the MVD, an overlapping area of the sensors positioned on the front and on the back side of the MVD stations has been included. Considering the distribution of the particles on the MVD stations found in the simulations carried out for the di-electron physics case [19], the geometrical acceptance of the MVD stations 1, 2 and 3 has been enlarged effectively utilizing lateral dimensions of the sensor carriers. With a preliminary sensor geometry of $30 \times 13 \text{ mm}^2$, this adds up to 292 sensors distributed over the four MVD stations.

The sensors have to be held in place and cooled inside the polar angles of the MVD. Specialized sensor carriers featuring a high radiation length as well as a high thermal conductivity are required to fulfill the demands regarding the thermal management and a minimum material budget. Two carbon-based materials, CVD diamond and carbon-fiber encapsulated TPG, meet those requirements best and have been chosen to be used as sensor carrier materials. The dimensions of the sensor carriers include dedicated space for the positioning of the FPCs which are required to read out the sensors. Due to constraints in the production process of the CVD diamond carriers related to their required dimensions for the third and the fourth MVD station as well as its costs, CVD diamond will only be used as material for the sensor carriers for the first and the second MVD station. For the third and the fourth MVD station, the sensor carriers might be made of carbon-fiber encapsulated TPG.

For the evacuation of the power dissipated by the sensors, dedicated heat sinks based on aluminum will be positioned outside of the acceptance of the detector and coupled thermally to the sensor carriers. The heat sinks are positioned and held by half-station support structures which compensate for the different dimensions of the heat sinks of the four MVD stations and allow for the mounting of the half-stations on a common base plate.

The dimensions of the complete MVD comprising four MVD stations, the sensors, their carriers, the heat sinks and the support structures, are $380 \times 387 \times 180 \text{ mm}^3$. A sketch of the entire MVD is presented in Figure 4.1.

The thermal management of the MVD has been simulated thermally on the level of the quadrants. For one examined quadrant of each MVD station, specific material properties have been assigned to the individual components. Accounting for two different possible power dissipation values of the MIMOSIS-1 sensors, the temperature gradients in the row and the column direction of the pixel matrix have been evaluated on the scale of the Full-Size-Building-Blocks employing their dedicated positions. The temperature gradients across the FSBBs of all four MVD stations do not exceed $\Delta T = 5 \text{ K}$ in both directions. The maximum and minimum temperatures found on each FSBB have been determined with respect to the temperature measured in the heat bath in which the thermal interface area defined by the contact areas of the sensor carrier and the heat sink has been positioned. While the maxi-

imum temperature does not vary by more than 0.6 K when applying the two different sensor power dissipation values for the first MVD station, the situation differs for the other stations. Due to the increased number of sensors positioned on the sensor carriers, the temperature difference between the maximum temperatures found for the different power dissipation values rises from about 7 K for the second and the third MVD station to 18.1 K for the fourth MVD station.

The proposed MVD model has been transformed from an engineering design to one which is compatible with the simulation framework. The transformation process of the MVD geometry has been examined applying two different criteria for the charge-sensitive sensor areas and the entire material of the MVD. For the examination of the transformation process of the charge-sensitive material, test particles produced in 50 UrQMD-events have been transported through the MVD, leaving hit points in the *sensitive*-set charge-sensitive sensor material. The hit distributions found on the individual layers of each MVD station have been checked to be in accordance with the arrangement of the sensors and their charge-sensitive areas on the dedicated sensor carrier. Since all charge-sensitive areas which have been implemented in the engineering model can be retrieved in the hit distributions on the MVD stations, it can be stated that the transformation process of the charge-sensitive material has been carried out successfully.

The transformation process of the entire material of the MVD is examined with the calculation of the material budget experienced by the test particles passing through the geometry. The material budget and the averaged material budget values are compared to the material budget target values introduced in Chapter 3. The averaged material budget values fall short of these target values given for the MVD stations. For the complete φ -interval ranging from $[0^\circ, 360^\circ]$, the averaged material budget is of a value of $x/X_0 = 0.239\%$ for the first MVD station, $x/X_0 = 0.313\%$ for the second, $x/X_0 = 0.468\%$ for the third and $x/X_0 = 0.494\%$ for the fourth MVD station. However, due to the optimization of the sensor arrangement with respect to the coverage of the required polar angles, the detection of inclined particle tracks on the MVD stations and the need to position the FPCs inside the polar angles to read out the sensors, a local overstepping of the material budget target values in the outer regions of the MVD stations cannot be circumvented.

Despite the fact that the MIMOSIS-1 sensors of the MVD have not yet been designed, the positioning and integration methods of the sensors onto their sensor carriers have to be tested and revised in case of possible failures. In addition, the cooling concept chosen for the MVD has to be evaluated in detail to identify potential difficulties with respect to the provision of the best sensor operation conditions. These issues are the subject of Chapter 5.

Chapter 5

The MVD Prototype Project

The aim of the MVD Prototype project is to prove the feasibility of essential key aspects and procedures which are used to design and construct the MVD. These comprise, e.g., the double-sided integration of thin sensors and the scalability of the read-out system.

To supplement these feasibility studies, the MVD Prototype has been built as sketched in Figure 5.1(a). The focus of the MVD Prototype is placed on the double-sided, back-to-back arrangement of the sensors, achieving at the same time a low material budget of $x/X_0 \sim 0.3\%$, featuring a close-to-final representation of a quadrant of the first station of the MVD.

Compared to the MVD Demonstrator which had been successfully built and tested in-beam in 2009 [40], the MVD Prototype has to define the next steps for the technological feasibility studies culminating in the construction of the MVD. The MVD Demonstrator followed a conservative approach integrating 750 μm thick sensors on carriers each made of 500 μm thick TPG. The sensors were based on an analog read-out and have been connected to the subsequent read-out electronics using a three-layer copper-based FPC, see [40, 56]. For the MVD Prototype, the technological requirements are increased. These are mainly defined by the use of state-of-the-art materials in terms of available technologies and by the integration of 50 μm thin sensors in a double-sided arrangement onto sensor carriers made of CVD diamond. In Section 5.1, the materials and components¹ are evaluated with respect to their feasibility of being integrated into a detector meeting the requirements introduced in Chapter 3. Their contribution to the material budget of the MVD Prototype is determined in Section 5.2.2 before the integration process is described in detail.

The use of ultra-thin CMOS sensors requires the definition and evaluation of reliable sequences of individual working steps in the integration process of the sensors. The working steps have to take into account the mechanical handling, a reproducible, accurate positioning and gluing of the sensors as well as the wire-bonding and the covering of the bonds with an

¹Some of the components and materials used, e.g., the sensor generation MIMOSA-26 (see Section 5.1.1 below) were specifically chosen to be integrated into the MVD Prototype as well as into the reference planes and will not be used in the MVD.

encapsulation² adhesive. The handling of the ultra-thin sensors demanded the development of dedicated custom-made tools. Their use significantly eased the assembly of the MVD Prototype and the reference planes and contributed to the gaining of experience in the handling of ultra-thin sensors.

The integration process as well as the assembly procedure applied for the construction of the MVD Prototype and the reference planes has to be investigated in order to identify potential risks for the components and materials used. Focusing on the construction of the MVD Prototype, the integration process and the assembly procedure are discussed in detail in Section 5.3.2 below.

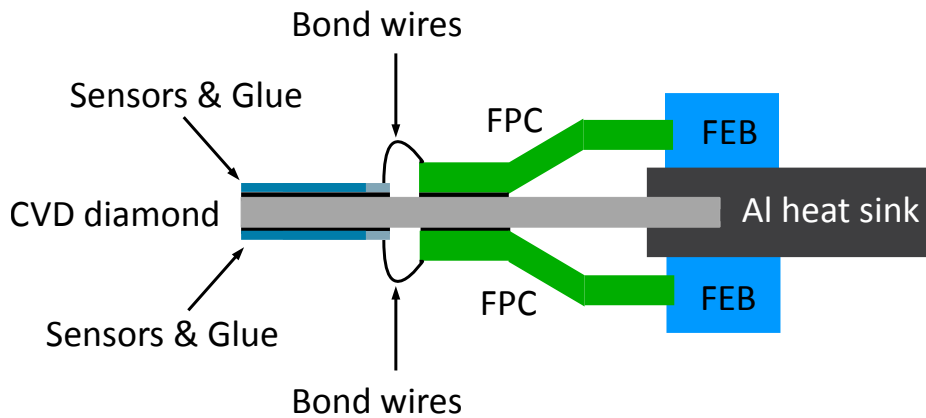
The cooling concept of the MVD, which has been introduced in Section 4.1.3 above, has been realized as part of the MVD Prototype. It is being evaluated within the MVD Prototype project focusing on dedicated thermal simulations and corresponding measurements using the MVD Prototype, see Sections 5.2.1 and 5.4.1, respectively. The integrated materials and components are examined focusing on their heat evacuation capability in order to provide the optimal operation conditions for the sensors, given that the MVD will be operated in vacuum. The vacuum operation of the MVD Prototype is not investigated in the context of this thesis, but is discussed in [53].

The read-out concept has to demonstrate its functionality and its scalability. It has to prove to be able to cope with a large amount of data knowing that the data of close to 300 sensors has to be processed in the MVD. For the evaluation of the scalability of the read-out system, several reference planes are set up featuring the same read-out electronics, read-out system and components which are used for the MVD Prototype. In both, single-layer copper-based FPCs are used to transmit the digital sensor signals to the read-out electronics. The construction of the reference planes, which are sketched in Figure 5.1(b), allowed to evaluate the integration process applied to the sensors in a larger quantity.

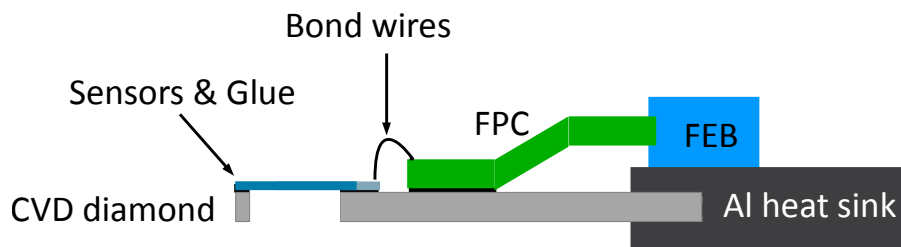
The read-out concept is not part of the work presented in this thesis, but it is discussed in [77] and [78] in detail.

The MVD Prototype and the reference planes have to be tested in the laboratory in order to verify that the applied integration process and the chosen assembly procedure do not lead to a reduction of the yields of the integrated components. In addition, it has to be shown that the sensors are operating as expected. The resolution and the efficiency of the sensors as well as the mechanical stability of the MVD Prototype has to be extracted from the data collected during an in-beam test.

²The encapsulation of the wire bonds has been executed during the assembly process of the MVD Prototype and the reference planes to protect the bonds from potential mishandling. The application of wire bond encapsulation in the MVD has to be decided in the context of the development of the FPC, see Section 4.1.4 above, as well as material budget target values of the individual MVD stations. This decision is not discussed as part of this thesis.



(a) Sketch of the MVD Prototype (not to scale).



(b) Sketch of the reference planes (not to scale).

Figure 5.1: The MVD Prototype and the reference planes. The key aspects and components in the integration process are the ultra-thin sensors (displayed in dark and light blue) and the glue (in black) placed on the CVD diamond (in grey). In addition, the FPCs (in green), the Front-End Board (FEB, in blue) and the aluminum heat sink (in dark grey) are shown.

5.1 The Components of the MVD Prototype and the Reference Planes

Definition of the “Core Module”

A “core module” allowing to follow the construction of the MVD Prototype and the reference planes consisting of common building blocks is established. Its components are listed in Table 5.1.

The “core module” comprises two 50 μm thin MIMOSA-26 AHR sensors featuring a digital read-out, a 200 μm thin high-performance cooling sensor carrier, an aluminum heat sink as well as a thin layer of glue and a Flex Print Cable (FPC) for the read-out of the sensors, see Figure 5.2.

For the MVD Prototype, two “core modules” are arranged in a double-sided, back-to-back arrangement, which allows to reference the sensor on one side of the CVD diamond carrier with the sensor positioned on the other side of the carrier using correlations of traversing particles.

The reference planes are focusing on the scalability of the read-out system and allow to evaluate the integration process applied to the sensors in a larger quantity. The single-sided reference planes host one “core module” each. They share the approach to reach a considerable reduction of the material budget in the charge-sensitive area of the sensors. Underneath the inner part of the charge-sensitive area of the sensors, openings are cut into the sensor carrier, see Figure D.4 in the Appendix. In this area, only the material budget of the 50 μm thin ($x/X_0 = 0.05\%$) sensors is contributing to the overall material budget of a reference plane. Thereby, a stand-alone experimental set-up³ consisting of MIMOSA-26 AHR sensors in each detector plane has been attained featuring a common read-out system for the sensors as well as data analysis software.

³The use of the existing beam telescope EUDET (“Detector Research and Development towards the International Linear Collider”) [79] has been abandoned due to the different data structure the sensor output is handled in. Its use would have led to the necessity of a major re-writing of the software code developed in the MVD Prototype project.

5.1. The Components of the MVD Prototype and the Reference Planes

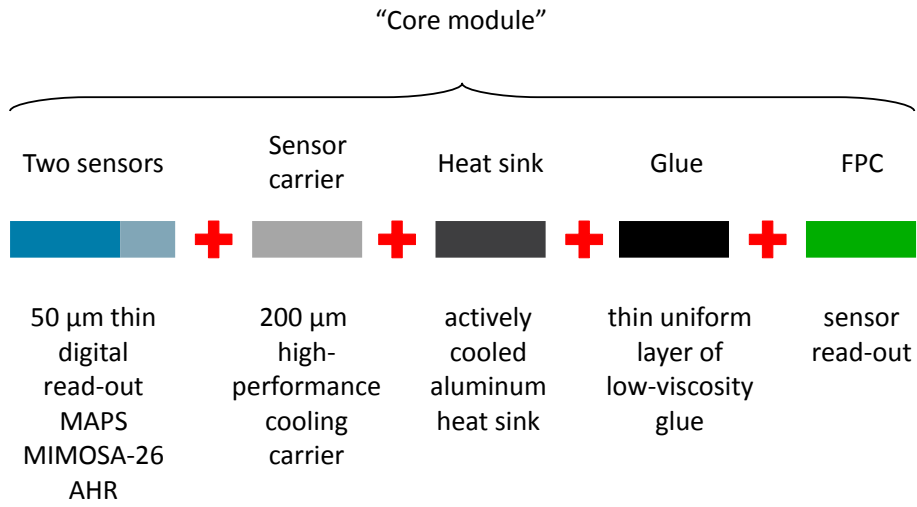


Figure 5.2: The components comprising the “core module”. The color code corresponds to the one used in Figure 5.1. Note that the sketch is not to scale.

Sensors	radiation hardness	granularity (pixel pitch)	spatial resolution	read-out time	power dissipation
	$\sim 10^{13}$ n _{eq} /cm ² at 20 °C ~ 300 krad at 20 °C	~ 18 μm	~ 5 μm	< 100 μs	< 750 mW/cm ²
Sensor carrier	radiation hardness	thermal conductivity	mechanical stiffness	material budget	
	see above	> 1800 W/mK	> 1000 GPa	$x/X_0 < 0.17\%$	
Glue	radiation hardness	thermal conductivity	viscosity / soft after curing	vacuum compatibility	re-workability
	unknown, standard epoxy, exceeding the limit above	0.05 W/mK	$\approx 1\text{Pa} \cdot \text{s}$ / no	10^{-3} to 10^{-5} mbar	using aggressive chemicals
Flex Print Cable	radiation hardness	inter-connectivity between sensors and FPC		material budget	
	exceeding the limit above	aluminum wire-bonds		$x/X_0 < 0.09\%$	

Table 5.1: The properties of the components which build up the “core module”.

5.1.1 The Sensor: MIMOSA-26 AHR

The sensor generation used within the MVD Prototype project is called MIMOSA-26 AHR, see [46, 80], developed at the IPHC in Strasbourg, France. MIMOSA-26 AHR is manufactured in a CMOS process using a 15 μm thick epitaxial layer featuring a high resistivity of about $\sim 400 \Omega\text{cm}$. It has been developed in the context of the EUDET project and is used in the EUDET “beam telescope” [79]. Since the sensor provides some of the features, e.g., JTAG and a digital output, which are also expected to be provided by the sensors developed for the MVD, it allows to evaluate the envisioned read-out system focusing on the handling of multiple sensors connected in a JTAG chain.

The outer dimensions of the sensor are $21.5 \times 13.8 \text{ mm}^2$. MIMOSA-26 AHR is manufactured on 750 μm thick wafers and has been thinned down to 50 μm in a post-manufacturing process. After thinning, the sensor is bent by a bending radius of about 20 – 30 cm resulting from intrinsic tensions, see [65] and Figure 5.3(b).

MIMOSA-26 AHR hosts 663552 pixels organized in a matrix featuring 1152 columns and 576 rows. The pixel pitch of 18.4 μm results in a charge-sensitive area of $21.5 \times 10.8 \text{ mm}^2$. The remaining sensor area of $21.5 \times 3 \text{ mm}^2$ hosts certain on-chip electronics. The on-chip electronics are represented by column-level discriminators (adjusting the threshold for each single sensor column, grouped in four matrices), the zero suppression logic, pre-amplifiers, memory, registers and sensor slow-control logic (JTAG), compare Figure 5.3(a). The sensor is read out in a rolling shutter mode. The read-out time of the sensor is determined by the time which is required to extract the information of one frame of the sensor which amounts to 115.2 μs [46].

The power dissipation of an individual MIMOSA-26 AHR has been estimated to be 750 mW. This value is not equally distributed over the complete sensor’s surface but rather concentrated in the on-chip electronics, see [81, 82]. For the discriminators located at the end of each pixel column, a value of 300 μW has been found, whereas for each pixel column a power dissipation value of 200 μW is stated.

The hardness of MIMOSA-26 AHR against ionizing radiation is stated to be of a value of 300 krad; its hardness against non-ionizing radiation is stated to be $3 \cdot 10^{13} \text{ neq/cm}^2$, both measured at room temperature, see [48].

Since a dedicated probe card has not been available prior to the integration process of the sensors into the “core modules”, their status could not be evaluated before this process had accomplished. After the sensors have been integrated into the MVD Prototype and the reference planes, they have to undergo a set of tests to evaluate their status. The status of their pixels (the appearance of dead pixels, columns/rows or/and matrices) has to be determined, and the response of the pixels and the sensor with respect to particles emitted by a radioactive source as well as the functionality of the sensors with the dedicated read-out electronics have to be evaluated. For these tests, dedicated sensor operation settings are applied in the laboratory and the in-beam test. These settings are defined as follows. The charge, which is deposited in the form of electron-hole pairs in the epitaxial layer by a traversing particle, is collected by the diode of the pixel and passed to the in-pixel Correlated Double Sampling (CDS) micro-circuitry. The outcome of a CDS operation contains a contribution of the use-

5.1. The Components of the MVD Prototype and the Reference Planes

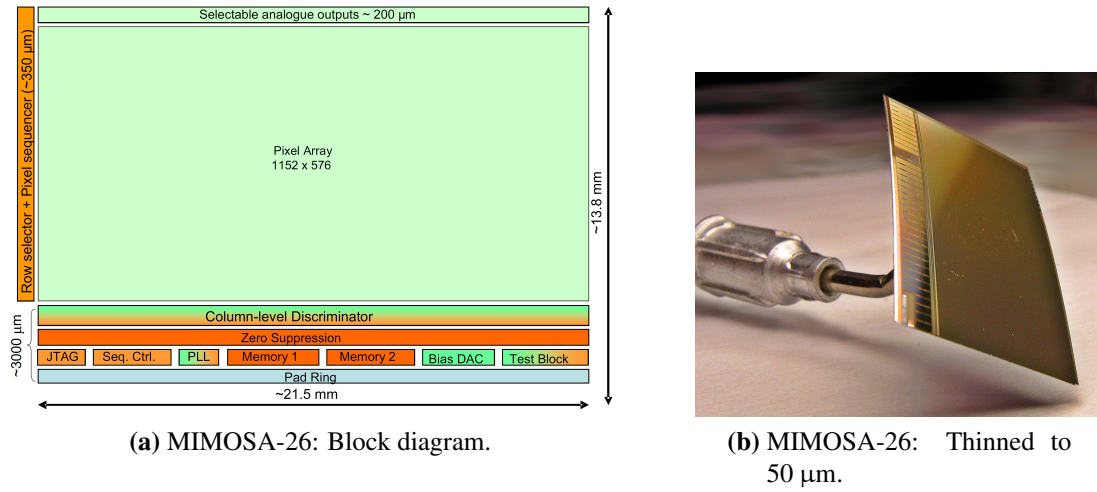


Figure 5.3: (a) The block diagram of MIMOSA-26 showing the pixel array in the middle of the sensor area; the on-chip electronics is placed in the lower part of the sensor, the figure is taken from [46].
 (b) A thinned MIMOSA-26.

ful signal (in case it exists) and of the electronic noise (mostly shot noise). It is compared to a common reference voltage which is applied to the comparators located at the end of the pixel column. The result of this comparison – a logical “0” when the CDS signal is higher than the reference voltage and a logical “1” in the opposite case – is propagated to the sensor’s data compression unit and afterward sent towards the read-out electronics using a differential output line.

The reference voltage can be adjusted separately for each of the four sub-matrices of MIMOSA-26 using an internal 8-bit Digital-to-Analog Converter (DAC). The DAC itself is programmed by internal sensor registers which can be accessed using the implemented JTAG protocol. The DAC values, also referred to as thresholds and “sensor operation settings”, are set per sensor sub-matrix.

Since the CDS signal also contains a contribution of noise, it is expected that the result of the comparison of the CDS signal with the reference voltage may differ from a logical “0” even for cases in which the signals of the traversing particles are not present. These cases originate from excessive noise of the individual pixel and/or too low threshold settings and are called “fake hits”. The frequency of the occurrence of such fake signals is referred to as “fake hit rate” which is being calculated per pixel and per frame.

Despite the fact that MIMOSA-26 AHR⁴ sensors do not meet all requirements for the MVD in terms of the required radiation hardness and the read-out time, they offer the opportunity to test the integration process as well as the read-out concept.

⁴In the following, the MIMOSA-26 AHR will be simply referred to as “MIMOSA-26”.

5.1.2 The Sensor Carriers

The combination of a high thermal conductivity and high radiation length required for the material of the sensor carriers is provided best by CVD diamond and carbon-fiber encapsulated TPG, derived and discussed above, in Section 4.1.3.

For the MVD Prototype, the sensors are glued onto a CVD diamond carrier featuring a size of $43.5 \times 44 \text{ mm}^2$ and a thickness of $200 \text{ }\mu\text{m}$ corresponding to $x/X_0 = 0.164\%$.

For the reference planes, the sensor carriers are based on $200 \text{ }\mu\text{m}$ thin CVD diamond and 1 mm thick aluminum.

5.1.3 The Glue

A glue had to be identified that would meet the requirements listed in Table 5.1 to the best extent possible. The glue should allow to form a uniform and thin layer between the sensors and the sensor carrier, hence, serving both, the improvement of the heat transfer from the sensors to the carriers and a minimum contribution to the overall material budget. Therefore, the formation of a thin layer has to be an intrinsic and required feature of the glue itself since pressing the $50 \text{ }\mu\text{m}$ thin sensors onto the glue is not an acceptable option. Because of their thickness, any action applied to the sensors which might lead to mechanical damage has to be prevented.

Since the sensors and their carriers feature different coefficients of thermal expansion, the appearance of a bi-metal effect leading to mechanical tensions is expected. To avoid a potential damage of the sensors originating from this effect, an elastic resin is of interest. The vacuum operation of the MVD and its assembly at atmospheric pressure requires a void-less glue dispensing as well as a low outgassing glue. The event that any voids (and air pockets) enclosed in the glue layer might expand during the pumping process of the MVD vacuum vessel and result in damaged or fully destroyed sensors has under any circumstances to be avoided. For further details see the calculation in the Appendix D.1.

Applying these requirements, the properties of various glues have been surveyed. From among these, a set of four different glues has been selected for a more detailed study of their usability [72]. Their properties are listed in Table 5.2.

The main focus has been placed on their ability to form a uniform and thin layer between the sensor carrier and the sensors themselves and to support the development of an optimal thermal interface between them. The different resulting glue distribution schemes and related numbers of dispensed gluing dots are depicted in Figure 5.4. Since the potential coverage of the bonding pads of the real sensors might hamper an electrical connection between the sensor and the FPC by use of wire-bonding to these pads, it has to be ensured that the glue is not leaking from underneath the sensors onto the bonding pads.

To allow for a direct visual inspection of the established layer of glue during the gluing studies, glass samples featuring different dimensions have been chosen to represent the CVD diamond sensor carriers and the sensors, respectively. For the first three glues listed in Table 5.2, the sketched gluing dot distributions have been applied. For the remaining glue

5.1. The Components of the MVD Prototype and the Reference Planes

Properties	Thorlabs		Epotecny Sarl	
	Torr Seal-10	E505	NOA88	E501
ρ	[g/cm ³]	1.55	1.3	1.1
η before curing	[Pa·s]	200 – 500	1.6 ± 20%	0.25
CTE	[10 ⁻⁶ K ⁻¹]	63	60 – 70	50 – 60
λ	[W/mK]	0.544	0.05	0.05
Curing time		60 min. at 80 °C	90 min. at 60 °C	30 – 60 sec. UV-light
Number of components		2	2	1

Table 5.2: Properties of the resins considered for the assembly of the MVD Prototype. The values are taken from [83, 84, 85, 86].

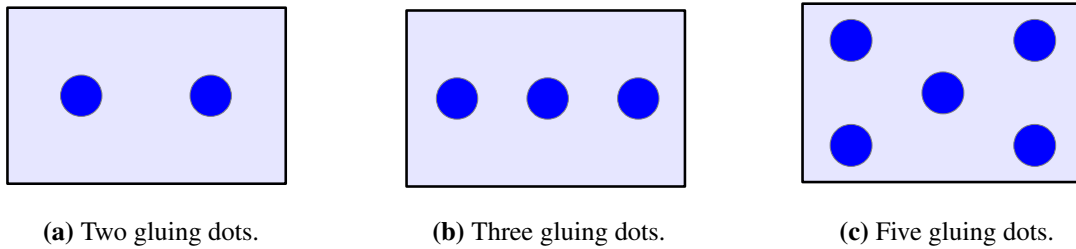


Figure 5.4: The glue dot distribution options. The sensors are represented by the rectangle, the glue by the blue dots.

listed, it has been found that the sole placing of a single gluing dot in the middle of the glass dummy is sufficient to fill the space between the glass dummy and the underlying glass completely. The sensor glass dummies have been positioned manually on top of the layer of glue. To achieve a defined and homogenous distribution of the glue underneath the glass dummies, a small metal block of 45 grams has been placed on top of the sensor glass dummies for the first ten minutes of the curing process which is carried out according to the guidelines provided by the manufactures, see Table 5.2.

Gluing Results

The glue Torr Seal-10, manufactured by Thorlabs [83], cannot be dispensed in a sufficiently thin layer for the given experimental set-up, due to its high viscosity. The thickness of the layer of glue has been evaluated to be $84 \pm 15 \mu\text{m}$ by using an outside digital caliper which provides an accuracy of $10 \mu\text{m}$ [87]. In addition, the high paste-like viscosity hampered every attempt to dispense a uniform layer of glue. The dispensed gluing dots are clearly visible in Figure 5.5(a).

Using the glue E505, fabricated by Epotecny Sarl [84], the dispensing of a thin layer of glue is eased as a result of a lower viscosity; however, a uniform layer showing no appearance of

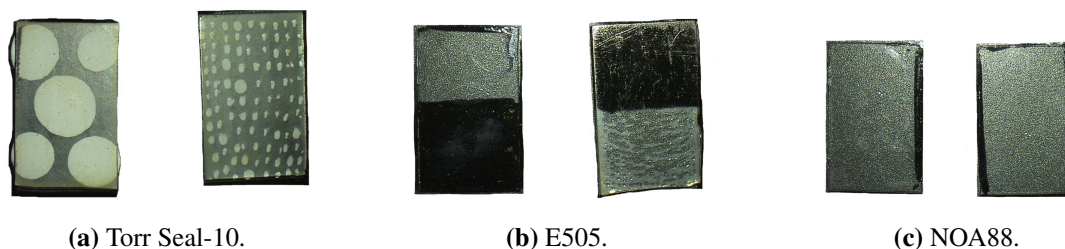


Figure 5.5: *The results of the distribution of the different glues. (a) depicts the result of dispensing Torr Seal-10; the gluing dots are clearly separated from each other. (b) shows the result using the more viscous E505, whereas (c) displays the result for the glue NOA88.*

enclosed voids and air pockets has not been feasible, see Figure 5.5(b).

NOA88, also manufactured by Epotecnny Sarl [85], represents a significant improvement in terms of the uniformity of the applied layer of glue, the thickness ($26 \pm 16 \mu\text{m}$) as well as the homogeneity with respect to the appearance of neither voids or air pockets nor air channels, see Figure 5.5(c). This can be attributed to the viscosity which is by one order of magnitude lower than the one of the previously tested glue. However, NOA88 cures using ultraviolet light which turned out to be practicable while using glass supports and glass sensor dummies. However, for the gluing process of MIMOSA-26 sensors onto the CVD diamond carriers, the feasibility to use ultraviolet light for the curing process of the glue is questionable. Due to the fact that the silicon sensors are not transparent to ultraviolet light, the only possible way to cure the glue would be through the CVD diamond and, thus, from the back side of the sensors. However, this curing method is not feasible as a result of the double-sided positioning of the sensors in the MVD Prototype as well as the MVD.

Using the glue E501, fabricated by Epotecnny Sarl [86], this problem is avoided since it cures within 12 hours at a room temperature of 25°C . At the same time, E501 provides a similar low viscosity as NOA88. The use of E501 results in a uniform and thin layer between the sensor dummies and the glass support for which the resulting thickness has been evaluated to be of $10 \pm 5 \mu\text{m}$ using a digital microscope [88].

Within the MVD Prototype project, E501 is used to glue the MIMOSA-26 sensors onto their sensor carriers. The vacuum compatibility of this glue has not been of interest within the MVD Prototype project and, therefore, has not yet been investigated.

5.1.4 The Heat Sink

The heat sink of the MVD Prototype, as shown in Figure 5.14(b), is designed to hold and cool up to two quadrants of the first MVD station comprising four “core modules”. The dimensions of the heat sink are $158 \times 170 \times 20 \text{ mm}^3$, including a cut-out of $60 \times 90 \text{ mm}^2$ in which two double-sided arranged “core modules” can be positioned. Furthermore, an area of $90 \times 15 \text{ mm}^2$ and $90 \times 30 \text{ mm}^2$ is removed on the heat sink to position the cover plate. The cover plate clamping the sensor carriers onto the heat sink is indicated with (2) in Figure 5.14(b). The dimensions of the cover plate correspond to the area on the heat sink which has been machined away to allow its positioning. Two deepenings are milled out in these two areas to allow for the positioning of the double-sided arranged “core modules”. In addition, special inclined surfaces are machined into the cover plate and the heat sink to guide the FPCs from the sensors to the FEBs. The thermal interface between the heat sink and the circulating cooling liquid, labeled with (3) in Figure 4.8, is defined by a buried cooling channel.

The design of the heat sink of the individual reference planes is guided by the dimensions of the single “core module”. The heat sink allows to hold, position and cool the integrated “core module”, see Figure 5.18. The cooling concept of the heat sink of the MVD Prototype applies to the heat sinks of the reference planes in terms of an incorporated cooling channel as well.

5.1.5 The Flex Print Cable

An FPC connecting two MIMOSA-26 sensors at once to an FEB⁵ has been designed and fabricated accounting for the arrangement of the sensors on the sensor carrier of the MVD Prototype as well as the design of the FEB. The FPC provides the necessary electrical connections to operate the two sensors comprising the “core module”. For each sensor, two signal lines and several supply lines (e.g., power, ground, clock and JTAG) are routed from the sensors through the FPC to the FEB.

Even though the reduction of the material budget of the FPC has not been of highest priority in the MVD Prototype project, the design of the FPC did investigate the possibility of using standard copper traces to achieve the lowest possible material budget. The electrical lines incorporated in the FPCs are based on copper and the material budget of the FPC can be estimated to have a value of $x/X_0 = 0.09\%$, assuming a 50%-fill factor for the electrical copper lines [89].

The interconnection between the FPC and the sensors is achieved using $25 \mu\text{m}$ thin aluminum wire bonds. To guarantee a precise and repeatable wire-bonding process, the FPC has to be positioned in a distance of 1 mm relative to the sensors of the dedicated “core module”. The positioning of the FPC is described in the integration process of the MVD Prototype in Section 5.3.2.

⁵The electrical specification of the FEB is not part of this thesis.

5.2 Thermal and Material Budget Simulations of the MVD Prototype

In preparation of the integration and construction process of the MVD Prototype, the thermal behavior of the materials to be integrated is simulated. In addition, the material budget of the MVD Prototype is determined.

5.2.1 Thermal Simulations Using the Example of the MVD Prototype

The study of the cooling concept to be applied to the MVD has been defined to be one of the key aspects to be investigated in the MVD Prototype project. These studies have been conducted with both, thermal simulations carried out in a dedicated simulation framework [57] and measurements using the MVD Prototype presented in Section 5.4.1.

Two different temperature profiles on the sensor, the temperature gradient ΔT across the sensor's surface and the absolute sensor temperature, are chosen to characterize the cooling concept.

The MVD Prototype is implemented in Autodesk Inventor by means of a double-sided version of the "core module". The thermal behavior of the four MIMOSA-26 sensors glued onto the CVD diamond sensor carrier which provides the thermal interface to the cooled aluminum heat sink is simulated using Autodesk Simulation CFD.

The parameters used for the thermal simulations are listed in Table 5.3. However, the power dissipation of the MIMOSA-26 sensors is non-uniform across their surface and requires a separate implementation of the charge-sensitive and the non-sensitive sensor area. A heat input of 100 mW/cm^2 and 550 mW/cm^2 , respectively, has been applied in the thermal simulation framework [81, 82].

The most important thermal interfaces in the thermal management of the MVD are numbered with (1) and (2) in Figure 4.8, defining the heat flow of the power dissipated by the sensors through the glue and the CVD diamond sensor carrier towards the aluminum heat sink. In the thermal simulation framework, the thermal interface between the CVD diamond sensor carrier and the aluminum heat sink is realized in an $11 \times 44 \text{ mm}^2$ large interface area on the CVD diamond opposite to the sensors, see Figure 5.6. This thermal interface is positioned in a heat bath with a temperature of $T_{\text{interface}}$. The corresponding temperature values of the heat bath $T_{\text{interface}} = 0 \text{ }^\circ\text{C} | 10 \text{ }^\circ\text{C} | 19 \text{ }^\circ\text{C}$ are taken from the temperature measurements presented in Section 5.4.1 below.

The thermal simulations are conducted for a running scenario of the MVD Prototype inside vacuum. Within the thermal simulation framework, the heat dissipated by thermal radiation is neglected. The calculation presented in Section D.2 in the Appendix shows that for a sensor temperature of $T_{\text{sensor}} = 23 \text{ }^\circ\text{C}$ the heat loss for an individual sensor by thermal radiation amounts to $P = 64 \text{ mW}$. Therefore, the resulting error is small but not negligible.

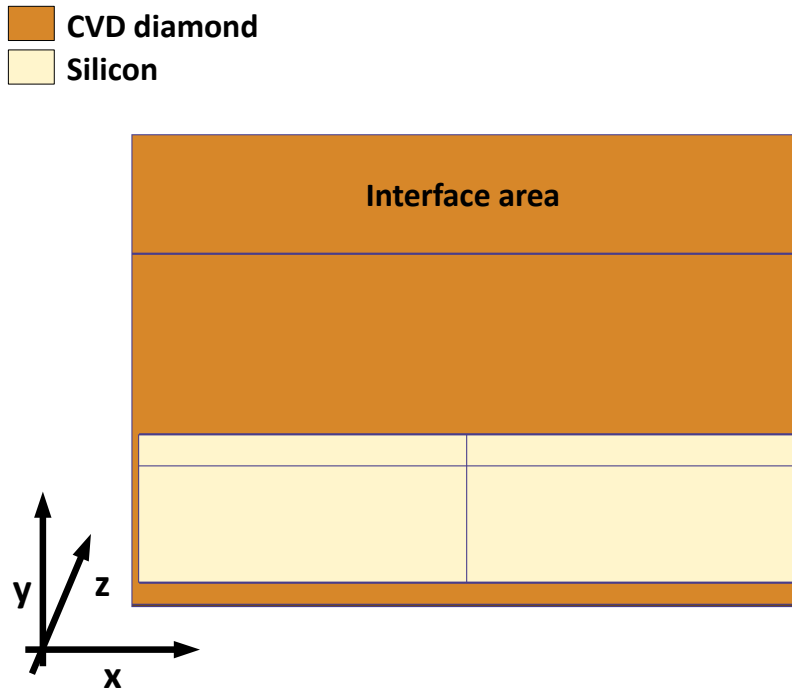


Figure 5.6: At the front, the sub-divided (charge-sensitive/non-sensitive) sensors are shown; the glue is interfacing the sensors and the CVD diamond and is hidden underneath the sensors. The cooling of the CVD diamond carrier is achieved by positioning the thermal interface area in a heat bath with the temperature $T_{interface}$.

Material		Dimensions [mm ³]	Power dissipation [mW/cm ²]	Heat conductivity [W/mK]
CVD diamond		43.5 × 44 × 0.2	–	1800
Silicon		21.5 × 13.8 × 0.05	–	150*
Glue		21.5 × 13.8 × 0.05	–	0.05
Sensor area	charge-sensitive	21.5 × 10.7 × 0.05	100	
	non-sensitive	21.5 × 3 × 0.05	550	

Table 5.3: The parameters used for the simulation of the thermal management of the double-sided “core module”.

*For the thermal conductivity of silicon, temperature-dependent values have been applied, see Figure C.7.

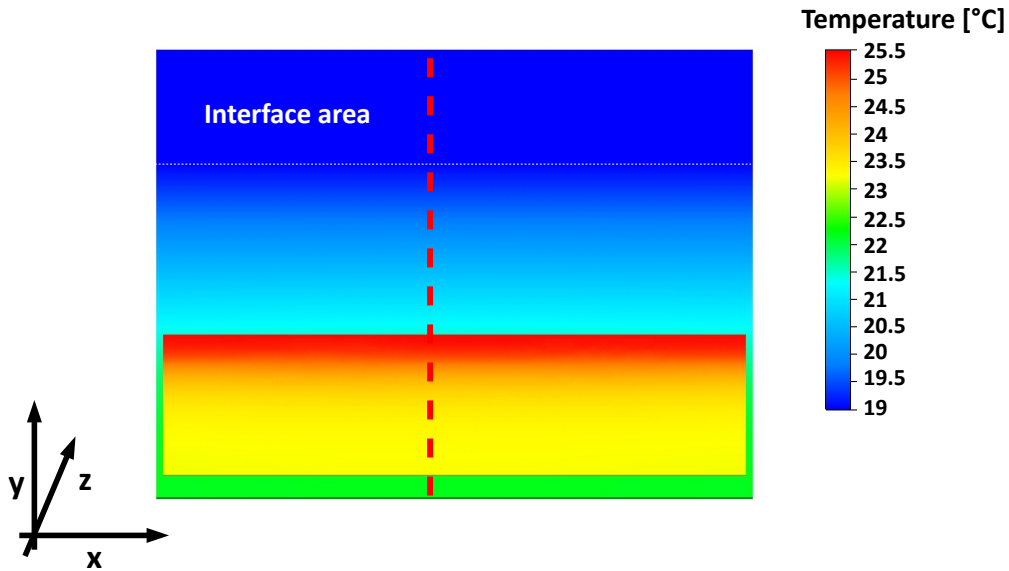
Temperature [°C]				
$T_{\text{interface}}$	T_{sensor}			Figure
	T_{maximum}	T_{minimum}	ΔT	
19	25.5	23.2	2.3	5.7
10	16.5	14.2	2.3	D.1
0	6.5	4.2	2.3	D.2

Table 5.4: *The temperatures measured on the sensors of the MVD Prototype extracted from the conducted thermal simulations. The first column shows the temperatures of the heat bath. In the second and the third column, the simulated respective maximum and minimum temperatures on the sensors are stated. In the last column, the temperature gradients on the sensor’s surface across the y-axis of the “core module” are listed.*

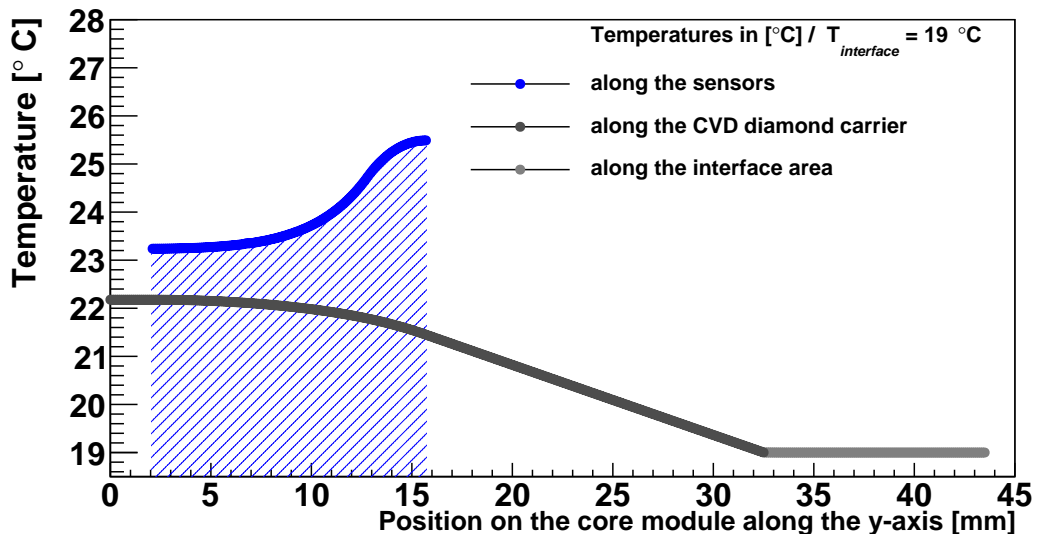
Results: Thermal Simulations of the MVD Prototype

The simulated temperature distributions across the MIMOSA-26 sensors and the CVD diamond sensor carrier are exemplarily shown in Figure 5.7(a) in case the temperature of the heat bath, in which the thermal interface area has been positioned, has been set to $T_{\text{interface}} = 19\text{ °C}$. A maximum temperature of $T = 25.5\text{ °C}$ is found in the non-sensitive part of the sensors. The lowest temperature on the sensors of $T = 23.2\text{ °C}$ is found on the opposite of the non-sensitive part, in the charge-sensitive area. The resulting temperature gradient across the sensor’s surface amounts to a value of $\Delta T_{\text{sensor}} \approx 2.3\text{ K}$. An overview of the resulting simulated temperatures is shown in Table 5.4.

Varying the temperature of the heat bath in which the thermal interface area is positioned to $T_{\text{interface}} = 10\text{ °C} | 0\text{ °C}$, equal temperature gradients of $\Delta T_{\text{sensor}} \approx 2.3\text{ K}$ can be found across the y-axis of the sensors. The temperature gradients in between the maximum temperature found on the sensors and the temperature of the heat bath has been determined to be $\Delta T_{\text{sensor-interface}} = 6.5\text{ K}$ for all simulated heat bath temperatures.



(a) Results for a heat bath temperature of $T_{\text{interface}} = 19^\circ\text{C}$.



(b) Temperatures along the y-axis (red dashed line in the upper picture (a)).

Figure 5.7: (a) Results of the thermal simulation carried out for a heat bath temperature of $T_{\text{interface}} = 19^\circ\text{C}$. The maximum temperature can be seen in the non-sensitive part of the sensor. (b) The simulated temperatures on the “core module” are plotted along the y-axis (red dashed line in Figure 5.7(a)). The blue-shaded area indicates the thermal interface of the sensors with the sensor carrier being provided by the glue, see (1) in Figure 4.8.

5.2.2 Material Budget of the MVD Prototype

The material budget of the MVD Prototype is determined focusing on the charge-sensitive area covered by the double-sided arrangement of the MIMOSA-26 sensors, see Figure 5.1(a). For the reference planes, the calculation is restricted to the charge-sensitive area positioned above the openings of the sensor carriers as only this part has been optimized with respect to the material budget.

The materials contributing to the material budget, their individual thicknesses and their corresponding radiation lengths are listed in Table 5.5. For the radiation length of the glue, a generic value has been assumed based on the experience of other heavy-ion experiments [20, 21].

The material budget of the MVD Prototype has been determined to have a value of $x/X_0 = 0.3\%$. The 200 μm thin CVD diamond carrier contributes 55% to the overall material budget. For the contribution of the two sensors, a value of 36% has been determined and for the two layers of glue a contribution of 9% to the overall material budget has been calculated, as represented graphically in Figure D.3 in the Appendix.

However, the results of the material budget calculation of the MVD Prototype cannot be directly transferred to the material budget of the first station of the MVD since the arrangement of the sensors and the FPC in the required polar angles is different.

The material budget of the individual reference plane is determined to have a value of $x/X_0 \sim 0.05\%$.

Material	Radiation length (Dahl form) [cm]	Thickness [μm]	x/X_0 [%]
Silicon (sensors)	9.48	50	0.053
Glue	35	50	0.0125
CVD diamond	12.22	200	0.164
MVD Prototype	—	400	~ 0.3
Reference planes	—	50	~ 0.05

Table 5.5: *The contributions of the materials integrated into the MVD Prototype and the reference planes to the overall material budget in the charge-sensitive sensor area. To account for the double-sided sensor arrangement of the MVD Prototype, the material budget contributions of the sensors and the glue are doubled.*

5.3 The Construction of the MVD Prototype and the Reference Planes

For the construction of the MVD Prototype, the mechanical handling of ultra-thin CMOS sensors requires the definition as well as the evaluation of reliable sequences of individual working steps for the integration process of the sensors. The working steps have to allow for a reproducible, accurate positioning and gluing of the sensors as well as their wire bonding and their encapsulation. Below, the executed working steps are described, followed by a description of the integration process and the assembly procedure of the MVD Prototype as well as the reference planes.

5.3.1 The Mechanical Handling of Ultra-Thin CMOS Sensors

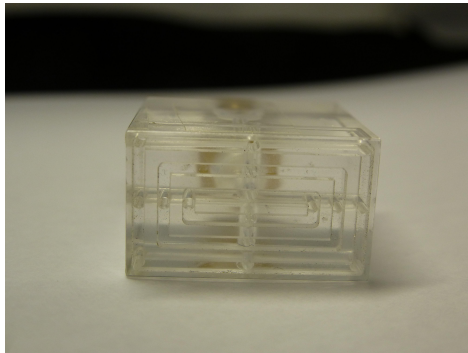
The mechanical handling of ultra-thin sensors demands the development of new dedicated custom-made tools allowing for the reproducible, accurate positioning and gluing of the sensors without damaging them. These tools have been developed focusing on their application in the integration process of the sensors into the “core modules”. While handling the sensors, particular attention has been devoted to the fact that the thinned sensors are bent due to intrinsic tensions, see Figure 5.3(b).

The envisaged strategy for the handling of the ultra-thin sensors is based on the application of underpressure to enable their lifting and holding during the integration process. Therefore, the area of the individual positioning tool which is in contact with the sensors is equipped with an alternating arrangement of air channels lowered into the material, see exemplarily Figure 5.8(a). The minimal underpressure required to lift and hold the sensors is estimated to be of about 10^{-5} bar according to the calculation presented in Section D.5 in the Appendix. After the positioning of the sensors on top of the glue layer on the sensor carriers, the underpressure is released from the tool and the sensors without any loss of positioning accuracy. Based on this principle, several tools for the positioning of the sensors have been manufactured.

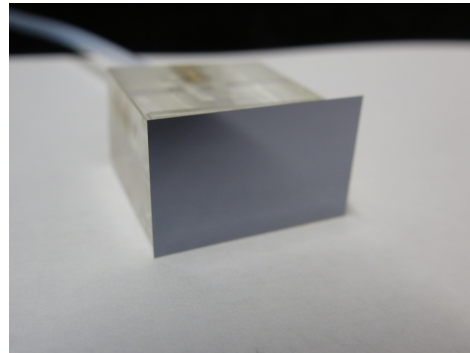
The Pick-Up Tool

The pick-up tool has been developed to gain first experience in the mechanical handling of the sensors and to visually study its impact on the sensors. A piece of transparent thermoplastic has been mechanically processed featuring the dimensions of the sensors, see Figure 5.8. The accuracy of the tool is defined by the production accuracy of the mechanical workshop of the IKF⁶, which is stated to be in the order of 100 μm . This pick-up tool is shown in Figure 5.8(a). The air channels are connected to an outlet on the opposite side of the sensors to which a low-power vacuum pump can be connected in order to provide the required underpressure. The underpressure impacting on the sensors can be estimated to have a value of 2.5×10^{-5} bar.

⁶IKF is the abbreviation for Institut für Kernphysik, Goethe-Universität Frankfurt.



(a) Pick-up tool for a single sensor.



(b) Pick-up tool holding a single sensor.

Figure 5.8: *The first developed tool to pick up and position a single sensor.*

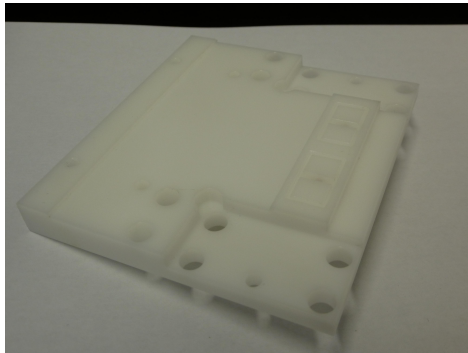
The pick-up tool allows to test the first working steps in the integration process of the sensors, in particular, their lifting and handling using mechanical sensor dummies, see Figure 5.8(b). These working steps have been proven to be feasible without damaging the sensors. However, it has to be noted that only a visual inspection of the sensors has been carried out.

The next working step to be conducted in the integration process of the sensors is the reproducible positioning of several sensors next to each other. The positioning of the sensors by hand causes a reduction of the positioning accuracy as a result of rotational degrees of freedom. Thus, a high precision mandatory to guarantee a given quality standard in the construction process of the “core module” cannot be provided.

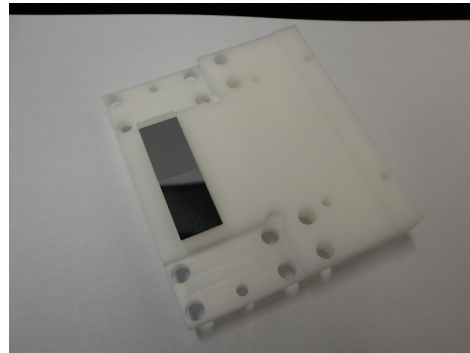
Here, two possible methods have been investigated in order to increase the positioning accuracy: The first option includes the use of the developed pick-up tool in combination with a step motor featuring a precision better than $100\ \mu\text{m}$. The second option relies on achieving the required positioning accuracy with custom-made mechanical tools which are compatible to the form factor of the “core module”. For both options, dedicated pins for the alignment of the positioning tools with respect to the sensor carriers have to be included in the further sensor positioning process. Due to the costs of the “on-shelf” positioning devices and the human power which would be needed to build such a step-motor-based tool, the second option is favored.

The Two-Sensor Positioning-Tool

For the simultaneous positioning of two sensors next to each other onto dedicated sensor carriers, a second tool made of transparent thermoplastic has been mechanically processed consisting of two mirrored pieces, see Figure D.5. Both incorporate the arrangement of alternating air channels to hold and support the sensors while applying underpressure, see Figure D.5(a). The pick-up tool is used to position the sensors onto these new tools. To assure a reproducible edge-to-edge positioning of the sensors, the area hosting the air channels has been lowered into the material by about $30\ \mu\text{m}$, thus giving guidance to the sensors for



(a) Final tool for positioning and gluing two sensors at once.



(b) Two sensors held by the final tool for positioning and gluing.

Figure 5.9: *The final tool for the positioning and gluing of the sensors.*

their alignment during the positioning process. The sensors are aligned against a 90° -angle which is determined by an aluminum plate screwed to one side of the positioning tool. This side touches the mirrored tool when both positioning tools are placed next to each other. After the underpressure is applied and the position of the aligned sensor is fixed, the aluminum plate is removed. The shape of the positioning tool originates from the form factor of the “core module”.

The Final Sensor Positioning-Tool

The final tool for the positioning of the sensors concludes the positioning process of the sensors over their dedicated sensor carrier and defines the last working step of the sensor integration process, see also Figure 5.10. Its task is to keep the sensors in their edge-to-edge aligned positions while the glue is curing. To minimize the risk that the tool is sticking to the sensors in an inseparable way after the curing of the glue, Polyoxymethylene, which is known to be very difficult to bond, has been chosen to serve as bulk material for this tool. The arrangement of the air channels has been changed to simplify the manufacturing process, compare Figure 5.9(a), which is associated with an increase of the underpressure acting on the sensors resulting from the reduction of the area available. The effective underpressure that impacts on the sensors has an estimated value of 5×10^{-5} bar. This increased underpressure does not cause any visible damage to the sensors. The shape of the tool has been adjusted so as to pick the sensors positioned edge-to-edge on the two-sensor positioning-tool and position them over the sensor carriers of the MVD Prototype and the reference planes using dedicated alignment pins.

5.3.2 Integration Process of the MVD Prototype and the Reference Planes

The steps required for the construction and the assembly of the MVD Prototype and the reference planes are presented in this section. In both cases, the “core modules” are integrated on one or on both sides of the sensor carrier material.

Integration of the MVD Prototype

Two “core modules” are integrated in a double-sided, back-to-back arrangement for the MVD Prototype, see Figure 5.1(a). After the completion of the double-sided module, its integration into the heat sink of the MVD Prototype, its positioning inside the MVD Prototype housing box as well as the connection of the sensors to the front-end electronics are presented.

The necessary integration steps to construct a “core module” are sketched in Figure 5.10.

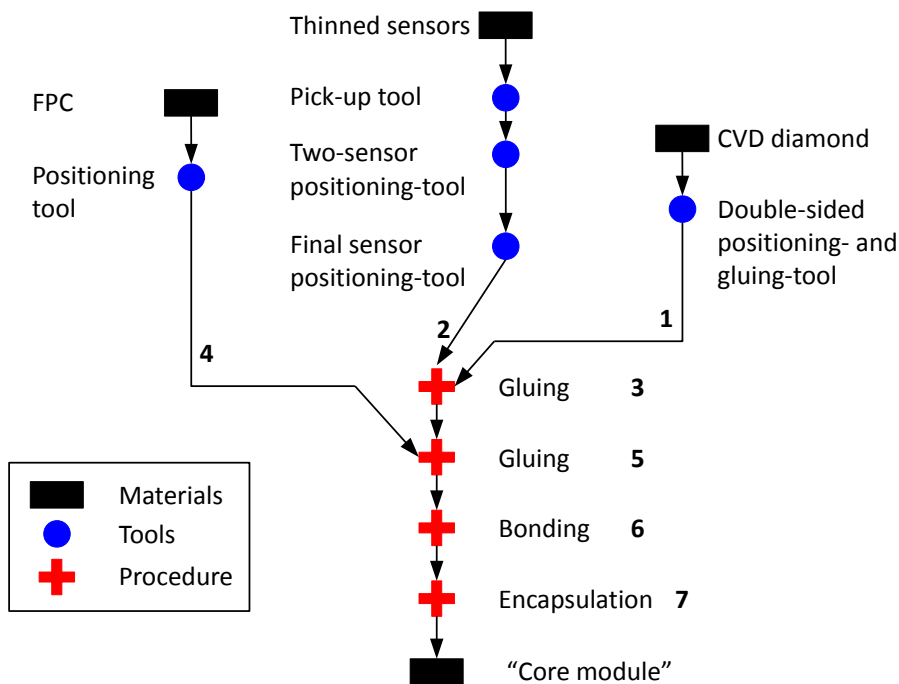


Figure 5.10: The steps required for the integration of the first “core module”. The integration process starts with the right branch indicated with (1), followed by the positioning of the thinned sensors (2) onto the sensor carrier on the glue and their gluing process (3). After that, the FPC is positioned (4) and glued onto the carrier (5). The integration process concludes with the bonding of the sensors to the FPC (6) and the encapsulation of the wire-bonds (7).

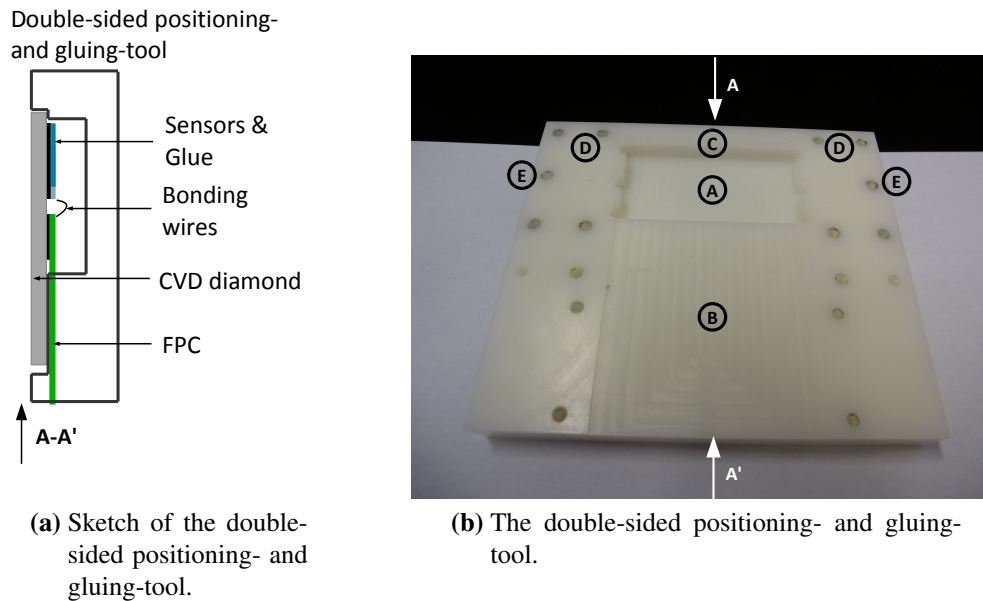


Figure 5.11: The double-sided positioning- and gluing-tool. The sketch indicates the working principle.

For the first integration step, represented by (1) in Figure 5.10, a CVD diamond sensor carrier featuring the dimensions of $43.5 \times 44 \times 0.2 \text{ mm}^3$ is positioned onto the double-sided positioning- and gluing-tool. The set-up of the double-sided positioning- and gluing-tool (depicted in Figure 5.11(b)) is described as follows:

In the middle of the tool, a deepening (A) is milled into the material to assure that the completed first “core module” on the front side of the sensor carrier does not contact the material of the tool while the sensor carrier is turned around. A lowering (B) provides guidance to the sensor carrier from two sides while the sensors are positioned and glued onto the sensor carrier. The position of the CVD diamond carrier on the double-sided positioning- and gluing-tool is fixed during the integration process of the sensors using a 2 mm wide lowering which has been machined into the material on the top side of the tool (C). In addition, this lowering provides support to the CVD diamond sensor carrier during the process of positioning, gluing and, especially, the bonding of the sensors.

Four out of the five holes (D) located on both sides of the deepening are used to mount dedicated clamps⁷ to provide additional guidance to the final sensor positioning-tool while lowering the sensors onto the sensor carrier. The remaining hole (E) is used to install dedicated alignment pins to control the lowering process of the sensors onto the sensor carrier and to increase the reproducibility.

The two MIMOSA-26 sensors to be integrated into the first “core module” are picked up individually using the pick-up tool. During the integration process, the sensors are held from all three introduced positioning tools until they are finally glued onto the CVD diamond

⁷The clamps are used to press the sensor carriers of the references planes onto their heat sinks.

sensor carrier (see the branch numbered with (2) in Figure 5.10). Thus, the orientation of the front and back side of the sensors with respect to the positioning tools is of importance. While they are transported with the pick-up tool, the front side of the sensors (defined by the metalization and the bonding pads) has to face the air channels.

The sensors are positioned individually onto the two-sensor positioning-tools. This process is eased by the guidance provided by the area which is lowered into the material. After the underpressure has been applied to the two-sensor positioning-tool to secure the position of the sensors, the underpressure holding the sensors on the pick-up tool is released and the pick-up tool is removed. The two-sensor positioning-tools are positioned next to each other to allow for the edge-to-edge positioning of the sensors. During this process, the possibility of wrongly-diced sensor edges has to be considered, see the situations (a) and (c) in Figure D.6 in the Appendix. In addition, a possible overlapping of the sensors has to be prevented.

The final sensor positioning-tool is lifting the sensors from the two-sensor positioning-tools using underpressure which is applied to the final positioning-tool while, at the same time, the underpressure is disconnected from the two-sensor positioning-tools. The front sides of the sensors are facing the area hosting the air channels of the final sensor positioning-tool, see Figure 5.9(b).

The first gluing procedure, indicated with (3) in Figure 5.10, can be applied in the integration process. The glue E501 is dispensed onto the CVD diamond sensor carrier according to the method explained in Section 5.1.3. The final sensor positioning-tool is placed above the double-sided positioning- and gluing-tool and lowered towards the sensor carrier while it is guided by the alignment pins, see (E) in Figure 5.11(b). The design of the final sensor positioning-tool allows the sensors to touch the glue dispensed on the sensor carrier first before the entire tool contacts the double-sided positioning- and gluing-tool. For the first ten minutes of the curing process of the glue, a weight is placed on top of the final sensor positioning-tool to assure the required uniform distribution of the glue underneath the sensors, see Section 5.1.3. After this period of time, the weight is removed and, in addition to that, the underpressure is released.

The curing process of the glue which establishes the thermal interface between the sensors and the sensor carrier, indicated with (1) in Figure 4.8, is followed by the positioning (4) and the gluing (5) of the FPC onto the sensor carrier. The FPC is positioned in a distance of about 1 mm from the sensors to allow for a reproducible wire bonding of the sensors and the FPCs. The positioning and the gluing process of the FPC is assisted by a dedicated tool, depicted in Figure 5.12(a), which locks the position of the FPC during the curing of the glue; it is removed after the curing process. The FPC positioning- and gluing-tool can be screwed onto the clamps used to guide the final sensor positioning-tool during the lowering of the sensors onto the sensor carrier.

In step number (6), the electrical connections between the FPC and the sensors are established using wire bonds. A set of 57 wire bonds with a thickness of 25 μm each is established between the sensor and the FPC to guarantee the electrical functionality of the sensors using a manual aluminum wire bonder [90]. The last integration step of the first “core module”

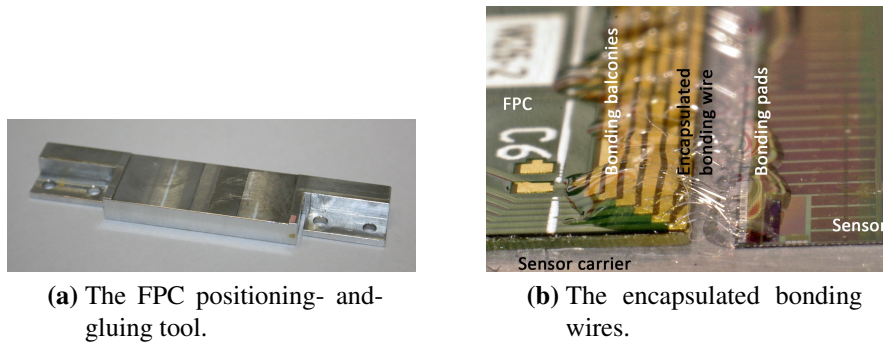


Figure 5.12: The integration of the FPC into the “core module”.

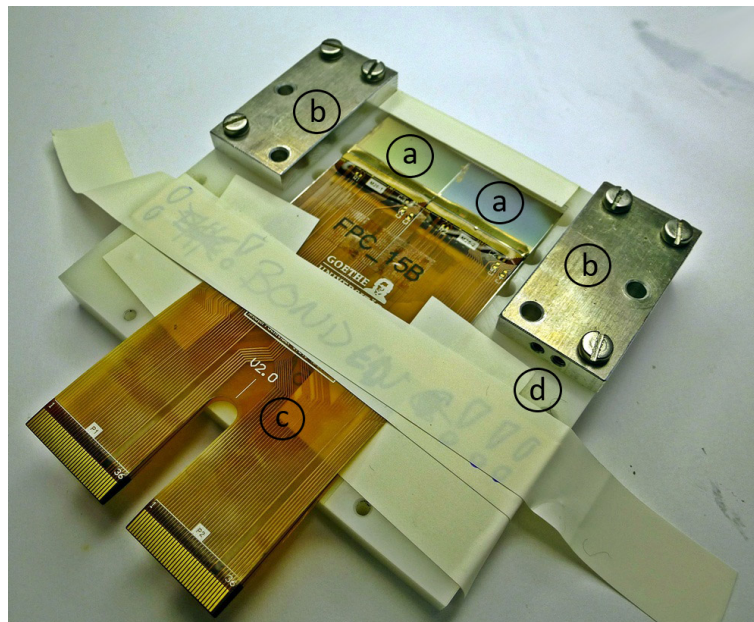


Figure 5.13: The double-sided module. It shows (a) the glued MIMOSA-26 sensors, (b) the clamps which guide the final sensor positioning-tool while lowering it onto the CVD diamond sensor carrier, (c) the FPC and (d) the double-sided positioning- and gluing-tool.

is the encapsulation of the wire bonds using the Sylgard 186 elastomer⁸ [91] (step (7) in Figure 5.10). The encapsulation of the wire bonds is carried out in order to protect them against any mechanical damage resulting from potential mishandling in the further integration process and to minimize the risk of any failures induced by a damaged bonding wire. The encapsulated wire bonds are shown in Figure 5.12(b).

After the curing of the encapsulant, the integration of the first of the two “core modules” equipping the MVD Prototype is accomplished. To integrate the second “core module” onto

⁸This encapsulant provides a viscosity of about 66.7 Pa · s and requires 24 hours to cure at room temperature.

the other side of the sensor carrier, the sensor carrier is turned upside-down ensuring that the sensors and the encapsulated bonding wires are correctly positioned in the deepening of the double-sided positioning- and gluing-tool and do not touch the material, see (A) in Figure 5.11(b).

For the integration process of the second “core module” onto the sensor carrier, the working steps sketched in Figure 5.10 are repeated. The integration process of both “core modules” results in the double-sided module shown in Figure 5.13.

The last integration steps of the MVD Prototype comprise the positioning of the double-sided module on the aluminum heat sink.

The constructed double-sided module is positioned in the dedicated deepenings on the MVD Prototype heat sink as shown in Figure 5.14(a) to be cooled and held during the laboratory tests and the in-beam test. The cover plate, numbered with (2) in Figure 5.14(b), provides a mirrored deepening to provide the required space for the 200 μm thin CVD diamond sensor carrier. Employing this cover plate, the sensor carrier is clamped onto the heat sink from above. The thermal interface between the sensor carrier and the heat sink is indicated with (3) in Figure 5.14(a), its dimensions are $45 \times 11 \text{ mm}^2$. To establish this interface reliably and not to solely rely on pressing the sensor carrier onto the heat sink, a combination of a thermally conductive paste [92] and a soft thermal conductive foil [93] is applied. In addition, the thermally conductive paste fills up the space between the sensor carrier and the side walls of the deepening resulting from their dimensional differences.

During the lowering of the cover plate onto the heat sink, special care of the FPCs bonded to the sensors has to be taken. The end of the FPC, which is not shown in Figure 5.14(a), has to be bent carefully towards the sensors without damaging the sensors or the encapsulated wire bonds until the cover plate is screwed to the heat sink. A limit of which force can be used to tighten the screws on the cover plate without breaking the sensor carrier has not been defined yet. After the fixation of the cover plate, the FPC has to be bent back and it has to be guided towards the dedicated FEB by use of the beveled areas of the heat sink.

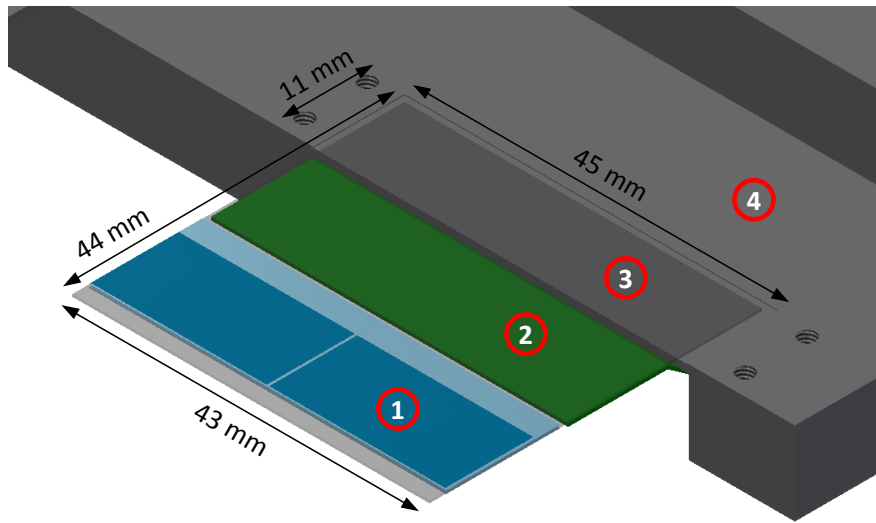
As a result of geometrical constraints arising from the maximal length of the FPCs, the FEBs are directly mounted onto the heat sink, see number (3) in Figure 5.15. The positioning on the heat sink allows to cool potentially generated power dissipated by the electrical components of the FEB. The electrical insulation of the FEB from the aluminum heat sink is provided by masking pins which reach through the FEB with a layer of adhesive tape. The FPCs connecting the sensors to the FEBs, which constitute the first part of the read-out electronics, are inserted into the dedicated ZIF⁹ connectors. Further details on the read-out electronics can be found in [77].

The MVD Prototype comprising the heat sink, the double-sided module and the FEBs is enclosed by a housing box ($255 \times 210 \times 62 \text{ mm}^3$) which serves several functions:

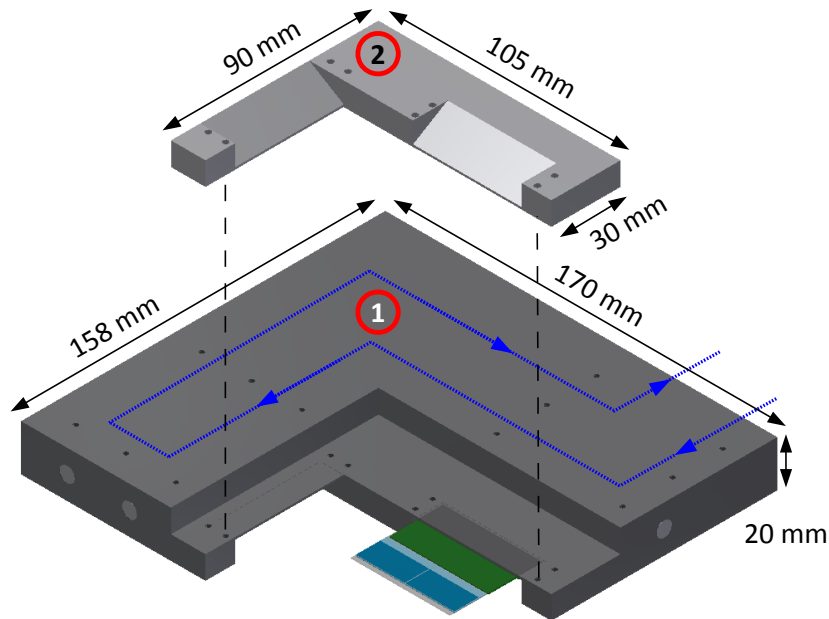
The “entrance windows” of the housing box, marked by (1) in Figure 5.16, through which the beam passes during an in-beam test have to be covered with a thin layer of aluminum foil during the operation of the sensors. Hence, the light-sensitive pixels in the MIMOSA-

⁹ZIF is the abbreviation for zero injection force.

5.3. The Construction of the MVD Prototype and the Reference Planes



(a) The double-sided module positioned on the heat sink (zoom).



(b) The double-sided module positioned on the MVD Prototype heat sink.

Figure 5.14: The integration of the double-sided module into the MVD Prototype heat sink. (a) The double-sided module positioned on the heat sink. The indicated components are (1) the MIMOSA-26 sensors, (2) the FPC, (3) the thermal interface area and (4) the heat sink. (b) The MVD Prototype heat sink. The blue dashed line indicates the path of the cooling liquid embedded in the heat sink (1). The cover plate is indicated with (2).

26 sensors are protected against light, an electrical shielding of the sensors against external noise sources is provided and an air volume is defined. This air volume is essential for two reasons: First, the air volume – which additionally has to be cooled by the heat sink during the operation of the sensors at low temperatures – is limited. Second, a volume is defined which can be filled with dry nitrogen to prevent condensation on the sensors during their operation below dew point. For that to happen, an inlet is mounted on top of the housing box, see number (4) in Figure 5.16.

As a final measure, the heat sink is connected to the cooling system [94] using 1.5 m long thermally insulated cooling hoses. The heat sink is equipped with a one-wire temperature sensor providing the temperature measurements required for the evaluation of the cooling concept with a precision of ± 0.5 °C, see Section 5.4.1. In addition, the connection of the FEBs to the subsequent front-end electronics is established, see Section 5.5.1.

Integration Process of the Reference Planes

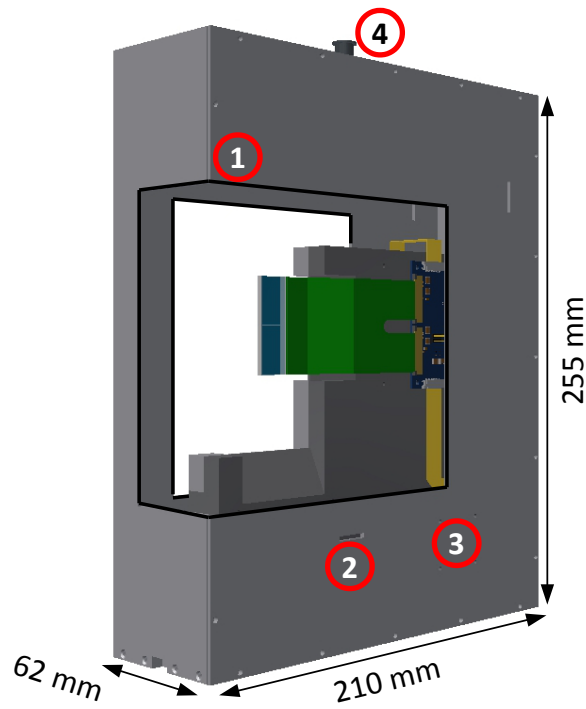
The integration of the “core module” into the reference planes starts with the first construction step of a reference plane shown in Figure D.7(a) in the Appendix. The sensor carrier chosen to equip the individual reference plane is positioned in its dedicated deepening. For reasons of simplicity, a deepening of 1 mm is milled into the heat sinks of the reference planes to account for the thickness of the aluminum sensor carrier. As a consequence, for the reference planes equipped with the 200 μm CVD diamond sensor carriers, an additional spacer is required to compensate for the discrepancy of the carrier thicknesses. The clamps are screwed onto the heat sinks to press the sensor carriers onto them, see Figure 5.17(a). A maximum limit of the force that can be used to tighten the screws without breaking the sensor carriers has not been defined yet.

The integration process of the “core modules” of the reference planes is conducted according to the working steps sketched in Figure 5.10. For the integration process, the heat sinks of the reference planes carrying their dedicated sensor carrier replace the double-sided positioning- and gluing-tool.

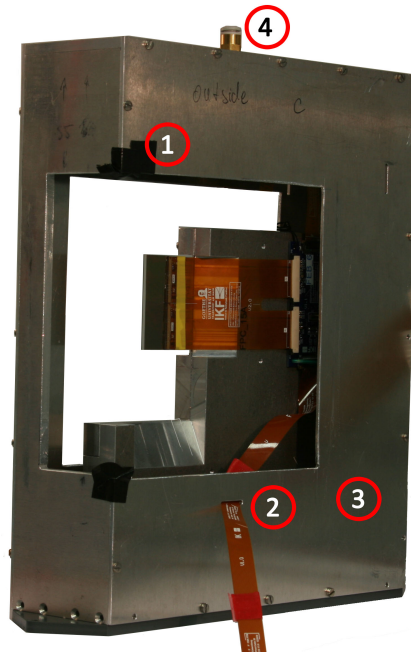
Once the integration process of the “core module” is concluded by the curing of the encapsulation of the wire bonds (cf. Figure 5.17(b)), the reference planes are assembled according to the remaining steps presented in Figures D.7 and D.8 in the Appendix. While doing so, special care has to be taken of the integrated sensors.

The integration process is repeated until a set of six reference planes is assembled ready to be tested in the laboratory and during an in-beam test. Out of these six reference planes, two are equipped with the 200 μm thin CVD diamond sensor carriers and the remaining four planes are assembled with the 1 mm thick aluminum carriers.

The result of the integration and assembly process of one of the reference planes is depicted exemplarily in Figure 5.18.



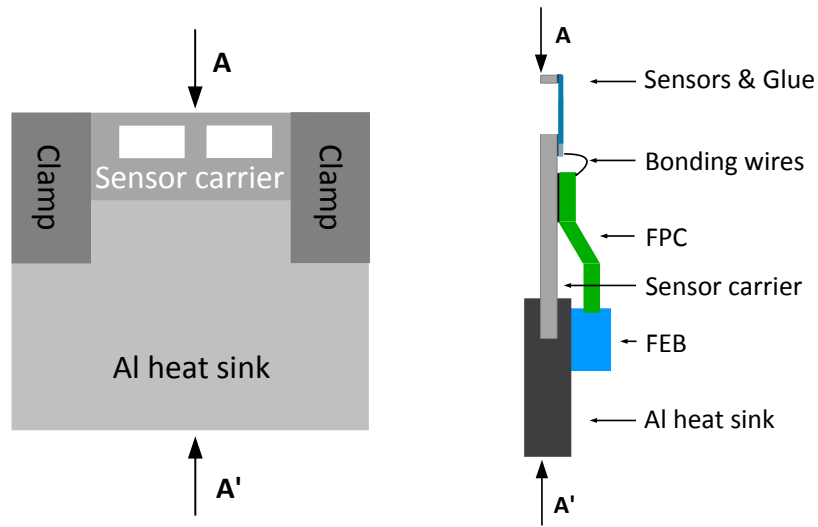
(a) The MVD Prototype (CAD).



(b) The MVD Prototype.

Figure 5.16: The CAD representation (a) and the real assembled MVD Prototype (b) in the housing box. The numbers indicating the respective components correspond in both figures: The opening for beam passing through (1), the outlet for the JTAG-FPCs (2), the mounting position for the JTAG-end board (3) and the inlet for nitrogen (4).

5.3. The Construction of the MVD Prototype and the Reference Planes



(a) Sketch of the sensor carrier clamped to the heat sink of one reference plane.

(b) Sketch of the reference planes (not to scale).

Figure 5.17: Sketch of the reference planes at different stages during the sensor integration process. (a) sketches the sensor carrier clamped on the heat sinks of the reference planes; (b) sketches the reference planes at the end of the integration process of the sensors.

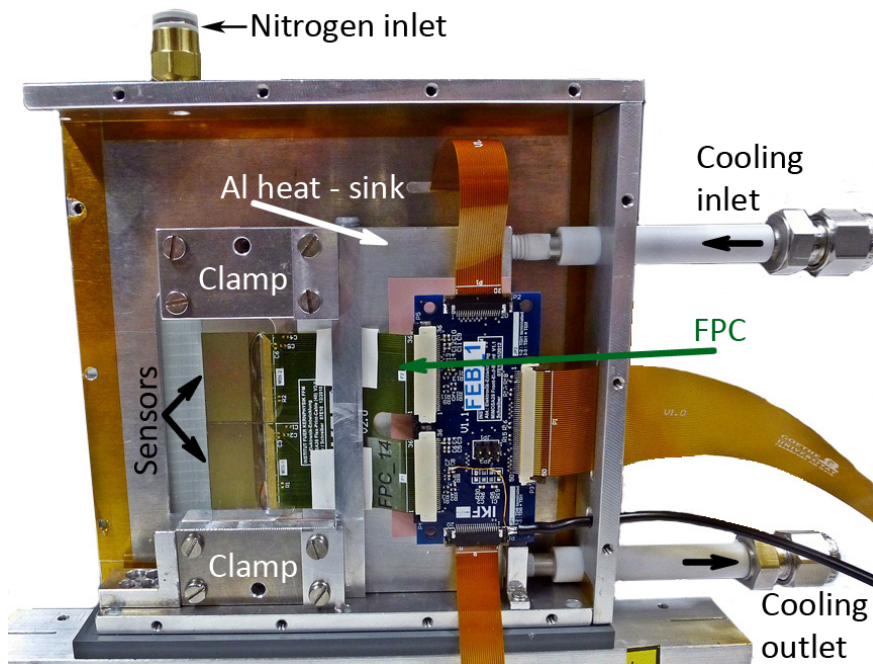


Figure 5.18: The set-up of one reference plane equipped with a CVD diamond sensor carrier.

5.3.3 Evaluation of the Sensor Distances in the “Core Modules”

The integration process of the sensors into the “core modules” of the MVD Prototype and the reference planes aims at their positioning on the sensor carriers with a minimum distance in between the two sensor edges. Therefore, the sensors are positioned as close as possible to each other on the two-sensor positioning tools without overlapping before they are lifted by the final positioning-tool and glued onto the dedicated sensor carrier.

After the completion of the integration process of the “core modules”, the distances as well as the angles between the integrated sensors are evaluated using the six constructed reference planes. A possible appearance of an angle between the positioned sensors may result from the precision the sensors can be diced, see Figure D.6 in the Appendix. The dicing accuracy of the sensors can be stated to be below $10\ \mu\text{m}$ [72].

The distances between the sensors are determined by means of a digital microscope [88] at three different sensor positions, depicted in Figure 5.19(a). At the positions indicated with (A) and (D) the distances between the two sensors are determined in y-direction, while at the positions (B), (C) and (E) the distances are measured in x-direction. At each position, ten distance measurements are executed in the corresponding coordinate direction. The extracted distance values are averaged¹⁰ and shown separately for each of the reference planes in Table D.2 in the Appendix.

For the sensors positioned on the reference planes *a*, *e* and *g*, the measured distance values at the positions *A*(*y*) and *D*(*y*) correspond within a maximum range of $10\ \mu\text{m}$, while for the reference planes *b*, *f* and *h*, the distance difference is found to be less than $5\ \mu\text{m}$, see Table D.2 in the Appendix. Comparing the measured sensor distances at *A*(*y*) and *D*(*y*) allows to determine the accuracy of the measuring method. It is assumed that the sensors are diced with a high accuracy which leads to the condition that the values measured for *A*(*y*) and *D*(*y*) should correspond. Since, according to the numbers listed in Table D.2 in the Appendix, this is not the case, the accuracy of the measuring method can be determined to be of a value of $\pm 5\ \mu\text{m}$. A value of $39 \pm 42\ \mu\text{m}$ can be determined for the averaged distance between the sensors on the six reference planes in the y-direction. Since the number of measurements resulting from the construction of six reference planes are limited, the average distance¹¹ between the sensors is highly dominated by the maximum value.

For the measurements of the distances in between the sensors at the positions *B*(*x*), *C*(*x*) and *E*(*x*), averaged values of $62 \pm 28\ \mu\text{m}$ at *B*(*x*), $63 \pm 19\ \mu\text{m}$ at *C*(*x*) and $57 \pm 24\ \mu\text{m}$ at *E*(*x*) are determined. For an individual set of measurements, the values indicate a very small angle by rising distance values from the measurements at the positions *B*(*x*) to *E*(*x*); the sensors are slightly tilted away from each other. The estimated error of at most 40% results from the small number of measurements using the six constructed reference planes.

The distance between the last pixel row on the sensor positioned on the left side of the “core module” and the first row of pixels positioned on the sensor on the right side is defining a built-in non-sensitive area between two sensors, independent of how precisely they are

¹⁰The stated error is derived using the standard deviation method.

¹¹The error is derived using the standard deviation method.

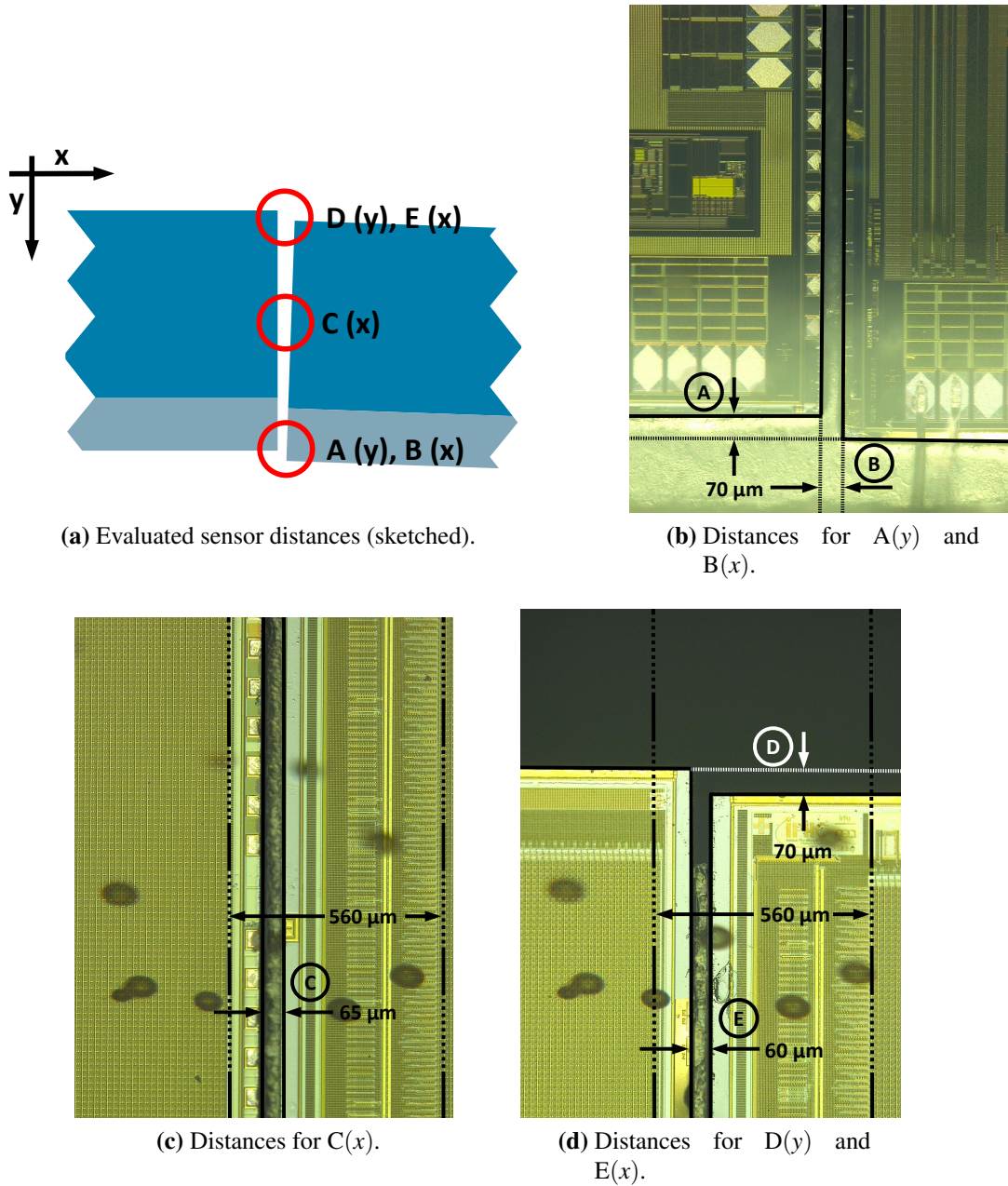


Figure 5.19: The evaluation of the distances between the sensors in a “core module”. The measured distances are shown exemplarily for the values of reference plane “a”, see Figure 5.26.

diced, positioned and glued next to each other. It is referred to as pixel-to-pixel distance. For its evaluation, the distances which are found between the sensors at the positions $C(x)$ and $E(x)$ are subtracted from the pixel-to-pixel distance. The averaged values for the distances between these pixel rows for all six reference planes are $550 \pm 12 \mu\text{m}$ in the middle of the sensor pixel array at position $C(x)$ and $556 \pm 14 \mu\text{m}$ at position $E(x)$, see Table D.3 in the Appendix.

5.3.4 The Grounding Concept of the MVD Prototype and the Reference Planes

The grounding concept applied to the MVD Prototype and the reference planes follows the concept to distribute the ground of the sensors by relying on the FPCs and the dedicated read-out electronics only. Focusing on the MVD Prototype, the mechanical consequences of this grounding concept are discussed below, the electrical realization is discussed in [77].

The grounding concept is guided by the distribution of the ground in a star-like topology starting from a common ground terminal, thus avoiding potential ground loops. These would occur by connecting, e.g., the sensor ground to a massive ground in close vicinity (e.g., to the sensor carrier and/or to the heat sink). The drawback of this concept is that the low-mass FPCs, by definition, do not represent the optimal connection to the ground. The relevant grounding interfaces between the involved materials are discussed with reference to Figure 5.15(a). The grounding lines between the sensors and the ground terminal are sketched in Figure 5.20.

For the MVD Prototype, the method to distribute the ground of the sensors employs their connection to the FEBs as well as to the subsequent read-out electronics using the FPCs, see Figure 5.20. An additional grounding line is routed from the FEBs to the dedicated Converter boards, parallel to the FPCs, to ensure a reliable ground distribution. The ground terminal, at which each of the grounding lines of the Converter boards end, is itself connected to the negative terminal of the sensor power supply. From a mechanical point of view, the first possible electrical interface is defined between the sensors and the CVD diamond carrier onto which the sensors are glued, indicated with (1) in Figure 5.15(a). The electrical resistivity of CVD diamond is $10^{13} - 10^{16} \Omega\text{cm}$ which is of the order of magnitude of an insulator [63]. The same applies to the electrical resistivity of the glue which has been determined to be $10^{13} \Omega\text{cm}$ [86]. As a result, these two interfaces provide a mechanical and thermal but not an electrical connection between the integrated materials. The housing box of the MVD Prototype and with it its heat sink are positioned on a PVC plate which is screwed underneath the housing box's base plate, indicated with (6) in Figure 5.15(a). This PVC plate is used to electrically decouple the entire MVD Prototype from the experimental table, see Figure D.12 in the Appendix. The last possible electrical interface is defined by the connection of the heat sink to the cooling system. The electrical insulation is achieved by the use of hoses made of nitrile butadiene rubber.

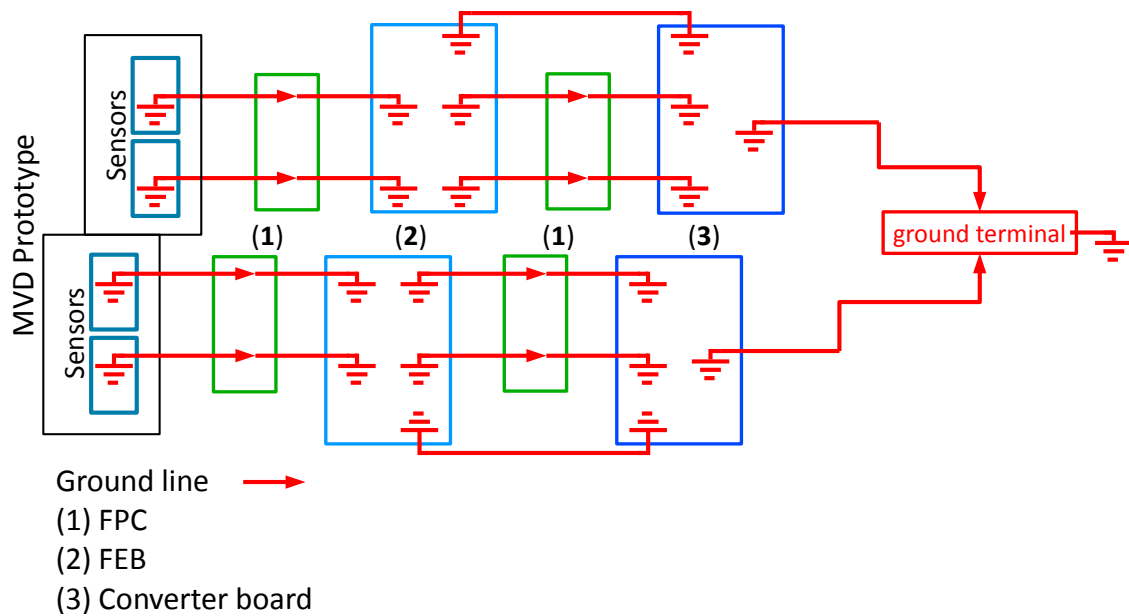


Figure 5.20: The block diagram of the ground lines between the sensors and the ground terminal.

5.4 Evaluation in the Laboratory

The evaluation of the constructed MVD Prototype and the reference planes in the laboratory focuses on the functionality of the integrated sensors and the evaluation of the cooling concept. The functionality of the sensors is studied investigating the response of the sensors to particles emitted by a radioactive source as well as determining a set of standard sensor operation settings. The cooling concept of the MVD is evaluated utilizing temperature measurements by means of the MVD Prototype.

5.4.1 Thermal Measurements Using the MVD Prototype

The temperature measurements¹² using the example of the MVD Prototype presented in this thesis are carried out in air and at ambient temperature.

The different temperature profiles characterizing the cooling concept are the absolute sensor temperature and the temperature gradient ΔT across the surface of the individual sensor.

As already discussed in Section 4.1.3, the operation of the sensors at a temperature below 0°C is mandatory to reduce radiation-induced defects and to achieve the best possible sensor

¹²Since the MVD is operating in vacuum, temperature measurements of operating sensors in vacuum are mandatory to evaluate the anticipated cooling concept of the MVD in detail. The in-vacuum measurements are not part of this thesis and are discussed in detail in [53].

operation values. At the same time, the temperature gradient ΔT across the sensor's surface has to be limited to a value of ~ 10 K due to the connection of the pixel columns inside the sensors to the discriminator array adjusting the thresholds. In MIMOSA-26, even though each column of pixels is connected to its individual discriminator, 288 columns are grouped together in a later stage allowing to apply the sensor operation settings for the whole sensor by means of four different values only. Therefore, it is important to limit the temperature gradient across the sensor's surface in the direction of the pixel rows to a small value. A combination of a radiation-induced leakage current, which is also temperature-dependent, and a high temperature gradient across the sensor's surface might lead to a situation in which for the same threshold in a column, some pixels are working as expected whereas others might always indicate "a signal". As a result of this, it is important to achieve a uniform temperature gradient across the pixel column to guarantee a similar pixel operation level.

Two adjustable parameters provide a direct impact on both temperature profiles. The first parameter is defined by the temperature of the heat sink of the MVD Prototype. In the course of the temperature survey, the temperature measured on the heat sink has been determined to three different values: -5.5 °C, 6.8 °C and 17 °C.

The second parameter is determined by the sensor operation settings¹³ leading to different sensor power dissipation values. Four different sensor operation settings have been selected to be studied comprising three different "fake hit rate"¹⁴ settings. The case in which the sensors are switched off is used as baseline measurement.

After the adjustment of one of the two parameters in order to provide comparable conditions for the temperature measurements, the MVD Prototype is left untouched for 60 minutes in order to achieve a thermal equilibrium. The temperature of the heat sink is monitored continuously using the temperature sensor glued to its surface. In case the temperature of the heat sink is lowered below dew point, dry nitrogen is injected into the housing box of the MVD Prototype to prevent condensation on the sensors. The heat extracted from the sensors by the flow of dry nitrogen can be neglected according to the calculation presented in Section D.2 in the Appendix.

The temperature survey is based on a contact-free approach using an infrared camera [96].

Preparation of the Temperature Measurements

The use of an infrared camera requires some preprocessing steps to correct for the impact of the reflexion coefficient and the emissivity of the material to be surveyed on the measured temperatures themselves. In case both material coefficients are unknown, a special black spray paint providing a minimal reflexion coefficient and an emissivity of $\varepsilon = 0.96$ is applied on the material. The measured temperature values on the painted materials have to be corrected accordingly.

Since it is not an option to paint the MVD Prototype sensors, a correlation is determined between the temperatures measured on two electrical non-functional MIMOSA-26 sensors,

¹³These settings can be applied by use of the slow control protocol JTAG [95].

¹⁴For a definition of the fake hit rate, see Section 5.1.1.

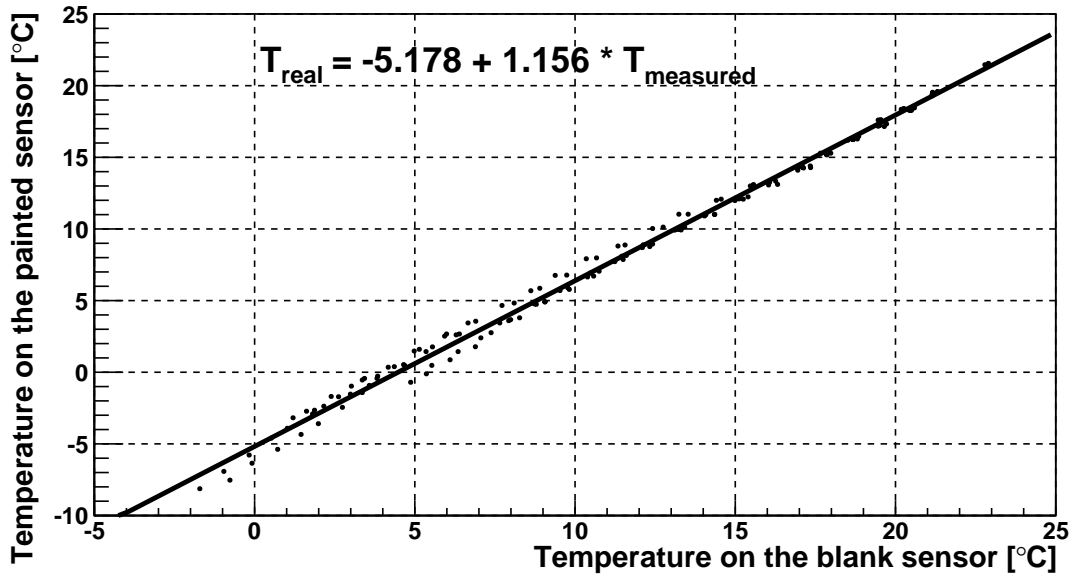


Figure 5.21: Extraction of the calibration parameter from the correlation of the temperature measured on the “painted” and the “blank” sensor.

of which the “painted” sensor is covered with a thin layer of the black spray paint and the “blank” sensor is not covered at all. The two sensors are glued next to each other on a copper plate presuming that the thermal interfaces established between the sensors and the copper plate are the same. The temperature of the copper plate is varied several times from $-30\text{ }^{\circ}\text{C}$ up to room temperature while the temperature on both sensors is continuously measured using the infrared camera.

Based on these measurements, the temperatures of the “painted” and “blank” sensors are plotted against each other, see Figure 5.21, and their extracted calibration parameter using linear regression is $T_{\text{real}} = -5.178 + 1.156 \times T_{\text{measured}}$ in which T_{measured} represents the temperature measured on the “blank” sensor. For measured temperature values of $T_{\text{real}} = T_{\text{painted sensor}} < 15\text{ }^{\circ}\text{C}$, a systematic uncertainty of $\pm 1\text{ }^{\circ}\text{C}$ can be read off the plotted temperature correlation.

Results of the Thermal Characterization of the MVD Prototype

The temperature gradient across the sensor’s surface is exemplarily shown for a heat sink temperature of $-5.5\text{ }^{\circ}\text{C}$ and a sensor operation setting of $10^{-6}\%$. The temperature gradients across the sensor’s surface are extracted from the infrared picture, see Figure 5.22, along the colored lines and plotted together with the simulated temperature gradient in Figure 5.23. The temperature gradient across half of the sensor length is determined to be $\Delta T_{\text{sensor}} \approx 0.6\text{ K}$, which is valid for different heat sink temperatures and sensor settings. The temperature gradients can only be accessed over a distance of 6 mm across the sensors due to the encapsulation of the wire bonds which is visible in Figure 5.22 as the “blue” structure on the “green” MIMOSA-26 sensors. The simulated temperature gradient across the sensor’s sur-

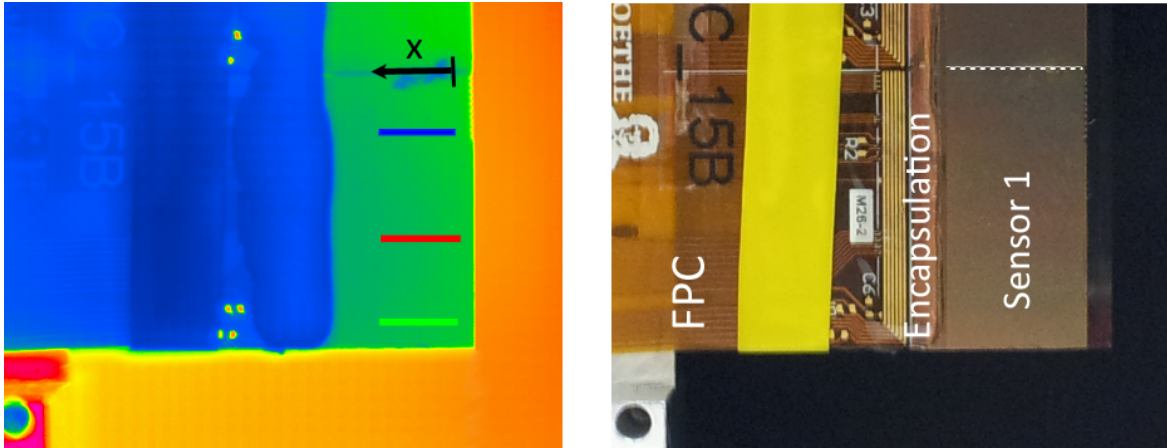


Figure 5.22: The MVD Prototype sensors in an infrared (left panel) and in their real representation (right panel). The heat sink is located on the left side of each picture. The x and the arrow represent the determined temperature gradient across a sensor column. The color codes of the three lines correspond to the ones in Figure 5.23.

face is adjusted to these geometrical constraints and is depicted as black stars in Figure 5.23. The simulated temperature gradient is determined to be half of the value of the measured one. In addition, the slope of the simulated temperature gradient is opposite. This different slope can be explained with the set-up of the double-sided module in the thermal simulation framework. In particular, a constant power dissipation value of 550 mW/cm^2 is assigned to the non-sensitive sensor area resulting in an increase of the temperature gradient across the pixel column of the sensor from the charge-sensitive towards the non-sensitive sensor area. For the used sensor operation settings of $10^{-6}\%$, it is assumed that the power dissipation value of the on-chip electronics of the MIMOSA-26 sensors is comparable to a value of 550 mW/cm^2 . However, this assumption is questionable, since the measured temperature gradient is decreasing in the direction of the on-chip electronics. In Figure 5.23, the on-chip electronics is located at an x -position of 0 mm and reaches towards lower x -values. A reduction of the power dissipation value assigned to the non-sensitive area of the MIMOSA-26 sensors in the thermal simulation framework from a value of 550 mW/cm^2 to a value of 50 mW/cm^2 leads to an equalization of the slopes of the simulated and the measured temperature gradients as depicted in Figure D.11 in the Appendix. The temperature gradient perpendicular to the arrow indicated in Figure 5.22, directed across the sub-matrices of the sensor is determined to be $\Delta T_{\text{across}} \approx 0.4 \text{ K}$.

The absolute temperatures measured on the MVD Prototype sensors are discussed separately for the two cases of running and switched-off sensors. In case the sensors are switched off, the difference between the temperature measured on the MVD Prototype sensors and the heat sink is discussed using the relation $\Delta T_{\text{sensor off} - \text{heat sink}}$. In case the sensors are switched on, the discussion focuses on the relation $\Delta T_{\text{sensor on} - \text{sensor off}}$.

The absolute temperatures measured on the MVD Prototype sensors are presented in Fig-

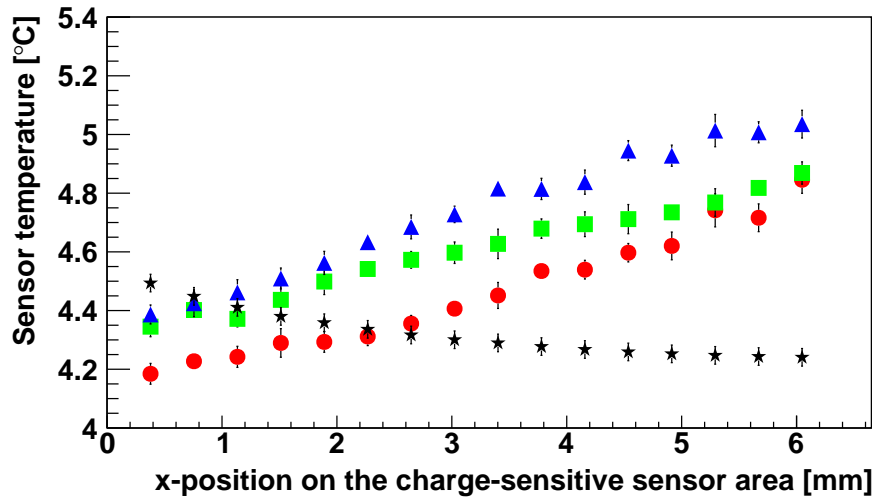


Figure 5.23: The temperature gradients across the surface of the MVD Prototype sensors. The color code of the lines corresponds to the ones in Figure 5.22 (left hand side). The blue triangles correspond to the upper line, the green squares to the lower line and the red dots to the middle line. The slope of the simulated temperature gradient represented by the black stars is the opposite resulting from the settings applied in the thermal simulations. In this figure, only the statistical errors are shown; the systematical error of $\pm 1^\circ\text{C}$ is not plotted for reasons of simplification and visibility of this figure.

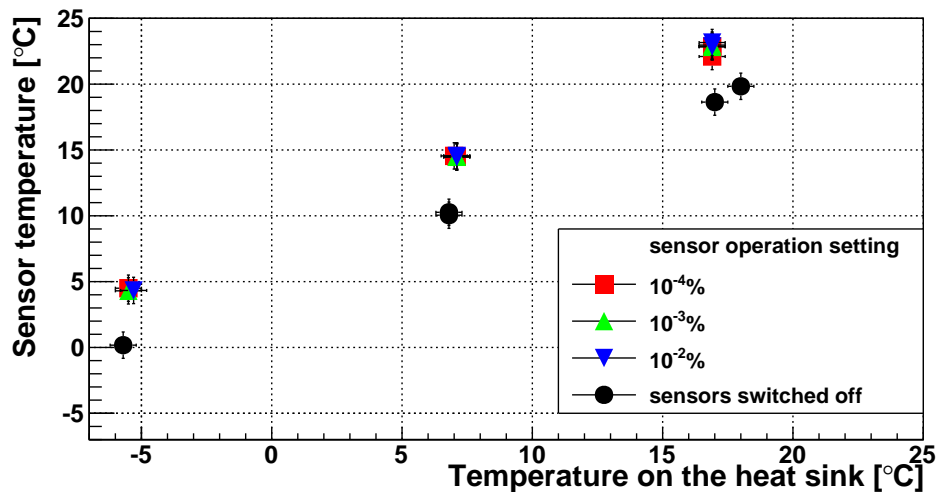


Figure 5.24: Absolute temperatures measured on the MVD Prototype sensors for the four sensor operation settings: the sensors are switched off (black circles), the setting of a value of $10^{-2}\%$ (blue full down-pointing triangles), the setting of $10^{-3}\%$ (green full up-pointing triangles) and the setting of $10^{-4}\%$ (red squares).

Temperature [$^{\circ}\text{C}$]		
$T_{\text{heat sink}}$	$T_{\text{sensor measured}}$	$T_{\text{sensor simulated}}$
16.9	22.8	23.2
6.8	14.5	14.2
-5.5	4.4	4.2

Table 5.6: Comparison of the simulated and measured absolute temperatures on the MVD Prototype sensors.

ure 5.24 and listed in Table D.4 in the Appendix.

The temperature difference ($\Delta T_{\text{sensor off - heat sink}}$) between the switched-off sensors and the aluminum heat sink is determined to range from $\Delta T \approx 3 \text{ K}$ to $\Delta T \approx 5.5 \text{ K}$, depending on the heat sink temperature ($T_{\text{heat sink}} = 17 \text{ }^{\circ}\text{C} \mid 6.8 \text{ }^{\circ}\text{C} \mid -5.5 \text{ }^{\circ}\text{C}$).

The temperature difference determined for the relation $\Delta T_{\text{sensor off - heat sink}}$ can be explained by the fact that the temperature measurements are carried out in atmosphere and at ambient air temperature and not in vacuum. Therefore, the air volume inside the housing box of the MVD Prototype which is built around the heat sink has to be cooled additionally by the heat sink. However, its non-insulated aluminum sled walls are exposed to the ambient air. The housing box is not constructed hermetically sealed since, as mentioned above, the assembly has to allow for the injection¹⁵ of dry nitrogen into the housing box for measurements below dew point in order to prevent condensation on the sensors.

The increase of the temperature difference $\Delta T_{\text{sensor off - heat sink}}$ while lowering the heat sink temperature may indicate additionally that the thermal coupling of the CVD diamond carrier to the heat sink is insufficient. For the later vacuum operation of the MVD, the method to establish the thermal interface between the sensor carriers and their dedicated heat sink has to be optimized and standardized.

An additional amount of $\Delta T_{\text{sensor on - sensor off}} = 4 \text{ K}$ is added to the temperature difference $\Delta T_{\text{sensor off - heat sink}}$ in case the sensors are switched on, see Table D.4 in the Appendix, resulting from the power dissipated by the running MIMOSA-26 sensors. This value is measured for all three evaluated heat sink temperatures. The operation of the sensors with one of the three different sensor operation settings¹⁶ does not result in a variation of the absolute sensor temperature within the systematic uncertainties of $\pm 1 \text{ }^{\circ}\text{C}$.

The absolute temperatures on the MVD Prototype sensors, measured and simulated, are listed in Table 5.6, separately for each of the heat sink temperatures. The measured absolute temperature values are averaged over their individual measurements. For the simulated absolute temperature, only the minimum values determined on the charge-sensitive area of

¹⁵The effect of cooling the sensors through a dry nitrogen injection can be neglected according to the calculations presented in Section D.2 in the Appendix.

¹⁶The sensor operation settings are adjusted to the values of $10^{-2}\%$, $10^{-3}\%$ and $10^{-4}\%$.

the sensors¹⁷ are taken into account. The absolute temperatures determined on the MVD Prototype sensors are in accordance within 0.5 K assuming a power dissipation value of 550 mW/cm² for the non-sensitive sensor area in the thermal simulation framework. For the lower power dissipation values of 250 mW/cm², 100 mW/cm² and 50 mW/cm², assigned to the non-sensitive sensor area, the difference between the measured and the simulated temperatures increases to a value of 2 K.

In conclusion, the cooling concept of the MVD realized as part of the MVD Prototype has been evaluated using thermal simulations as well as thermal measurements. This holds for the constraint that the temperature measurements of the MVD Prototype sensors are carried out in air and at ambient temperature, and for the material budget achieved during the integration process. Since the temperature difference between the heat sink and the switched-off sensors has been found to be up to $\Delta T \approx 5.5$ K, the thermal interface between the CVD diamond carrier and the aluminum heat sink has to be further improved. Reducing this temperature difference is of primary importance, particularly because the MVD has to be operated inside vacuum¹⁸. During the operation of the sensors, a linear dependence of the sensor temperature with respect to the heat sink temperature has been measured. In addition, no significant temperature differences of the overall sensor temperature have been observed in the charge-sensitive area (which is optically accessible and not covered with encapsulant) while using different sensor operation settings. The temperature gradient across the sensor's surface has been measured to be smaller than 1 K. Compared to the maximal acceptable temperature gradient across the sensor's surface of 10 K [65], the measured value leaves a substantial margin for the in-vacuum operation of the MVD.

Results of the Thermal Characterization of the Reference Planes

The absolute sensor temperatures for the reference planes are determined separately for the two different sensor carrier materials. Since the temperatures of the reference planes are kept constant throughout an in-beam test in order to provide the same sensor operation conditions at all times, only one heat sink temperature is evaluated.

The absolute sensor temperatures measured for the different sensor operation settings are averaged for reasons of simplification. Their variation of maximal ± 0.4 °C is below the systematic uncertainties of ± 1 °C of the extraction of the calibration parameter.

The operation of the sensors results in a temperature rise of a value of $\Delta T_{\text{sensor on - sensor off}} \approx 4$ K in case the sensors are glued onto the CVD diamond carrier. In case the sensors are glued onto the aluminum carrier, this temperature difference has been determined to be $\Delta T_{\text{sensor on - sensor off}} \approx 7$ K.

The temperatures measured on the sensors are presented in Figure D.9 and listed in Table D.5, both in the Appendix. The impact of the design of the sensor carriers on the temperature distribution across the surface of the sensors is depicted in the corresponding infrared pictures in Figure D.10 in the Appendix.

¹⁷As mentioned above, the power dissipation of 550 mW/cm² applied to the area hosting the on-chip electronics in the thermal simulations might differ from the one dissipated by the sensors during the temperature measurements.

¹⁸The in-vacuum temperature measurements are not part of this thesis and will be discussed in [53].

5.4.2 Commissioning of the MVD Prototype in the Laboratory

For the commissioning of the MVD Prototype and the reference planes in the laboratory, their sensors are connected to the subsequent read-out electronics which are briefly discussed in Section 5.5.1 and in detail in [77].

Since a dedicated probe card has not been available prior to the integration process of the sensors into the “core modules”, their status could not be evaluated before this process had accomplished. The yield of the sensors after their mechanical thinning and electrical testing is stated by IPHC to be $65 \pm 10\%$ for MIMOSA-26 [97]. The connection of the sensors to their read-out electronics allows to evaluate their electrical functionality as well as their yield. During the integration process, a set of eighteen $50 \mu\text{m}$ thin MIMOSA-26 sensors has been integrated into dedicated “core modules” of which twelve are contained in the MVD Prototype and the reference planes. Out of the 18 integrated sensors, one sensor has been discovered to be non-functional due to a short circuit in the power supply lines [65]. Two sensors showed minor failures in terms of a dead pixel row or column [65]. Therefore, the number of working sensors is in accordance with the expected yield.

The electrical functionality of the sensors is being evaluated by applying various threshold settings to the sensors. The chosen thresholds for the operation of the sensors have to permit their stable operation while exhibiting a fake hit rate which is not higher than 10^{-6} per pixel and per frame [98]. The sensor thresholds are adjusted by use of the sensors’ JTAG-interface [95].

The data sent by the sensors is checked for consistency and the synchronization of the operating sensors is evaluated. For these tests, the response of the sensors to electrons with an energy of 546 keV emitted by a radioactive strontium (Sr-90) source which is positioned in front of the MVD Prototype is investigated. The response of the sensors positioned in the double-sided module to the traversing particles is depicted in a correlation plot in Figure 5.25. The contribution of the multiple scattering to the width of the correlation distribution can be determined using

$$\theta_0 = \frac{13.6 \text{ MeV}}{\beta pc} z \sqrt{x/X_0} [1 + 0.038 \ln(x/X_0)] = 1.06 \text{ rad}, \quad (5.1)$$

with $\beta = z = 1$ and $x/X_0 = 0.003$, the material budget value of the MVD Prototype. Thus, the diversification of the electrons resulting from the multiple scattering after passing the charge-sensitive area of the double-sided module¹⁹ amounts to

$$\theta_{ms} = d \times \theta_0 = 372 \mu\text{m}. \quad (5.2)$$

Therefore, it is obvious that the distribution shown in Figure 5.25 is dominated by the multiple scattering of the electrons since the estimated value exceeds the spatial resolution of the

¹⁹The thickness of the double-sided module in the charge-sensitive area can be determined to be $350 \mu\text{m}$ according to Table 5.5.

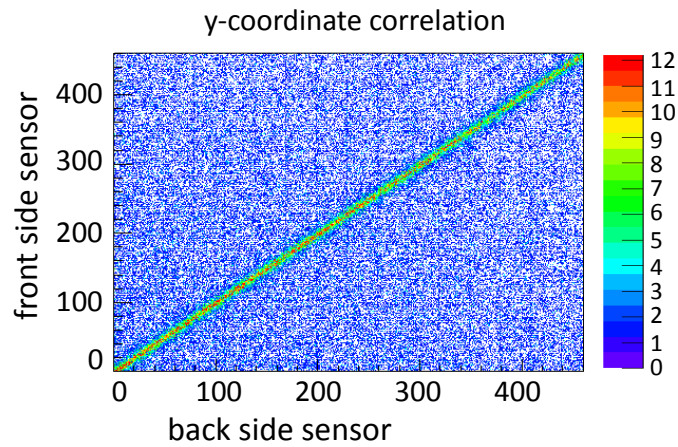


Figure 5.25: *The correlated response of the MVD Prototype sensors to electrons emitted by a radioactive strontium source. The correlation distribution is evaluated in the y-coordinate of both sensors.*

sensors, measured to have a value of $\sim 3.5 \mu\text{m}$, by a substantial margin. As a consequence, it can be omitted to determine the width of the correlation distribution. The extraction of the correlation distribution from the recorded sensor data demonstrates that the synchronization of the sensors is achieved as well as maintained over the time period of the data collection and that the sensors are functional and can be operated in a stable mode.

5.5 In-Beam Test

The response of the sensors integrated in the MVD Prototype to minimum ionizing particles has been evaluated at the CERN-SPS. A beam of pions with a kinetic energy of up to 120 GeV has been used to determine several specific sensor parameters. The energy of the beam particles ensures that the particle tracks can be assumed to be straight and their suffering from multiple scattering to be minimal. The data taken is analyzed with regard to these sensor parameters and the extracted values are compared to their reference values which are obtained at the same beam line by the IPHC group developing the MIMOSA sensors [48] using particles with the same energy.

The set-up used in the in-beam test is described below. It allows to evaluate several key aspects which are important for the construction of the MVD. This thesis mainly evaluates the impact of the mechanical set-up on the detection performances of the sensors which are defined by the efficiency and spatial resolution of the sensors. The position stability of the sensors is investigated to evaluate the mechanical support structures. The position stability should be small and as constant as possible during the in-beam test in order to reproduce the intrinsic properties of the sensors. For the read-out and data acquisition system, the synchronization of the continuous multi-channel read-out as well as its long-term stability are studied. These findings are presented in [77].

During the in-beam test, the traversing particles allow to test the sensors, the read-out system and the data acquisition system in realistic conditions.

5.5.1 In-Beam Set-Up

The in-beam set-up is sketched in Figure 5.26. The MVD Prototype, comprising the two sensor planes (c) and (d), is positioned in the middle of the set-up. The reference planes are positioned in two sets of two planes each, located next to the MVD Prototype; two planes are installed upstream (equipped with CVD diamond carriers, reference planes (a) and (b)) and the other two planes are positioned downstream (equipped with aluminum carriers, reference planes (e) and (f)) of the MVD Prototype. Two scintillators are enclosing the set-up from the upstream and the downstream direction.

The description of the in-beam set-up is sub-divided into four parts, discussing separately the arrangement of the sensors, the read-out as well as the data acquisition system, the mechanical set-up and the cooling set-up.

The Sensor Arrangement

The MVD Prototype and the reference planes are arranged so as to form a common acceptance for the traversing pions using the integrated sensors. As a result, the charge-sensitive area of an individual sensor plane overlaps with the charge-sensitive area of the dedicated sensor on each of the other sensor planes. The overlapping charge-sensitive areas are indi-

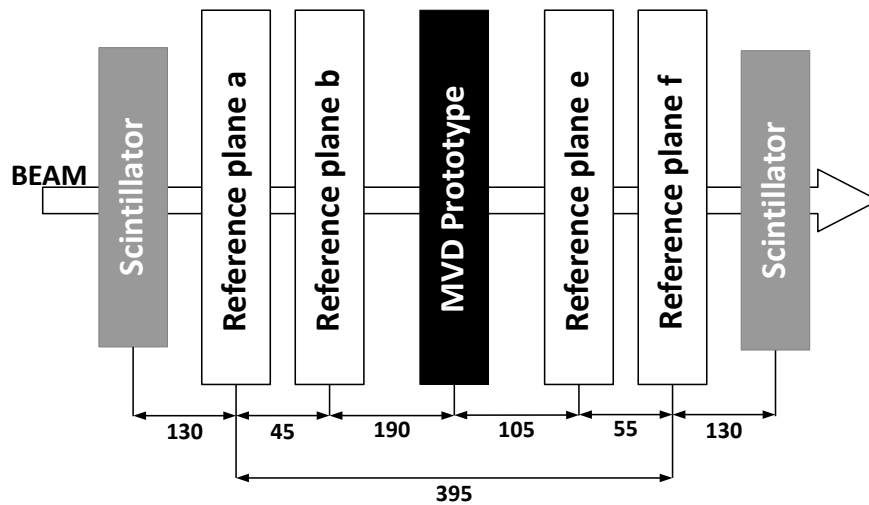


Figure 5.26: The in-beam test set-up comprises seven components exposed to the pion beam. The MVD Prototype is positioned in the center of the set-up and is surrounded by two sets of two reference planes each. The set-up is enclosed by two scintillators. The distances between the sensor planes are given in mm.

cated with a red frame in Sketch 5.27(a). The pion beam, indicated by the red dashed line, is passing through these overlapping charge-sensitive areas.

The hatched area in Sketch 5.27(b) illustrates the case in which one of the sensors of a dedicated sensor plane is malfunctioning. The solution to achieve the restoration of the common acceptance for the traversing pions using all available sensor planes has already been implemented in the design and the set-up of the “core module” by integrating two sensors in each module, see Section 5.1.

The affected sensor plane²⁰ is lifted up by the width of about one sensor using a dedicated spacer replacing the malfunctioning sensor with a working one.

The Read-Out and Data Acquisition System

The read-out and data acquisition system, sketched in Figure 5.28, focuses on the route of the sensor data sent towards the data storage PC. The routes for the slow and fast control signals steering the sensors are not discussed. They are described in detail in [77, 95].

The sketch depicts the sensors, the FEBs, the Converter boards, the Read-out controller and the HUB as well as the PC.

²⁰In case of a malfunction of a dedicated sensor integrated into the MVD Prototype, all reference planes have to be lifted to restore the common acceptance.

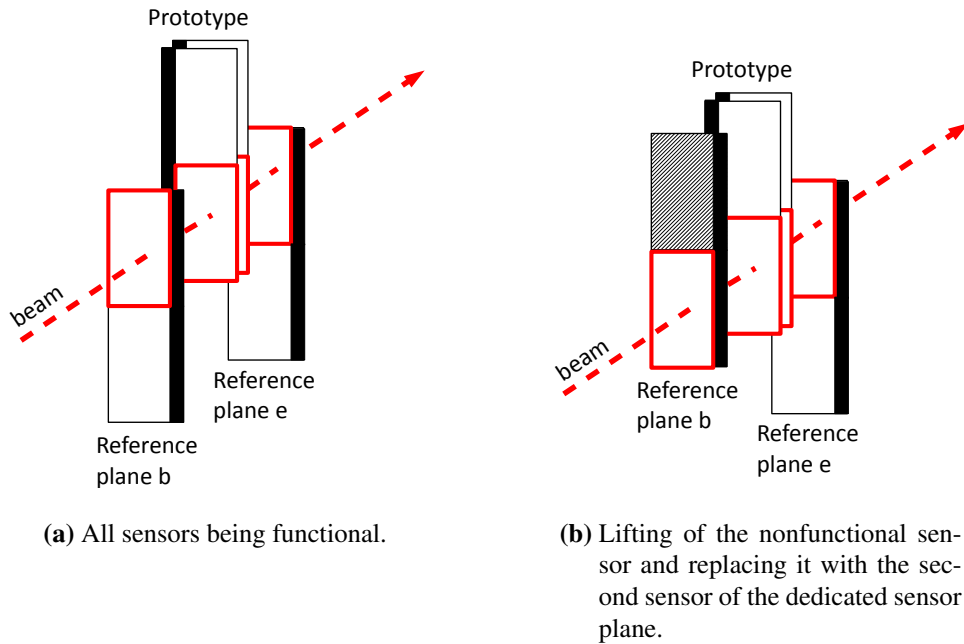


Figure 5.27: *The sensor arrangement in the in-beam test. It aims at forming a common acceptance for the traversing pions using the sensor planes of the MVD Prototype and the reference planes. The reference planes closest to the MVD Prototype (b and e) are shown. The white area symbolizes the charge-sensitive sensor area, the black square indicates the on-chip electronics.*

The two sensors (see Section 5.1.1) send their data via the bonded FPC (see Section 5.1.5) to their dedicated FEB. For each sensor, several signal lines as well as several supply lines are routed to and from the FEB to the sensors using the FPC. The FEB hosts passive electronic components only and serves as signal stabilizer and as distribution point for the sensors' slow control signals.

The FEBs are connected to their dedicated Converter boards using additional FPCs which are bridging a distance of up to 50 cm between the two boards. The Converter board²¹ comprises the electronic components for the regulation of the power, its distribution and the stabilization of the required sensor voltages. The data sent by the sensors is transmitted from the Converter boards to the Read-out controller using dedicated RJ-45 cables.

The Read-out controller is based on the HADES TRBv2 [99], it provides the slow control of the sensors as well as the required logic for the further transmission of the sensor data. The sensor data is transmitted to the HUB board using optical fibers.

The HUB board is based on the HADES TRBv2 as well. It serves as a data concentration point and transmits the sensor data via Ethernet protocols to the data storage and analysis PC.

²¹A detailed description of the Converter board can be found in [77].

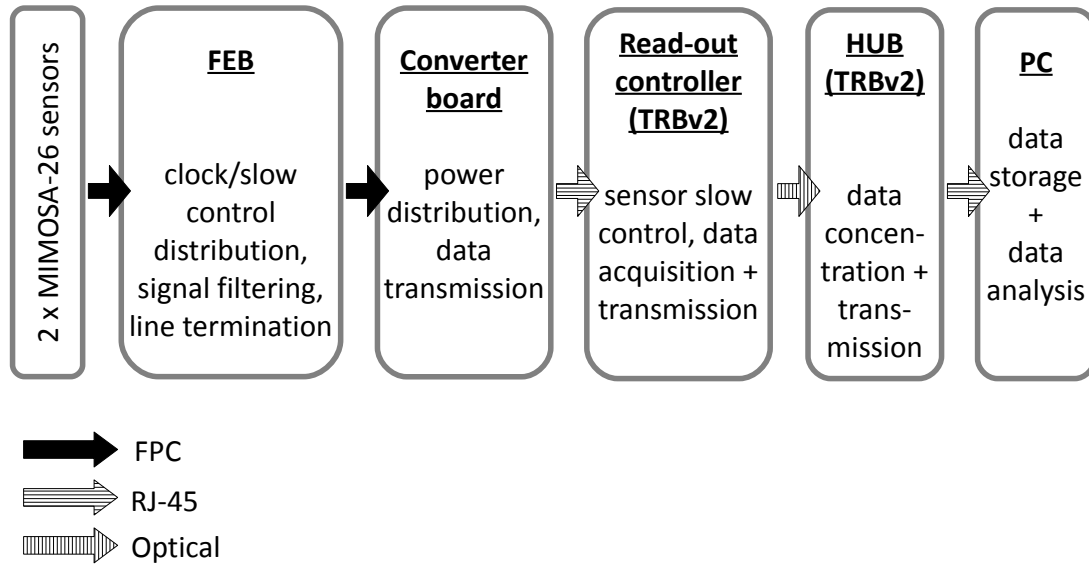


Figure 5.28: The read-out scheme used to transport the data sent by the two sensors towards the data storage PC. The scheme comprises the sensors, the FEB, the Converter board, the Read-out controller and the HUB as well as the PC. Their individual tasks are specified.

The read-out system has to provide the synchronization of the sensor output to allow for the subsequent analysis of the sensor data. This synchronization is realized applying dedicated features of the data handling protocol TrbNet [99]. The required clock distribution scheme is discussed in [77]. In addition, the sensor operation settings have to be checked regularly for consistency by use of dedicated protocols, e.g., the JTAG standard, see [95]. The sensor data is checked by default for consistency as well, using dedicated implemented features, e.g., header information and check-sums, cf. [77].

The Mechanical Set-Up

The in-beam set-up is positioned on a common base plate, see Figure D.12 in the Appendix. The MVD Prototype is positioned in the center of the base plate at position (1) according to the sketch of the in-beam test set-up shown in Figure 5.26. The orientation of the MVD Prototype to the beam axis can be varied to study the impact of various incident angles of the beam to the sensors and their response (in terms of cluster shape and size) [100]. Therefore, fixation points for the MVD Prototype, indicated with (2), are provided for various possible incident angles ranging from 0° to 75° with a subdivision of 5° each. The reference planes are placed onto rails, numbered with (3), using two dedicated sliding carriages per plane. The rails themselves are attached to the base plate parallel to the beam and allow to adjust the distance of the reference planes to the MVD Prototype for a given measurement scenario as well as with respect to each other.

The base plate has to be positioned in the beam line in a way that the common acceptance formed by the overlapping charge-sensitive areas of the sensor planes, see Figure 5.27(a), and the beam axis coincide with each other. The positioning of the MVD Prototype and the reference planes onto the common base plate allows to adjust their common orientation to the beam axis by changing only the position of the base plate with respect to the beam axis.

The Cooling Set-Up

The cooling of the sensors integrated into the MVD Prototype and the reference planes is provided by two separated cooling circuits allowing for different sensor operation temperatures. During the in-beam test, the sensor performance is studied at different heat sink temperatures of the MVD Prototype, namely at $T_{\text{heat sink}} = 17\text{ }^{\circ}\text{C} \mid 6.8\text{ }^{\circ}\text{C} \mid -5.5\text{ }^{\circ}\text{C}$. In contrast, the temperatures of the heat sinks of the reference planes are kept constant throughout the in-beam test at $T_{\text{heat sink reference planes}} = 17\text{ }^{\circ}\text{C}$ in order to provide the same sensor operation conditions at all times.

The cooling tubes of the MVD Prototype are guided over the top side of the base plate. For the reference planes, the distribution of the cooling liquid is provided from underneath the base plate to avoid electrical shorts which may occur as a result of the contact of condensed water along the cooling pipes and the read-out electronics positioned on the base plate. A schematic view of the distribution of the cooling liquid is depicted in Figure D.13, its realization is shown in Figure D.14, both in the Appendix.

The in-beam set-up focusing on the arrangement of the MVD Prototype and the reference planes is depicted in Figure 5.29. The complete in-beam set-up is shown in Figure D.15 in the Appendix.

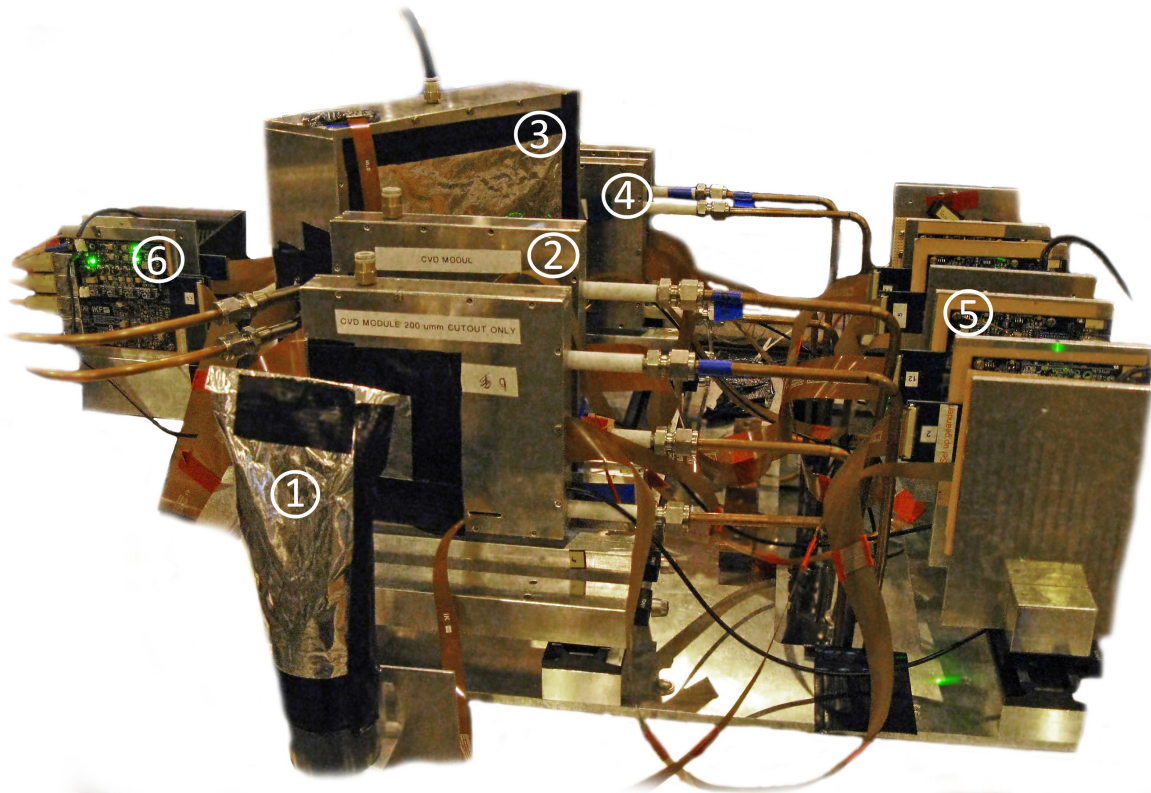


Figure 5.29: The MVD Prototype and the reference planes integrated in the in-beam set-up according to the sketch showed in Figure 5.26. The first two reference planes (2) are positioned in between the first scintillator (1) and the MVD Prototype (3). In this picture which does not show the standard arrangement (no incident angle), the MVD Prototype is positioned at an angle of 60° to the beam to allow for the study of a different incident angle of the beam to the sensors. The two aluminum carrier-based reference planes (4) are partially hidden behind the MVD Prototype. The Converter boards of the reference planes are located on the right side of the assembly (5), while the ones of the MVD Prototype can be found on the left side (6).

5.5.2 In-Beam Running Conditions

The performance of the MVD Prototype as well as the read-out system are evaluated focusing on the applied in-beam running conditions, which are listed below. Special emphasis is placed on the operation of the sensors integrated into the MVD Prototype and their detection performance, the reliability of the read-out system and the long-term stability of the cooling system as well as the mechanical support structures.

The different running conditions applied to the MVD Prototype during the in-beam test are:

- Different sensor operation settings in combination with three different heat sink temperatures, see Section 5.4.1
 - The sensor performances, defined as the efficiency, the resolution and the fake hit rate, are examined as a function of the heat sink temperature and the applied sensor operation settings
 - The long-term stability of the cooling concept as well as the position stability of the sensors glued on the CVD diamond carrier is investigated
- Different incident angles of the beam with respect to the MVD Prototype
 - The sensor response to particle tracks impinging with an angle of 0° , 30° , 45° and 60° to the sensors is studied, see [78, 100]
- Different beam energies and intensities
 - The capability of the read-out electronics to cope with various data rates is studied, see [77]

In contrast to the MVD Prototype, for the reference planes, the sensor operation settings and the heat sink temperature have been set once and are kept constant during the whole in-beam test.

5.5.3 Data Analysis

The data recorded during the in-beam test of the MVD Prototype and the reference planes is analyzed [98]. It has to be noted that a direct temperature measurement of the MVD Prototype sensors during the in-beam test has not been possible. This results from the fact that the temperature diode of the individual MIMOSA-26 sensor shares a ground terminal with the sensor power supply. The current consumption of the operating sensor creates a varying voltage drop on the ground line which leads to inconsistent temperature readings. As a consequence, the results of the sensor performance are presented as a function of the temperature measured on the heat sink of the MVD Prototype. The heat sink temperature

can be related to the sensor temperatures using the temperature differences measured in Section 5.4.1.

Within the analyzed data, the alignment of the sensors and their position stability is evaluated. The sensor position stability can be assessed by evaluating the spatial resolution of the sensors. The appearance of vibrations might cause a broadening of the residual distributions. A possible temperature-dependent behavior of the sensor performance might be observed in a change of the sensor alignment within the measuring time of a dedicated run. For this investigation, the alignment of the sensors integrated into the MVD Prototype and the reference planes has to be compared relative to each other, since only the temperature of the heat sink of the MVD Prototype is varied.

A run is defined as a time interval in which the running conditions applied to all components of the MVD Prototype are kept constant. The sensor performance parameters are continuously monitored but the different parameters have to be extracted at different time slots during a run. The fake hit rate of the sensors has to be determined during the spill breaks. The assessment of the efficiency of the sensors and their spatial resolution has to be conducted in-beam. The assessment of the sensor performance parameters requires that the recorded sensor data has been synchronized and that an alignment of the sensors has been carried out. Since the initial positions of the sensors of the MVD Prototype relating to the positions of the sensors in the reference planes can only be determined with respect to each other within an accuracy of millimeters by measuring the distances in between their housing boxes, a dedicated routine is required to align the sensors with a precision in the order of micrometers to take advantage of their spatial resolution. A “master” alignment is conducted for the data sampled in a dedicated run featuring high statistics. During this run, a high threshold setting is applied to the sensors to suppress fake hits and to achieve a clean data set. The alignment strategy is explained in detail in Section D.13 in the Appendix, analog to [98].

All subsequently taken data sets are aligned relatively to this “master” alignment unless a major change in the set-up is applied, e.g., a change of the orientation of the MVD Prototype to the beam.

Performance Test of the Alignment within the Root Framework

The performance of the alignment procedure is tested with the help of simulations within the Root framework [101].

Different set-ups, comparable to the one used in the in-beam test, have been implemented allowing for the variation of their alignment parameters. Random tracks are generated and the sensors are aligned accordingly. For the resolution of the sensors, two different values of $4\ \mu\text{m}$ and $3.3\ \mu\text{m}$ are assumed. The simulated tracks are used to reconstruct the alignment parameters relative to an ideal geometrical adjustment.

The set-up exhibits different sensitivities to the alignment parameters – the translation of the sensors in the x-, y- and z-direction²² as well as the rotation in α , β and γ ²² – which are

²²The optimization of the alignment parameters is carried out in the following order: first the x- and y-parameters are optimized, followed by the rotation in γ and finally the optimization of α , β and z.

shown in Table D.6 in the Appendix. The reconstructed alignment parameters agree within a maximal error of 1% in case of the simulated pointing resolution and within a maximal error rate of 0.1% for the simulated residuals, as shown in Table D.7 in the Appendix. It has to be kept in mind that in the simulation, the assignment of the hits to the tracks is known and that the effects of a possible multiple scattering within the in-beam set-up are not taken into account. In contrast to this, for the data taken during the in-beam test, the effects of a possible assignment of fake hits to the tracks as well as the multiple scattering of the pions within the sensor planes should not be neglected.

5.5.4 Sensor In-Beam Performance

After the alignment of the sensors has been carried out, their in-beam performance can be assessed. The sensor efficiency and the spatial resolution of the sensors, to which the support structures of the MVD Prototype might contribute to, are determined with regard to their dependency on the heat sink temperature of the MVD Prototype as well as their dependency on a defined set of sensor operation settings. They constitute the running conditions which are listed in Table 5.7. These sensor operation settings are chosen to define the “standard” threshold²³ values for the evaluation of the sensor in-beam performance. They have been determined to allow for a stable sensor operation and a fake hit rate not higher than 10^{-6} per pixel and per frame at a heat sink temperature of $T_{\text{heat sink}} = 17 \text{ }^\circ\text{C}$ [98]. The MVD Prototype sensor facing the beam is referred to as “front”/“sensor 1”, while the sensor facing the upstream part of the set-up is referred to as “back”/“sensor 2”.

²³The threshold setting for a sensor matrix is explained in Section 5.1.1 above.

$T_{\text{heat sink}} [^\circ\text{C}]$	Sub-matrix threshold setting				Beam energy [GeV]
	front sensor				
	1	2	3	4	
17					80
6.8	174	132	190	–	10
–5.5					10
	back sensor				
17					80
6.8	114	217	174	215	10
–5.5					10

Table 5.7: The sensors’ in-beam performance is examined for the listed running conditions. The fourth sub-matrix of the front sensor has been disabled as a result of a high noise value. The numbers are taken from [98].

Efficiency of the MVD Prototype Sensors

The efficiency of the two MVD Prototype sensors is depicted as a function of the measured heat sink temperature in Figure 5.30.

At a heat sink temperature of 17 °C, the efficiency of the sensor positioned on the front side is determined to be above 95% for all displayed sensor matrices, compare Figure 5.30(a). For the sensor positioned on the back side of the CVD diamond carrier, the efficiency is found to be above 90% for all sensor matrices.

During a dedicated threshold scan which is conducted at a heat sink temperature of 17 °C [98], different sensor operation settings are applied. The “standard” sensor operation settings (see Table 5.7) are chosen to determine a reference point for this investigation. The other applied sensor operation settings relate to these “standard” settings by subtracting or adding a defined value. The efficiency as a function of the applied sensor operation settings relative to the “standard” ones is shown in Figure 5.31. The efficiency values of the sensors are rising with lower threshold settings. For a sensor operation setting which is lowered by eight relative discrimination values, sensor 1 demonstrated an efficiency of close to 100%, and sensor 2 showed an efficiency of above 96%. For a sensor operation setting which is lowered by 12 relative discrimination values, the efficiency of both sensors is found to be close to 100%.

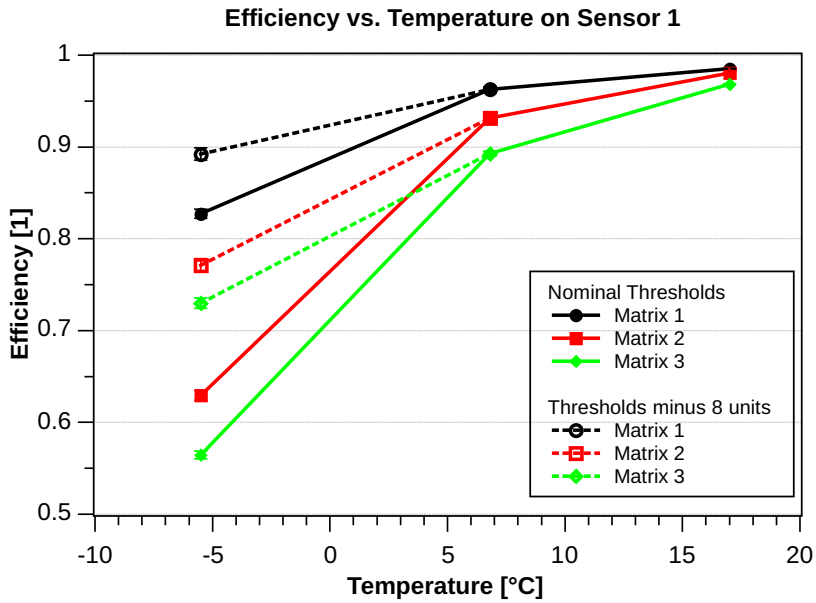
Since the detailed analysis of the recorded data has been carried out after the completion of the in-beam test, it could not be prevented that the use of the “standard” sensor operation settings led to a lower sensor efficiency.

The efficiency of the sensors is found to decrease while the heat sink temperature is being lowered, see Figure 5.30. In this figure, the filled symbols represent the efficiency values in case the “standard” sensor operation settings have been applied. For a heat sink temperature of 6.5 °C, the efficiency is lowered to a value of about 90% for the front side sensor. For the back side sensor, the efficiency values of the individual sensor matrices vary in a wide range between 76% for the second sensor matrix to 94% for the first matrix. Lowering the heat sink temperature to –5.5 °C and applying the “standard” operation settings, the efficiency of both sensors drops further.

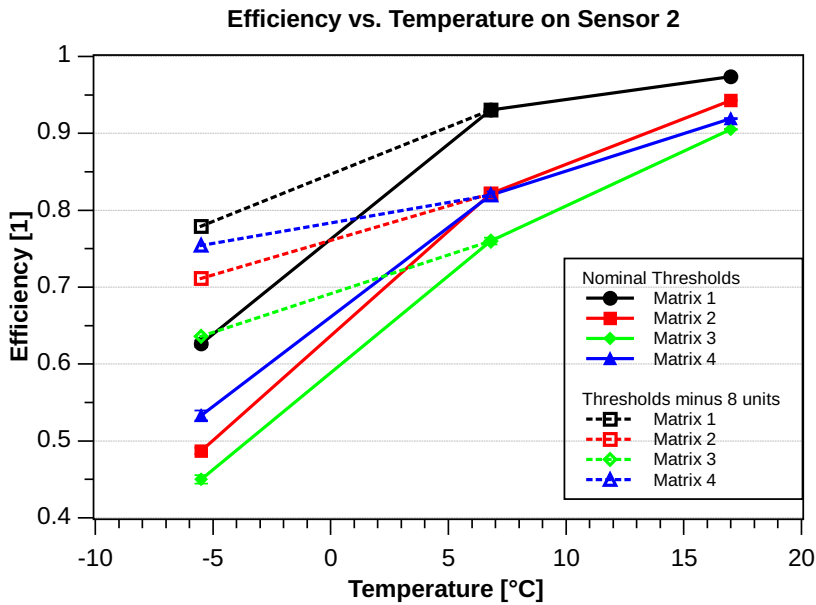
For the dashed lines ending in the open symbols in Figure 5.30, a sensor operation setting which is lowered by eight relative discrimination values has been applied throughout all matrices for a heat sink temperature of –5.5 °C. The examined efficiency values have been found to increase towards higher values.

Due to the limited time available to test the different in-beam running conditions listed in Section 5.5.2, a comprehensive threshold scan as it has been carried out for a heat sink temperature of 17 °C (cf. Figure 5.31) has not been executed for the heat sink temperatures of 6.8 °C and –5.5 °C. For a heat sink temperature of 6.8 °C, the efficiency values are extracted only from measurements carried out using the “standard” sensor operation settings.

In addition, a decrease of the cluster size as a function of the temperature is found while applying the “standard” operation sensor settings. For a heat sink temperature of 17 °C, the average cluster multiplicity is found to be 2.2 ± 1.2 for sensor 1 and 1.9 ± 1.2 for sensor 2. The average cluster multiplicity is lowered to a value of 1.5 ± 1 for sensor 1 and to a value

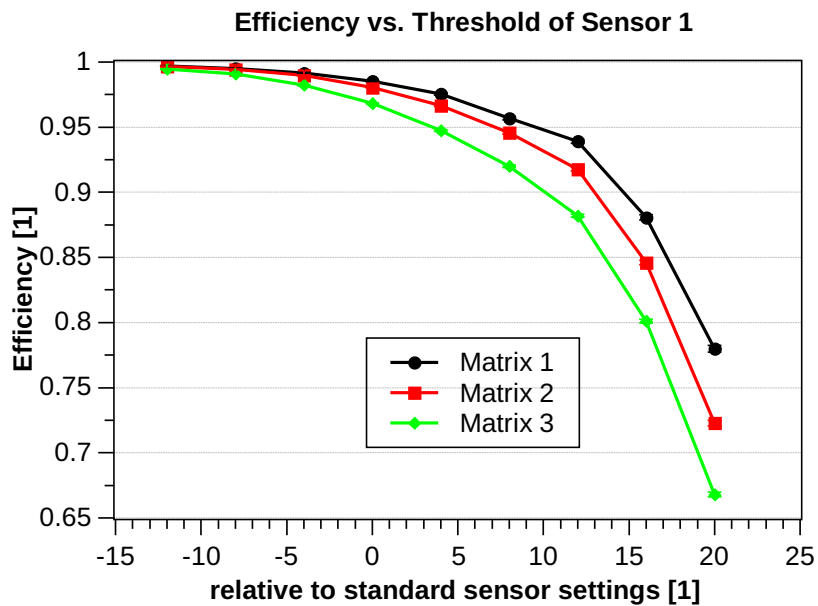


(a) Sensor 1 is positioned on the front side of the double-sided module.

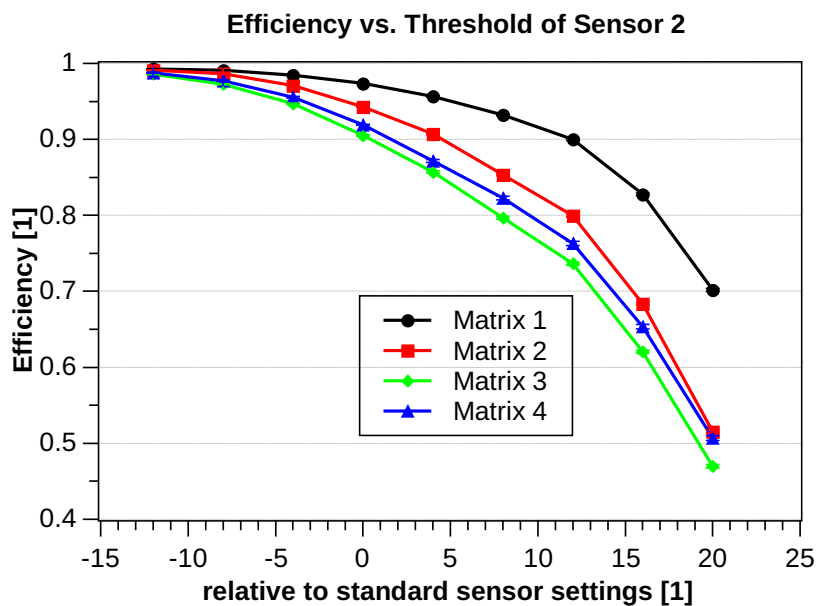


(b) Sensor 2 is positioned on the back side of the double-sided module.

Figure 5.30: The temperature dependence of the efficiency of the two MVD Prototype sensors. For the full symbols, the running conditions listed in Table 5.7 are applied, while for the open symbols, the threshold settings have been lowered by eight units throughout all sensor matrices. The figures are taken from [98].



(a) Sensor 1 is positioned on the front side of the double-sided module.



(b) Sensor 2 is positioned on the back side of the double-sided module.

Figure 5.31: The dependence of the efficiency of the two MVD Prototype sensors on the applied sensor operation settings for a heat sink temperature of 17°C . The sensor operation settings are expressed relative to the “standard” ones which are normalized to 0. The figures are taken from [98].

of 1.3 ± 0.8 for sensor 2 at a heat sink temperature of -5.5 °C, compare Figure D.17 in the Appendix.

It is possible that the effect of the efficiency decreasing while the temperature of the heat sink is being lowered has been intensified by applying the “standard” sensor operation settings throughout all measurements. The “standard” sensor operation settings have been optimized for a dedicated fake hit rate per pixel and per frame of the order of magnitude of 10^{-6} for a heat sink temperature of 17 °C. They were only varied during the dedicated threshold scans. As a result of this, it can be read off Figure 5.33 that the average fake hit rate for a heat sink temperature of -5.5 °C is of the order of magnitude of 10^{-7} instead of 10^{-6} .

For lower discriminator thresholds than the “standard” sensor operation settings, an increase of the sensor efficiency is observed, compare Figure 5.31. The lower discriminator thresholds result in a lower level which has to be overcome by a signal before it is identified as such. At the same time, the probability of the signal to be dominated by the noise of the pixels increases since the noise has to overcome this lower threshold level to be identified as signal as well. Resulting from the operation at lower temperatures, the noise contribution to the signal is expected to be reduced to a smaller value.

Due to the absence of measured data, a determination as to whether the efficiency of the sensors could be raised to about 100% by applying lower sensor operation settings for the heat sink temperatures of -5.5 °C and 6.8 °C cannot be made yet.

For the sensors to be integrated into the MVD, comprehensive threshold scans at various heat sink temperatures are necessary to operate the sensors with high efficiency. Dedicated methods to extract the optimal operation threshold settings for the sensors must be developed and thoroughly tested.

Resolution

As a result of the above described uncertainty, especially by the assessment of the alignment parameters and the multiple scattering of the particles traversing the in-beam set-up, the pointing resolution was not unfolded from the residuals. The multiple scattering of the particles traversing the set-up is estimated in Section D.13 in the Appendix.

The spatial resolution of the sensors of the MVD Prototype is determined according to the following equation

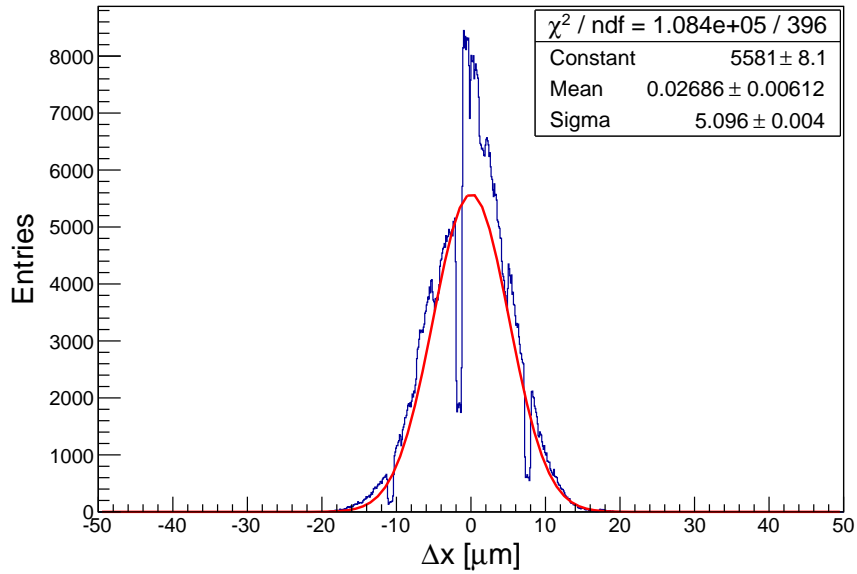
$$\sigma_{\text{residual}}^2 = \sigma_{\text{spatial resolution}}^2 + \sigma_{\text{pointing}}^2. \quad (5.3)$$

The residuals of the MVD Prototype sensor planes referencing each other were found to be 5.1 μm in x- and 5.3 μm in y-direction, as displayed in Figure 5.32. The structure of both distributions, the drop of entries around 0, can be related to the digital read-out scheme of the sensors which results in the occurrence of discrete values only.

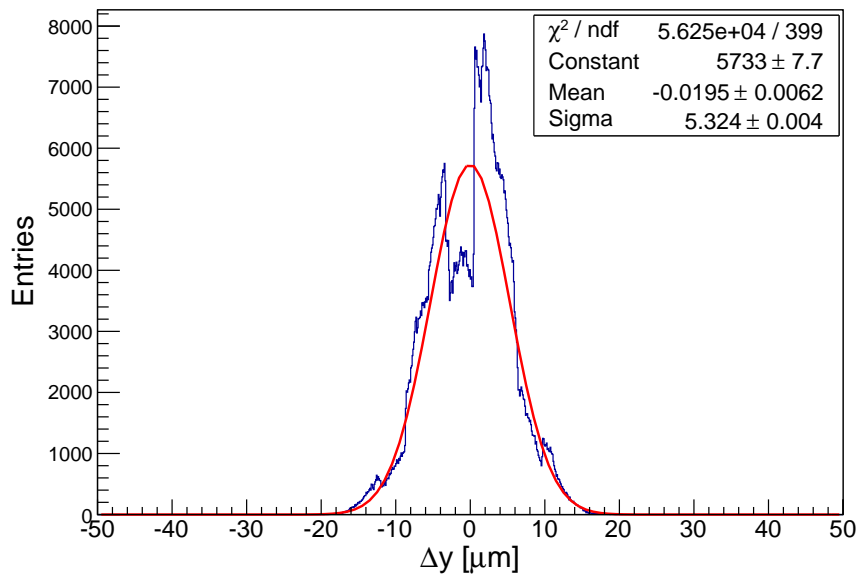
For the determination of the spatial resolution of the MVD Prototype sensors the fact that both sensors are separated only by the 200 μm thin CVD diamond carrier and two layers of glue is utilized. As a consequence, only tracks which display a minimum divergence are taken into account. With this, the spatial resolution of the sensors can be stated to have a value of 3.6 μm and 3.7 μm in the x- and y-direction, respectively.

The residuals of the two MVD Prototype sensors with respect to reconstructed tracks in the reference planes are shown in Figure D.18 in the Appendix as a function of the heat sink temperature. In comparison with the sensor performance previously discussed, an inverted temperature dependence is determined for these residuals. They increase from about 4 μm , which has been measured at a heat sink temperature of 17 $^{\circ}\text{C}$, to about 6 μm at a heat sink temperature of -5.5 $^{\circ}\text{C}$, in x- as well as in y-direction, while the “standard” sensor operation settings have been applied throughout the measurements.

The reproduction of the reference value of the spatial resolution of the MIMOSA-26 sensors, being obtained at the same beam line by the IPHC group developing the MIMOSA sensors [48], permits a conclusion for the applied integration process. It is suitable for the ultra-thin sensors since it does not result in any deterioration of this sensor performance value.



(a) Residuals of the MVD Prototype sensors in the x-direction.



(b) Residuals of the MVD Prototype sensors in the y-direction.

Figure 5.32: The residuals of the two MVD Prototype sensor planes referencing each other have a value of $5.1 \mu\text{m}$ in the x-direction and $5.3 \mu\text{m}$ in y-direction. The figures are taken from [98].

Fake Hit Rate

The fake hit rate, defined in Section 5.1.1 above, is depicted in Figure 5.33 as a function of the temperature measured on the heat sink of the MVD Prototype. It has been normalized to the number of pixels of the individual sensor matrix as well as to the number of read-out cycles. For the determination of the fake hit rate, the sensor operation settings listed in Table 5.7 are applied.

The relation of the fake hit rate to the efficiency and the fact that the efficiency is found to be temperature-dependent does not permit a qualitative discussion of the average fake hit rate. It is found to decrease from a value of 10^{-6} to a value of about 10^{-7} while the heat sink temperature is being lowered from $17\text{ }^{\circ}\text{C}$ to $-5.5\text{ }^{\circ}\text{C}$. For the matrix 2 of the sensor 1, the average fake hit rate is found to be one order of magnitude higher than the other ones. This might be attributed to some “hot” pixels which result from a strong contribution of noise indicating a signal in each read-out cycle.

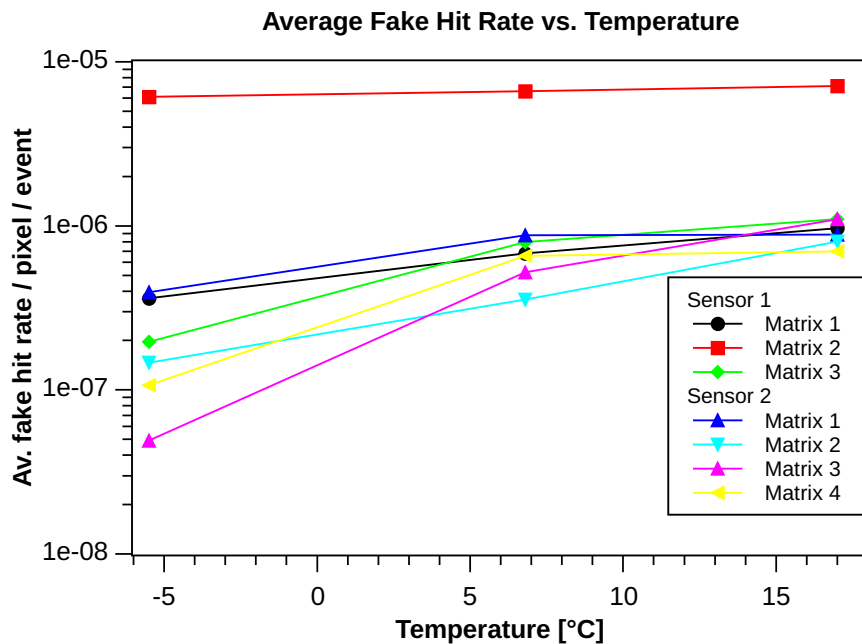


Figure 5.33: The average fake hit rate of the MVD Prototype sensors as a function of the temperature measured on the heat sink of the MVD Prototype. The figure is taken from [98].

Mechanical Stability

The recorded data enabled the study of the position stability of the sensors and the mechanical stability of the set-up. The sensors integrated into the MVD Prototype are used to investigate a possible appearance of vibrations coupled to the system from anywhere, e.g., the cooling system.

Sensor Position Stability

A shift of ~ 3 nm per minute is found in the x- as well as in the y-coordinate of the MVD Prototype sensor planes with respect to the reference planes in the global coordinate system of the in-beam set-up. This shift, which is depicted in Figure 5.34, occurs during the time period in which the data is taken to define the “master” alignment, see Section D.13 in the Appendix. Each entry in the histogram is averaged over the time interval of one beam spill traversing the set-up, i.e., of about 9.5 seconds.

The direction of the sensor shift can be described as follows: In the y-coordinate, it is directed towards the heat sink of the MVD Prototype, whereas in the x-coordinate the sensor shift is directed towards the base plate of the in-beam set-up.

The shift of the sensors might be associated with a constant temperature change on components of the MVD Prototype resulting in a thermal expansion of the different integrated materials. The effect of a temperature change is investigated focusing on two different scenarios, namely a temperature change on the MVD Prototype “core modules” or a temperature change on the mechanical components of the MVD Prototype, the latter comprising the heat sink, the double-sided module and the housing box.

For a constant temperature change on the “core modules”, the different coefficients of thermal expansion of the integrated materials are compared. In case the coefficients of thermal expansion of CVD diamond and the sensors (the value of silicon is being assumed) are compared with each other, a temperature change below 0.5 K results in an expansion comparable to the extracted shift (see in more detail below). A similar expansion can be found for the comparison of the coefficient of thermal expansion of CVD diamond with the one of the aluminum heat sink.

The temperature change in the y-coordinate can be traced to the heat dissipated by the sensors being evacuated towards the heat sink (in y-direction). However, this heat flow does not explain the sensor shift in the x-coordinate.

For a temperature change on the mechanical components of the MVD Prototype, two potential sources are investigated by means of a temperature change on the heat sink or in the experimental hall.

The temperature of the MVD Prototype heat sink has been set to a constant value and remained unchanged during the individual runs. The heat sink temperature has been measured continuously employing its glued temperature sensor, compare Figure 5.15(b). These measurements did not show any temperature change until the temperature of the heat sink had been lowered to -5.5 °C.

The question whether this sensor shift might emerge from a temperature change inside the

experimental hall cannot be answered as a result of a lack of continuous temperature measurements in the close vicinity of the experimental set-up. In this case, an additional sensor shift should be observed in the data extracted from the integrated sensors in the reference planes. However, this shift has not been found in the corresponding data.

The source of the temperature change which has to be stable over the entire time period of the alignment run has not yet been finally determined.

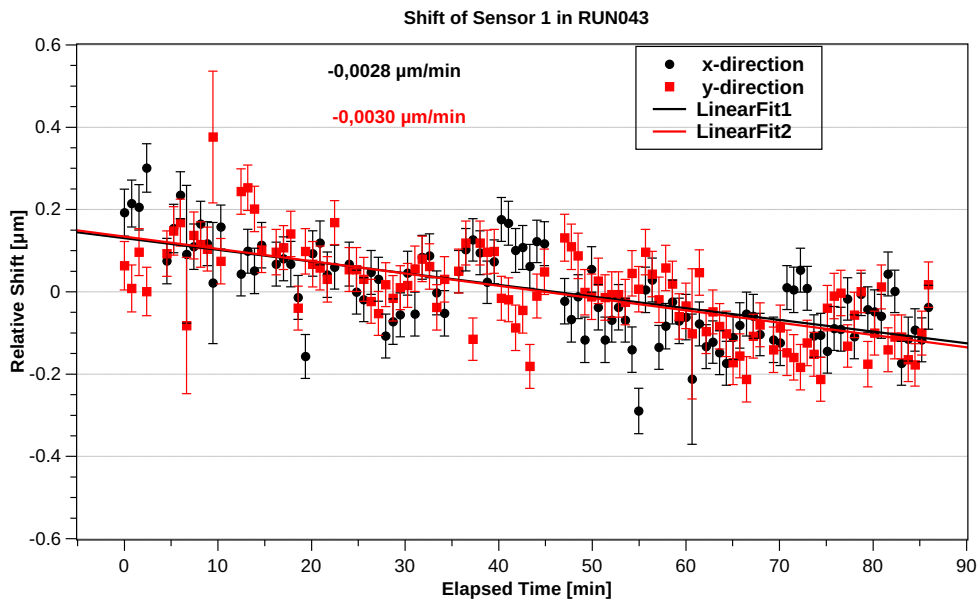
Vibrations

The investigation focusing on a possible appearance of vibrations coupled to the system is carried out using a dedicated run in which the amount of beam particles passing through the set-up has been highest²⁴. However, it has to be noted that the statistics on this issue are limited. The tracks of the traversing particles are reconstructed in the reference planes using the method introduced in Section D.13 in the Appendix. The positions of the reconstructed particle tracks going through the sensors of the MVD Prototype are compared with the positions of the indicated hits on these sensors. Their distances with respect to each other are stored in a histogram in units of the pixel pitch as a function of the elapsed time during the run, thus ensuring a time stamping of the data, see Figure D.19 in the Appendix. The mean value over all entries of this distance is calculated separately for each histogram bin, see Graph D.21(a) in the Appendix; its error is determined as the standard deviation of the entries divided by the square root of the number of entries. The resulting values have been transformed into the frequency domain by use of a fast Fourier transform (FFT), introduced in Section D.13 in the Appendix, to investigate the frequency and the amplitudes of possible vibrations. As the resulting distributions do not differ for any of the chosen coordinates, all results are exemplarily shown for the x-coordinate only. However, a pronounced amplitude that would hint at the appearance of vibrations cannot be found.

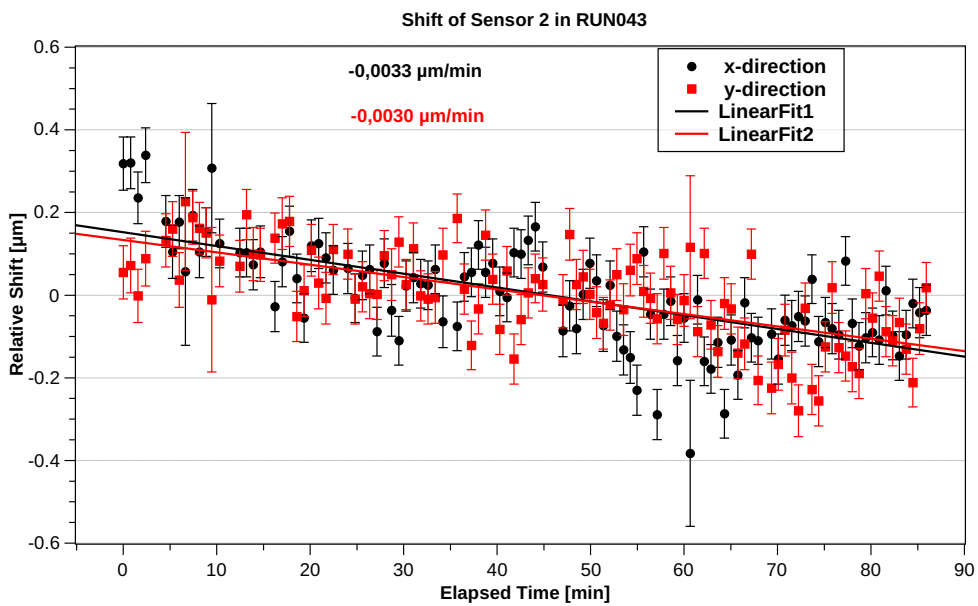
The frequency and amplitude values are examined further focusing on the possible appearance of multiple of the extracted frequencies. The first frequency is taken and multiplied by one to ten to examine consecutive modal numbers. An error margin of $\pm 0.1\%$ of the resulting frequency is taken into account. In case an accordance is detected between the multiplied frequencies and an extracted one, the extracted one is removed from the data set. The process is repeated until all extracted frequencies have been scanned. The results are shown in Figure D.20 in the Appendix for both, the x- and y-direction. In Figure 5.35, a zoom into the frequency band from 0 to 200 Hz is depicted.

In addition, these values are compared to known vibration sources, e.g., the frequency of the pump of the cooling system (of about $41.\bar{6}$ Hz). To simplify the comparison of the pump frequency with the frequencies extracted from the data, they are depicted with their corresponding amplitude in Table D.9 in the Appendix in a range of 40 to 43 Hz for the x- and y-direction, respectively. The frequencies indicate a spectrum with low amplitudes, except for one single frequency (41.42 Hz) in the y-direction of the sensors, which shows a higher

²⁴The time in which the beam particles have passed through the set-up, about 9.5 seconds, has to be related to the source of the potential vibration, e.g., the pump of the cooling system and its frequency (of about $41.\bar{6}$ Hz).



(a) Sensor 1 is positioned on the front side of the double-sided module.



(b) Sensor 2 is positioned on the back side of the double-sided module.

Figure 5.34: The change of the translational alignment for the data collected as part of the “master” alignment data set. The figures are taken from [98].

amplitude of 0.716. However, it has to be questioned whether this single frequency provides evidence that a possible vibration caused by the two pumps of the used cooling systems is coupled to the system and that this frequency can be retrieved in the recorded sensor data since the materials employed in the in-beam set-up might attenuate possible vibrations.

Modal Analysis

A modal analysis has been carried out using Autodesk Inventor to estimate possible frequencies of the in-beam set-up which could be excited by external sources. In the course of this analysis, several assumptions have been taken into account, e.g., the forming of solid connections between the sub-components of the in-beam set-up by assigning standard dependencies to them, the fixation of the cooling liquid distribution system of the reference planes to the in-beam set-up as well as the fixation of the position of the in-beam set-up to the ground.

Based on these assumptions and the fact that the entire system could only be described approximately, only a rough frequency estimate can be made. The extracted frequencies are not found to be in close vicinity to the frequency of the cooling pump.

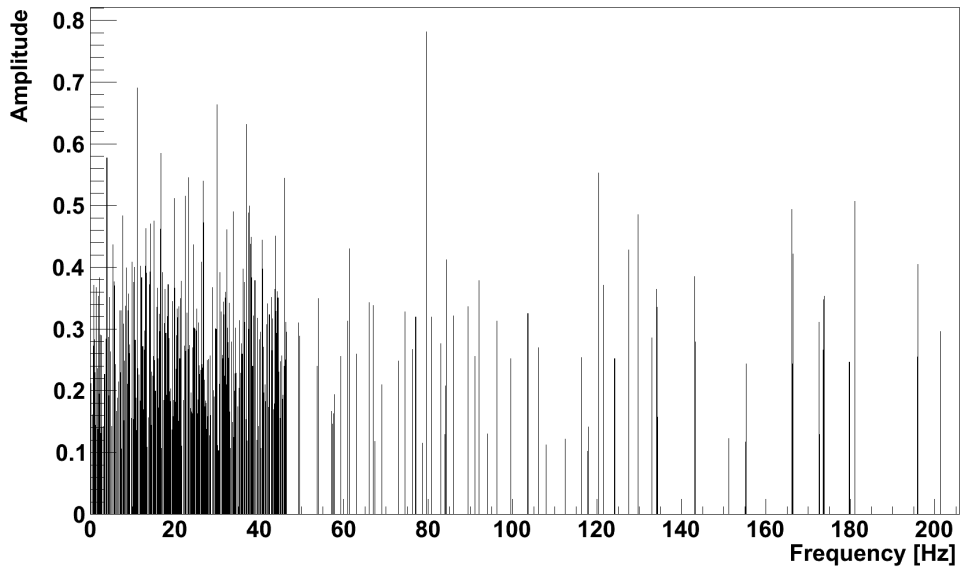
Thermal Expansion

The study of the mechanical stability involves the interplay of the components integrated into the MVD Prototype and their coefficients of thermal expansion during a temperature change of the set-up.

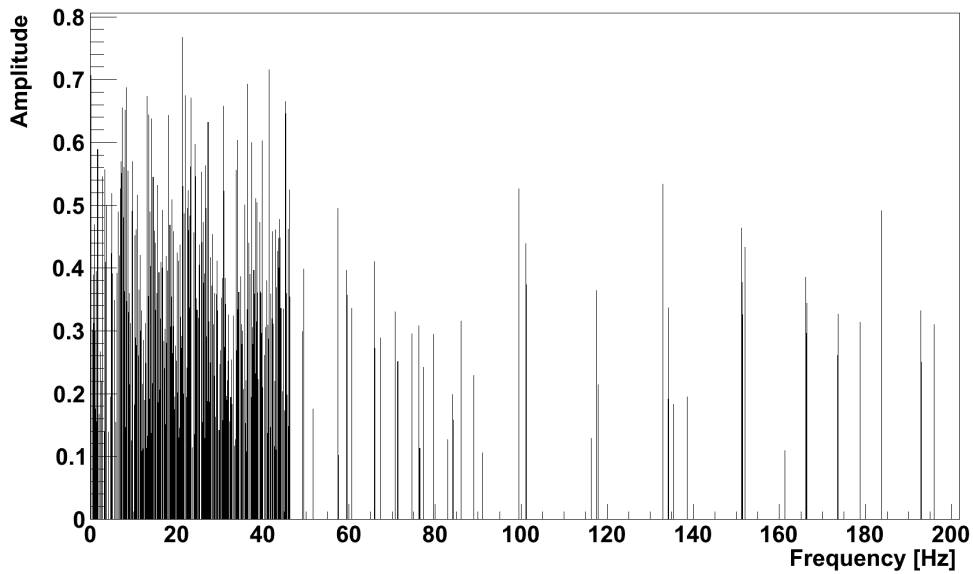
It has to be proven that the different coefficients of thermal expansion of the MVD Prototype components do not result in a failure of the sensors, e.g., due to emerging cracks. In Table D.10 in the Appendix, a list of the coefficients of thermal expansion of the involved materials, the overlapping area of the sensors with glue and the overlapping area of CVD diamond with glue as well as the temperature difference and the resulting maximum changes in length are presented.

The coefficients of thermal expansion of the materials integrated into the double-sided module are found to differ by a factor of two. For an assumed temperature gradient of 10 K across the width of the MIMOSA-26 sensors, the thermal expansion is found to be below 1 μm for the sensors as well as for the CVD diamond. Both materials are held together by the glue which expands in the order of 20 μm . This difference accentuates the fact that the glue has to be soft after curing to compensate for the resulting changes of the dimensions of the involved materials.

Since no sensor failures have been detected during the in-beam test, it can be concluded that the glue does not induce any measurable mechanical damage to the sensors.



(a) Possible frequencies in x-direction.



(b) Possible frequencies in y-direction.

Figure 5.35: Zoom into the extracted frequency spectrum reaching from 0 to 200 Hz. The frequencies in x-direction are represented by (a), the ones in y-direction by (b).

5.6 Summary and Discussion

As highlighted at the beginning of this chapter, proving the feasibility of key aspects of the MVD is an important objective. The steps that have been taken in the construction of the MVD Prototype as well as the reference planes have been presented above. Both have been extensively tested in the laboratory and during an in-beam test at the CERN-SPS which focused on different running conditions of the sensors to determine their specific parameters, in particular, their spatial resolution and efficiency (see Section 5.5 above).

Within the MVD Prototype project, the feasibility of the integration of ultra-thin sensors, the selection as well as the handling of the required materials to construct a detector, the cooling concept and the read-out concept have been studied. Special emphasis was placed on the construction of a detector which does not exceed the envisioned material budget target value of the first MVD station of $x/X_0 = 0.3\%$.

Even though the sensors used within the MVD Prototype project are precursors of the sensors to be designed for the MVD, they permitted the study of gluing, positioning and handling issues of 50 μm thin silicon foils. Dedicated tools were developed to arrange two MIMOSA-26 sensors next to each other, and to align and glue them onto both sides of a CVD diamond carrier which was used as mechanical and cooling support. The developed tools have proven to work, hence, their handling and the procedures that were applied to integrate the sensors will remain unchanged once the tools are adopted to the different form factor of the MIMOSIS-1 sensors.

In the course of the integration process, 18 ultra-thin sensors have been integrated successfully, 12 of them into dedicated “core modules” which were evaluated during an in-beam test. Out of these 18 sensors, one sensor was found to be non-functional (due to a short circuit in the power supply lines) and two sensors showed minor failures in form of a dead pixel row or column, see [65]. These sensor failures cannot be attributed to the applied integration process since the status²⁵ of the individual sensor could not be evaluated using probe tests prior to their integration into the “core modules” since a dedicated probe card had not been available at the beginning of the integration process. Therefore, the question of whether these sensor failures could have been related to the integration process in case their status had been evaluated prior to their integration cannot be answered. Nevertheless, during the integration process of the sensors into the MVD, a continuous determination of the sensor status has to be conducted.

The construction process and the thermal evaluation of the MVD Prototype has revealed that CVD diamond is capable of evacuating the heat dissipated by the sensors while offering the required stiffness and the desired low material budget.

Within the MVD Prototype project, comprehensive studies on several types of adhesives have been conducted. The glues in question can be divided into two groups: glues based on silicone and glues based on epoxy resins. Within this thesis, the advantages and the

²⁵The sensor yield after thinning and electrical testing was specified as $65 \pm 10\%$ for MIMOSA-26 by the supplier, which, in the meantime, has also been established for the subsequent sensor generation [102].

disadvantages of both groups of adhesives have been examined. The silicone-based glues feature good thermal conductivity and remain soft even at -20°C , which is the envisioned operation temperature of the MIMOSIS-1 sensors in the MVD. On the other hand, they feature high viscosity and the application of a uniform layer with a thickness below $200\ \mu\text{m}$ is almost impossible. A thick layer of adhesive would contribute unacceptably to the material budget of the detector and, consequently, cannot be used. The epoxy resins feature very low viscosity and can form a uniform and thin layer. However, it is difficult to find commercial off-the-shelf epoxy resins which remain soft at negative temperatures after curing. This called for the dedicated development of a radiation-hard, low-viscosity and soft epoxy resin suitable for the MVD. Since lowering the material budget is also of interest for the future LHC experiments, a common interest exists to develop a glue which combines the best properties of both groups of adhesives. This development is led by “Science and Technology Facilities Council” at the Rutherford Appleton Laboratory in the United Kingdom.

The cooling concept of the MVD, which is realized as part of the MVD Prototype, is based on the approach of conductive cooling and has been evaluated in detail both in air and at room temperature. Since the temperature difference between the heat sink and the switched off sensors has been found to be up to $\Delta T \approx 5.5\ \text{K}$, the thermal interface between CVD diamond carrier and the aluminum heat sink has to be further improved. Reducing this temperature difference is of primary importance, in particular since the MVD has to be operated inside vacuum.

During the operation of the sensors, a linear dependence of the sensor temperature with respect to the heat sink temperature has been measured. In addition, no significant temperature differences of the overall sensor temperatures have been observed in the charge-sensitive area (which is optically accessible and not covered with encapsulant) while using different sensor operation settings. The temperature gradient across the sensor’s surface has been measured to be smaller than $1\ \text{K}$. Compared to the maximal acceptable temperature gradient across the sensor’s surface of $10\ \text{K}$ [65], the measured value leaves a substantial margin for the in-vacuum operation of the MVD.

The MVD Prototype has been successfully assembled and comprehensively tested in the laboratory as well as in an in-beam test. The read-out concept has been successfully evaluated by operating the sensors integrated into the MVD Prototype and the reference planes stable and synchronous throughout the in-beam test. The reproduction of the spatial sensor resolution from the data collected during the in-beam test permits the conclusion that the integration process applied to the sensors does not deteriorate their performance, as presented in Section 5.5.3.

For the operation of the MVD at SIS100, the feasibility of several aspects, e.g., the integration of more than one sensor ladder per sensor carrier side, which could not be studied within the MVD Prototype project, will be discussed in Chapter 6.

Chapter 6

Towards the MVD at SIS100 - Discussion

The original MVD was designed guided by the physics case of identifying open charm mesons in the energy range covered by SIS300. During the process of refining the detector, the need to equip the MVD with more than two stations has emerged [29], arriving at an MVD comprising four stations.

The first station determines the secondary vertex resolution along the beam axis and should be positioned as close as possible to the target. Its material budget has to be minimal. The achieved radiation hardness of the sensors allows to install this station in a distance of 50 mm to the target. The last MVD station interfaces the tracking from the STS to the MVD. Hence, its position has to be as close as possible to the vacuum window separating the MVD and the STS, i.e., at $z = 200$ mm. The second and the third station are placed in an equidistant position between these two MVD stations, i.e., at $z = 100$ and $z = 150$ mm. The geometrical acceptance of the MVD is defined in the polar angle interval $\vartheta = [2.5^\circ, 25^\circ]$ equal to the one of the CBM experiment [26].

The start version of the MVD at SIS100 is presently the subject of new simulations with advanced detector descriptions (e.g., digitizers) and tracking algorithms. The energy coverage of SIS100 compared to the one of SIS300 suggests to appreciate the physics case of di-electrons better. This motivates an extension of the geometrical acceptance, in particular, of the MVD stations 1, 2 and 3 in order to allow tracking of the low-momentum electrons originating from conversion. For the MVD start version at SIS100, it is assumed that dedicated sensors (MIMOSIS-1) are available which meet the needed performance with respect to the granularity, the read-out speed and the radiation hardness as well as the power dissipation.

This chapter discusses the feasibility for the production of the MVD's start version, based on the more generic achievements laid down in the previous chapters. Open questions focusing on the material budget, the thermal management of the detector and the sensor integration which define the cooling concept, the support materials as well as the impact of the thermal management on the operation of the sensors will be accentuated. The assembly of the detector and its integration into CBM is evaluated as well. The goal is to develop a strategy for the start version of the MVD at SIS100, presently envisaged for the year 2020.

Material Budget

The requirement to minimize the material budget in the required polar angles of the detector as much as possible result in the selection of highly specialized materials and components for the MVD. The material budget target values are defined to be $x/X_0 = 0.3\%$ for the first MVD station and $x/X_0 = 0.5\%$ for the other MVD stations. The contribution of the material budget of each individual MVD station in the required polar angles has been simulated, see Section 4.2.2. It has been found that the individual contribution of the current materials to the averaged material budget of the individual MVD stations falls short of the given material budget target values. In addition, the construction of a detector satisfying a material budget value of $x/X_0 \sim 0.3\%$ has been proven within the MVD Prototype project, see Section 5.2.2.

- Reduction of the contribution of the MVD components to the overall material budget

The material budget contributed by the sensors cannot be reduced any further since their thickness of $50\ \mu\text{m}$ defines a rigid technological, mechanical as well as handling limit.

The reduction of the sensor carriers' contribution to the overall material budget of the first and second MVD station is technically not feasible since their thickness of $150\ \mu\text{m}$ represents what is already possible from a mechanical, a production and a handling point of view.

For a reduction of the material budget contribution of the sensor carriers of the third and the fourth MVD station, it has to be ensured that this optimization is not conducted at the expense of the thermal and mechanical properties of the carriers, especially with respect to their mechanical stiffness and their heat evacuation capability.

In case of the FPC, a reduction of the contribution to the overall material budget requires a dedicated material budget optimized design for copper-based lines or the exchange of copper lines with aluminum-based ones which is from a technological point of view more advanced.

Thermal Management

The cooling concept of the MVD is based on the approach to use highly thermal conductive materials positioned in the geometrical acceptance of the detector to evacuate the heat dissipated by the sensors, while contributing as little as possible to the material budget of each individual MVD station in this region. The cooling concept of the MVD has been presented in Section 4.1.3 and has been realized as part of the MVD Prototype, including its detailed evaluation using thermal simulations as well as measurements at ambient temperatures and in air, compare Sections 5.2.1 and 5.4.1.

The thermal management of the MVD will be reviewed in three parts: The first part deals with the evaluation of the cooling concept, the second part deals with its impact on the support materials and the third part with its impact on the sensor operation.

-
- Validation of the cooling concept in vacuum

It is of major interest to validate the performance of the cooling concept featuring the interplay of the involved materials (e.g., the sensor carrier, the glue, the heat sink and the cooling system) obtained with thermal simulations (see Section 4.1.3) using appropriate experiments in vacuum. The results of these experiments combined with the corresponding thermal simulations have to be employed to further optimize the thermal management of the MVD.

- Optimization of the thermal interfaces

The thermal interfaces are defined as the contact area of two different materials, e.g., between the sensor carriers and the heat sinks, see Figure 4.8. They have to be optimized to guarantee the smallest possible temperature gradient between the materials since the cooling power of the set-up is not unlimited. The thermal interfaces also impact on the intended sensor operation conditions with respect to the temperature gradient across the sensor's surface and the absolute temperature of the sensor.

In particular, the thermal interfaces between the sensor carriers and their dedicated heat sinks are of paramount importance. Dedicated studies have to be conducted to investigate materials which can be used to establish a reasonable thermal interface between these materials. At the same time, the mechanical properties of the material of the sensor carriers as well as the accuracy and reproducibility needed in the positioning process of the sensor carriers onto the heat sink have to be considered. A starting point for this investigation could be defined by the materials which have been studied in the framework of the PANDA luminosity monitor to provide a thermal interface between a CVD diamond carrier and an aluminum heat sink. Here, the use of a thermal compound as well as a vacuum grease resulted in the smallest temperature gradient between the two materials [69].

- Mechanical stress on the sensor carriers

The temperature difference while building, mounting and servicing the detector and the operation temperature of the sensors will be in the order of $\Delta T = 40$ K to limit the effects induced by radiation damage [51].

Therefore, the assembled quadrants have to be surveyed focusing on mechanical stress resulting from the different coefficients of thermal expansion of the integrated materials.

Additional mechanical stress could result from the fact that the sensor carrier is fixed with two sides onto the heat sink to define an optimal thermal interface and that a maximum temperature difference of $\Delta T_{\text{maximum} - \text{interface}} = 20$ K has been found in the thermal simulations on the sensor carrier of the fourth MVD station, assuming a power dissipation value of the sensors to be of a value of 0.185 W/cm².

Using the example of assembled dummy quadrants, it has to be investigated whether these effects result in a potential misalignment of the sensors with respect to each other as well as of the sensor carrier with respect to the heat sink.

- Sensor carriers

The sensor carriers define the essential part of the thermal cooling concept of the MVD but, at the same time, they majorly contribute to the material budget of the individual MVD station.

For the first and the second MVD station, the sensor carriers will be made of 150 μm thin CVD diamond.

The sensor carriers integrated into the third and the fourth MVD station will be made of carbon-based materials. The examination of the mechanical properties of bare TPG and carbon-fiber encapsulated TPG will lead to the selection of the material to be used for these sensor carriers. The main question guiding this examination is whether the carbon-fiber encapsulation around the TPG could be substituted for a different sealing material, e.g., glue or Parylene, to provide a surface which is more homogeneous than the one of bare TPG.

- Impact on the operation of the sensors

The radiation hardness requirements attributed to the sensors integrated into the MVD by the physics cases call for a sensor operation at low temperatures [51].

It is important to further decrease the energy dissipated by the sensors (e.g., $< 200 \text{ mW per cm}^2$) to guarantee the mandatory low operation temperatures for all sensors, see Section 4.1.3. This stated request is in accordance with the sensors to be developed for the upgrade of the ALICE ITS and their envisioned power dissipation [103].

The non-uniform temperature distributions for both, the absolute sensor temperature as well as the temperature gradients across the sensor's surface, which are extracted from the thermal simulations, directly correlate to the cooling of the sensor carrier from two adjacent sides, see Section 4.1.3.

Consequently, these sensor operation conditions require comprehensive studies of the sensor operation settings with respect to the temperature distributions on each sensor positioned on the individual MVD station.

Sensor Integration

The proof of principle of the double-sided integration of two ultra-thin sensors positioned next to each other has been carried out as part of the MVD Prototype project, see Section 5.3 above. It can be stated that the applied integration process combined with the developed tools is suitable for the integration of ultra-thin CMOS sensors. This can be extracted from the fact that the nominal sensor performance could be reproduced in the in-beam test, see Section 5.5. Beyond the proven integration concept, the integration of more than one ladder per carrier side, in which a ladder is made of up to four sensors, with an accuracy of better than 100 μm has to be demonstrated.

- Integration density per quadrant

The ladders to be integrated on the quadrants of the MVD stations comprise up to four

sensors in a row. The size of the area defined by the polar angles which have to be covered with charge-sensitive sensor area requires the positioning of multiple ladders on an individual sensor carrier of the MVD stations 1, 2 and 3.

- Sensor positioning and integration tools

The tools developed for the sensor integration within the MVD Prototype project (see Section 5.3.2 above) have proven to work. Their handling and the applied methods remain unchanged while their form factors will be adjusted to allow the positioning of several sensors forming the ladders.

To increase the precision of the sensor positioning within a dedicated ladder, e.g., below $O(50\ \mu\text{m})$, the sensors will be aligned using defined stops, as it is conducted in the positioning process of the sensors integrated in the PXL part of the HFT [102].

The positioning of multiple ladders on an individual sensor carrier requires the implementation of distinct positioning pins in an assembly tool comparable to the double-sided positioning- and gluing-tool, see Figure 5.11 and [102].

The distance between the sensors, which has been determined to be $63 \pm 19\ \mu\text{m}$ in case of the sensors being integrated into the reference planes, will be reduced using the so-called “butting-edges technique”. Using this technique, the first sensor will be aligned with respect to a precise mechanical stop. The other sensors required to build a dedicated ladder will be positioned with respect to and butted against the first one allowing an edge-to-edge positioning of the sensors [102].

- Metrology of the quadrants

The positions of the sensors on the individual sensor carrier have to be determined using an automated routine based on metrology. In addition, the determination of the surface planarity of the integrated sensors has to be evaluated, as it is being carried out for the PXL part of the HFT [102].

The recorded data will be used to define a precise starting point for the later alignment of the sensors within the data analysis framework of CBM.

- Glue

The task of the utilized glue is to fix the positions of the sensors on their dedicated sensor carrier as well as to establish a thermal interface between both components. Its selection has to be guided accounting for several highly specialized properties like a low viscosity, a high radiation hardness as well as softness after curing. After the selection of the glue for the MVD, extensive dispensing, gluing, temperature cycling, radiation hardness and outgassing studies have to be carried out in order to characterize its properties and to evaluate its applicability for the MVD. The reliable procedure to position and fix several sensors in their ladders on a sensor carrier has to account for the curing time and re-workability of the glue as well.

Detector Assembly and its Integration into the CBM Experiment

The assembling procedure based on a modular construction of the MVD Prototype and the reference planes has been found to be suitable for the integration of a detector comprising ultra-thin sensors.

- **Detector mock-up**

The geometry of the MVD proposed in the context of this thesis has been realized in a 1 : 1 mock-up shown in Figure E.1 in the appendix. The not yet functional components will be substituted with functional ones.

It has to be investigated, especially with regard to the operation of the real heat sinks, whether potential vibrations coupled to the detector from outside, e.g., cooling pumps, affect the stability of the positions of the individual MVD stations. In addition, the long-term stability of the mechanical design of the MVD has to be examined in detail focusing on mechanical parameters, e.g., temperature driven drifts of the integrated components, as well as on electrical parameters. The mechanical set-up of the detector has to guarantee that the spatial resolution of the sensors of below 5 μm is not washed out by potential mechanical weaknesses. This applies, in particular, to the long-term stability (e.g., over several weeks).

- **Detector supply lines**

A connection scheme for the cooling and the electronics of the MVD in vacuum has not been subject of this thesis and remains to be developed.

The development of dedicated feedthroughs for the electrical signals of the MVD has been started in the context of the preparation of the measurements in vacuum and require further optimization. Instead of gluing FPCs in flanges, a more promising way forward seems to be using small boards with FPC connectors on both sides which are glued into dedicated flanges. The challenge will be to meet the demands of the density of signal lines and accessibility of the feedthroughs, jointly.

Several issues will have to be addressed by dedicated engineering studies.

- **Remote positioning system of the MVD**

A remote positioning system for the MVD has to be established to reliably re-position the two groups of half-stations in their measuring position after having moved them away from the beam axis while the beam is tuned or focused. Providing the required precision does not necessarily have to be a feature of the system moving the MVD half-stations. The use of mechanical stops to define positions of the MVD half-stations might be an appropriate solution.

- **Front flange of the MVD vacuum vessel**

The MVD will be mounted to a dedicated front flange which will host the necessary

feedthroughs for the cooling pipes and the electrical connections, see Figure 4.14. This flange remains to be designed and requires, in addition, a more detailed description of the target and its demanded volume.

- MVD vacuum vessel

The vacuum vessel housing the MVD has to fit into the space defined between the STS and the target, see Figure 4.14 in Section 4.1.6. The MVD vacuum vessel remains to be designed and specified in further detail.

Chapter 7

Summary and Outlook

This thesis examined, and elaborated on, the mechanical integration of the MVD. The discussion was guided by the requirements derived from the open charm and di-electron physics cases of the CBM experiment. The type of sensors chosen to equip the MVD stations are CMOS Monolithic Active Pixel Sensors, which are being developed at the IPHC, Strasbourg. These sensors offer the best compatibility in terms of the required spatial resolution, radiation hardness as well as read-out speed and, at the same time, a low contribution to the material budget of an individual MVD station.

The arrangement of these sensors in the required polar angles of the MVD led to a distribution of 292 sensors on four MVD stations positioned at 50, 100, 150 and 200 mm downstream the target, inside a moderate vacuum.

The cooling concept of the MVD has to cope with the operation of the detector in vacuum which is required to reduce the multiple scattering of the produced particles between the target and the first MVD station as well as in between the other MVD stations. To evacuate the power dissipated by the sensors, the cooling concept of the MVD is based on an approach of using highly thermal conductive materials positioned in the geometrical acceptance of the detector while contributing as little as possible to the material budget of the individual MVD station in this region. Therefore, the materials to be used as sensor carriers also have to feature high radiation length. These requirements can be fulfilled by carbon-based high-performance materials such as CVD diamond and carbon-fiber encapsulated TPG which are, thus, advocated to be used as sensor carriers for the first two stations and for the last two stations of the MVD, respectively.

The thermal management of the MVD has been simulated on the level of a quadrant of the individual MVD station. The difference $T_{\text{maximum}} - T_{\text{interface}}$ between the maximum temperature found on a building block of the sensors and the temperature of the heat bath, in which the thermal interface area of the sensor carrier and its dedicated heat sink has been positioned, has been determined on the fourth MVD station to be of a value of $\Delta T \approx 40$ K for an assumed power dissipation value of the yet to be developed MIMOSIS-1 sensors of 0.35 W/cm^2 , and to be of a value of $\Delta T \approx 20$ K for a power dissipation value of 0.185 W/cm^2 .

The temperature gradients across the pixels in the direction of the rows and columns were found to be of a value of below 5 K, independent of the applied power dissipation value.

The proposed design of the MVD includes the realistic implementation of the material thicknesses of the sensors, sensor carriers, glue, heat sinks and support structures. The geometry of the MVD has been transformed from the engineering design to a format which can be used within the CBM simulation framework. In this simulation framework, test particles traversing the MVD with different ϑ -angles were used to evaluate the material budget of the individual MVD stations in the geometrical acceptance. The calculated averaged material budget values of the individual MVD stations are falling short of the corresponding material budget target values demanded by the physics cases.

Within the MVD Prototype project, several key aspects of the MVD have been evaluated, e.g., the integration process of ultra-thin MIMOSA-26 sensors into a detector, the development of dedicated sensor positioning tools, the thermal management as well as the material budget of the MVD Prototype.

The thermal management of the MVD Prototype was investigated in terms of thermal simulations and measurements which had been carried out in air but not yet in vacuum. The absolute temperature measured on the MVD Prototype sensors and the simulated absolute temperature agree within 2 K. The temperature gradient across the sensor's surface has been measured to be smaller than 1 K. Compared to the maximal acceptable temperature gradient across the sensor's surface of 10 K [65], the measured value leaves a substantial margin for the in-vacuum operation of the MVD.

The material budget of the MVD Prototype has been determined to be of a value of $x/X_0 \sim 0.3\%$ in the charge-sensitive area of the sensors. As a consequence, the feasibility of constructing a detector satisfying the material budget target value of the first MVD station has been proven.

During the concluding in-beam test of the constructed MVD Prototype and the reference planes, the nominal sensor performance parameters were successfully reproduced. Hence, there is no indication that the proposed integration process degrades sensor performance. The developed positioning tools in combination with the employed integration process are consequently well suited for the construction of a detector based on ultra-thin CMOS sensors.

Furthermore, no evidence of potential impact on the sensor performance arising from mechanical instabilities of the MVD Prototype mechanics, e.g., from temperature driven mechanical movements or from vibrations associated with the in-beam set-up (which could possibly result from the pump of the cooling system), has been found in the recorded and analyzed beam test data.

For the construction of the MVD start version to be installed at SIS100, the evaluation of the cooling concept in vacuum is of primary interest. The integration of multiple sensor ladders in a double-sided arrangement needs to be evaluated to ensure its feasibility with respect to the integration density, gluing, handling, bonding, as well as, most crucially, with respect to the required precision. These working steps have to be concluded with the in-vacuum operation of a quadrant positioned onto and thermally interfaced to a heat sink of an MVD

half-station to evaluate potential optimization steps relating to the vacuum compatibility of the assembly.

In conclusion, the feasibility of the concept for the integration of the ultra-thin sensors has successfully been proven. In addition, the cooling concept of the MVD has successfully been evaluated based on results from the MVD Prototype. The knowledge gained within the MVD Prototype project has to be applied to the construction of the MVD.

Zusammenfassung

Einführung

Die vorliegende Arbeit befasst sich mit der mechanischen Integration des Mikrovertexdetektors (MVD) des *Compressed Baryonic Matter (CBM)*-Experimentes. Die in diesem Zusammenhang entwickelten Schlüsselkonzepte für die Integration der Sensoren, das thermische Verhalten sowie das Material-Budget des Detektors werden in Hinblick auf ihre Realisierbarkeit mithilfe des im Rahmen dieser Arbeit angefertigten MVD Prototypen überprüft. Dessen Eigenschaften werden in einer abschließenden Teststrahlzeit im Detail evaluiert.

Das CBM-Experiment, das an der sich im Aufbau befindlichen Beschleuniger-Anlage FAIR in Darmstadt realisiert wird, soll das Phasendiagramm stark wechselwirkender Materie mithilfe von Schwerionenkollisionen in einem Strahl-Energiebereich von 2 bis zu 45 AGeV erforschen. Innerhalb dieses Energiebereichs werden die Eigenschaften der Kernmaterie unter extremen Bedingungen, die in der Region eines hohen baryo-chemischen Potentials bei zeitgleichen moderaten Temperaturen vorhergesagt werden, untersucht. Diese Messungen sind weitestgehend komplementär zu den Schwerionenexperimenten am LHC (CERN, Schweiz) und am RHIC (BNL, Brookhaven, USA/nicht innerhalb des *Beam Energy Scan*-Programms), die darauf abzielen, die Eigenschaften des Phasendiagrammes bei minimalem baryo-chemischem Potential und hohen Temperaturen zu untersuchen. Die hohen Strahlintensitäten an der zukünftigen Beschleunigeranlage FAIR werden es dem CBM-Experiment erstmalig ermöglichen systematische Untersuchungen von seltenen Teilchen vorzunehmen. Für die nähere Erforschung der durch die Schwerionenkollisionen erzeugten Zustände sollen hauptsächlich selten auftretende Teilchen, zum Beispiel Vektormesonen und Teilchen mit schweren (charm-)Quarks, verwendet werden.

Aufgrund ihrer hohen Masse ist die Erzeugung von charm-Quarks in dem an FAIR verfügbaren Energiebereich nur für die Anfangsphase einer jeden Schwerionenkollision möglich und vorhergesagt. Die charm-Quarks und die nach der Hadronisierungsphase des Mediums diese enthaltenen charm-tragenden Teilchen stellen dabei eine vielversprechende Observable des in der Schwerionenkollision erzeugten Mediums dar, da die charm-Quarks bis zu ihrem schwachen, d.h. im Vergleich zu den typischen Reaktionszeiten sehr späten, Zerfall den vorherrschenden Bedingungen, insbesondere dem sich verändernden und ausdehnenden sogenannten Feuerball, ausgesetzt sind.

Für die Untersuchung der Vektormesonen ist deren Zerfall innerhalb des Mediums in ein Di-Elektronen-Paar von großer Bedeutung. Aufgrund ihrer Kopplung an die elektromagne-

tische Wechselwirkung tragen diese Elektronen ein unverfälschtes Signal des Vektormesons in dichter Kernmaterie zu den Detektorstationen.

Der Nachweis der charm-tragenden Teilchen - für den das in dieser Arbeit diskutierte Konzept des MVDs optimiert wird - kann aufgrund ihrer kurzen Lebensdauer ($c \times \tau = 100$ bis $300 \mu\text{m}$) jedoch nicht direkt in den Detektorstationen erfolgen, sondern ist nur über ihre Zerfallstopologie und die daraus resultierenden Zerfallsteilchen möglich. Hierzu müssen die Spuren der Zerfallsteilchen im Detektor identifiziert sowie rekonstruiert und bis zu dem Zerfallspunkt des charm-tragenden Teilchens, dem sogenannten sekundären Zerfallsvertex, präzise verfolgt werden. Der Nachweis der Zerfallsteilchen wird dabei jedoch durch eine hohe Anzahl an Teilchen gleicher Identität erschwert, die infolge einer jeden Nukleon-Nukleon-Kollision aus Zerfällen anderer Teilchen entstehen oder direkt im Feuerball erzeugt werden und zu einem hohen Signaluntergrund beitragen.

Sowohl die charm-tragenden Teilchen als auch die Vektormesonen treten nur mit geringer Wahrscheinlichkeit in den zu untersuchenden Zerfallskanälen einer einzelnen Schwerionenkollision auf. Um eine ausreichende Messgenauigkeit der genannten Teilchen zu garantieren, werden sowohl eine hohe Strahlintensität als auch eine hohe Interaktionsrate des Teilchenstrahls mit dem *Target* benötigt.

Der Nachweis der charm-tragenden Teilchen und der Vektormesonen mithilfe ihrer Zerfallsteilchen erfordert einen hochortsauflösenden, ratenfesten, strahlenharten sowie möglichst dünnen Detektor.

Optimierung des Detektoraufbaus

Der Aufbau des Mikrovertexdetektors wird in Hinblick auf den Nachweis des sekundären Zerfallsvertex der charm-tragenden Teilchen optimiert. Dieser noch zu bauende Detektor soll aus vier Detektorstationen bestehen, die in vorgegebenen Abständen zum *Target* positioniert werden.

Die Position der ersten MVD-Station in einem Abstand von 50 mm zum *Target* resultiert aus der Anforderung des Erreichens einer - unter Berücksichtigung aller zu diskutierenden Anforderungen - maximal möglichen Auflösung des sekundären Zerfallsvertex der charm-tragenden Teilchen. Die *target*-nahe Positionierung der ersten MVD-Station muss mit der an dieser Stelle auf die zu verwendende Sensortechnologie einwirkende Strahlendosis abgewogen werden. Die voraussichtliche Strahlendosis von mehr als $10^{13} \text{ n}_{\text{eq}}/\text{cm}^2$ für nicht-ionisierende und mehr als 1 Mrad für ionisierende Strahlung in einer Distanz von 50 mm zum *Target* stimmt mit der aktuellen Strahlenhärte der zu verwendenden Sensortechnologie überein und begrenzt somit den minimalen Abstand der ersten MVD-Station zum *Target*.

Die zweite MVD-Station, die zur Bestimmung eines Vektors auf den sekundären Zerfallsvertex verwendet werden soll, wird in einem Abstand von 100 mm zum *Target* positioniert werden. Die Positionierung der dritten und vierten MVD-Station in den Abständen von 150 und 200 mm zum *Target* dient der Minimierung von potentiellen Mehrdeutigkeiten innerhalb des *Trackings* der in den Schwerionenkollisionen erzeugten Teilchen sowie, insbesondere für die Position der vierten Station, der optimalen Verbindung der im *Silicon Tracking*

System (STS) nachgewiesenen Spuren mit den Punkten, die auf den Stationen des MVDs nachgewiesen wurden.

Für das Erreichen einer optimalen Auflösung des sekundären Zerfallsvertex der charmtragenden Teilchen sowie dem präzisen Nachweis ihrer Zerfallsteilchen kommt dem Material-Budget der einzelnen MVD-Stationen eine entscheidende Bedeutung zu. Damit die nachzuweisenden Zerfallsteilchen möglichst wenig mit dem Material des Detektors selbst wechselwirken und der Einfluss der Vielfachstreuung auf die Auflösung des sekundären Zerfallsvertex beschränkt werden kann, muss das maximale Material-Budget der ersten MVD-Station auf einen Zielwert von $x/X_0 = 0,3\%$ und das für alle anderen Stationen auf einen Zielwert von $x/X_0 = 0,5\%$ begrenzt werden. Um einer weiteren Beeinträchtigung der Auflösung des sekundären Zerfallsvertex durch Vielfachstreuung in der Luft entgegenzuwirken, wird der MVD zusätzlich im Vakuum betrieben.

Durch die Optimierung der MVD-Stationen in Hinblick auf ein möglichst minimales Material-Budget wird gleichzeitig die Di-Elektronen-Spektroskopie unterstützt, da durch die Minimierung des Material-Budgets die Erzeugung von Elektronenpaaren durch Konversion im Detektormaterial verringert werden kann. Der MVD erlaubt *target*-nah insbesondere die Spuren von niederenergetischen Konversionselektronen zu identifizieren und letztlich auch zu eliminieren, wodurch deren Beitrag zum Signal der nachzuweisenden Di-Elektronen aus Vektormesonzerfällen herausgefiltert und eine Reduzierung des Signal-Untergrundes erreicht werden kann.

Die vorgenannten Anforderungen an die Sensortechnologie werden nach dem derzeitigen Forschungs- und Entwicklungsstand am besten von *Monolithic Active Pixel Sensors* (MAPS), die am IPHC in Strasbourg, Frankreich, entwickelt werden, erfüllt. Die zurzeit möglichen Auslesegeschwindigkeiten der gewählten Sensortechnologie sind insbesondere in Hinblick auf die zu erwartenden Strahlintensitäten an FAIR noch zu optimieren und somit Gegenstand aktueller Forschungsprojekte.

Die lateralen Dimensionen der einzelnen MVD-Stationen werden durch den die Akzeptanz des CBM-Experimentes und dessen Detektoren bestimmenden Polarwinkelbereich von $[2,5^\circ, 25^\circ]$, der mit aktivem Sensormaterial überdeckt werden muss, definiert. Aufgrund der Ablenkung von niederenergetischen Teilchen im Magnetfeld und deren Einfluss in der Di-Elektronen-Spektroskopie wird die geometrische Akzeptanz der hinteren MVD-Stationen in horizontaler Richtung zusätzlich vergrößert.

Der Betrieb des MVDs im Vakuum erfordert die ständige Kühlung der Sensoren, um die durch ihren Betrieb entstehende Verlustleistung aus dem Detektor abzuleiten. Die fortlaufende Kühlung der Sensoren dient zusätzlich der Minimierung des Rauschens der individuellen Pixel und der Reduzierung der Schäden, die durch die auf das Sensormaterial einwirkende Strahlung hervorgerufen werden, sowie deren Effekte.

Aufgrund der Definition eines Zielwertes für das Material-Budget der einzelnen Detektorstationen empfiehlt sich die Kombination einer aktiven Kühlung - in Form von aktiv gekühlten Aluminium-Kühlsenken, die außerhalb des Polarwinkelbereichs positioniert werden - mit hoch-wärmeleitfähigen und mit einer hohen Strahlenlänge ausgestatteten Materialien innerhalb dieses Polarwinkelbereichs. Eine mögliche aktive Kühlung der Sensoren in diesem Polarwinkelbereich ist bei der gleichzeitig notwendigen Minimierung des Material-Budgets

technologisch zwar möglich, jedoch sehr aufwendig und kostenintensiv, und wurde daher im Rahmen dieser Arbeit nicht weiter verfolgt.

Zusätzlich muss die Möglichkeit vorgesehen werden, dass die laterale Position des MVDs in Bezug auf den Abstand zum Teilchenstrahl fernsteuerbar verändert werden kann. Dies ist notwendig, um eine direkte Kollision des Teilchenstrahls mit den Sensoren des MVDs für den Fall zu vermeiden, dass der Teilchenstrahl während des Betriebs erneut optimiert oder neu fokussiert werden muss.

Charakterisierung des MVDs

Anhand der vorgenannten Kriterien wurde im Rahmen der vorliegenden Arbeit ein Konstruktionsvorschlag für den MVD entwickelt.

Das Material-Budget des MVDs

Die detailliert entwickelte Geometrie des MVDs wurde mithilfe eines speziellen Computerprogramms von einer CAD-Darstellung in eine Darstellung übertragen, die in Physiksimulationen verwendet werden kann. Mit dieser übertragenen Geometrie konnten sodann die Leistungsmerkmale des Detektors mittels Simulationen hinsichtlich des Material-Budgets eingehend untersucht werden.

Die unter Berücksichtigung von realistischen Beiträgen der verwendeten Materialien zum Material-Budget der einzelnen MVD-Stationen extrahierten und über den definierten Polarwinkelbereich der MVD-Stationen gemittelten Werte des Material-Budgets zeigen, dass die festgelegten Zielwerte des Material-Budgets der einzelnen MVD-Stationen unterboten werden konnten.

Bei einer Betrachtung des lokalen Material-Budgets der jeweiligen MVD-Station hingegen lassen sich geringfügige Überschreitungen dieser Zielwerte feststellen. Diese lokalen Überschreitungen treten vorwiegend in den Bereichen der beiden hinteren MVD-Stationen auf, in denen die Positionierung eines zweiten Auslesekaabels zur Auslese aller positionierten Sensoren erforderlich ist. Um diese Überschreitungen zu verringern und schlussendlich möglichst komplett zu vermeiden, ist eine weitere Optimierung des Auslesekaabels in Hinblick auf einen geringeren Beitrag zum Material-Budget der jeweiligen MVD-Stationen notwendig. Diese Verringerung stellt ein definiertes Ziel in derzeit durchgeführten Studien dar.

Das thermische Management des MVDs

Die erforderliche Kühlung der Sensoren wird durch die Kombination eines in dem erforderlichen Polarwinkelbereich positionierten Sensorenträgers und die außerhalb dieses Bereiches angeordneten, aktiv gekühlten Kühlsenken gewährleistet, die zusammen die Hauptbestandteile des thermischen Managements des MVDs darstellen. Um die Bildung eines belastbaren thermischen Überganges zwischen diesen Materialien zu ermöglichen, werden die Sensorenträger mithilfe einer Adapterplatte auf die Kühlsenken gepresst.

Aufgrund ihrer Positionierung in dem erforderlichen Polarwinkelbereich des Detektors müs-

sen die Sensorenträger aus Materialien bestehen, die sowohl eine hohe Wärmeleitfähigkeit als auch eine hohe Strahlenlänge und eine hohe Steifigkeit aufweisen. Diese Eigenschaften werden von spezialisierten, auf Kohlenstoff basierenden Materialien, wie z.B. *Thermal Pyrolythic Graphite* (TPG) und CVD-Diamant, erfüllt.

Die schieferartige Struktur von TPG und die daraus resultierende stark richtungsabhängige Steifigkeit und Wärmeleitfähigkeit dieses Materials führt dazu, dass die Verwendung von purem TPG als Material der Sensorenträger im MVD nicht zu empfehlen ist. Als mögliche Sensorenträger für die dritte und vierte Station werden derzeit etwaige Beschichtungen und Oberflächenvergütungen des TPGs - mit dem Hauptaugenmerk auf dessen Einfassung mit Kohlenstofffasern oder mit Parylene - auf ihre Realisierbarkeit und Beständigkeit hin untersucht.

CVD-Diamant weist hingegen alle der geforderten Eigenschaften auf. Jedoch lassen sowohl die technologischen Möglichkeiten innerhalb des Produktionsprozesses - hierbei übertreffen die Abmessungen der benötigten Sensorenträger für die dritte und vierte MVD-Station die möglichen *Wafer*-Dimensionen -, als auch wirtschaftliche Gründe eine Verwendung von CVD-Diamant nur in den ersten beiden MVD-Stationen zu.

Das thermische Verhalten der durch die Sensoren, den Kleber und die Sensorenträger gebildeten Einheit wurde für jede der MVD-Stationen mittels entsprechender Simulationen untersucht. Dabei wurde ein Schwerpunkt auf die simulierten Temperaturgradienten entlang der Anordnung der Pixel in Spalten und in Zeilen in den *Full-Size-Building*-Blöcken, aus denen die zukünftigen MIMOSIS-1 Sensoren bestehen werden, gelegt. Für zwei verschiedene Verlustleistungen dieser Sensorbausteine ($0,35 \text{ W/cm}^2$ und $0,185 \text{ W/cm}^2$) konnten die Temperaturgradienten auf einen Wert von je weniger als 5 K bestimmt werden. Auf Grundlage von Erfahrungswerten für den Betrieb der aktuell verfügbaren Sensoren liegen diese Werte in einem akzeptablen Bereich. Zusätzlich wurde die Differenz zwischen den auf den Sensorbausteinen gemessenen Maximal- und Minimaltemperaturen und der an der Kontaktfläche zwischen der Kühlsenke und dem Sensorenträger gemessenen Temperatur bestimmt. Die Kontaktfläche wurde während dieser Simulationen in einem Wärmebad mit einer definierten Temperatur von -20 °C positioniert. Im Fall der maximalen Temperatur beträgt die Differenz für eine Verlustleistung der Sensorbausteine von $0,35 \text{ W/cm}^2$ auf der ersten MVD-Station 5 K und auf der vierten Station 40 K. Diese maximale Temperaturdifferenz von 40 K auf der vierten Station unterstreicht die Notwendigkeit der Optimierung der Temperaturübergänge zwischen den integrierten Materialien sowie die Entwicklung von Sensoren, die unter Berücksichtigung der erforderlichen Leistungsmerkmale eine möglichst niedrige Verlustleistung aufweisen, damit eine ausreichende Kühlung der Sensoren auf allen MVD-Stationen gewährleistet werden kann.

Der Aufbau des MVDs

Die Dimensionen der bislang noch nicht entwickelten MIMOSIS-1 Sensoren wurden unter Berücksichtigung der erforderlichen technologischen Anforderungen, die zum Erreichen der anvisierten Leistungsmerkmale erfüllt werden müssen, bestimmt. Anschließend wurden diese Sensoren derart auf den Sensorträgern der einzelnen MVD-Stationen verteilt, dass

die geforderten Polarwinkel vollständig mit aktiven, ladungssensitiven Bereichen der Sensoren überdeckt werden. Die notwendige doppelseitige Anordnung der Sensoren auf den Sensorenträgern resultiert hierbei aus der Tatsache, dass die Sensoren aus zwei verschiedenen Bereichen bestehen. Der aktive Bereich des Sensors ist mit dedizierten zur Ladungssammlung implementierten Schaltkreisen (Pixeln und im Pixel positionierten Verstärkern) bestückt, während der nicht-aktive Bereich mit der auf dem Sensor implementierten Elektronik belegt ist und nicht zur Sammlung der in dem *epitaxial layer* der Sensoren erzeugten Ladungsträger beiträgt.

Da die in den Schwerionenkollisionen erzeugten Teilchen mit einem etwaigen Einfallswinkel auf die einzelnen MVD-Stationen treffen können, sind die auf der Vorder- und der Rückseite der Sensorenträger positionierten Sensoren so gegeneinander verschoben, dass ihre aktiven, ladungssensitiven Bereiche mit einem Wert von je 500 μm übereinander liegen. Für eine auf diese Weise erfolgte Anordnung der Sensoren auf den vier MVD-Stationen werden insgesamt mindestens 292 Sensoren benötigt, die auf die unterschiedlichen, je nach MVD-Station dimensionierten Sensorenträger zu kleben sind. Die Geometrie des MVDs erlaubt jedoch die Anzahl der Sensoren insbesondere unter größeren Polarwinkeln zu erhöhen, oder sogar Detektorstationen baugleich auszulegen. Dies wurde im Rahmen dieser Arbeit nicht weiter verfolgt, ist jedoch Gegenstand aktueller Designüberlegungen.

Die Kühlsenken werden unter Zuhilfenahme von speziell hierfür entwickelten Halterungen so positioniert, dass die einzelnen Quadranten - bestehend aus Sensoren, FPCs und Sensorenträgern - den erforderlichen Polarwinkelbereich der jeweiligen MVD-Station ausfüllen. Die vorgenannten Halterungsstrukturen werden auf gemeinsame Basisplatten montiert, um das Herausfahren der linken und rechten Seite der MVD-Halbstationen aus der unmittelbaren Nähe des Teilchenstrahls zu ermöglichen.

Das MVD Prototyp-Projekt

Im Rahmen des MVD Prototyp-Projektes wurde die Möglichkeit der Realisierung wichtiger Schlüsselkonzepte für den Aufbau und die Konstruktion des MVDs untersucht.

Der Aufbau des MVD Prototypen und der Referenzebenen

Ein Schwerpunkt lag hierbei auf der Entwicklung und der Konstruktion des MVD Prototypen, der die Realisierbarkeit der doppelseitigen Integration mithilfe von vier auf einem Sensorenträger positionierten und mit diesem verklebten Sensoren evaluierte und durch das Erreichen des Material-Budget-Zielwertes von $x/X_0 = 0,3\%$ den oben ausgeführten Anforderungen an die erste MVD-Station entsprach. Die Operation des MVD Prototypen im Vakuum und im magnetischen Feld wurde im Rahmen dieser Arbeit nicht untersucht.

Der entwickelte Integrationsprozess konnte durch mehrere einseitig, mit je zwei Sensoren bestückten Referenzebenen auf eine größere Anzahl von Sensoren angewendet werden und ermöglichte im Rahmen dieser Anzahl von Sensoren eine Aussage hinsichtlich der Effizienz der gewählten Integrationsmethoden zu treffen.

Für die Anfertigung des MVD Prototypen und der Referenzebenen wurden 50 μm dünne MIMOSA-26 Sensoren verwendet. Weitere Bestandteile des MVD Prototypen bildeten der 200 μm dünne, aus CVD-Diamant bestehende Sensorenträger sowie ein niedrig-viskoser, auf Epoxidharz basierender Kleber. Das Design der Kühlsenke des Prototypen orientierte sich an jenem der Kühlsenken des MVDs. Für die Konstruktion der Referenzebenen wurden die gleichen Bestandteile verwendet; allerdings wurden die Dimensionen der Sensorenträger verkleinert, das Material-Budget der Referenzebenen durch ein spezielles Design der Sensorenträger im ladungssensitiven Bereich des Sensors auf ein Minimum reduziert und für vier der sechs Referenzebenen Aluminium anstelle von CVD-Diamant als Sensorenträgermaterial verwendet.

Die Konstruktion des MVD Prototypen und der Referenzebenen

Die Entwicklung und Konstruktion des MVD Prototypen erlaubte die Erprobung der Handhabung und der doppelseitigen Integration von dünnen Sensoren, deren Verklebung sowie deren Betrieb. Weiterhin konnten wichtige Arbeits- und Qualitätssicherungsschritte definiert, evaluiert und etabliert werden.

Für die Integration der dünnen Sensoren wurden spezielle Positionierungs- und Klebewerkzeuge entwickelt und hergestellt. Diese ermöglichten auf Grundlage eines speziell dafür erarbeiteten und klar definierten Ablaufs verschiedener Arbeitsschritte die Integration von 18 Sensoren, von denen 12 erfolgreich in die jeweiligen Sensorebenen des MVD Prototypen und der Referenzebenen integriert werden konnten. Zum Zeitpunkt der Integration der Sensoren stand eine dedizierte *Probecard* noch nicht zur Verfügung, so dass die Sensoren vor ihrem Einbau in die jeweiligen Sensorebenen nicht elektrisch charakterisiert werden konnten. Erst nach Beendigung des Integrationsprozesses konnte mittels des Standard-Auslesesystems sodann festgestellt werden, dass von den 18 integrierten Sensoren ein Sensor nicht funktionstüchtig war. Zwei weitere Sensoren wiesen kleinere Beeinträchtigungen in ihrer Funktionalität aufgrund beschädigter Pixelreihen oder Pixelspalten auf.

Ein direkter Zusammenhang zwischen diesen Störungen der Sensoren und dem durchgeführten Integrationsprozess konnte jedoch nicht festgestellt werden. Die Anzahl der vorliegenden Einschränkungen der Funktionalität der Sensoren stimmte mit den Erwartungen (dem sogenannten *Yield*) für die verwendeten Sensoren nach Abschluss ihres Dünnungs- und Schneideprozesses überein.

Charakterisierung des MVD Prototypen

Innerhalb des Prototyp-Projektes konnte mithilfe der auf den Sensoren des MVD Prototypen durchgeführten Temperaturmessungen und den entsprechenden thermischen Simulationen die Übereinstimmung zwischen experimentellen, an der Luft und bei Raumtemperatur (nicht im Vakuum) durchgeführten Temperaturmessungen und thermischen Simulationen im Rahmen einer Messungenauigkeit von ~ 2 K bestätigt werden. Mithilfe dieser festgestellten Übereinstimmung konnten die Ergebnisse der im Rahmen des Designs des MVDs durchgeführten thermischen Simulationen bekräftigt werden.

In-beam-Performanz und Validierung

Die Eigenschaften des MVD Prototypen wurden in Hinblick auf die Effizienz der integrierten Sensoren und deren Ortsauflösung am CERN-SPS mit minimal ionisierenden Teilchen (hauptsächlich mit Pionen) untersucht. Zusätzlich wurde die Lagestabilität der verwendeten Halterungs- und Kühlungsmechanik der Sensoren innerhalb des Teilchenstrahls evaluiert.

Zunächst wurden die Sensitivitätseinstellungen der Sensoren, die deren Ansprechschwelle regulieren, für die Standardsituation optimiert. Diese Sensoreinstellungen lieferten die bekannte und zu erwartende maximale Detektionseffizienz sowie die entsprechende *Purity* der aufgenommenen Daten. Als Resultat der Verringerung der Kühlsenktemperatur, die unter anderem als Betriebsparameter des MVD Prototypen verwendet wurde, konnte eine Veränderung der Detektionseffizienz hin zu niedrigeren Werten festgestellt werden, die im Rahmen der vorgenommenen Sensitivitätseinstellungen und der bekannten Eigenschaften der Sensoren verstanden ist.

Mit den gewonnenen und analysierten Daten konnte des Weiteren die intrinsische Auflösung der Sensoren reproduziert werden. Dabei konnte ein potentieller Einfluss des angewendeten Integrationsprozesses auf die Funktionstüchtigkeit der Sensoren nicht festgestellt werden.

Schließlich konnte im Rahmen der Messkampagne die mechanische Stabilität der Halterung der Sensoren bestätigt werden, da innerhalb der gewonnenen Daten keine Indizien für ein potentielles Einkoppeln der Frequenz der Kühlmittelpumpe gefunden wurde. Es konnte jedoch eine Bewegung der Sensoren des MVD Prototypen relativ zu den rekonstruierten Referenzspuren von 3 nm pro Minute festgestellt werden. Dieser Wert zeigt zum einen die Sensitivität der Spurvermessung mit den Referenzebenen, deutet zum anderen aber auch auf die Notwendigkeit einer maximalen Stabilisierung der Betriebsparameter hin. Der Ursprung dieser Bewegung der Sensoren konnte noch nicht abschließend geklärt werden, wobei etwaige Temperatureffekte nicht auszuschließen sind.

Abschließend lässt sich feststellen, dass mithilfe des MVD Prototypen die Evaluierung der Realisierbarkeit wichtiger Materialien, Bestandteile und Arbeitsschritte für die Konstruktion des MVDs erfolgreich durchgeführt werden konnte.

Ausblick auf die Operation des MVDs am SIS100

In Hinblick auf die Operation des MVDs am SIS100 wurden das Material-Budget, die notwendige thermische Auslegung des Detektors für die optimalen Operationsbedingungen der Sensoren, der Integrationsprozess der Sensoren in einem größeren Maßstab und der Aufbau des vollständigen MVDs sowie dessen Einbindung in das CBM-Experiment evaluiert.

Schlussfolgerung

Die im Rahmen der vorliegenden Arbeit entwickelte Geometrie des Mikrovertexdetektors stellt zusammen mit den innerhalb des MVD Prototyp-Projektes erlangten Erkenntnissen

wichtige Bausteine für die Konstruktion des MVDs und für dessen Operation am SIS100 dar und bildet eine wichtige Basis zur erfolgreichen Umsetzung der hier erarbeiteten Schlüsselkonzepte. Dabei sind insbesondere die erfolgreiche doppelseitige Integration der dünnen Sensoren, die Evaluierung des thermischen Verhaltens des MVD Prototypen sowie das Erreichen des anvisierten Material-Budgets hervorzuheben.

Appendix A

Physics Case

A.1 Observables

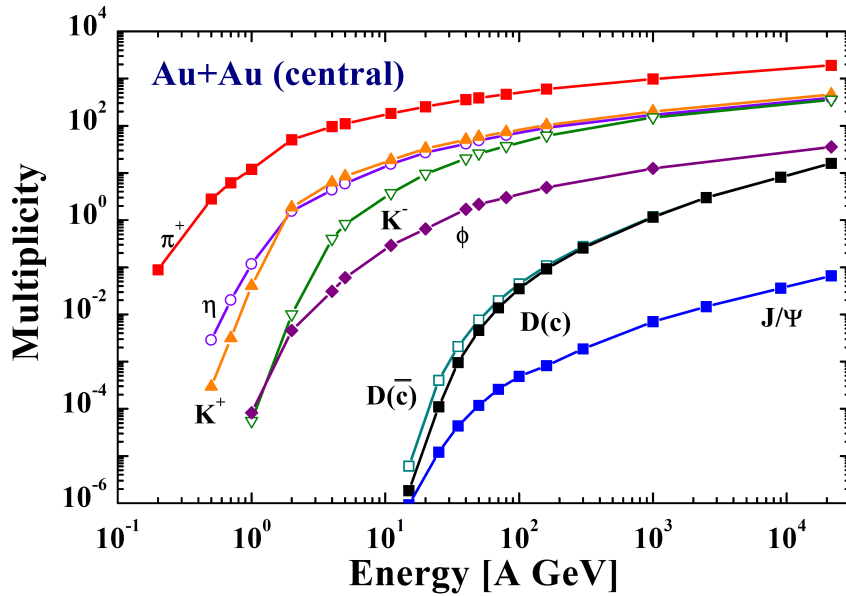


Figure A.1: The particle multiplicity for a central Au+Au collision as function of the energy as predicted by the HSD approach. The above shown calculations do not include in-medium modifications of the spectral functions but incorporate elastic and inelastic reactions. The slopes represent the multiplicities for π^+ , η , K^+ , K^- , ϕ , D , and \bar{D} as well as J/Ψ . The graphical representation is taken from [15].

Selection of D -meson signal candidates				
Cut name	Description	Cut range	Suppression [%] in	
			Background	Signal
vt_z	1	$< 850 \mu\text{m}$	23.3	1.5
χ^2	2	$> 1.6 \sigma$	99.8	27
D -meson impact parameter	3	$< 1 \mu\text{m}$		
Sum of the signal cuts			99.82	27.6

Table A.1: Selection criteria for D -meson signal candidates. The cuts are applied as follows: Cut 1: the distance between the D -meson decay particles and the primary vertex projected onto the beam axis; cut 2: the distance of the closest approach between the reconstructed vertex to the track triplet of the particles divided by the extrapolation of the uncertainties of the tracks; cut 3: the impact parameter of the momentum vector of the triplet to the primary vertex has to be smaller than $1 \mu\text{m}$. The numbers are taken from [16].

Background suppression strategy for the D -mesons				
Cut name	Description	Cut range	Suppression [%] in	
			Background	Signal
Momentum	momentum of D -meson larger	$p < 1.2 \text{ GeV}/c$	36.5	12.4
Transverse momentum	momentum of D -meson larger	$p_t < 0.3 \text{ GeV}/c$	58.5	21.5
χ^2_{prim}	uncertainty of the tracks	$< 5 \sigma$	94.3	52.8
Sum of cut 1 – 3			98	59
maximum impact parameter	cuts on secondaries from long-lived particles	$> 0.08 \text{ cm}$	66.8	11.7
$Z_{Y=0}$	cuts on secondaries of strange particles	$> 1 \text{ cm}$	30	5.6
Sum of cut 4 + 5			72.7	14

Table A.2: Background suppression strategy for the open charm simulation. The first two rows are assigned to a “pre-selection of track candidates”. The third, fourth and fifth rows are attributed to “topological cuts”. The first three cuts are summed up and based on this result, the cuts listed in the fourth and fifth row are applied. The background of unphysical signals could be rejected by 98% and additional 72.7%, while the signal has been lowered by 59% and 14%, respectively. The numbers are taken from [16].

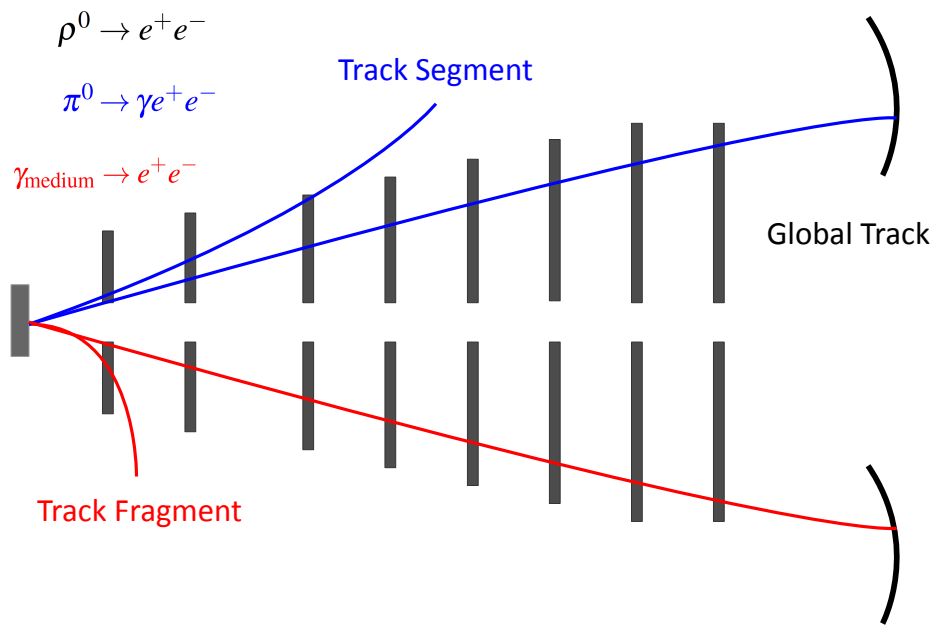


Figure A.2: The naming convention for the tracks of the e^+e^- -pairs: Tracks which have not been reconstructed and for which only single hits have been found in the MVD are defined as “Track Fragment”; reconstructed tracks which have been assigned momentum and charge information are called “Track Segment”; a track which has been identified as electron is defined as “Global Track”. The blue lines represent the tracks originating from π^0 -Dalitz decays, the red lines symbolize tracks from γ -conversion. The black vertical lines sketch the detector stations of MVD and STS, the black curved lines correspond to the RICH detector. The sketch is taken from [19].

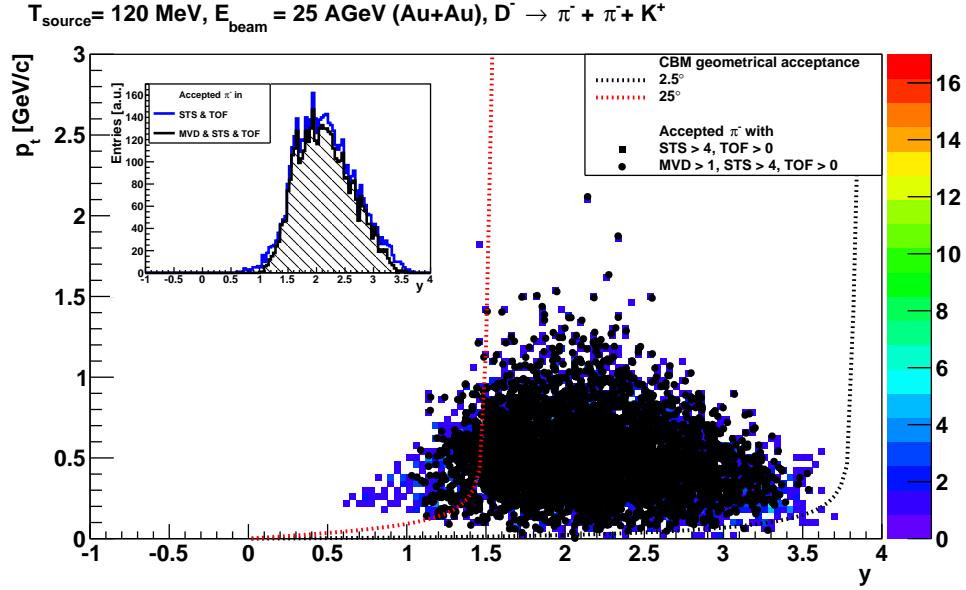
Background suppression strategy for mesons decaying in e^+e^-			
Cut name	Description	Cut range	Background suppression in [%]
Conversion pair	1	$m < 25 \text{ MeV}/c^2$	20
Hit topology	2	$d_{\text{max}} < 0.4 \text{ cm} /$ $p < 1.2 \text{ GeV}/c$	25
Track topology	3	$\theta_{e^\pm, \text{rec}} < 2^\circ /$ $p < 2 \text{ GeV}/c$	10 survive
Transverse momentum	4	$p_t < 0.2 \text{ GeV}/c$	3 – 10
Pair opening angle	5	$\theta_{1,2} \leq 2^\circ$	< 1
π^0 -Dalitz decay	6	$m_{\text{inv}} < 0.2 \text{ GeV}/c^2$	

Table A.3: Background suppression strategy for mesons decaying in e^+e^- . The cuts are applied as follows:

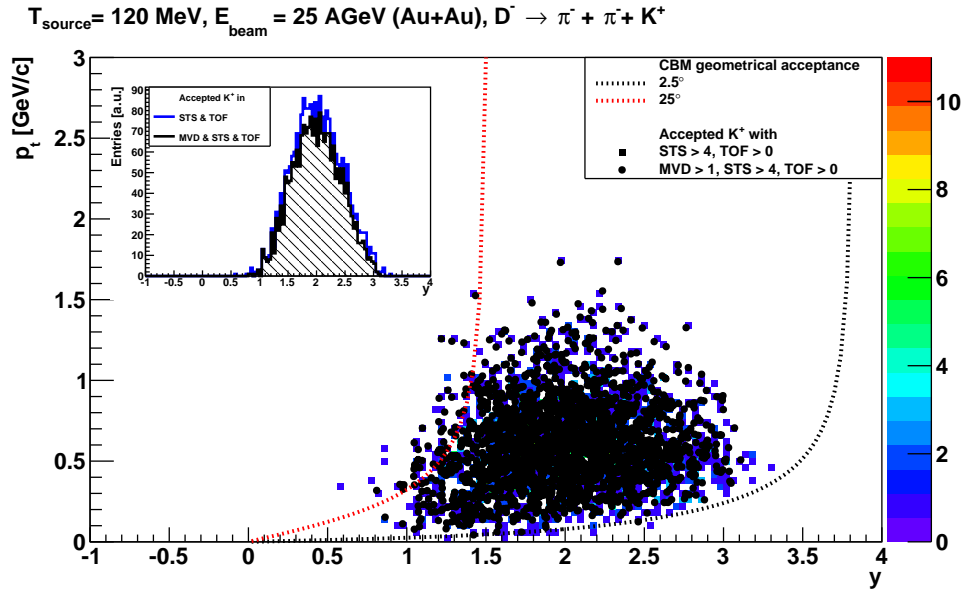
Cut 1: on the contribution of conversion pairs from γ s; *cut 2:* on the distance between the e^+e^- -pairs and additionally on the momentum; *cut 3:* on the opening angle of an identified electron track to its closest neighbor “Track Segment”, see Figure A.2, and the product of the electron momentum with the momentum of the “Track Segment”; *cut 4:* on the transverse momentum of identified leptons; *cut 5:* on the opening angle between an electron-positron pair; *cut 6:* on pairs resulting from the π^0 -Dalitz decay reconstruction. The numbers are taken from [19].

Appendix B

Requirements for the MVD Design

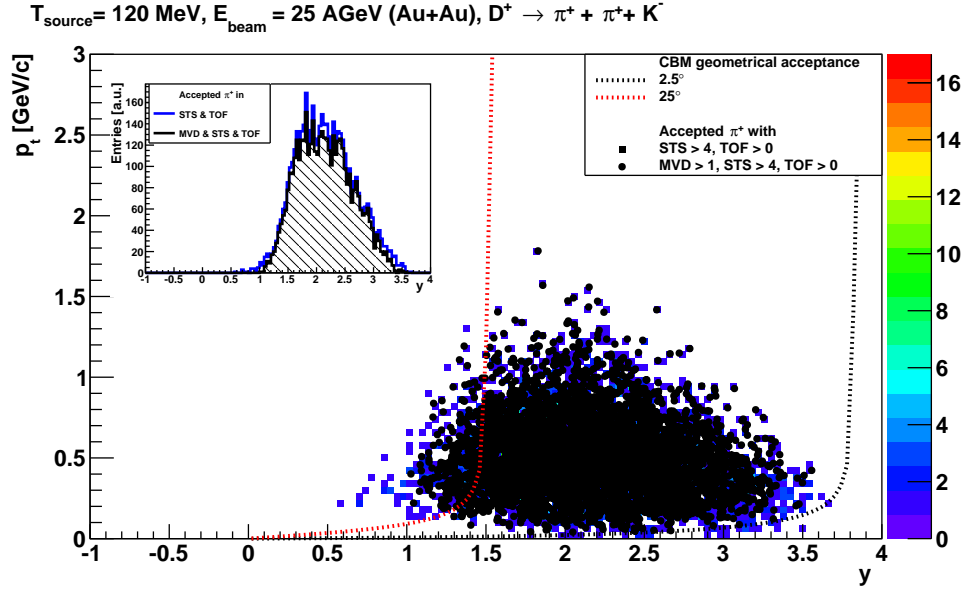


(a) P_t - y -distributions of π^- s decaying from 10.000 D^- -mesons. Colored: 4748 pions which are geometrically accepted in STS (more than 4 hits) and TOF (minimum 1 hit). Black: 4138 pions requiring additionally more than 1 hit in any 2 MVD stations. To be accepted, the same criteria have to be fulfilled for the K^+ . The inlay depicts the corresponding y -distributions.

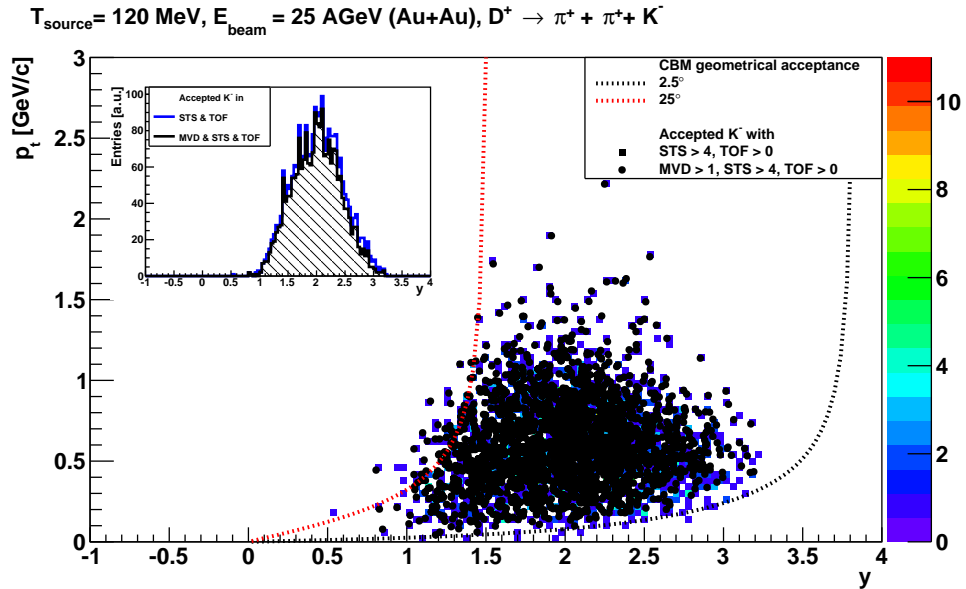


(b) P_t - y -distributions of K^+ decaying from 10.000 D^- -mesons. Colored: 2374 kaons which are geometrically accepted in STS (more than 4 hits) and ToF (minimum 1 hit). Black: 2069 kaons requiring additionally more than 1 hit in any 2 MVD stations. To be accepted, the same criteria have to be fulfilled for the π^- s. The inlay depicts the corresponding y -distributions.

Figure B.1: P_t - y -distributions of accepted π^- s (a) and K^+ (b) originating from D^- decays assuming a thermal source with $T = 120 \text{ MeV}$, at $E_{\text{beam}} = 25 \text{ AGeV}$.

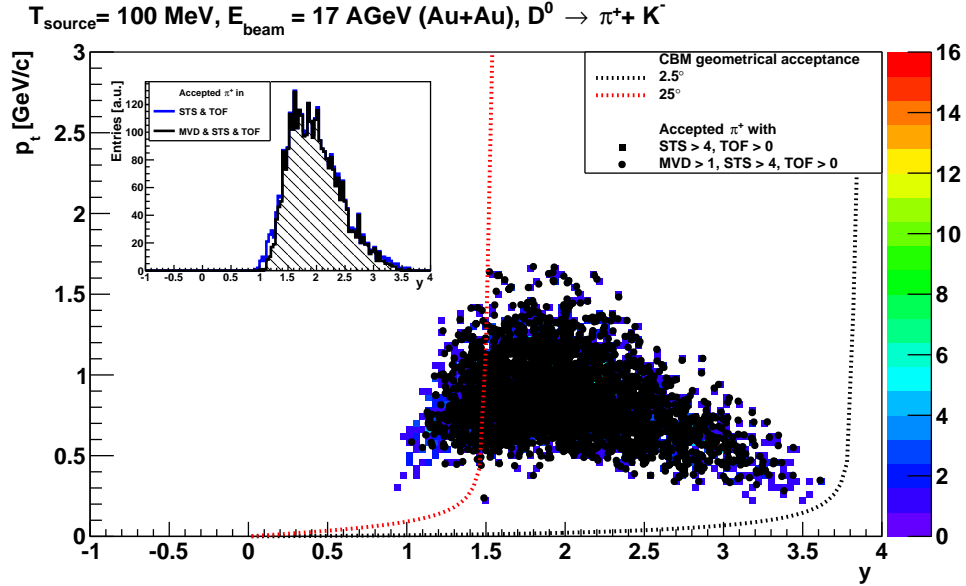


(a) P_t - y -distributions of π^+ s decaying from 10.000 D^+ -mesons. Colored: 4860 pions which are geometrically accepted in STS (more than 4 hits) and TOF (minimum 1 hit). Black: 4312 pions requiring additionally more than 1 hit in any 2 MVD stations. To be accepted, the same criteria have to be fulfilled for the K^- . The inlay depicts the corresponding y -distributions.

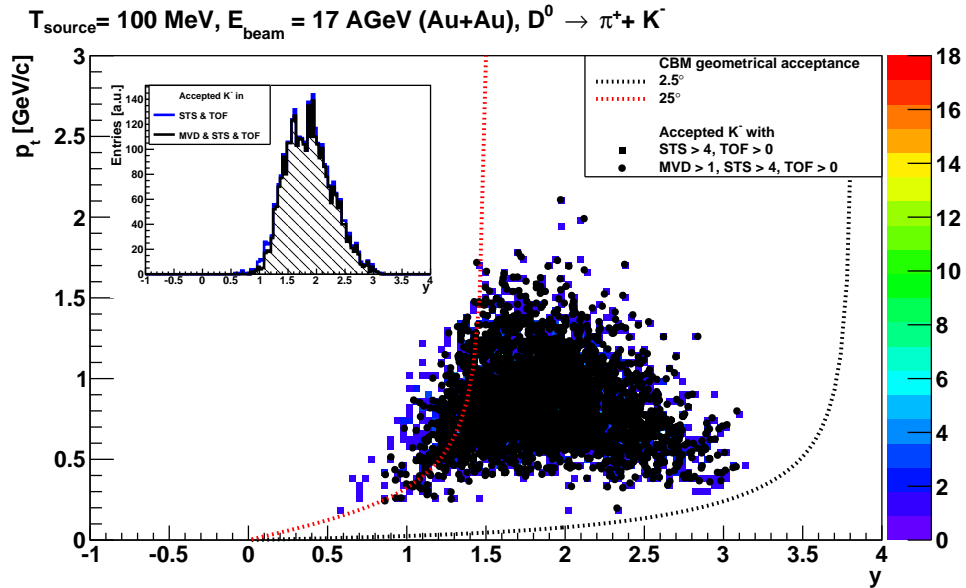


(b) P_t - y -distributions of K^- decaying from 10.000 D^+ -mesons. Colored: 2430 kaons which are geometrically accepted in STS (more than 4 hits) and ToF (minimum 1 hit). Black: 2156 kaons requiring additionally more than 1 hit in any 2 MVD stations. To be accepted, the same criteria have to be fulfilled for the π^+ s. The inlay depicts the corresponding y -distributions.

Figure B.2: P_t - y -distributions of accepted π^+ s (a) and K^- (b) originating from D^+ decays assuming a thermal source with $T = 120 \text{ MeV}$, at $E_{\text{beam}} = 25 \text{ AGeV}$.

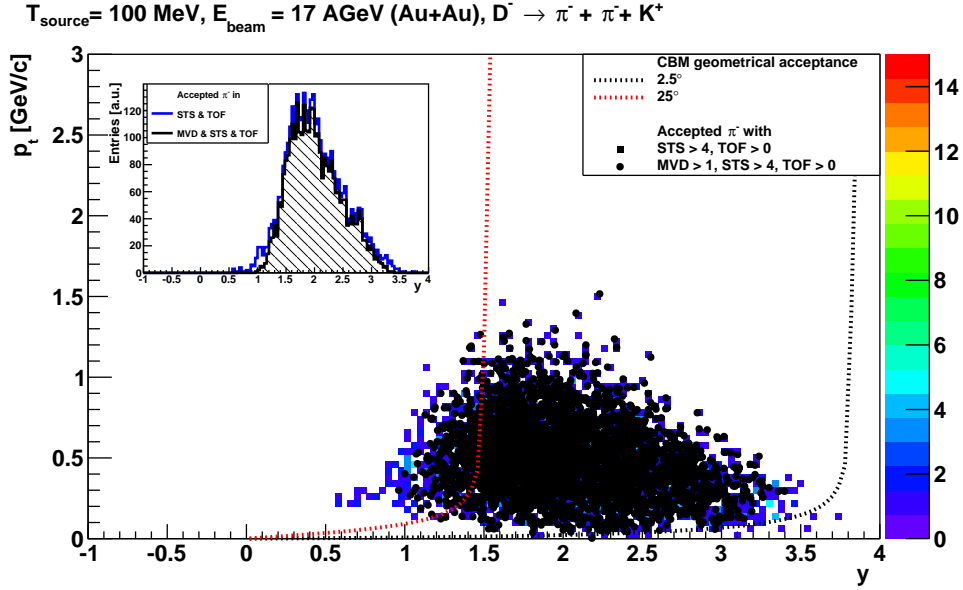


(a) P_t - y -distributions of π^+ decaying from 10.000 D^0 -mesons. Colored: 3265 pions which are geometrically accepted in STS (more than 4 hits) and TOF (minimum 1 hit). Black: 3101 pions requiring additionally more than 1 hit in any 2 MVD stations. To be accepted, the same criteria have to be fulfilled for the K^- . The inlay depicts the corresponding y -distributions.

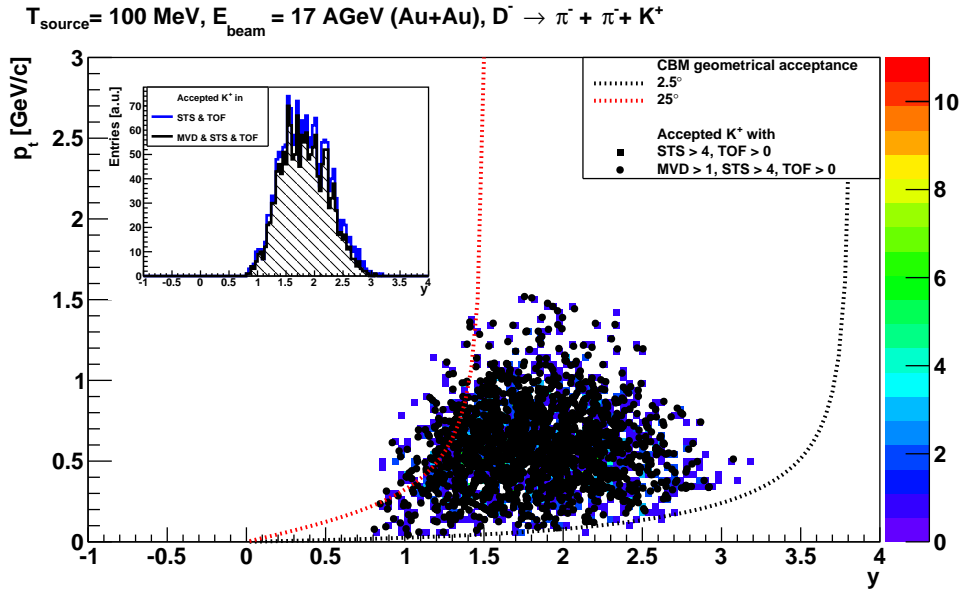


(b) P_t - y -distributions of K^- decaying from 10.000 D^0 -mesons. Colored: 3265 kaons which are geometrically accepted in STS (more than 4 hits) and ToF (minimum 1 hit). Black: 3101 kaons requiring additionally more than 1 hit in any 2 MVD stations. To be accepted, the same criteria have to be fulfilled for the π^+ . The inlay depicts the corresponding y -distributions.

Figure B.3: P_t - y -distributions of accepted π^+ (a) and K^- (b) originating from D^0 decays assuming a thermal source with $T = 100 \text{ MeV}$, at $E_{\text{beam}} = 17 \text{ AGeV}$.

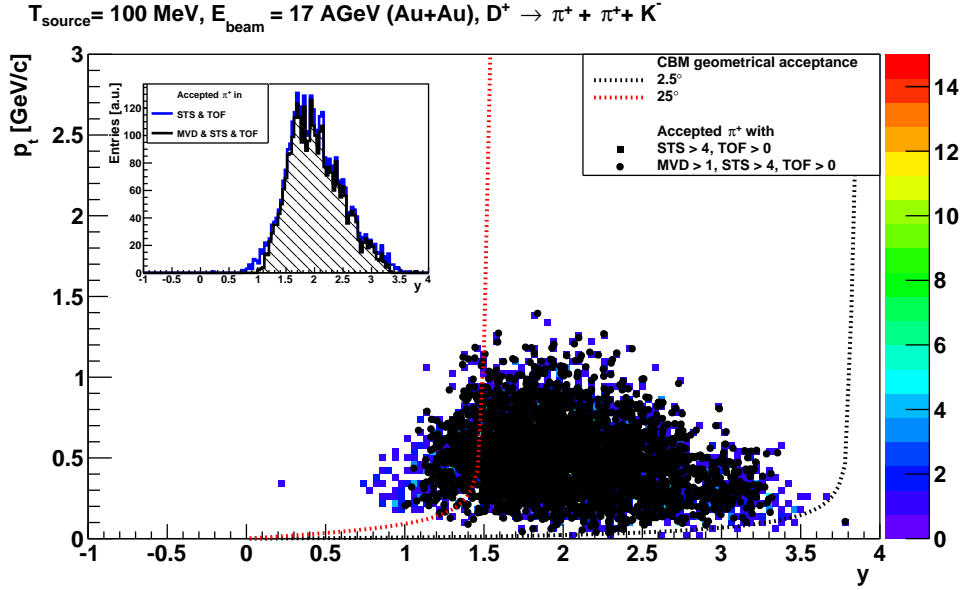


(a) P_t - y -distributions of π^- s decaying from 10.000 D^- -mesons. Colored: 3620 pions which are geometrically accepted in STS (more than 4 hits) and TOF (minimum 1 hit). Black: 3160 pions requiring additionally more than 1 hit in any 2 MVD stations. To be accepted, the same criteria have to be fulfilled for the K^+ . The inlay depicts the corresponding y -distributions.

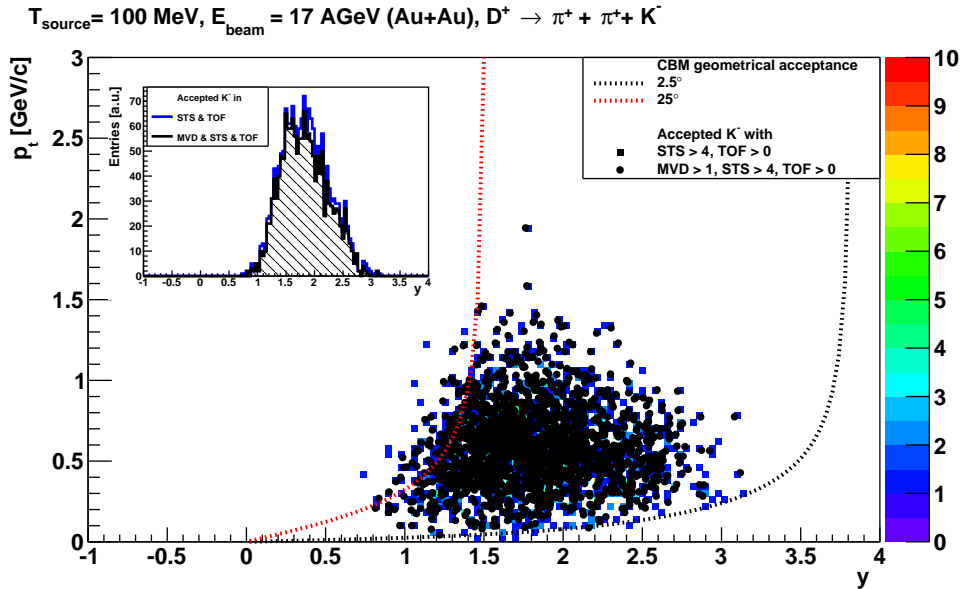


(b) P_t - y -distributions of K^+ decaying from 10.000 D^- -mesons. Colored: 1810 kaons which are geometrically accepted in STS (more than 4 hits) and ToF (minimum 1 hit). Black: 1580 kaons requiring additionally more than 1 hit in any 2 MVD stations. To be accepted, the same criteria have to be fulfilled for the π^- s. The inlay depicts the corresponding y -distributions.

Figure B.4: P_t - y -distributions of accepted π^- s (a) and K^+ (b) originating from D^- decays assuming a thermal source with $T = 100 \text{ MeV}$, at $E_{\text{beam}} = 17 \text{ AGeV}$.

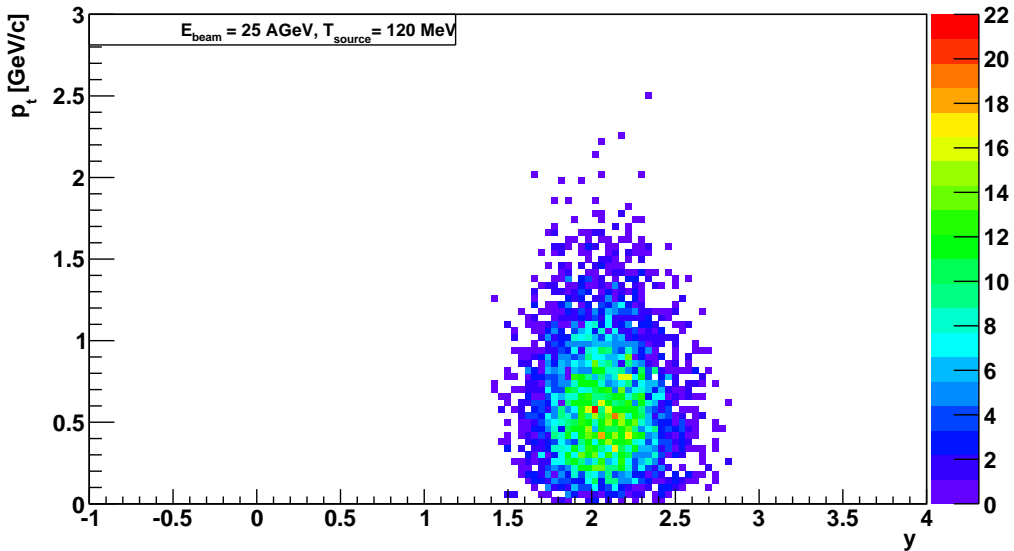


(a) P_t - y -distributions of π^+ s decaying from 10.000 D^+ -mesons. Colored: 3500 pions which are geometrically accepted in STS (more than 4 hits) and TOF (minimum 1 hit). Black: 3126 pions requiring additionally more than 1 hit in any 2 MVD stations. To be accepted, the same criteria have to be fulfilled for the K^- . The inlay depicts the corresponding y -distributions.

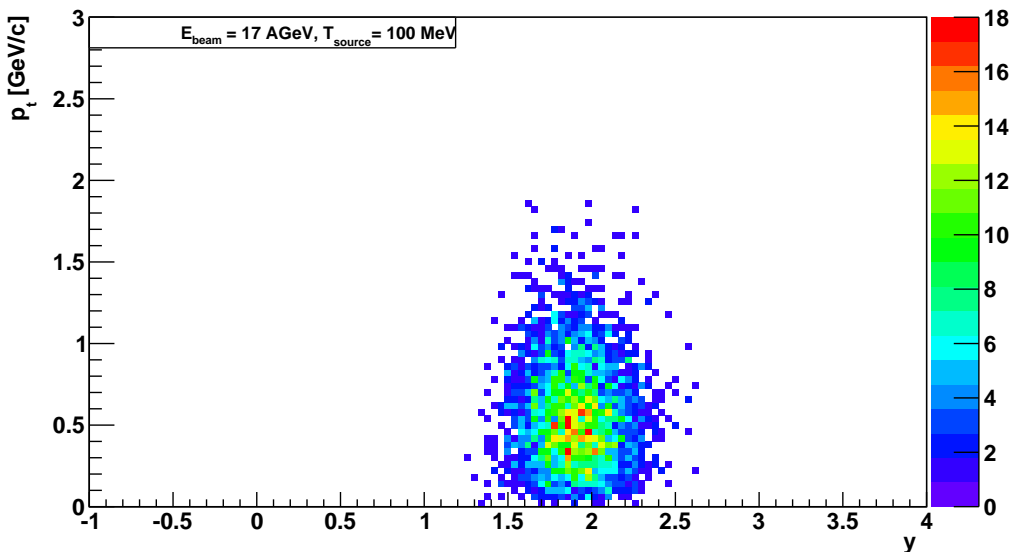


(b) P_t - y -distributions of K^- decaying from 10.000 D^+ -mesons. Colored: 1750 kaons which are geometrically accepted in STS (more than 4 hits) and ToF (minimum 1 hit). Black: 1563 kaons requiring additionally more than 1 hit in any 2 MVD stations. To be accepted, the same criteria have to be fulfilled for the π^+ s. The inlay depicts the corresponding y -distributions.

Figure B.5: P_t - y -distributions of accepted π^+ s (a) and K^- (b) originating from D^+ decays assuming a thermal source with $T = 100 \text{ MeV}$, at $E_{\text{beam}} = 17 \text{ AGeV}$.

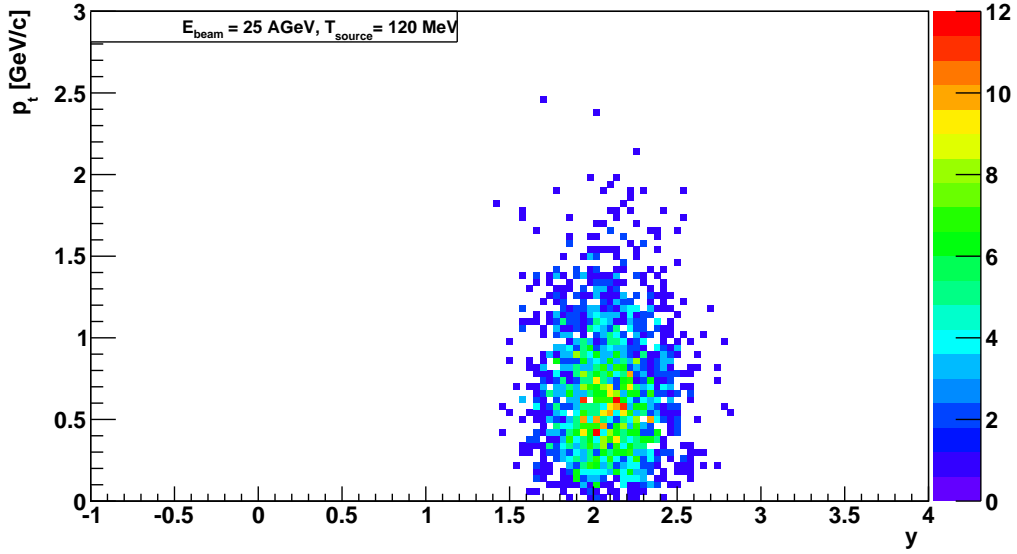


(a) P_{t-y} -distributions of D^0 s for which the decay particles have been accepted assuming a thermal source with the properties of $E_{\text{beam}} = 25$ AGeV and $T = 120$ MeV.

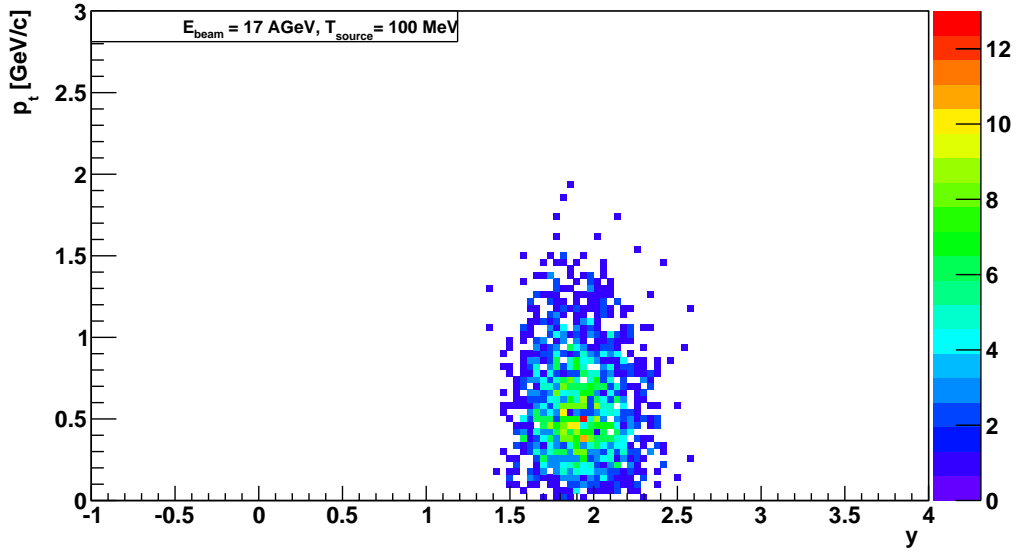


(b) P_{t-y} -distributions of D^0 s for which the decay particles have been accepted assuming a thermal source with the properties of $E_{\text{beam}} = 17$ AGeV and $T = 100$ MeV.

Figure B.6: P_{t-y} -distributions of D^0 s for which the decay particles have been accepted. The criterion required for the decay particles to be accepted is defined as more than 1 hits in any 2 MVD stations, more than 4 hits in the STS and minimum 1 hit in the TOF. The standard magnetic field has been applied but no particle tracking. Mid-rapidity is located at $y = 1.987$ for $E_{\text{beam}} = 25$ AGeV and at $y = 1.794$ for $E_{\text{beam}} = 17$ AGeV.

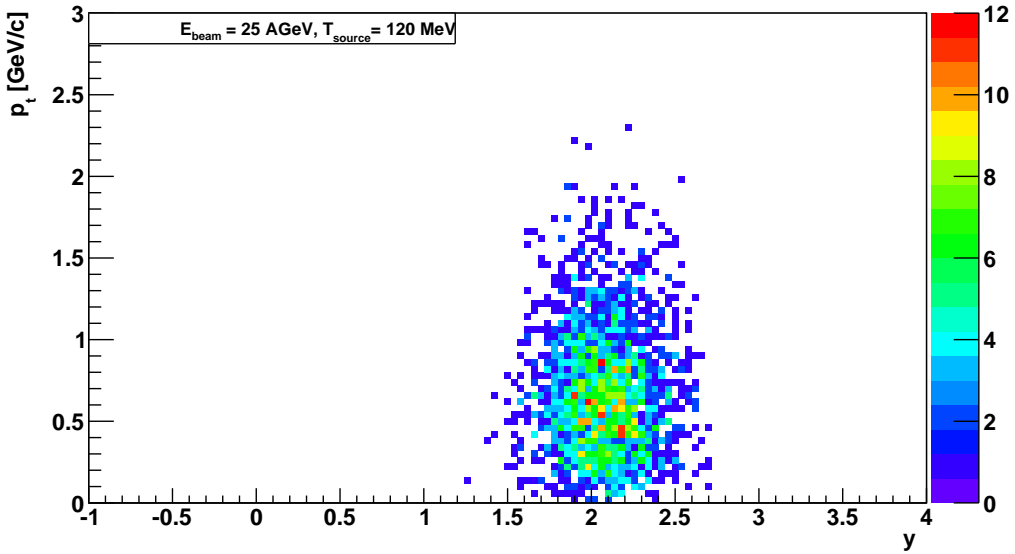


(a) P_t - y -distributions of D^- s for which the decay particles have been accepted assuming a thermal source with the properties of $E_{\text{beam}} = 25$ AGeV and $T = 120$ MeV.

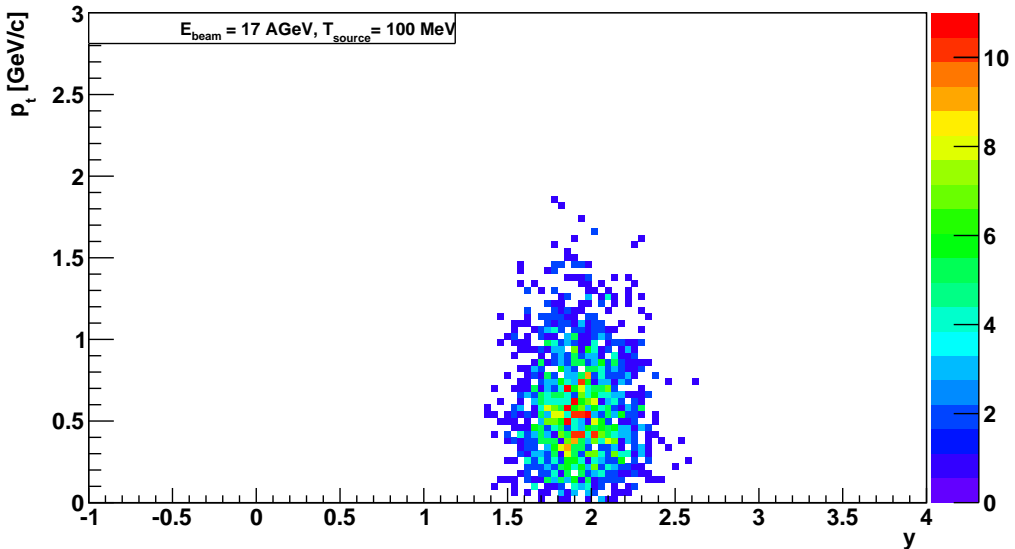


(b) P_t - y -distributions of D^- s for which the decay particles have been accepted assuming a thermal source with the properties of $E_{\text{beam}} = 17$ AGeV and $T = 100$ MeV.

Figure B.7: P_t - y -distributions of D^- s for which the decay particles have been accepted. The criterion required for the decay particles to be accepted is defined as more than 1 hits in any 2 MVD stations, more than 4 hits in the STS and minimum 1 hit in the TOF. The standard magnetic field has been applied but no particle tracking. Mid-rapidity is located at $y = 1.987$ for $E_{\text{beam}} = 25$ AGeV and at $y = 1.794$ for $E_{\text{beam}} = 17$ AGeV.

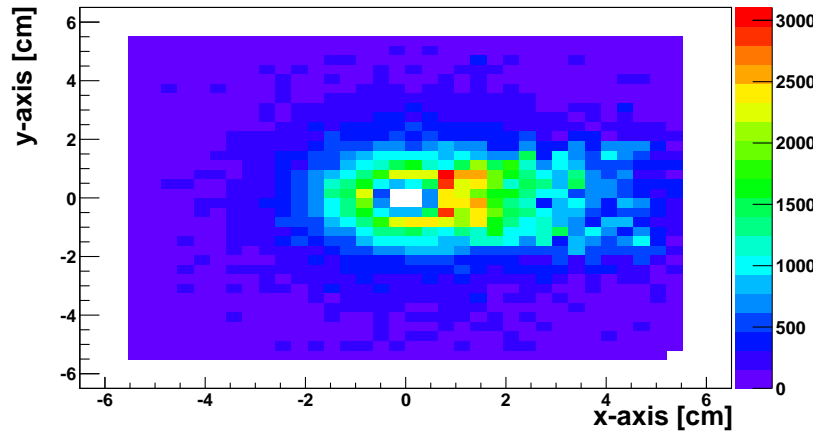


(a) P_t - y -distributions of D^+ s for which the decay particles have been accepted assuming a thermal source with the properties of $E_{\text{beam}} = 25$ AGeV and $T = 120$ MeV.

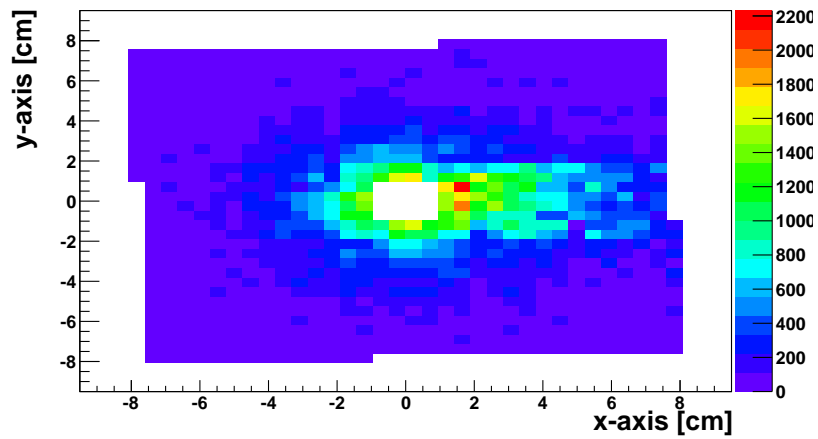


(b) P_t - y -distributions of D^+ s for which the decay particles have been accepted assuming a thermal source with the properties of $E_{\text{beam}} = 17$ AGeV and $T = 100$ MeV.

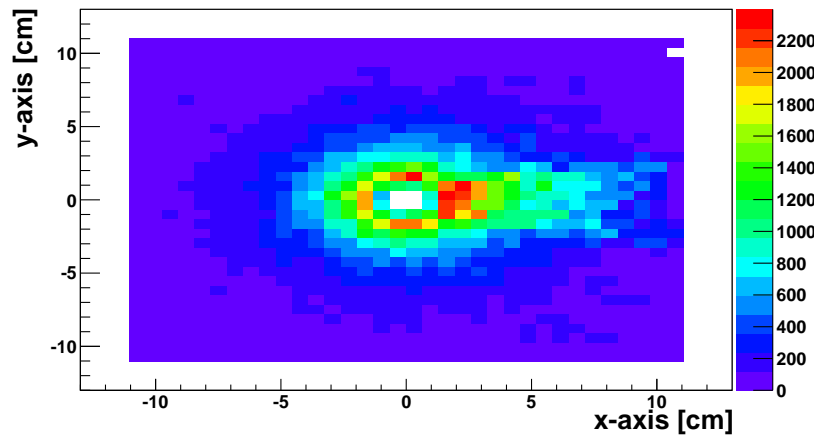
Figure B.8: P_t - y -distributions of D^+ s for which the decay particles have been accepted. The criterion required for the decay particles to be accepted is defined as more than 1 hits in any 2 MVD stations, more than 4 hits in the STS and minimum 1 hit in the TOF. The standard magnetic field has been applied but no particle tracking. Mid-rapidity is located at $y = 1.987$ for $E_{\text{beam}} = 25$ AGeV and at $y = 1.794$ for $E_{\text{beam}} = 17$ AGeV.



(a) Occupancy distribution on the second MVD station.



(b) Occupancy distribution on the third MVD station.



(c) Occupancy distribution on the fourth MVD station.

Figure B.9: Occupancy distribution on the first MVD station. For the distribution, 100 events with a beam collision energy of 25 AGeV have been averaged together with a pile-up of 3 and a number of 100 δ -electrons per pile-up.

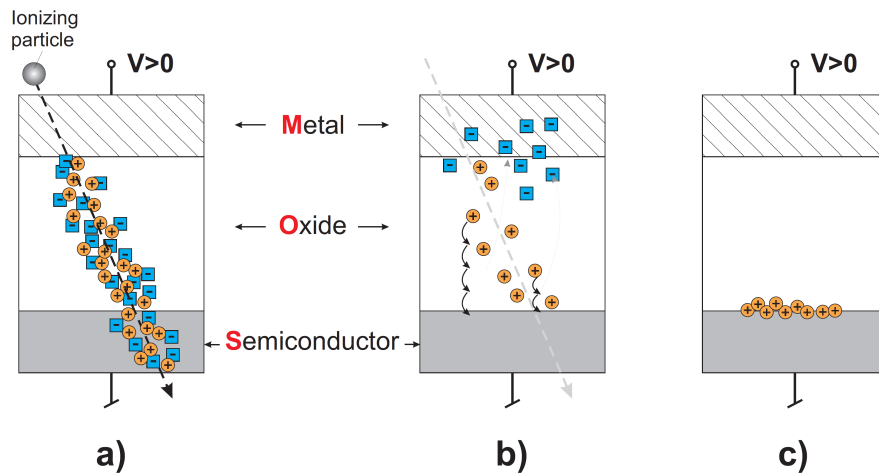


Figure B.10: Creation of the ionizing radiation damage in the sensors. a) The electron-hole pairs are created in the SiO_2 by an impinging particle. b) The electrons and holes drift in the oxide in the presence of an electric field. c) The holes are trapped at the $\text{Si} - \text{SiO}_2$ interface. The figure is taken from [39].

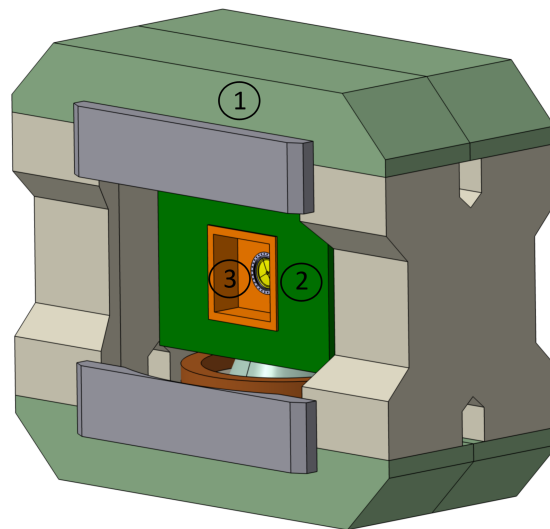
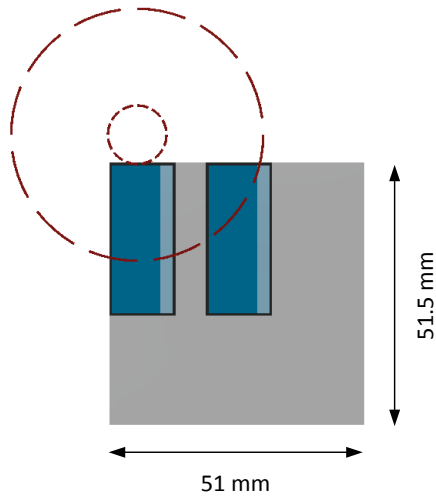


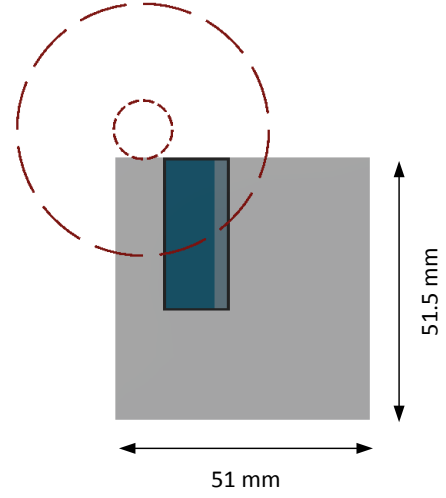
Figure B.11: The space available for the MVD inside the CBM magnet. The magnet (1) surrounds the STS in its thermal enclosure (green, (2)). The width of the inner gap of the magnet measures $1400 \times 2500 \text{ mm}^2$, [22]. The MVD has to be positioned inside the volume which is defined by the orange walls (3). The figure is taken from [22].

Appendix C

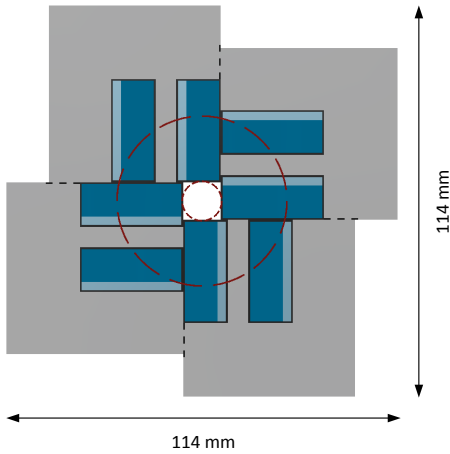
Design Proposal of the MVD



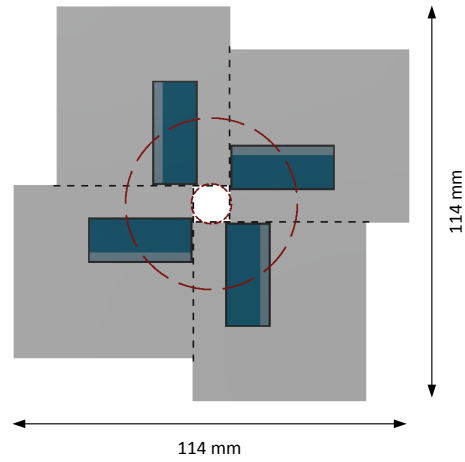
(a) Polar angle interval (dashed circles) of the first MVD station and the two MIMOSIS-1 positioned on the front side of one quadrant.



(b) The third MIMOSIS-1 positioned on the back side of the quadrant.



(c) All sensors on the front side of the first MVD station.



(d) All sensors on the back side of the first MVD station.

Figure C.1: The vertical sensor arrangement on the first MVD station. The sensors are depicted in dark blue for the charge-sensitive and light blue for the non-sensitive sensor area on the front side. From the sensors on the back side of the station, the charge-sensitive area is visible in a darker blue. The polar angle interval to be covered is indicated with red dashed circles, while the sensor carrier is indicated with light grey. To visualize the dimensions of the sensors, a black frame has been applied to them. The dashed lines indicate the dimensions of the quadrants and the sensor carriers.

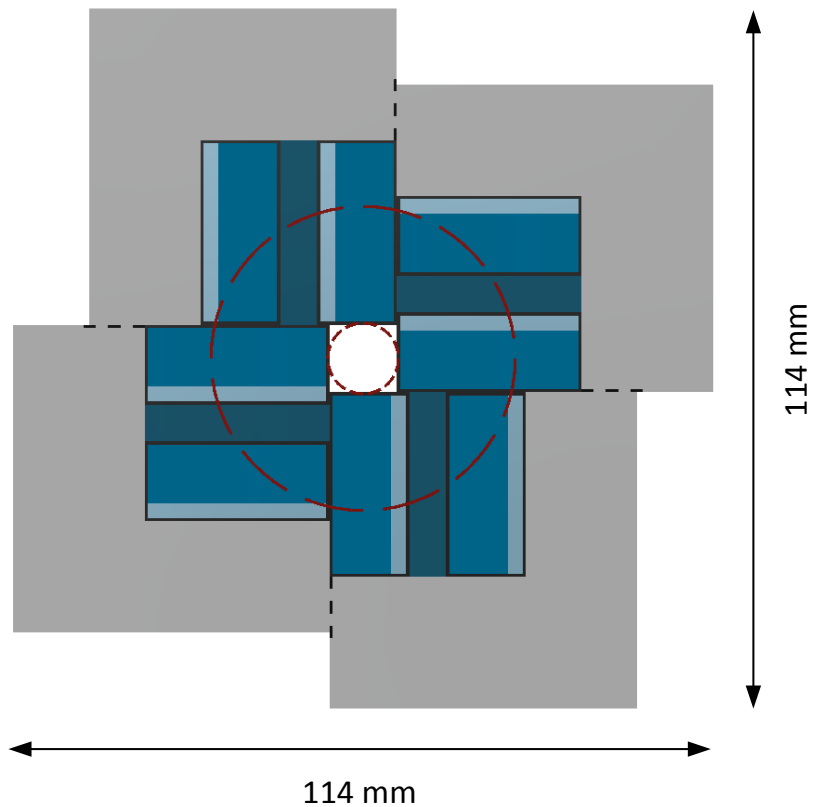
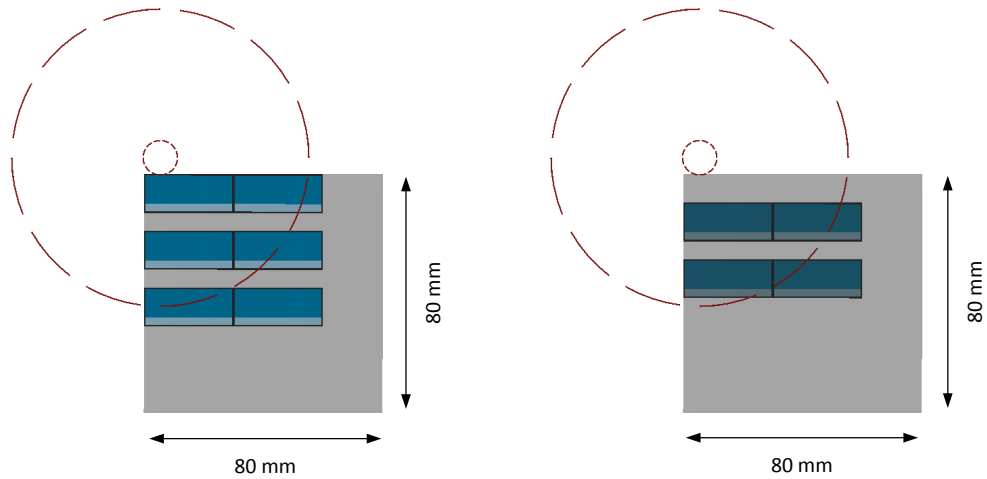
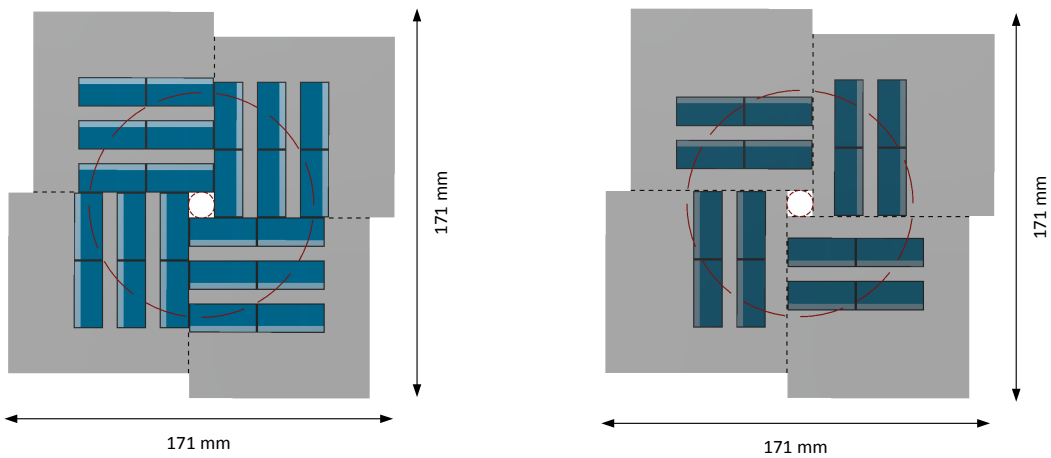


Figure C.2: The first MVD station positioned at 50 mm downstream the target using a vertical sensor arrangement. The sensors are depicted in dark blue for the charge-sensitive and light blue for the non-sensitive sensor area on the front side. From the sensors on the back side of the station, the charge-sensitive area is visible in a darker blue. The polar angle interval to be covered is indicated with red dashed circles, while the sensor carrier is indicated with light grey. To visualize the dimensions of the sensors, a black frame has been applied to them. The dashed lines indicate the dimensions of the quadrants and the sensor carriers.



(a) Polar angle interval (dashed circles) of the second MVD station and the MIMOSIS-1 positioned on the front side of one quadrant.

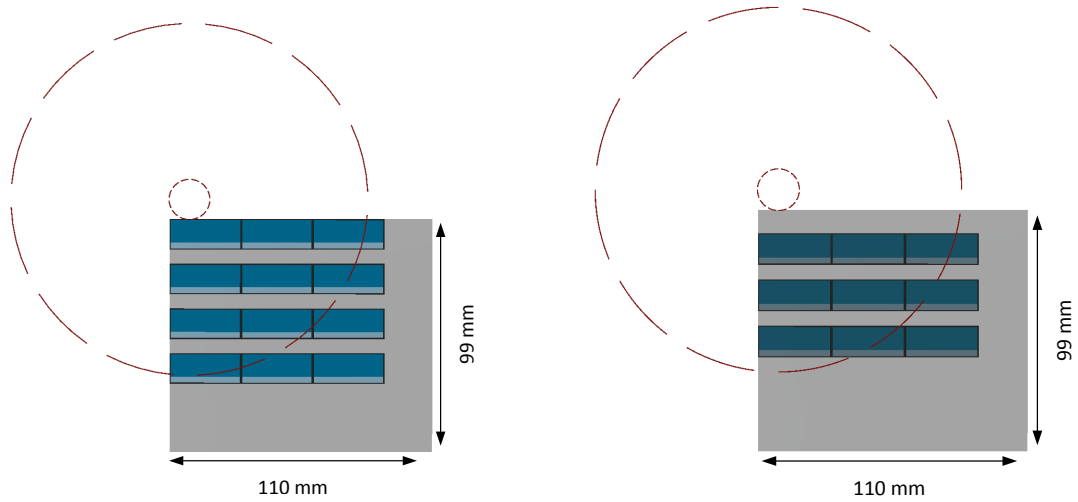
(b) The MIMOSIS-1 positioned on the back side of the quadrant.



(c) All sensors on the front side of the second MVD station.

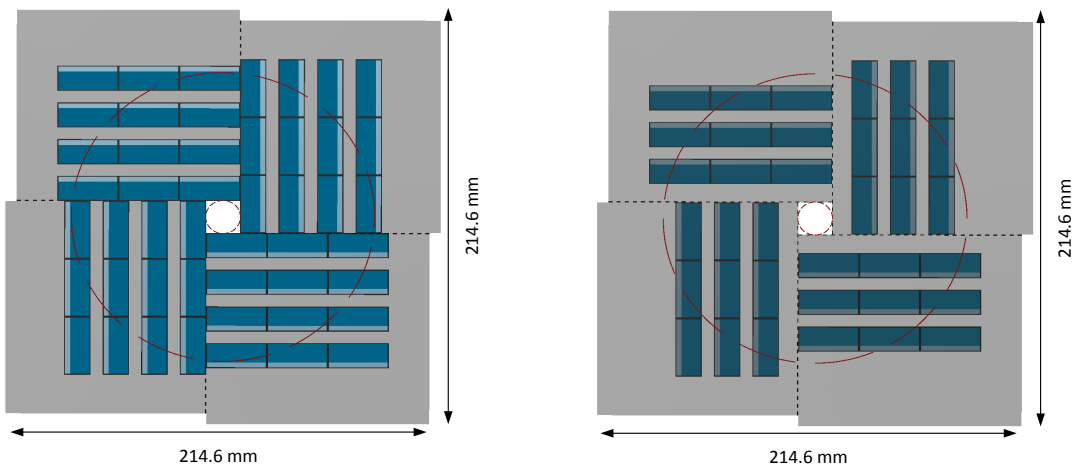
(d) All sensors on the back side of the second MVD station.

Figure C.3: The sensor arrangement on the second MVD station. The sensors are depicted in dark blue for the charge-sensitive and light blue for the non-sensitive sensor area on the front side. From the sensors on the back side of the station, the charge-sensitive area is visible in a darker blue. The polar angle interval to be covered is indicated with red dashed circles, while the sensor carrier is indicated with light grey. To visualize the dimensions of the sensors, a black frame has been applied to them. The dashed lines indicate the dimensions of the quadrants and the sensor carriers. The dashed lines indicate the dimensions of the quadrants and the sensor carriers.



(a) Polar angle interval (dashed circles) of the third MVD station and the MIMOSIS-1 positioned on the front side of one quadrant.

(b) The MIMOSIS-1 positioned on the back side of the quadrant.



(c) All sensors on the front side of the third MVD station.

(d) All sensors on the back side of the third MVD station.

Figure C.4: The sensor arrangement on the third MVD station. The sensors are depicted in dark blue for the charge-sensitive and light blue for the non-sensitive sensor area on the front side. From the sensors on the back side of the station, the charge-sensitive area is visible in a darker blue. The polar angle interval to be covered is indicated with red dashed circles, while the sensor carrier is indicated with light grey. To visualize the dimensions of the sensors, a black frame has been applied to them. The dashed lines indicate the dimensions of the quadrants and the sensor carriers.

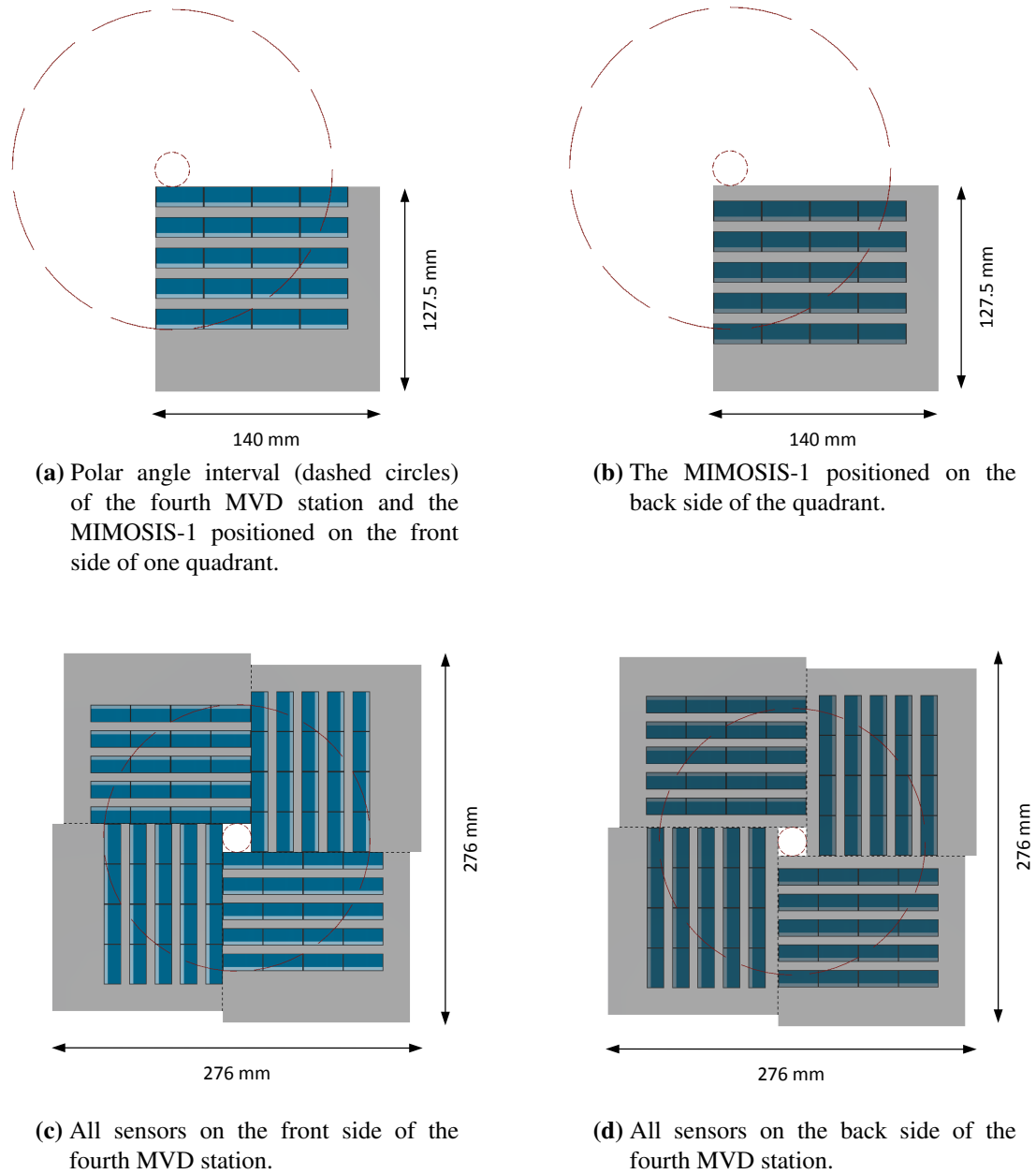


Figure C.5: The sensor arrangement on the fourth MVD station. The sensors are depicted in dark blue for the charge-sensitive and light blue for the non-sensitive sensor area on the front side. From the sensors on the back side of the station, the charge-sensitive area is visible in a darker blue. The polar angle interval to be covered is indicated with red dashed circles, while the sensor carrier is indicated with light grey. To visualize the dimensions of the sensors, a black frame has been applied to them. The dashed lines indicate the dimensions of the quadrants and the sensor carriers.

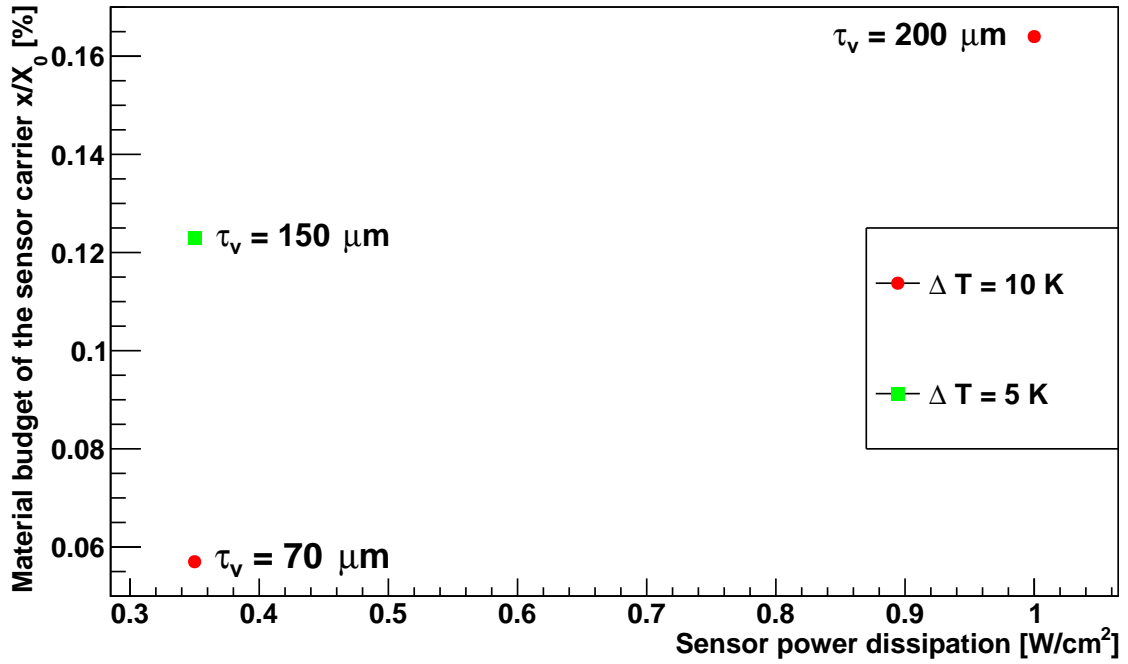


Figure C.6: The thickness of the CVD diamond carriers assuming various power dissipation values for the sensors and different temperature gradients across the sensor's surface.

Station number	Distance to target [mm]	Outer dimensions per heat sink [mm^3]	Dimensions of the inner cut-out [mm^3]	Figure
0	50	$106 \times 196 \times 10$	$81.5 \times 41.5 \times 10$	4.7(a)
1	100	$136 \times 246 \times 10$	$140 \times 70 \times 10$	C.8(a)
2	150	$165 \times 294 \times 10$	$189 \times 89 \times 10$	C.8(b)
3	200	$184 \times 343 \times 10$	$247.5 \times 117.5 \times 10$	C.8(c)

Table C.1: Dimensions of the MVD heat sinks. The outer dimensions of the heat sinks of the individual MVD stations are listed as well as the dimensions of the inner cut-out in which the two sensor carriers have to be positioned.

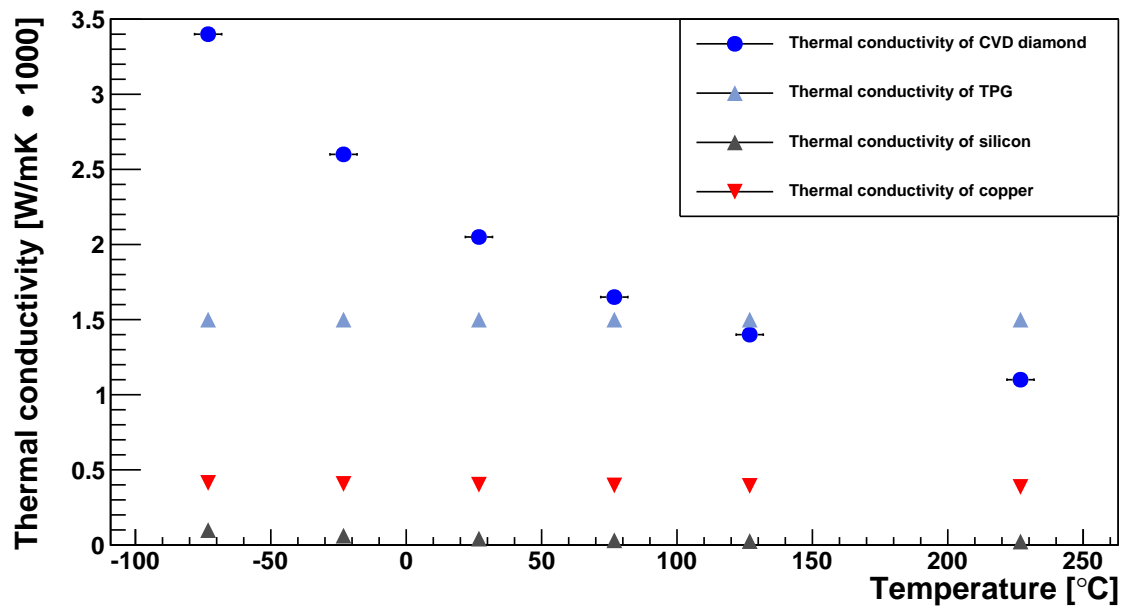
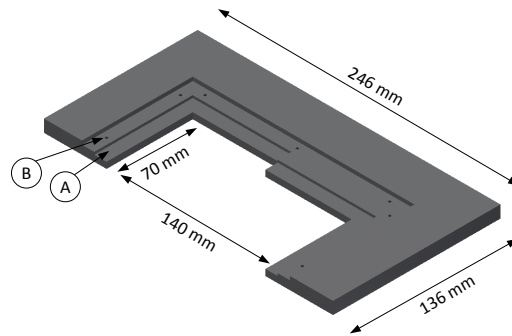
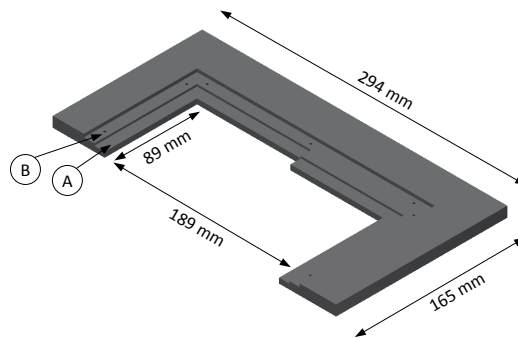


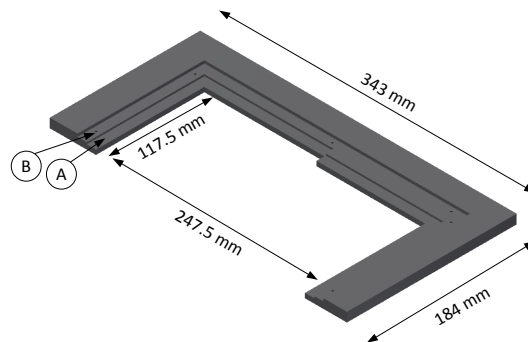
Figure C.7: Thermal conductivities of the materials used in the thermal simulation framework. Temperature-dependent thermal conductivity values have been applied to the silicon representing the sensors. For TPG and copper, constant values are applied (see Table 4.6). For CVD diamond, the corresponding values are taken from [63]. The displayed errors result from the method used to read the values from the graph [63]. The values for copper and silicon are taken from [104]. The value for TPG is taken from [64].



(a) Heat sink of the second MVD station.



(b) Heat sink of the third MVD station.



(c) Heat sink of the fourth MVD station.

Figure C.8: The heat sinks of the MVD stations 1, 2 and 3. Their respective dimensions are listed in Table C.1. (A) indicates the thermal interface area on which the sensor carriers will be positioned. There they will be clamped onto the heat sinks from above by dedicated cover plates. These cover plates will be screwed onto the heat sink at the level indicated with (B).

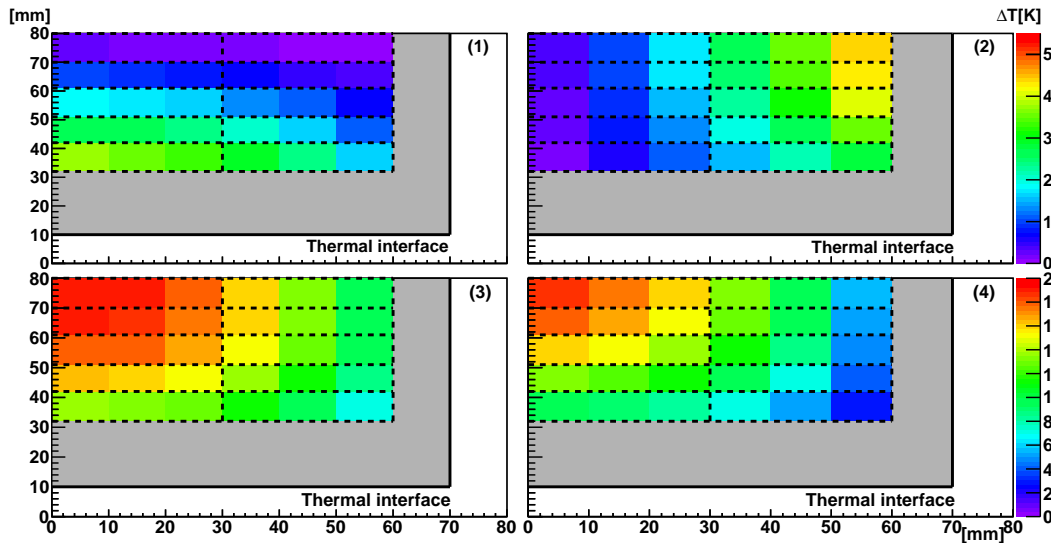
Appendix C. Design Proposal of the MVD

Station	Power dissipation [W/cm ²]	ΔT [K]		T_{maximal}	Figure
		pixel column	pixel row	$-T_{\text{interface}} [^{\circ}\text{C}]$	
0	0.35	0.8	1.6	5.0	4.10(a)
	0.185	0.4	0.6	4.4	4.10(b)
1	0.35	3.7	4.5	19.2	C.9(a)
	0.185	1.3	1.7	12.0	C.9(b)
2	0.35	3.3	3.6	19.5	C.10(a)
	0.185	1.1	1.6	12.2	C.10(b)
3	0.35	3.0	4.6	38.3	C.11(a)
	0.185	1.6	2.4	20.2	C.11(b)

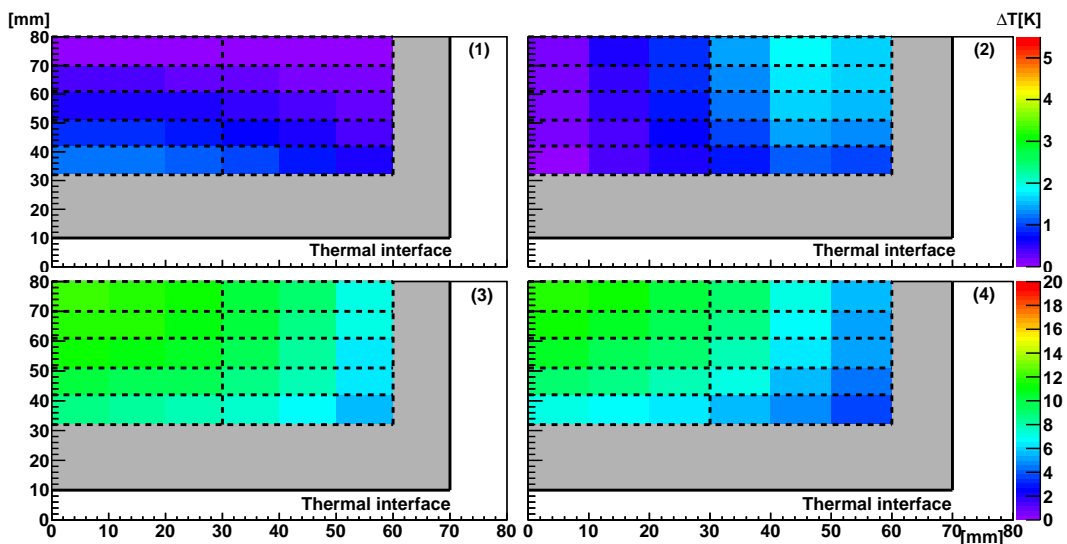
Table C.2: The results extracted from the thermal simulations applying different power dissipation values to the FSBBs on the individual MVD stations. For the temperature gradients and the absolute temperature, the maximum values on the FSBBs of the MIMOSIS-1 sensor are listed.

Station number	Distance to target [mm]	Outer dimensions per support [mm ³]	Dimensions of the inner cut-out [mm ³]	Figure
0	50	121 × 377 × 10	106 × 196 × 10	4.12
1	100	161 × 377 × 10	136 × 246 × 10	C.12(a)
2	150	180 × 377 × 10	165 × 294 × 10	C.12(b)
3	200	199 × 377 × 10	184 × 343 × 10	C.12(c)

Table C.3: Dimensions of the MVD half-station support structures. The outer dimensions of the half-station support structures are listed as well as the dimensions of the inner cut-out in which the dedicated heat sinks will be positioned.

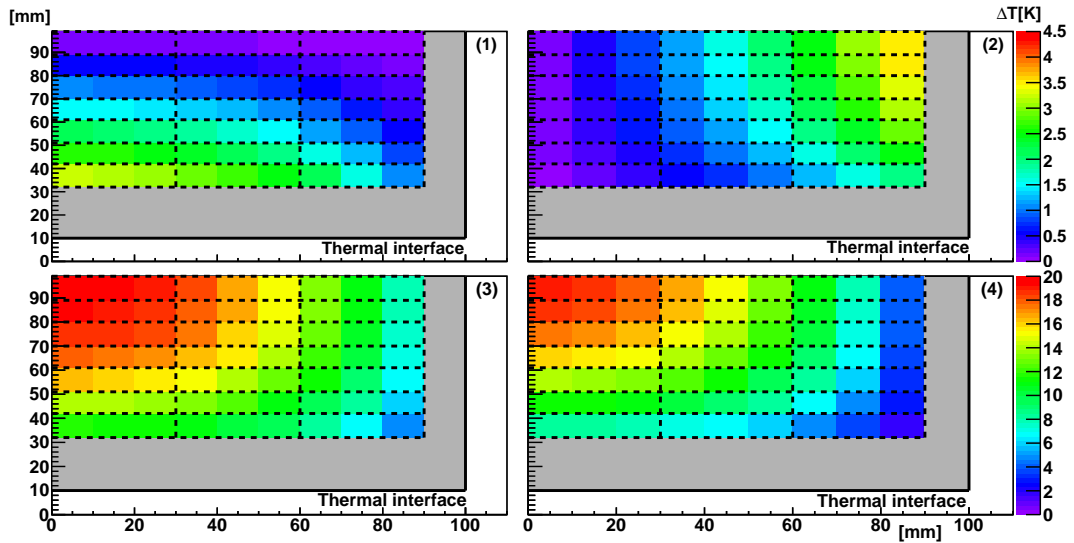


(a) Results for a power dissipation value of 0.35 W/cm^2 .

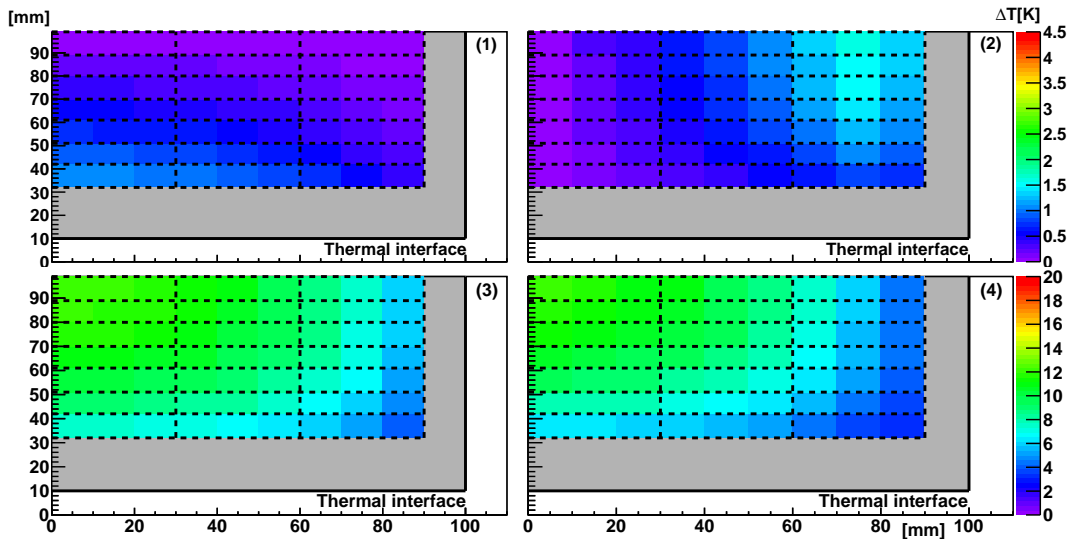


(b) Results for a power dissipation value of 0.185 W/cm^2 .

Figure C.9: The results of the thermal simulations for the second MVD station. The dimensions of the sensor carriers mark the borders of each individual sub-plot. The dimensions of the MIMOSIS-1 sensors are indicated by dashed lines. Within these borders, each individual FSBB is symbolized by a single block. The thermal interface area which is positioned in a heat bath with a temperature of -20°C is indicated by the continuous line. The sensor-free area on the sensor carriers is depicted in grey. The temperature gradients across the individual FSBB surface are evaluated with respect to the pixel column (upper left plots, (1)) and the pixel row (upper right plots, (2)). The lower left and lower right plots show the results of the evaluation of the maximum (3) and minimum (4) temperature found on an FSBB with respect to the temperature applied to the thermal interface area.

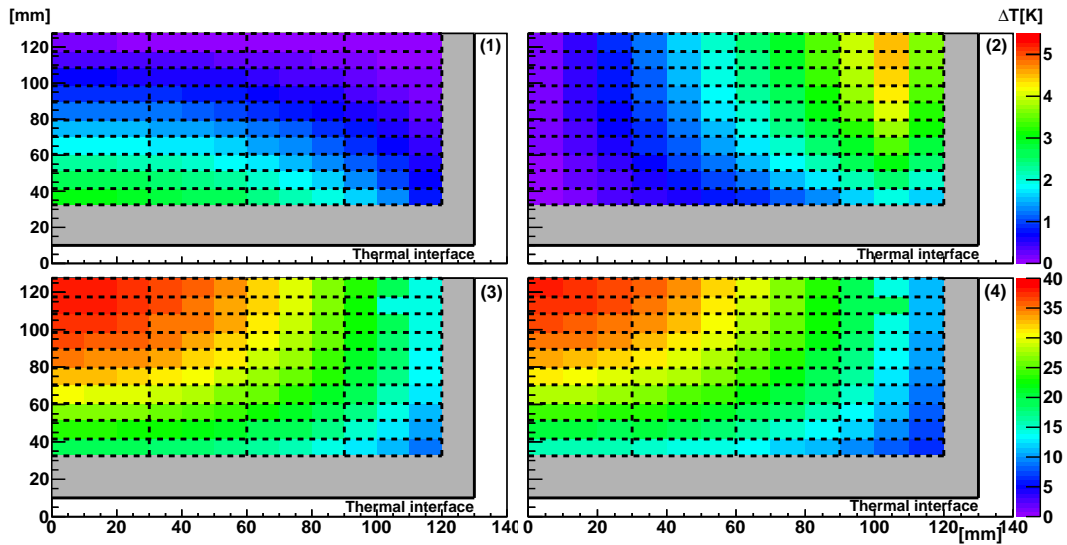


(a) Results for a power dissipation value of 0.35 W/cm^2 .

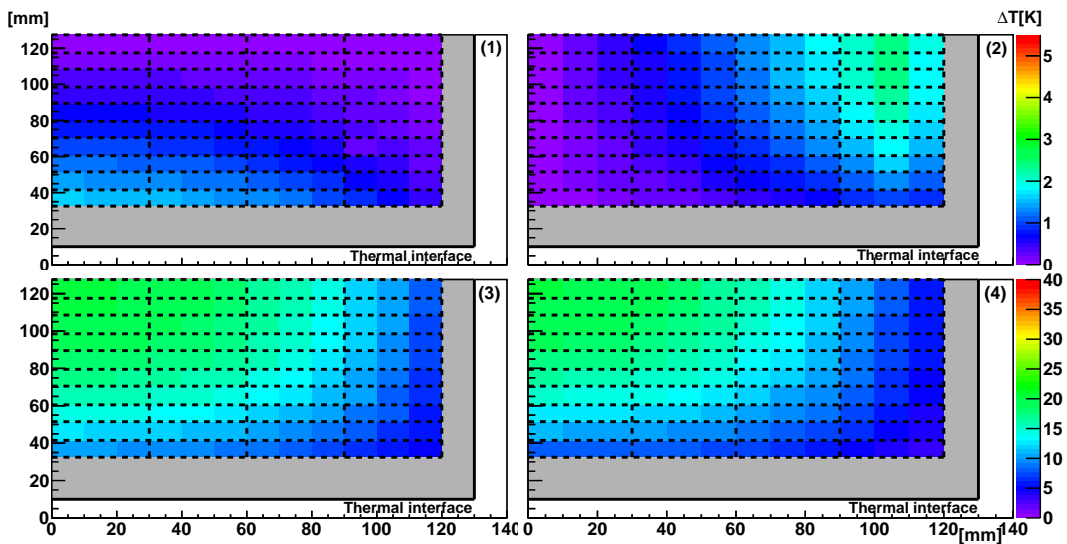


(b) Results for a power dissipation value of 0.185 W/cm^2 .

Figure C.10: The results of the thermal simulations for the third MVD station. The dimensions of the sensor carriers mark the borders of each individual sub-plot. The dimensions of the MIMOSIS-1 sensors are indicated by dashed lines. Within these borders, each individual FSBB is symbolized by a single block. The thermal interface area which is positioned in a heat bath with a temperature of -20°C is indicated by the continuous line. The sensor-free area on the sensor carriers is depicted in grey. The temperature gradients across the individual FSBB surface are evaluated with respect to the pixel column (upper left plots, (1)) and the pixel row (upper right plots, (2)). The lower left and lower right plots show the results of the evaluation of the maximum (3) and minimum (4) temperature found on an FSBB with respect to the temperature applied to the thermal interface area.

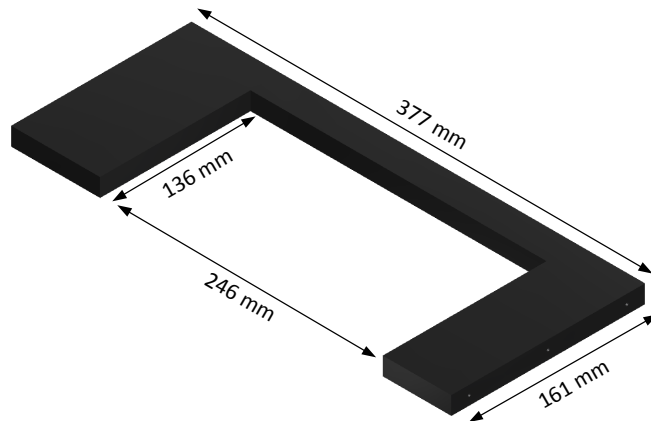


(a) Results for a power dissipation value of 0.35 W/cm^2 .

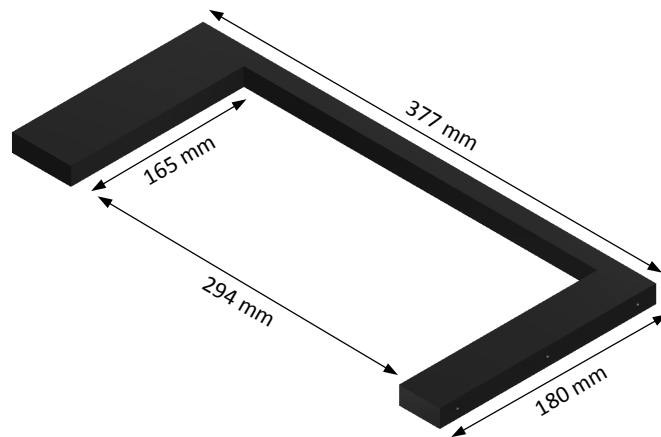


(b) Results for a power dissipation value of 0.185 W/cm^2 .

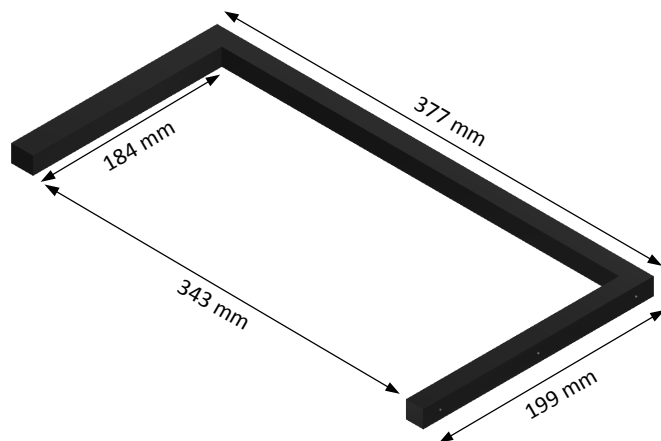
Figure C.11: The results of the thermal simulations for the fourth MVD station. The dimensions of the sensor carriers mark the borders of each individual sub-plot. The dimensions of the MIMOSIS-1 sensors are indicated by dashed lines. Within these borders, each individual FSBB is symbolized by a single block. The thermal interface area which is positioned in a heat bath with a temperature of -20°C is indicated by the continuous line. The sensor-free area on the sensor carriers is depicted in grey. The temperature gradients across the individual FSBB surface are evaluated with respect to the pixel column (upper left plots, (1)) and the pixel row (upper right plots, (2)). The lower left and lower right plots show the results of the evaluation of the maximum (3) and minimum (4) temperature found on an FSBB with respect to the temperature applied to the thermal interface area.



(a) Half station support of the second MVD station.

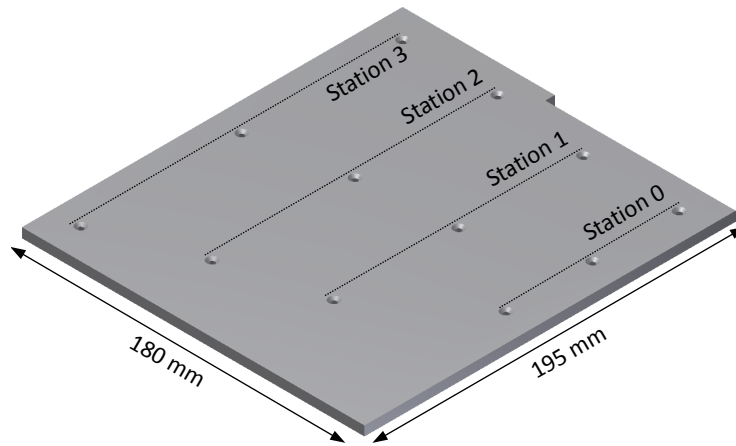


(b) Half station support of the third MVD station.

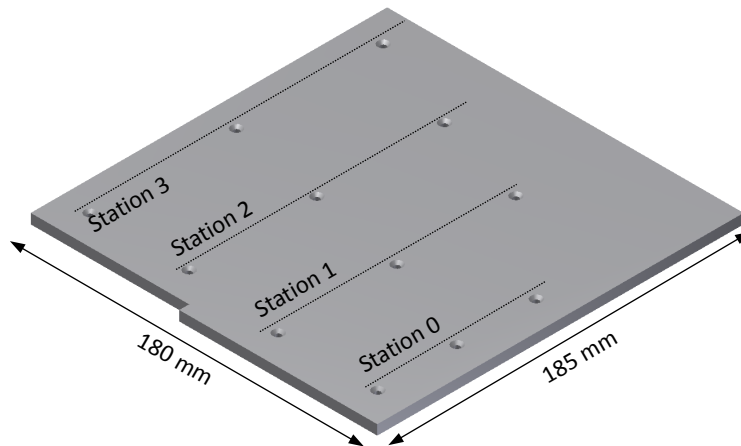


(c) Half station support of the fourth MVD station.

Figure C.12: The half-station support of the MVD stations 1, 2 and 3. Their dimensions can be found in Table C.3.



(a) Base plate for the positioning of the MVD half-stations, type a.



(b) Base plate for the positioning of the MVD half-stations, type b.

Figure C.13: The base plates for the positioning of the MVD half-stations. The positions of the individual MVD half-stations are indicated. Due to the symmetry of the detector stations with regard to the beam, only two types of base plates are required, each of which features a thickness of 5 mm. Their design ensures a precise final position of the half-stations mounted onto the base plates.

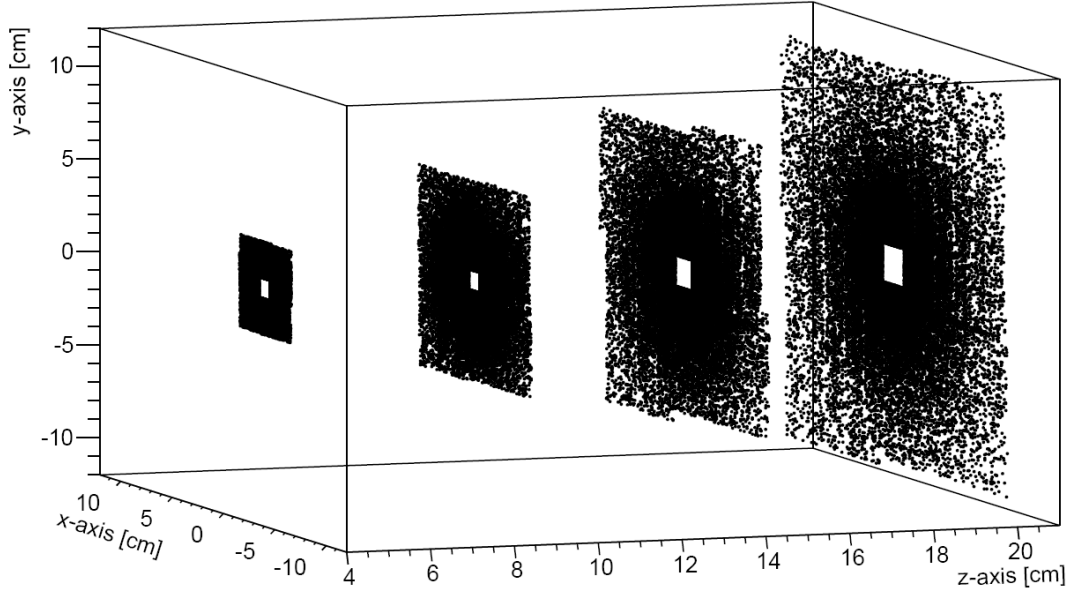


Figure C.14: Monte-Carlo hits registered on the four MVD stations. The hits are generated by simulated particles (50 central Au+Au UrQMD events with an energy of 25 AGeV) transported through the detector model.

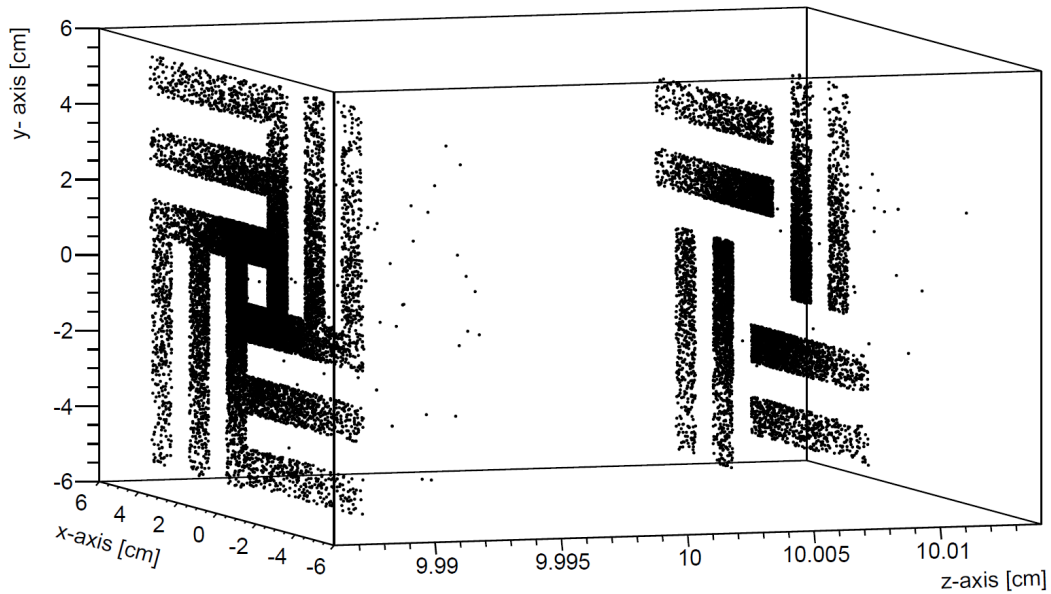
Region	A	B	C
Thickness x/X_0 [%]	0.182	0.241	0.251

Table C.4: The material budget of the first MVD station as a function of the distance to the beam axis for both ϕ -intervals. The letters indicate the regions depicted in Figure C.18(a).

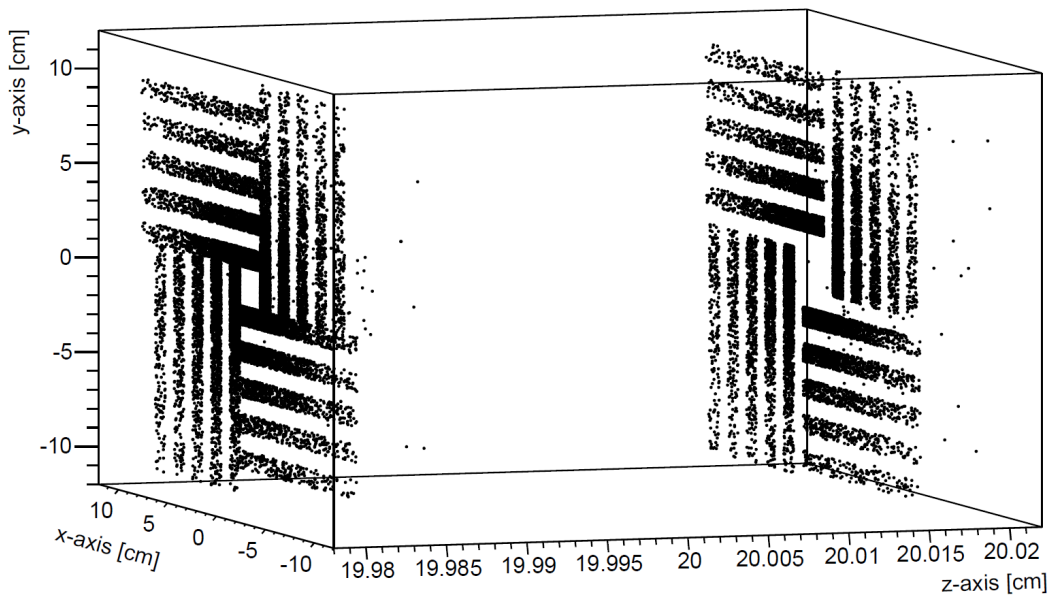
Region	A	B	C	D	E	F	G	H	I
Thickness x/X_0 [%]	0.306	0.365	0.375	0.425	0.435	0.485	0.435	0.485	0.435

Region	J	K	L	M
Thickness x/X_0 [%]	0.485	0.435	0.485	0.435

Table C.5: The material budget of the third MVD station as a function of the distance to the beam axis for the small ϕ -intervals. The letters indicate the regions depicted in Figure C.18(b).

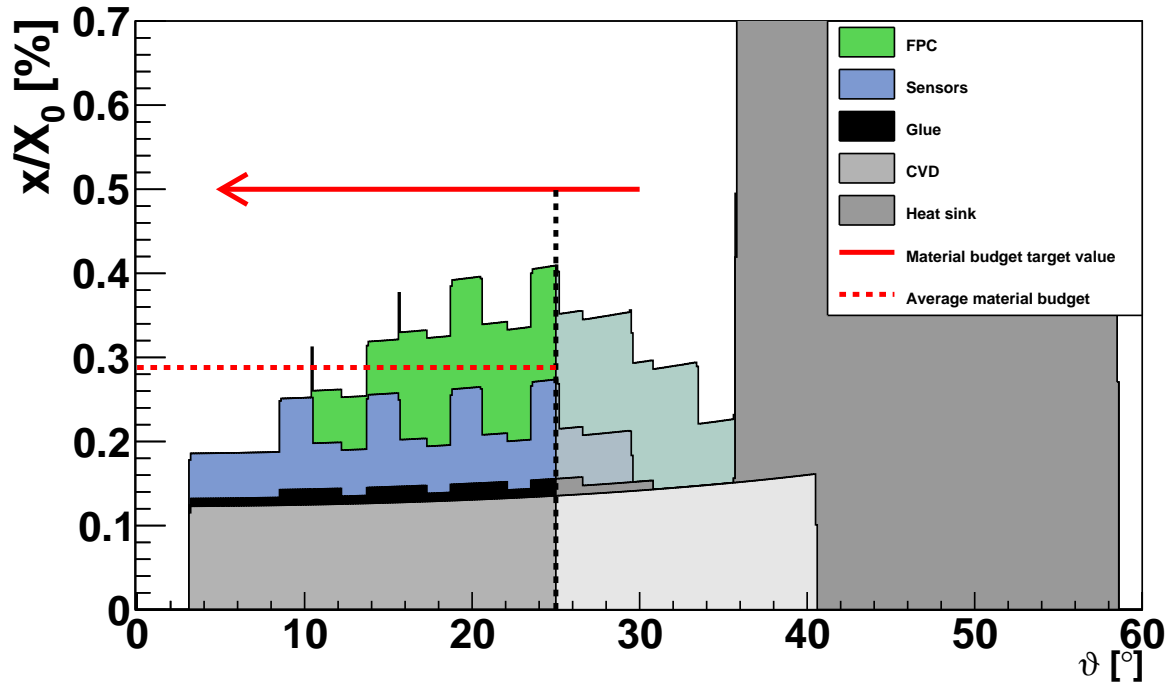


(a) Simulated particle hits on the second MVD station. Note the scale of the z-axis, indicating the CVD diamond carrier thickness of 150 μm .

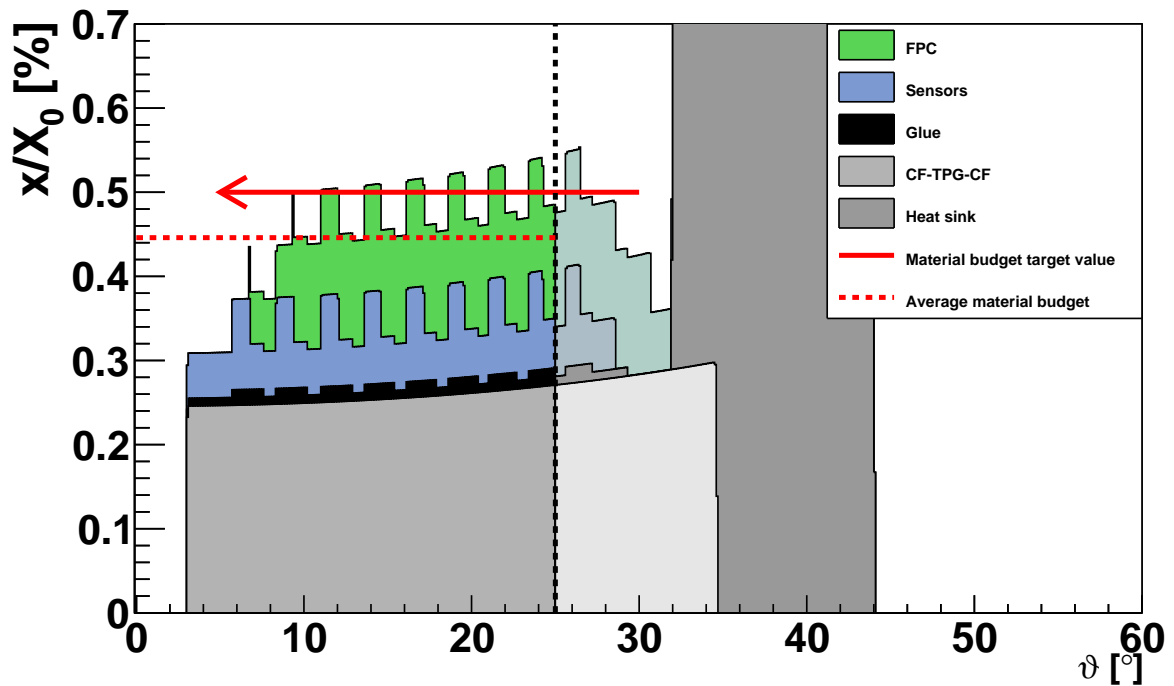


(b) Simulated particle hits on the fourth MVD station. Note the scale of the z-axis, indicating the thickness of the CF-TPG-CF sensor carrier implemented by means of the material budget contribution of CVD diamond.

Figure C.15: Monte-Carlo hits registered on the separated sensor layers of the second and the fourth MVD station. The hits are generated by simulated particles (50 central Au+Au UrQMD events with an energy of 25 AGeV) transported through the detector model.

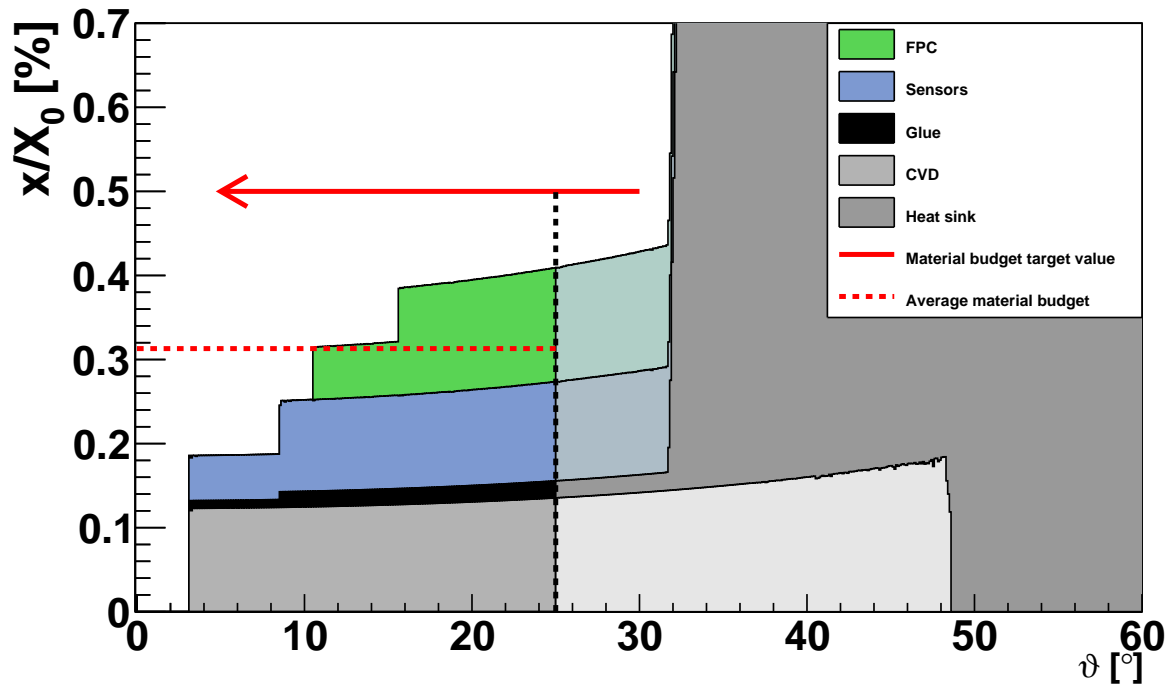


(a) Simulated material budget for the second MVD station in the **small** φ -interval.

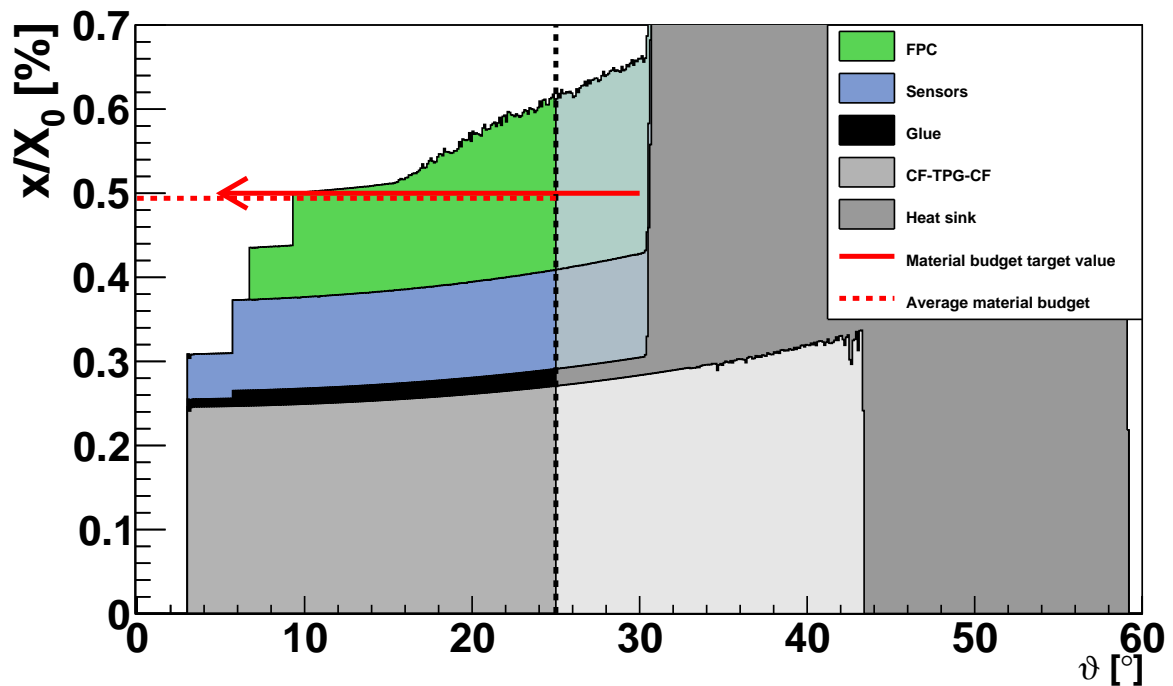


(b) Simulated material budget for the fourth MVD station in the **small** φ -interval.

Figure C.16: The material budget as function of the polar angles of the second (a) and the fourth (b) MVD station in the φ -range of $[0^\circ, 2.5^\circ]$. The target value for the material budget is indicated with the red arrow at $x/X_0 \sim 0.5\%$ for both stations. The required polar angle coverage reaches towards the black dashed vertical line and includes the ϑ -values featuring a color code with higher saturation.

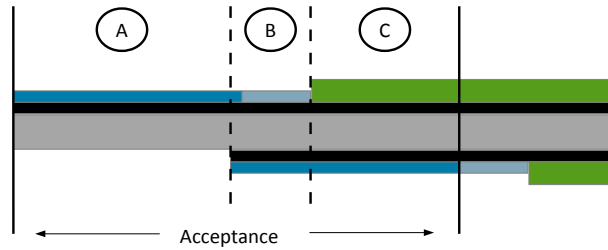


(a) Simulated material budget for the second MVD station in the **complete** φ -interval.

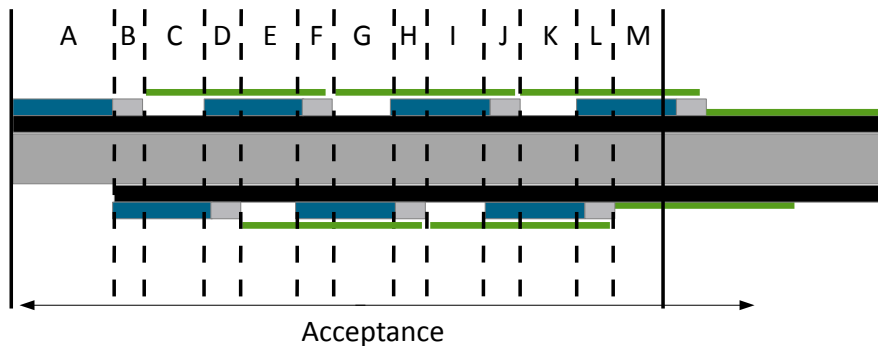


(b) Simulated material budget for the fourth MVD station in the **complete** φ -interval.

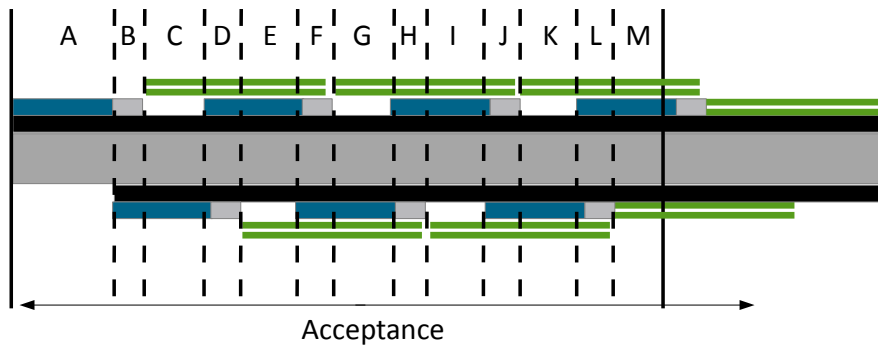
Figure C.17: The material budget as function of the polar angles of the second (a) and the fourth (b) MVD station in the φ -range of $[0^\circ, 360^\circ]$. The target value for the material budget is indicated with the red arrow at $x/X_0 \sim 0.5\%$ for both stations. The required polar angle coverage reaches towards the black dashed vertical line and includes the ϑ -values featuring a color code with higher saturation.



(a) Cross-section of the first MVD station for both φ -intervals.

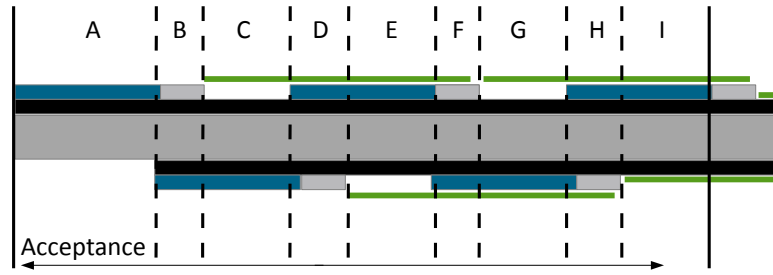


(b) Cross-section of the third MVD station for the small φ -interval and the inner areas of the quadrants in the complete φ -interval.

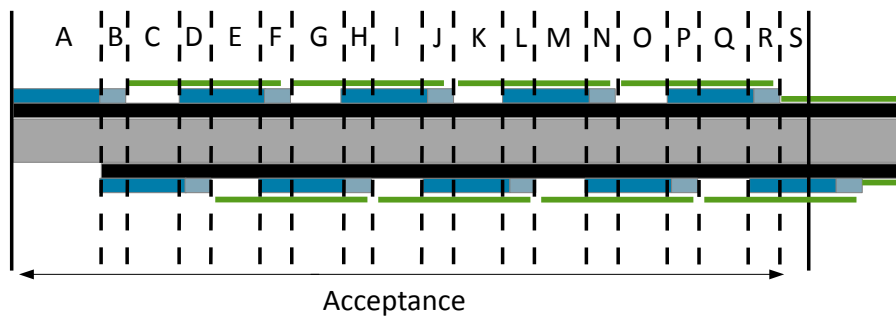


(c) Cross-section of the third MVD station for the outer areas of the quadrants in the complete φ -interval.

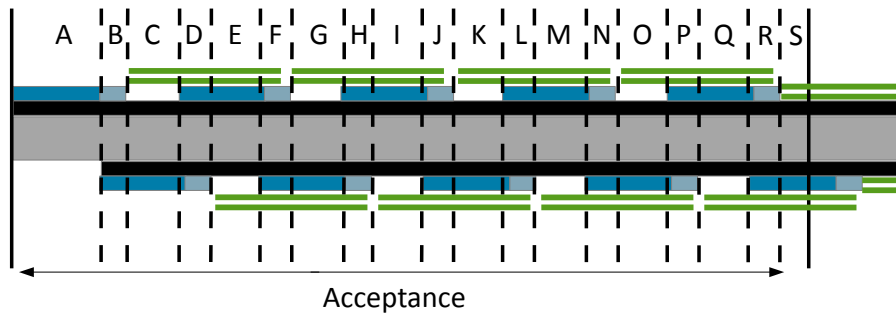
Figure C.18: The cross-sections of the first and the third MVD station emphasizing the different contributions to the material budget in the φ -range of $[0^\circ, 2.5^\circ]$ as well as for the range of $[0^\circ, 360^\circ]$ in sub-figure (a) and (b). In sub-figure (c), the contributions to the material budget in the outer areas of the quadrants of the third MVD station are depicted in the φ -range of $[0^\circ, 360^\circ]$ due to the positioning of the additionally required FPCs for the read-out of the third sensor of the sensor ladders. The material budget values of the regions indicated by the letters are listed in Tables C.4, C.5, C.6, respectively.



(a) Cross-section of the second MVD station for both ϕ -intervals.



(b) Cross-section of the fourth MVD station for the small ϕ -interval and the inner areas of the quadrants in the complete ϕ -interval.



(c) Cross-section of the fourth MVD station for the outer areas of the quadrants in the complete ϕ -interval.

Figure C.19: The cross-sections of the second and the fourth MVD station emphasizing the different contributions to the material budget in the ϕ -range of $[0^\circ, 2.5^\circ]$ as well as in the range of $[0^\circ, 360^\circ]$ in sub-figure (a) and (b). In sub-figure (c), the contributions to the material budget in the outer areas of the quadrants of the fourth MVD station are depicted in the ϕ -range of $[0^\circ, 360^\circ]$ due to the positioning of the additionally required FPCs for the read-out of the third and fourth sensor of the sensor ladders. The material budget values of the regions indicated by the letters are listed in Tables C.7, C.8 and C.9, respectively.

Appendix C. Design Proposal of the MVD

Region	A	B	C	D	E	F	G	H	I
Thickness x/X_0 [%]	0.306	0.365	0.435	0.485	0.555	0.605	0.555	0.605	0.555
Region	J	K	L	M					
Thickness x/X_0 [%]	0.605	0.555	0.605	0.555					

Table C.6: The material budget of the third MVD station as a function of the distance to the beam axis for the outer areas of the quadrants for the complete φ -interval. The letters indicate the regions depicted in Figure C.18(c).

Region	A	B	C	D	E	F	G	H	I
Thickness x/X_0 [%]	0.182	0.241	0.251	0.301	0.311	0.361	0.311	0.361	0.311

Table C.7: The material budget of the second MVD station as a function of the distance to the beam axis for both φ -intervals. The letters indicate the regions depicted in Figure C.19(a).

Region	A	B	C	D	E	F	G	H	I	J
Thickness x/X_0 [%]	0.306	0.365	0.375	0.425	0.435	0.485	0.435	0.485	0.435	0.485
Region	K	L	M	N	O	P	Q	R	S	
Thickness x/X_0 [%]	0.435	0.485	0.435	0.485	0.435	0.485	0.435	0.485	0.435	

Table C.8: The material budget of the fourth MVD station as a function of the distance to the beam axis for the small φ -interval. The letters indicate the regions depicted in Figure C.19(b).

Region	A	B	C	D	E	F	G	H	I	J
Thickness x/X_0 [%]	0.306	0.365	0.435	0.485	0.555	0.605	0.555	0.605	0.555	0.605
Region	K	L	M	N	O	P	Q	R	S	
Thickness x/X_0 [%]	0.555	0.605	0.555	0.605	0.555	0.605	0.555	0.605	0.555	

Table C.9: *The material budget of the fourth MVD station as a function of the distance to the beam axis for the outer areas of the quadrants for the complete φ -interval. The letters indicate the regions depicted in Figure C.19(c).*

Appendix D

MVD Prototype Project

D.1 Estimation of the Air Pocket Pressure Resulting on the Sensor

The force which may impact on a MIMOSA-26 sensor by air pockets/voids enclosed in the glue has to be evaluated in order to estimate the risk of a potential mechanical impact on the sensors. The dimensions of the air pockets are assumed to have a value of $100 \times 100 \mu\text{m}^2$, at a surrounding pressure of 1×10^{-4} mbar inside the vacuum vessel. Furthermore, it is assumed that a number of five air pockets are homogeneously distributed over the area of one mm^2 .

The pressure inside an air pocket is defined to be 1 bar = 10 N/cm (standard pressure). The pressure difference between the standard pressure and the pressure inside the vacuum vessel can be determined to $\text{dp} = 1000 \text{ mbar} - 1 \times 10^{-4} \text{ mbar} = 1 \text{ bar}$. The air pocket area is defined to be $A = (0.01\text{cm})^2 = 1 \times 10^{-4} \text{ cm}^2$. The resulting force can be estimated to be

$$F = \text{dp} \cdot A = 10 \text{ N/cm}^2 \times 1 \times 10^{-4} \text{ cm}^2 = 1 \times 10^{-3} \text{ N}.$$

Projecting the assumed number of five air pockets per mm^2 to an area of cm^2 results in estimative 500 pockets per cm^2 and ≈ 1000 for the area of one MIMOSA-26 sensor. The total force impacting on a MIMOSA-26 sensor is $F = 1 \text{ N} \approx 100 \text{ g}$.

This force has to be compared to the mass of an individual MIMOSA-26 sensor. Its dimensions are given by $2.15 \text{ cm} \times 1.38 \text{ cm} \times 0.0045 \text{ cm} = 1.33 \times 10^{-2} \text{ cm}^3$. The mass of an individual sensor can be calculated to

$$m = 1.33 \times 10^{-2} \text{ cm}^3 \times 2.330 \text{ g/cm}^3 = 0.0311 \text{ g} = 3.11 \times 10^{-5} \text{ kg} \Rightarrow F_g = 3.11 \times 10^{-4} \text{ N}.$$

This mass value is in accordance with weight measurements [72] which have been carried out as part of the MVD Prototype project using a precision scale, see [105].

The force which may impact on the sensors resulting from enclosed enclosed air pockets in the glue is higher by a factor of almost four than the mass of the sensor. Therefore, the

preparation of the glue in terms of mixing the different components has to be carried out in such a way that the enclosure of air pockets or voids in the glue itself is prevented.

D.2 Estimation of the Heat Extracted from a Single Sensor via Thermal Radiation and Convection

The heat which can be extracted from a single sensor by thermal radiation and convection has to be estimated in order to evaluate their relevance for the thermal management. The thermal radiation of a material can be described with the Stefan–Boltzmann law,

$$P_S = \sigma_{SB} \cdot \varepsilon \cdot A \cdot T^4 \quad (\text{D.1})$$

taken from [70], in which σ_{SB} is the Stefan–Boltzmann constant, A the area of an individual sensor, ε the emissivity of the material and T the temperature of the material.

For the sensor area of $A = 2.967 \times 10^{-4} \text{m}^2$, the thermal radiation can be estimated to be $P = 0.064 \text{ W}$ for a sensor temperature of $T = 23 \text{ }^\circ\text{C}$ and $P = 0.05 \text{ W}$ for a sensor temperature of $T = 5 \text{ }^\circ\text{C}$. The effect of the heat extracted from the sensor by thermal radiation is small compared to the lateral heat which is to be evacuated and which has a value of 1 W per sensor.

The heat extracted from a single sensor by the air flow of nitrogen has to be estimated. Dry nitrogen is injected in the housing box of the MVD Prototype in order to prevent condensation on the individual sensor during measurements that require a heat sink temperature below dew point. The arrangement of the individual sensor of the MVD Prototype in the air flow of nitrogen is vertical, see Figure 5.15(b) in the main text. The used formula [70] for this estimation is given with

$$P_C = h \cdot A \cdot (T_{\text{sensor}} - T_{N_2}) \quad (\text{D.2})$$

in which h is the heat transfer coefficient, A the sensor area, T_{sensor} the temperature of the sensor and T_{N_2} the temperature of the nitrogen. The value of h can be determined by use of the formula

$$h = Nu \frac{\lambda}{d}, \quad (\text{D.3})$$

which includes the Nusselt number, defined as the ratio of the convective to the conductive heat transfer perpendicular to the contact surface, the thermal conductivity of nitrogen λ and the width of the sensor d . The Nusselt number itself is defined as

$$Nu = 0.664 \cdot \sqrt[3]{Pr} \cdot \sqrt{Re} \quad (\text{D.4})$$

in which the Reynolds number Re , defined as the ratio of inertial forces to viscous forces, and the Prandtl number Pr , given as the ratio of kinetic viscosity to thermal diffusivity, are included. The Reynolds number and the Prandtl number can be calculated using the following equations:

$$Re = \frac{\rho \cdot v \cdot d}{\eta} = \frac{v \cdot d}{\nu} \text{ and } Pr = \frac{\nu}{d} = \frac{v \cdot p \cdot c_p}{\lambda}. \quad (\text{D.5})$$

The heat transfer coefficient can be calculated using the properties of nitrogen which are listed in Table D.1. Using these numbers, the Reynolds number can be determined to have a value of $Re = 0.3861$, indicating a laminar flow of the nitrogen. In conjunction with the Prandtl number ($Pr = 0.7157$) and the Nusselt number given with $Nu = 0.3579$, the heat transfer coefficient can be determined to be of a value of $h = 0.4262 \text{ W/m}^2\text{K}$. Assuming a sensor temperature of $23 \text{ }^\circ\text{C}$ and a nitrogen temperature of $20 \text{ }^\circ\text{C}$, this leads to a heat extracted from a single sensor by convection of

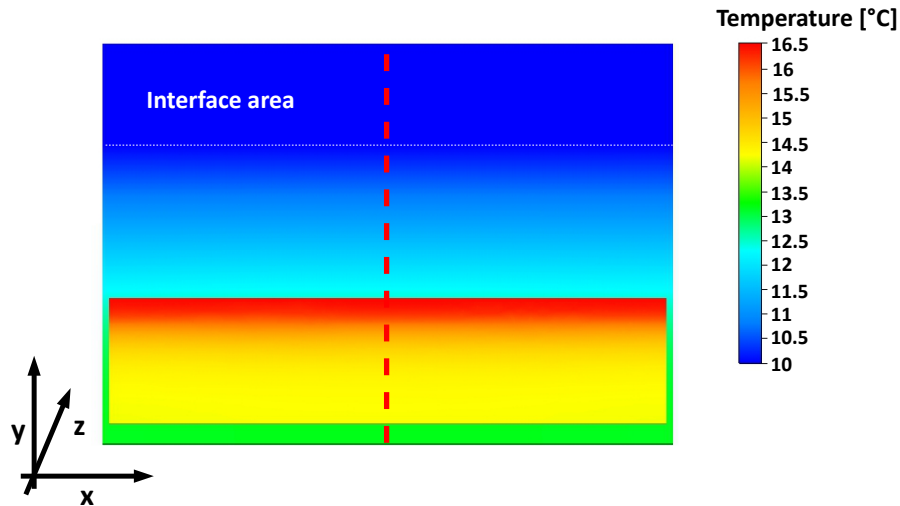
$$P_C = 0.4262 \frac{\text{W}}{\text{m}^2\text{K}} \times 2.967 \times 10^{-4} \text{ m}^2 \times (296 \text{ K} - 293 \text{ K}) = 0.0274 \text{ W}. \quad (\text{D.6})$$

The effect of the heat extracted from the sensor by convection is small compared to the lateral heat of 1 W of the individual sensor.

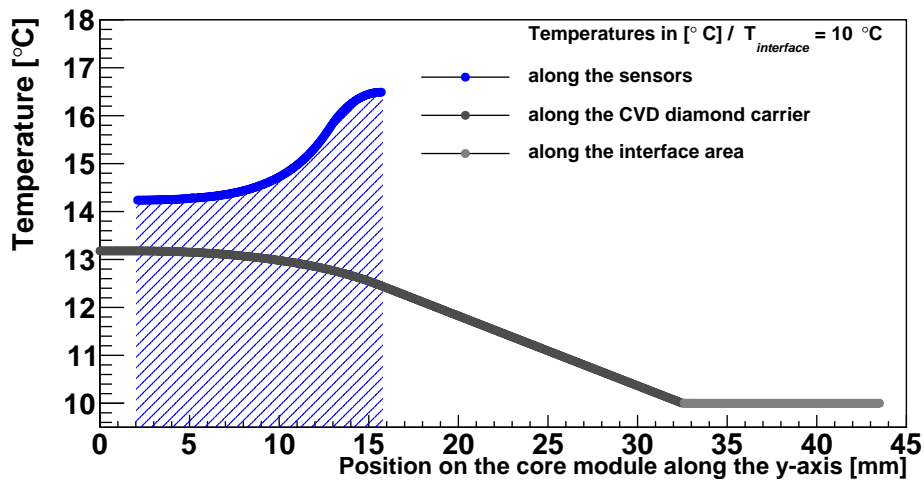
		nitrogen
ρ	[kg/m ³]	1.1496
η	[10 ⁻⁶ Pa s]	17.60
ν	[10 ⁻⁷ m ² /s]	153.1
λ	[10 ⁻³ W/mK]	25.60
c_p	[kJ/kg K]	1.041
v	[10 ⁻⁴ m/s]	2.75

Table D.1: The properties of nitrogen at a temperature of $20 \text{ }^\circ\text{C}$; the numbers are taken from [106]. The velocity has been determined by use of the dimensions of the housing box of the MVD Prototype and a gas exchange rate of $200 \text{ cm}^3/\text{min}$.

D.3 Thermal Simulations of the MVD Prototype

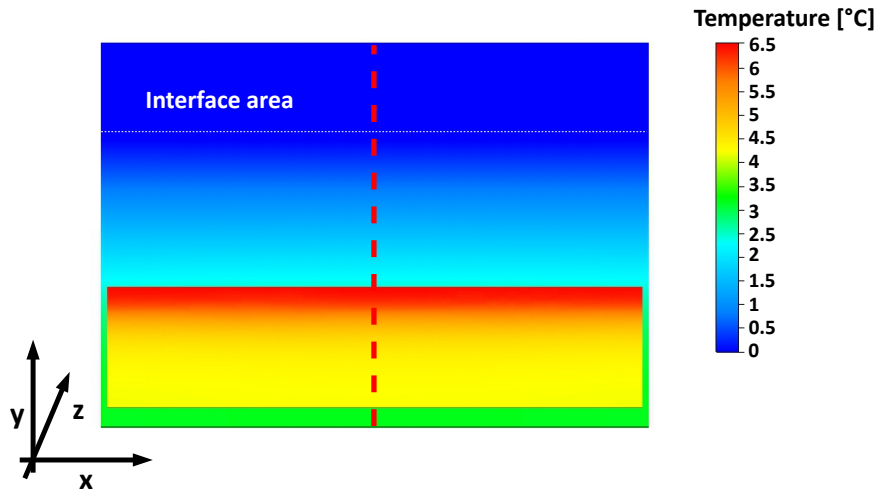


(a) Results for a heat bath temperature of $T_{\text{interface}} = 10^\circ\text{C}$.

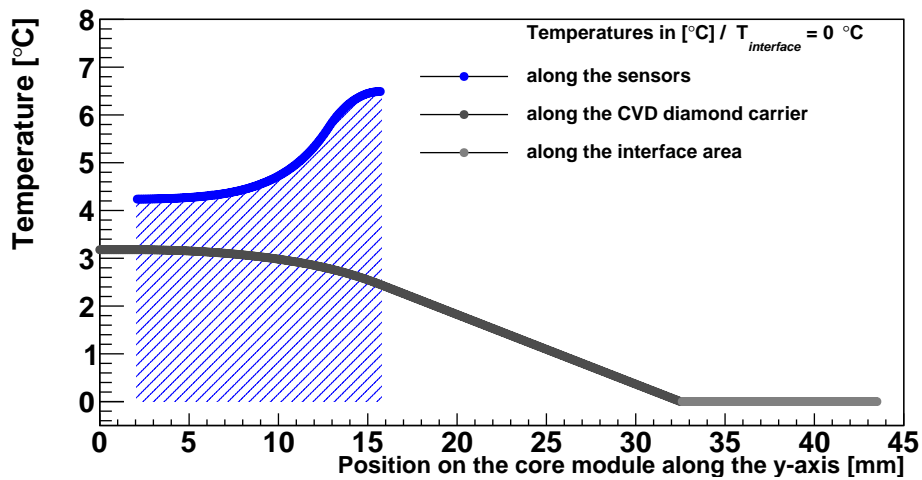


(b) Temperatures along the y-axis (red dashed line in the upper picture (a)).

Figure D.1: (a) Results of the thermal simulation carried out for a heat bath temperature of $T_{\text{interface}} = 10^\circ\text{C}$. The maximum temperature can be seen in the non-sensitive part of the sensor. (b) The simulated temperatures on the “core module” are plotted along the y-axis (red dashed line in Figure D.1(a)). The blue-shaded area indicates the thermal interface of the sensors with the sensor carrier being provided by the glue, see (1) in Figure 4.8.



(a) Results for a heat bath temperature of $T_{\text{interface}} = 0\text{ }^{\circ}\text{C}$.



(b) Temperatures along the y-axis (red dashed line in the upper picture (a)).

Figure D.2: (a) Results of the thermal simulation carried out for a heat bath temperature of $T_{\text{interface}} = 0\text{ }^{\circ}\text{C}$. The maximum temperature can be seen in the non-sensitive part of the sensor. (b) The simulated temperatures on the “core module” are plotted along the y-axis (red dashed line in Figure D.2(a)). The blue-shaded area indicates the thermal interface of the sensors with the sensor carrier being provided by the glue, see (1) in Figure 4.8.

D.4 Material Budget of the MVD Prototype

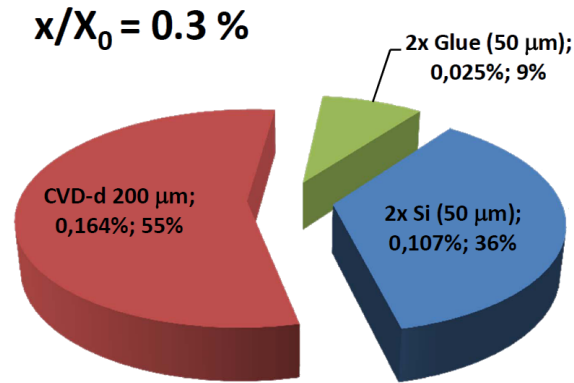


Figure D.3: The contribution of the integrated materials to the overall material budget of the MVD Prototype. The calculation is limited to the overlapping charge-sensitive areas of the sensors of the double-sided module.

D.5 The Sensor Carriers of the Reference Planes

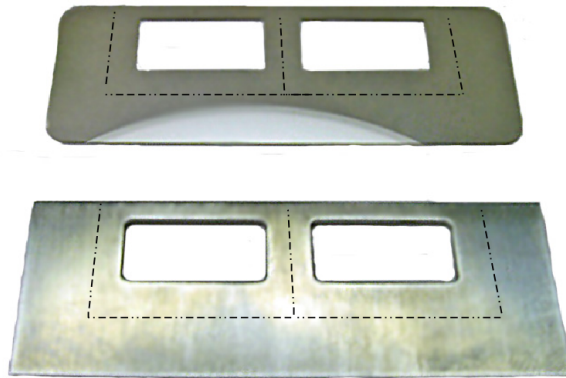


Figure D.4: The sensor carriers of the reference planes. The upper sensor carrier is made of 200 μm thin CVD diamond, the lower one is made of 1 mm thick aluminum. The contribution of the sensor carriers to the material budget of an individual reference plane is reduced introducing two openings centered around the charge-sensitive sensor area, leaving 2.5 mm cooling and support material on each side. The area which is covered by the MIMOSA-26 sensors is sketched by the dashed and dotted lines.

D.6 The Mechanical Handling of the Ultra-Thin CMOS Sensors

During the integration process, the MIMOSA-26 sensors have to be lifted and positioned onto their dedicated carriers using customized tools and underpressure. The minimal required underpressure can be estimated according to the following equations:

The dimensions of the sensors are given with $2.15 \text{ cm} \times 1.38 \text{ cm} = 2.9 \times 10^{-4} \text{ m}^2$. The mass of an individual sensor and the resulting force due to gravity, taken from Section D.1, has been determined to be of a value of $m = 3.11 \times 10^{-5} \text{ kg} \Rightarrow F_g = 3.11 \times 10^{-4} \text{ N}$.

Therefore, the minimal underpressure which is required to lift a sensor can be estimated to have a value of

$$p_{\min} = \frac{F}{A} = \frac{3.11 \times 10^{-4} \text{ N}}{2.9 \times 10^{-4} \text{ m}^2} = 1.012 \frac{\text{N}}{\text{m}^2} = 1.012 \times 10^{-5} \text{ bar.} \quad (\text{D.7})$$

Estimation of the Underpressure Impacting on a MIMOSA-26 Sensor Using the Pick-Up and Handling Tool

To pick up an individual bent sensor, the pick-up tool has been equipped with a special alternating arrangement of air channels to apply and distribute the underpressure over the sensor's surface. The air channel area which is available to apply underpressure to the sensor is $A = 1.2 \times 10^{-4} \text{ m}^2$. The minimal underpressure required to lift a sensor with this pick-up tool amounts to

$$p_{\min \text{ pick-up}} = \frac{F}{A} = \frac{3.11 \times 10^{-4} \text{ N}}{1.2 \times 10^{-4} \text{ m}^2} = 2.591 \frac{\text{N}}{\text{m}^2} = 2.6 \times 10^{-5} \text{ bar.} \quad (\text{D.8})$$

Compared to the minimal underpressure required to lift the sensor estimated in Equation D.7, this value is larger by a factor of 2.5. It is concluded that the sensors are able to tolerate the applied underpressure, since they do not show any visible impacts originating from the integration process.

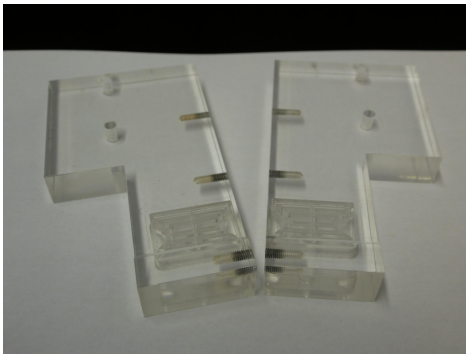
Estimation of the Underpressure Impacting on a MIMOSA-26 Sensor Using the Final Sensor Positioning-Tool

For the final sensor positioning-tool used to pick-up and position two sensors on the sensor carriers at the same time, the dimensions of the air channels have been changed to ease the manufacturing process. The air channel area which is available to apply the underpressure to an individual sensor is reduced to a value of $A = 6.68 \times 10^{-5} \text{ m}^2$. The minimal underpressure required to lift a sensor using the final sensor positioning-tool can be calculated to be of a value of

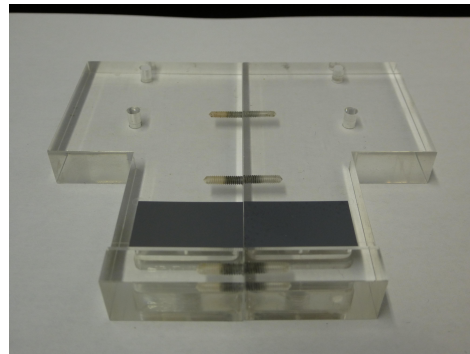
$$p_{\min \text{ final}} = \frac{F}{A} = \frac{3.11 \times 10^{-4} \text{ N}}{6.68 \times 10^{-5} \text{ m}^2} = 4.655 \frac{\text{N}}{\text{m}^2} = 4.66 \times 10^{-5} \text{ bar} \approx 5 \times 10^{-5} \text{ bar.} \quad (\text{D.9})$$

Compared to the minimal underpressure required to lift the sensor estimated in Equation D.7, this value is larger by a factor of 4.5. It is concluded that the underpressure used to pick up an individual sensor with the final sensor positioning-tool can be tolerated by the sensors since they do not show any visible impacts originating from the tool itself.

D.7 The Two-Sensor Positioning-Tool



(a) Positioning tools for two sensors.



(b) Positioning tools holding two sensors.

Figure D.5: The developed and manufactured tools for the positioning of two sensors.

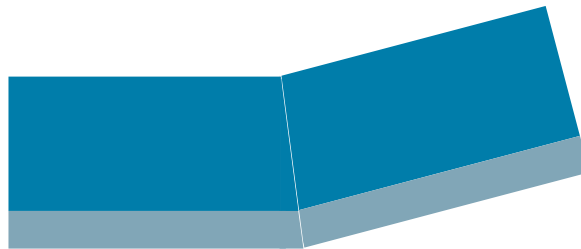
D.8 Impact of Wrongly Diced Sensors on their Edge-to-Edge Positioning



(a) Optimal sensor positioning.



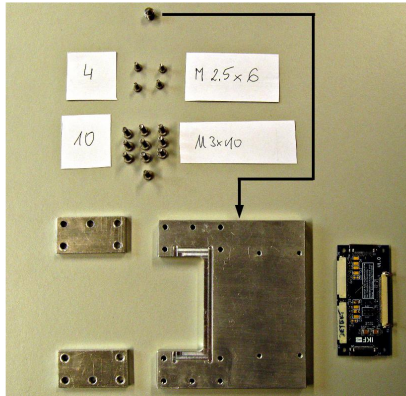
(b) Parallel but not edge-to-edge positioned sensors.



(c) Edge-to-edge but not parallel positioned sensors.

Figure D.6: *The possible impact of wrongly diced sensors on the edge-to-edge positioning. The effects of the wrongly diced sensors are exaggerated to improve the clarity.*

D.9 Construction Steps of the Reference Planes



(a) Step 1.



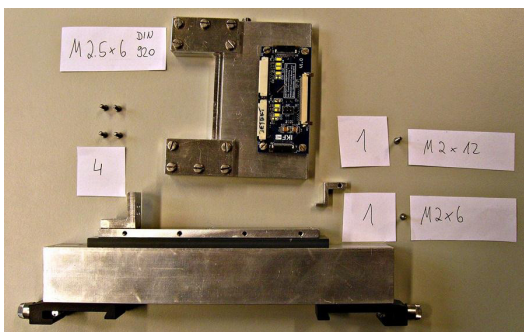
(b) Step 2.



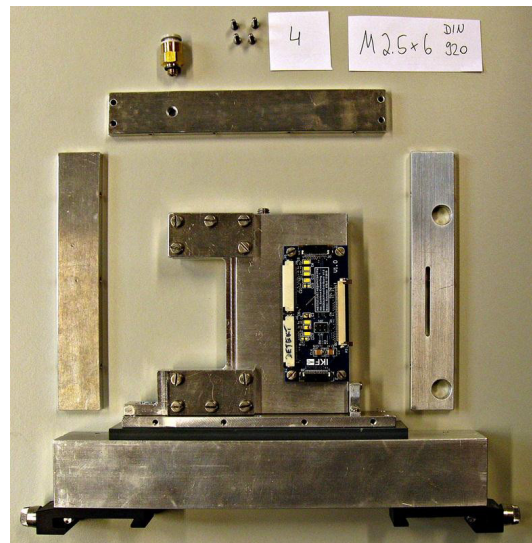
(c) Step 3.



(d) Step 4.

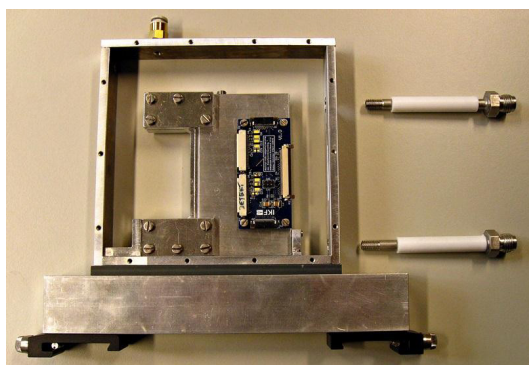


(e) Step 5.

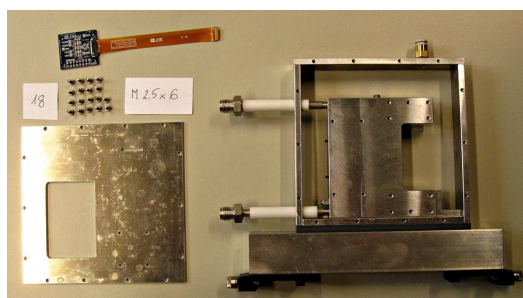


(f) Step 6.

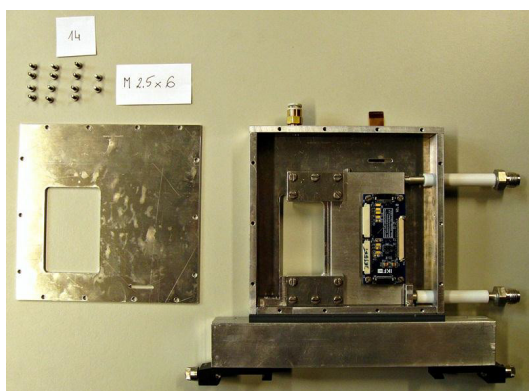
Figure D.7: Construction steps 1 to 6 of the reference planes.



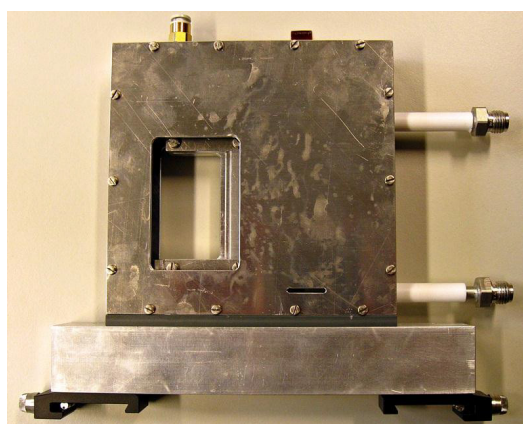
(a) Step 7.



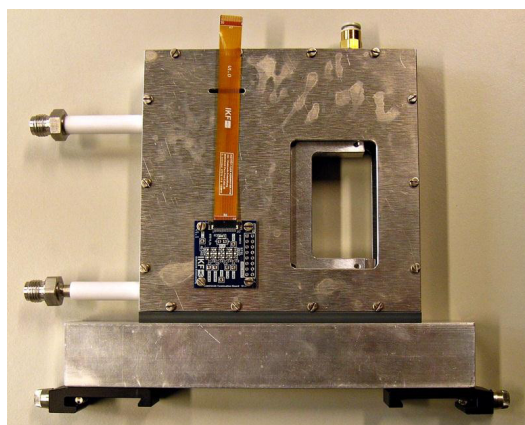
(b) Step 8.



(c) Step 9.



(d) Step 10.



(e) Step 11.

Figure D.8: Construction steps 7 to 11 of the reference planes.

D.10 Evaluation of the Sensor Distances in the “Core Modules”

Reference plane		Sensor distance [μm]				
Number	Carrier type	A(y)	B(x)	C(x)	D(y)	E(x)
<i>a</i>	1	76 ± 1	69 ± 2	67 ± 1	69 ± 1	60 ± 1
<i>b</i>	1	102 ± 1	89 ± 1	68 ± 1	104 ± 2	47 ± 2
<i>e</i>	2	8 ± 1	65 ± 1	52 ± 1	1 ± 1	37 ± 1
<i>f</i>	2	3 ± 3	90 ± 2	94 ± 1	2 ± 1	95 ± 2
<i>g</i>	2	38 ± 3	25 ± 2	57 ± 3	29 ± 1	74 ± 1
<i>h</i>	2	4 ± 1	34 ± 2	39 ± 2	1 ± 1	30 ± 1
Average distance		39 ± 42	62 ± 28	63 ± 19	34 ± 43	57 ± 24

Table D.2: The evaluation of the distances between the sensors in a “core module”. The two different carrier materials are represented with 1 (CVD diamond) and 2 (aluminum). The reference planes *a*, *b*, *e* and *f* are part of the in-beam test set-up discussed in Section 5.5, *g* and *h* are used as spares. The values are rounded to the nearest whole number accounting for the accuracy of the measuring method which has been determined to be of a value of $\pm 5 \mu\text{m}$.

Reference plane Number	pixel-to-pixel distance [μm]	
	C(x)	E(x)
<i>a</i>	558 ± 2	562 ± 1
<i>b</i>	535 ± 2	543 ± 1
<i>e</i>	558 ± 3	565 ± 3
<i>f</i>	534 ± 1	534 ± 2
<i>g</i>	558 ± 3	562 ± 2
<i>h</i>	559 ± 2	570 ± 2
Average distance	550 ± 12	556 ± 14

Table D.3: The evaluation of the distances between the last pixel of the left sensor and the first pixel of the right sensor in a “core module”. The values are rounded to the nearest whole number accounting for the accuracy of the measuring method which has been determined to be of a value of $\pm 5 \mu\text{m}$.

D.11 Temperature Measurements on the MVD Prototype Sensors and the Reference Plane Sensors

		Temperature [$^{\circ}\text{C}$]		
Heat sink	sensors are switched off	sensors are switched on / different sensor operation settings		
		$10^{-2}\%$	$10^{-3}\%$	$10^{-4}\%$
-5.5	0.17	4.34	4.30	4.51
6.8	10.27	14.55	14.55	14.55
	10.04	14.46	14.49	14.49
17	19.84	23.17	22.97	22.10
	18.64	22.88	22.83	22.87

Table D.4: *The absolute temperatures measured on the MVD Prototype sensors in case they are switched off (baseline measurement) and for three different sensor operation settings. The statistical errors are dominated by the systematic uncertainty found in the calibration method of the temperature measurement. The systematic error is determined to be of a value of $\pm 1^{\circ}\text{C}$. The statistical error for the measurement at a heat sink temperature of -5.5°C and 6.8°C is determined to be of a value of $\pm 0.01^{\circ}\text{C}$, while the statistical error for a heat sink temperature of 17°C a value of $\pm 0.02^{\circ}\text{C}$ has been estimated.*

D.11. Temperature Measurements on the MVD Prototype Sensors and the Reference Plane Sensors

		Temperature [°C]			
Carrier	Heat sink	sensors are switched off	sensors switched on / different sensor operation setting		
			10 ⁻² %	10 ⁻³ %	10 ⁻⁴ %
Aluminum	16.9 ± 0.3	18.9 ± 0.8			
	18.2 ± 0.1		25.93	25.25	25.23
			25.25	25.44	25.31
CVD	17	18			
	18.1 ± 0.1		22.7	22.72	22.74

Table D.5: The absolute temperatures measured on the sensors of the reference planes for a heat sink temperature of 17 °C in case the sensors are switched off (baseline measurement) and in cases of three different sensor running scenarios. The statistical errors are dominated by the systematic uncertainty found in the calibration of the temperature measurements. The systematic error is determined to have a value of ± 1 °C. The statistical error is estimated to be of a value of ± 0.02 °C.

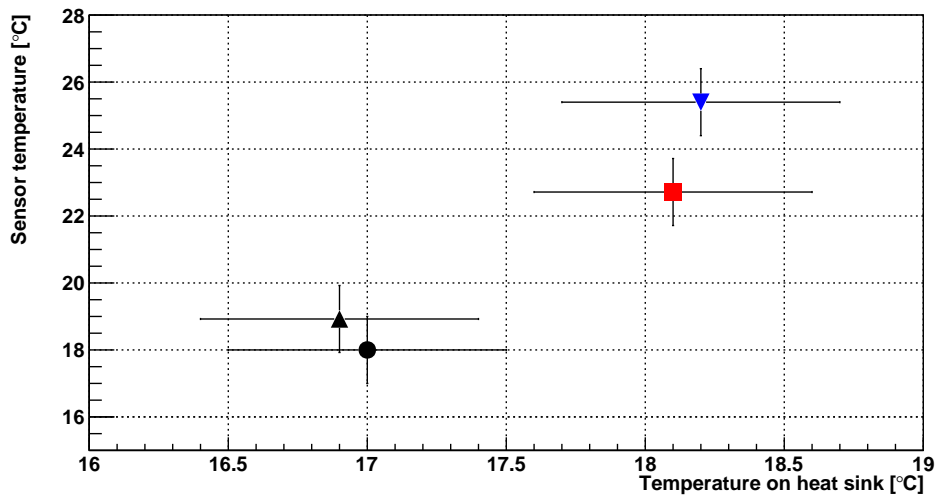
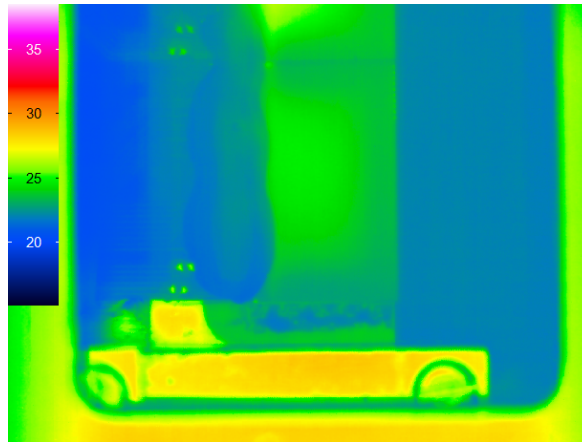
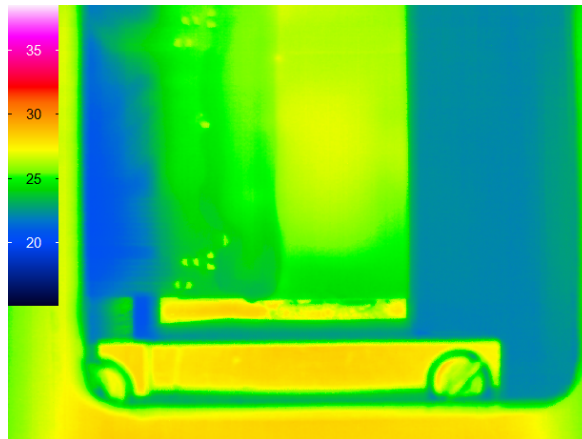


Figure D.9: The absolute temperatures measured on the sensors of the reference planes. The black circle represents the temperature measured on the sensors glued onto the CVD diamond carrier, the black up-pointing triangle shows the temperature on the sensors glued onto the aluminum carrier - both in case the sensors are switched off; the red square depicts the average temperature on the running sensors glued onto the CVD diamond carrier and the blue triangle represents the average temperature on the sensors glued onto the aluminum carrier.



(a) Reference plane - CVD diamond carrier.



(b) Reference plane - Aluminum carrier.

Figure D.10: Infrared pictures of the reference planes. A sensor operation setting of 0.001% has been applied to the examined sensors. The depicted temperature scale has not been corrected for the reflexion coefficient and the emissivity of the sensors. (a): The higher thermal conductivity of the CVD diamond carrier compared to the aluminum carrier (b) is visible resulting in a lower temperature measured on the sensors in the area which is supported by the cooling material. The openings in the center of the charge-sensitive area are visible by an increase of the measured temperature. (b): The temperatures measured on the sensors glued to the aluminum carrier indicate higher values compared to the ones measured on the sensors glued on the CVD diamond carrier. In addition, the temperatures measured on the sensor area above the openings and the ones measured in the area where the two MIMOSA-26 sensors integrated on an aluminum carrier are touching each other are higher compared to the one found in (a).

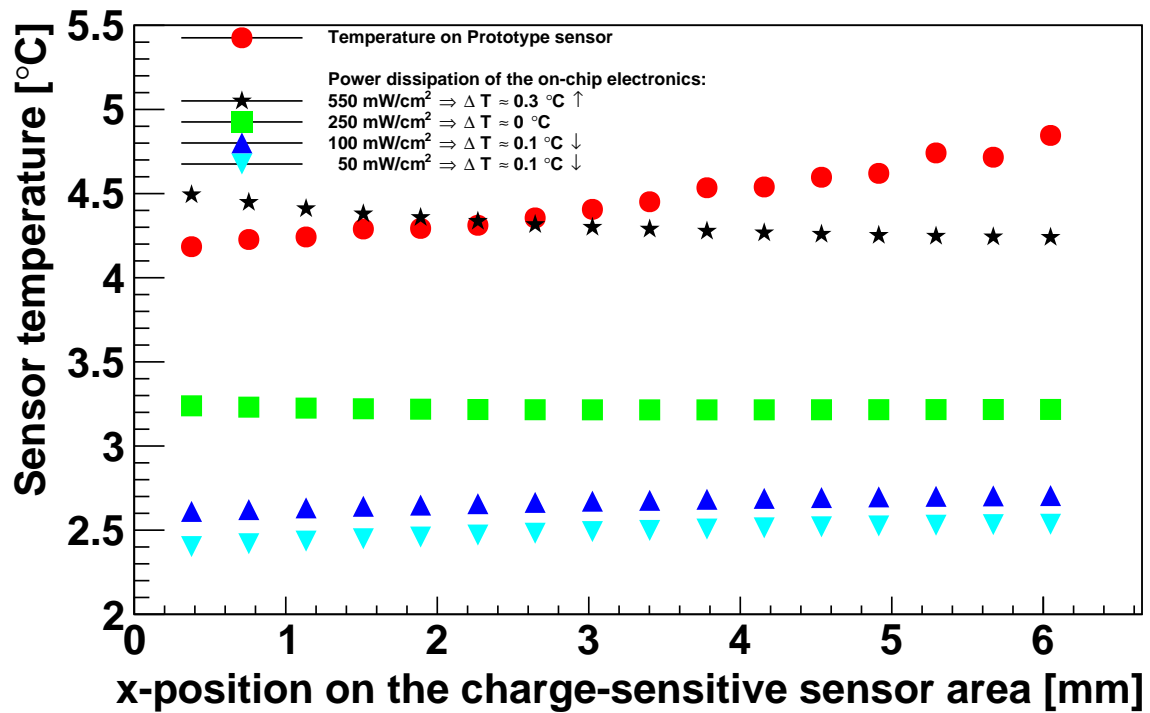


Figure D.11: The simulated and measured temperature gradients across the sensor's surface for different power dissipation values assigned to the sensor area hosting the on-chip electronics. The red dots and the black stars represent the temperature gradients displayed in Figure 5.23.

The temperature gradient displayed by black stars, which represents a power dissipation value of 550 mW/cm² and which is assigned to the non-sensitive sensor area, is increasing. For the temperature gradients displayed by the up-pointing and down-pointing triangles, which represent power dissipation value of 100 mW/cm² and 50 W/cm², and which are assigned to the non-sensitive sensor area, correspond to the measured slopes. The up- and down-pointing arrows in the legend indicate the trend of the individual temperature gradient for an assigned power dissipation (increase or decrease).

D.12 In-Beam Set-Up

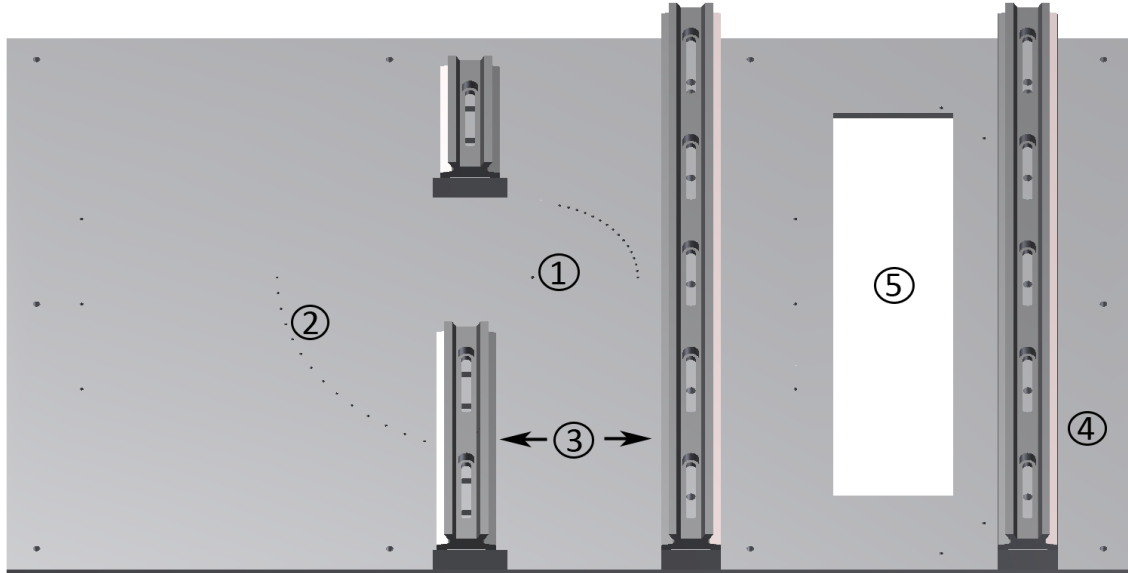


Figure D.12: The base plate of the in-beam set-up. In the middle of the base plate (1) the MVD Prototype (not shown) is to be positioned. The two quarter circles (2) represent the fixation points in case the MVD Prototype is turned to allow for studies using different beam incident angles. The four reference planes are to be positioned on the first and second rail (3), while the rail (4) positioned on the right side of the base plate is dedicated to the movement of the Converter boards. The rectangular opening (5) serves as feedthrough from below to guide the cooling tubes to the reference planes. Therefore, potential crossing points of the cooling pipes and electrical cables are limited to avoid possible electrical short circuits. The realization of the base plate is shown in Figure D.14.

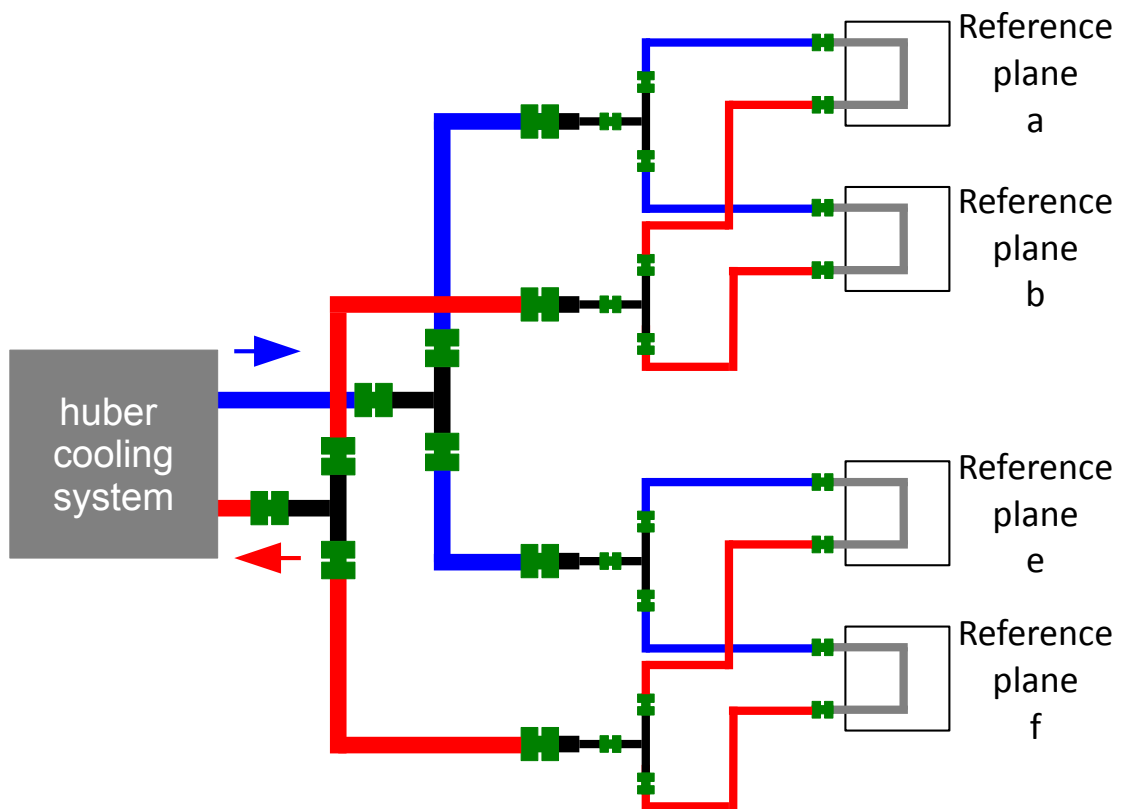


Figure D.13: Sketch of the cooling distribution system of the reference planes. The blue lines symbolize the tubes guiding the cold liquid, while the red lines show the tubes guiding the warmer liquid. The green H-like and the black T-like structures represent different Swagelok [107] interconnections.

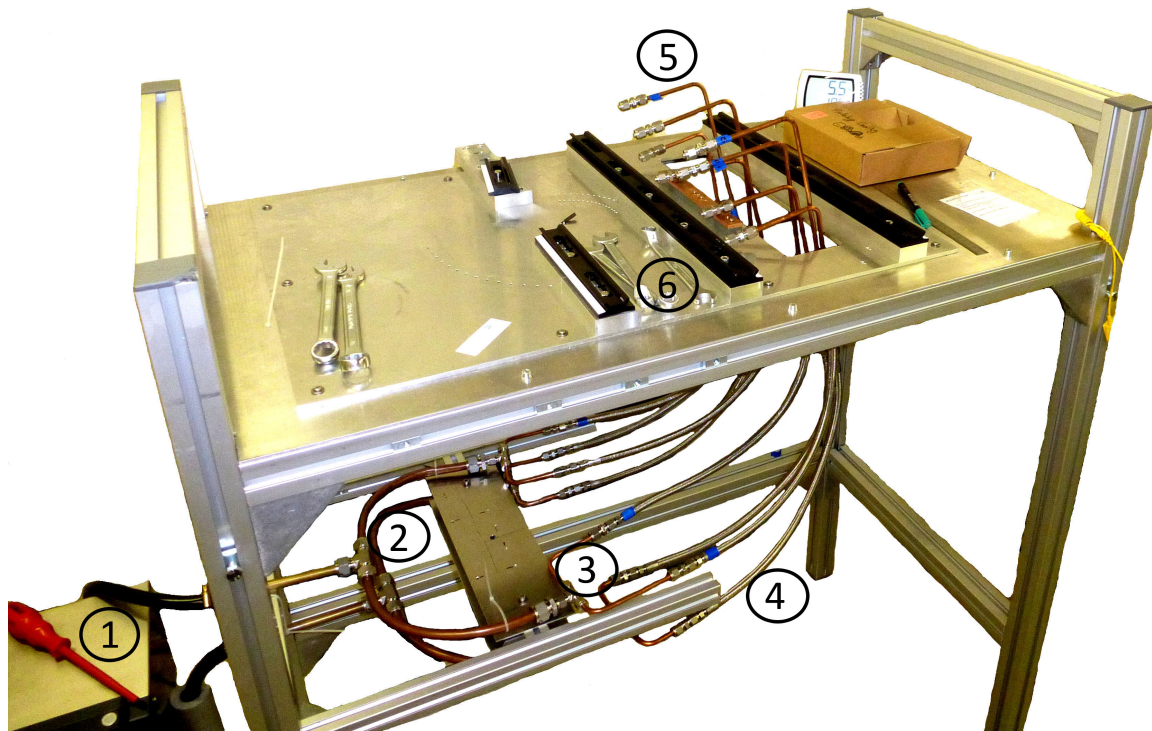


Figure D.14: The cooling distribution system of the reference planes. The huber cooling system [94] (1) is situated in the left lower corner. The thick black cooling tubes bridge the distance from the huber cooling system to first manifolds (2) which are splitting the cooling lines into two separate ones. The second manifold stage (3) provides the required amount of cooling lines for the four reference planes. After this second manifold stage, flexible hoses (4) from Swagelok [107] are used as cooling tubes. These pass over to cover tubes before they are guided through the opening in the base plate D.12. The copper cooling tubes (5) are connected to the reference planes (not shown) in the next step. To do so, they will be mounted on the two left black rails (6).

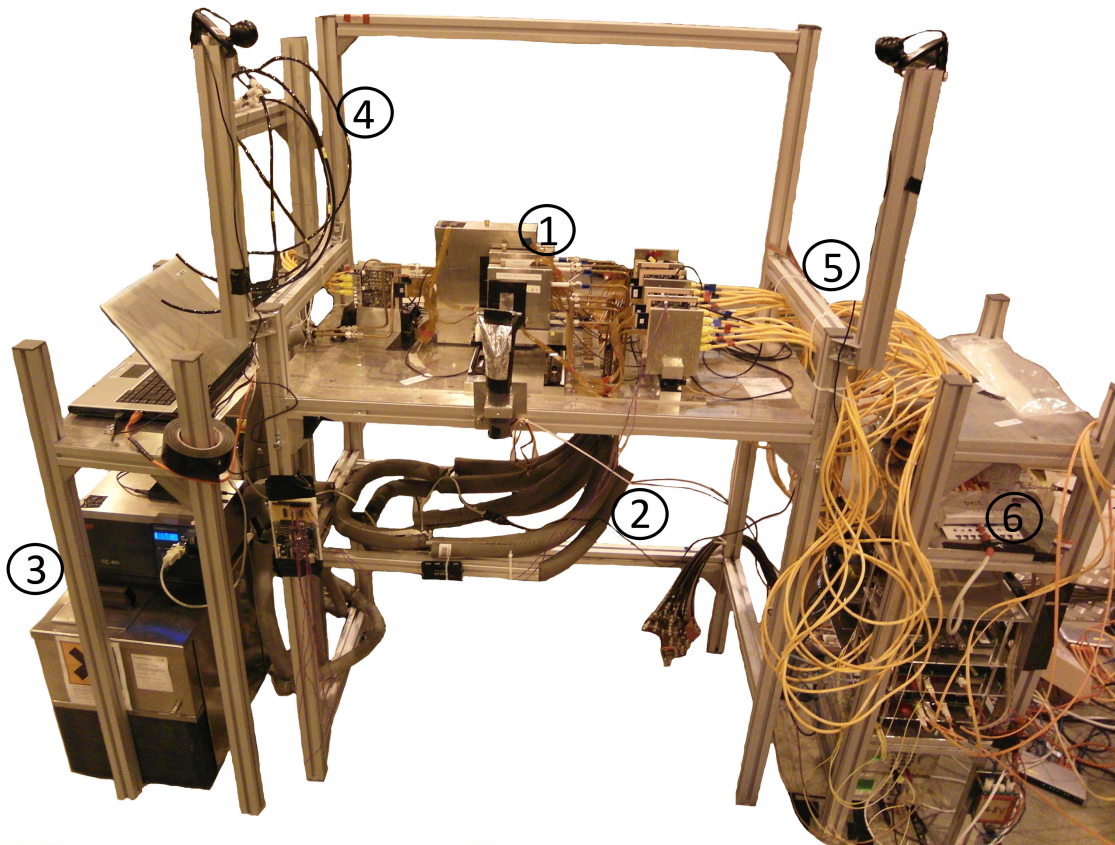


Figure D.15: The complete in-beam set-up. The MVD Prototype as well as the reference planes (1) are visible in the center of the picture. The cooling distribution system (2) of the reference planes is attached to these from below. On the left side of the base plate, the cooling systems (3) and the distribution system for dry nitrogen (4) are placed. The yellow cables in the right side of the picture (5) provide the connection and the data transfer between the Converter boards and the TRBv2-based read-out boards (6).

D.13 Data Analysis

Sensor Alignment

To extract an unbiased value of the sensor performance parameters of the integrated sensors their alignment is required.

A “master” alignment is carried out for the data sampled in a dedicated long-run featuring high statistics. During this run, a high threshold setting is applied to the sensors to suppress fake hits and to achieve a clean data set. All subsequently taken data sets are referenced to these extracted alignment parameters unless a major change in the set-up with respect to the MVD Prototype is applied, e.g., a change of orientation with respect to the beam axis, to study the response of the sensors to different incident angles of the particles.

In the data set, all single pixels indicating a signal, which might also be associated with the occurrence of a fake hit, and all clusters – comprising more than five firing pixels positioned next to each other in an arbitrary arrangement – have been removed at the beginning of the alignment procedure.

The alignment procedure is initiated with a first approximate tracking of the pions through the set-up. For this, only the data samples showing a maximum number of two hits per sensor plane (in both, the MVD Prototype as well as the reference planes) in a given time interval (= frame) are taken into account.

The particle hits on the first and on the last reference planes are connected with a straight line and the distances of the particle hits found on the other sensor planes – represented by the red cross in Figure D.16(b) – up to this line are determined. The question of which of the indicated hits on the inner sensor planes will be associated with the spanned track is chosen randomly and, therefore, only a preliminary and approximate tracking can be achieved. The same applies to the extracted positions of the six sensor planes.

The resulting position parameters of the sensor planes are used to achieve a reasonable sensor alignment. The translational and rotational degrees of freedom of the sensor planes with respect to the global coordinate system of the set-up are considered within the alignment procedure, as depicted in Figure D.16(a).

The alignment procedure is based on the common optimization of the χ^2 of all tracks. To ease the calculation of the alignment, the tracks are projected onto planes defined by the x-z- and the y-z-coordinate representing the 3D-tracks in a 2D-description. For the minimization of the χ^2 , the ROOT TMinuit package is used [101].

The association of hits to the particle tracks involves a certain uncertainty which depends, in addition, on the quality of the set of alignment parameters. In determining the “master” alignment, this problem is solved by exchanging the chosen tracks in an iterative procedure. To avoid ambiguities or difficulties within the minimization process caused by weak or constant modes, two main constraints have to be taken into account. For the first reference plane (a), see Figure D.16(b), the translational and rotational degrees of freedom are fixed. For the last reference plane (f), the translation is also fixed and the rotation in α and β is optimized separately. For the other reference planes, a common optimization of the variables α and β is executed.

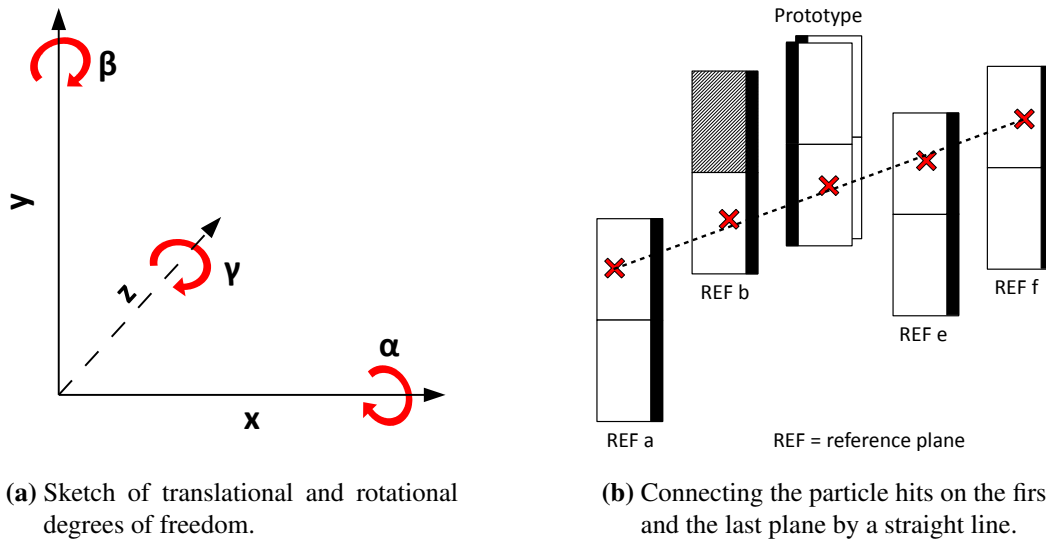


Figure D.16: The translational and rotational degrees of freedom in (a). For the rotation around the x -axis the angle α is used. The rotation around the y -axis is described by the angle β , whereas γ describes the rotation around the z -axis. In (b), the tracking strategy is sketched.

Alignment parameter	Absolute error
x, y	$O(10^{-1} \mu\text{m})$
z	$O(10^2 \mu\text{m})$
α, β	$O(10^2 \text{ mrad})$
γ	$O(10^{-2} \text{ mrad})$

Table D.6: The extracted sensitivity of the alignment parameters. The numbers are taken from [98].

A different sensitivity to the corrections of the minimization function requires a certain order for the optimization of the parameters. In this regard, it turned out to be most productive to optimize the parameters in x - and y -direction first, followed by the rotation in γ and the optimization of α , β and z .

Alignment parameter set	Residuals [μm]	Pointing resolution [μm]
Known	4.49 (3.71)	2.04 (1.69)
Reconstructed	4.50 (3.71)	2.06 (1.69)
Relative error	0.2% (0.0%)	1% (0.1%)

Table D.7: The simulated residuals and pointing resolution which have been evaluated with the known and reconstructed sets of alignment parameters assuming a sensor resolution of $4 \mu\text{m}$ ($3.3 \mu\text{m}$) and the given set-up. The numbers are taken from [98].

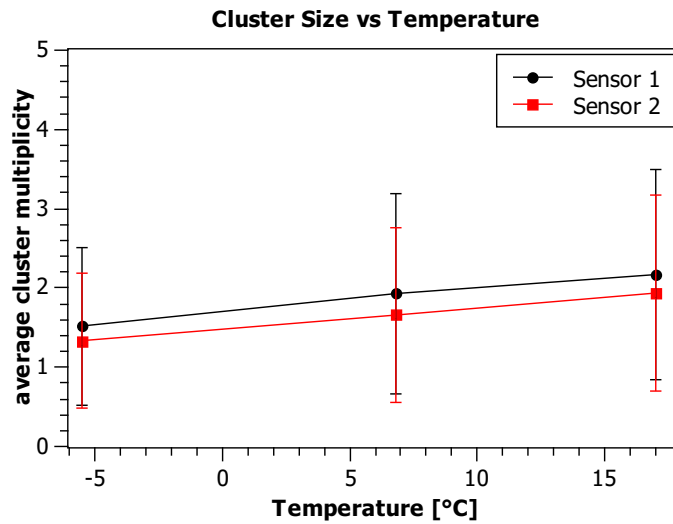


Figure D.17: The average cluster multiplicity as a function of the heat sink temperature. The error bars denote the corresponding standard deviation of the multiplicity distribution. The figure is taken from [98].

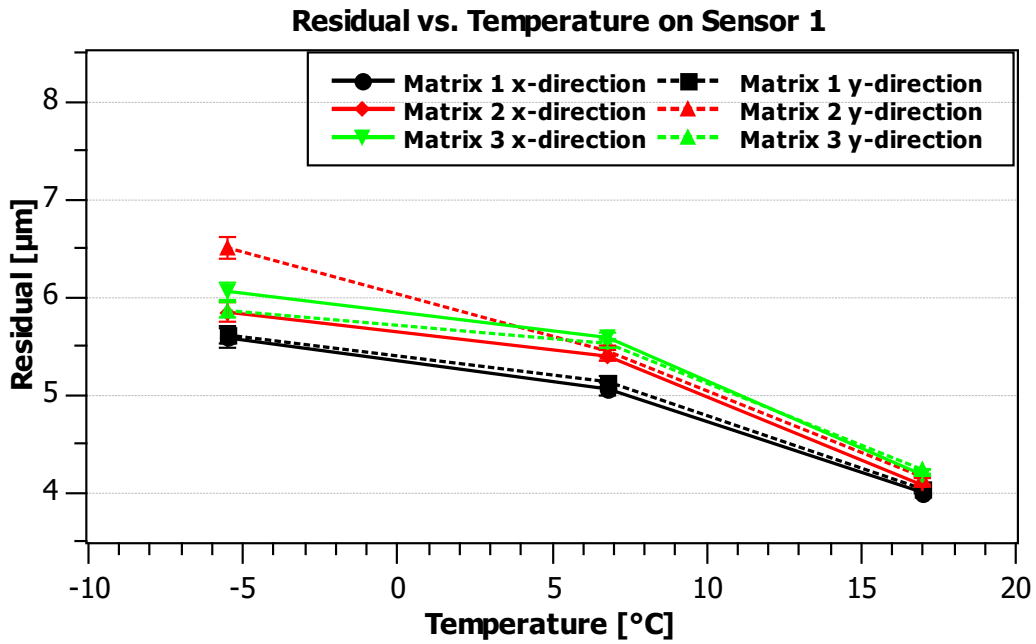
Multiple Scattering through Small Angles in the In-Beam Set-Up

The multiple scattering through small angles of the particles traversing the in-beam set-up can be calculated using Equation 3.2 in Section 3.1.2. Two different values for x/X_0 can be stated depending on the particle track length through the in-beam set-up:

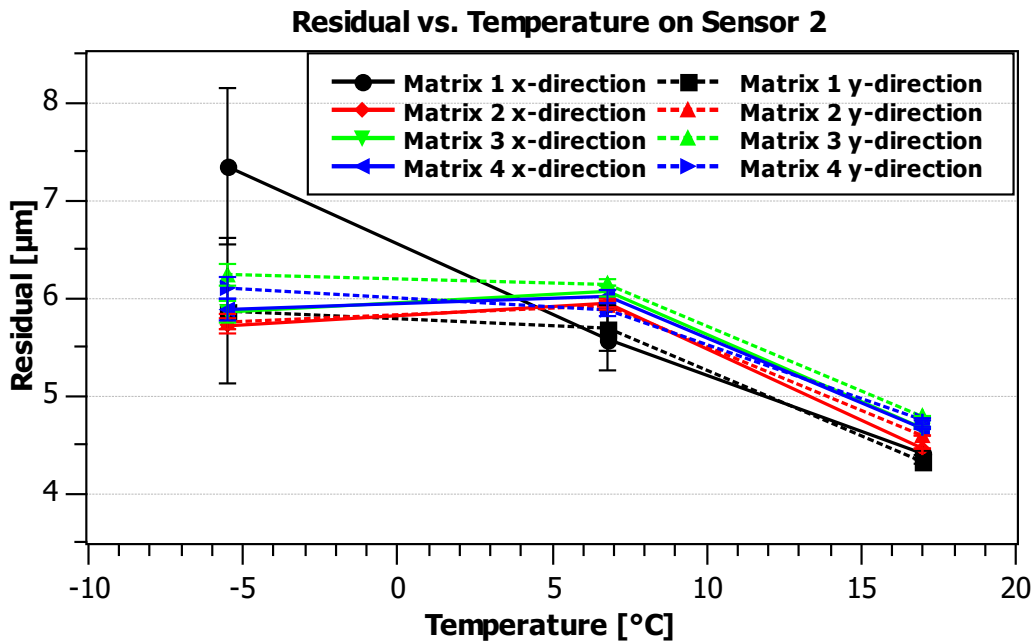
The material budget is of a value of $x/X_0 = 0.00506$ in case the position in which the particles traverse the upstream core module of the MVD Prototype is taken into account. A material budget value of $x/X_0 = 0.00662$ is determined in case the particles are traversing the complete set-up, i.e. up to the position in which the particles cross the sensors of the last reference plane. Both values assume that the aluminum windows, positioned at the entrance and the exit of the reference plane and the MVD Prototype housing boxes, are contributing to the material budget with a value of $x/X_0 = 16.68 \times 10^{-5}$ each and that the particles are passing through the openings of the sensor carriers of the reference planes. The contribution of air in between the different sensor planes has been neglected. The resulting values are listed in Table D.8.

Particle track length		Beam energy [GeV]		
		80	10	
Prototype (244 mm)	Scattering angle	[rad]	9.66×10^{-6}	7.73×10^{-5}
		[°]	5.5×10^{-4}	4.43×10^{-3}
	$\sigma_{\text{scattering}}$	[μm]	2.36	18.86
complete in-beam set-up (416 mm)	Scattering angle	[rad]	1.11×10^{-5}	8.93×10^{-5}
		[°]	6.4×10^{-4}	5.11×10^{-3}
	$\sigma_{\text{scattering}}$	[μm]	4.64	37.14

Table D.8: The possible contributions of the multiple scattering to the pointing resolution of the sensors. The multiple scattering is caused by the material positioned in-beam.



(a) Sensor 1 is positioned on the front side of the double-sided module.



(b) Sensor 2 is positioned on the back side of the double-sided module.

Figure D.18: The temperature dependence of the residuals of the two MVD Prototype sensors. For lower heat sink temperatures, a deterioration of the residuals has been extracted from the data. The figures are taken from [98].

Vibrations

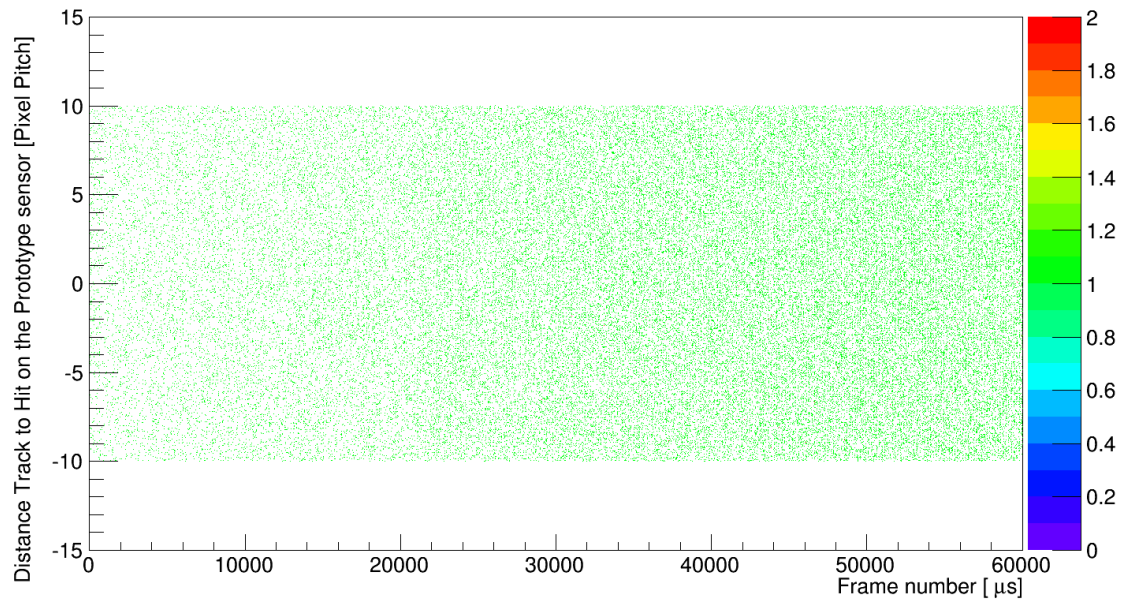
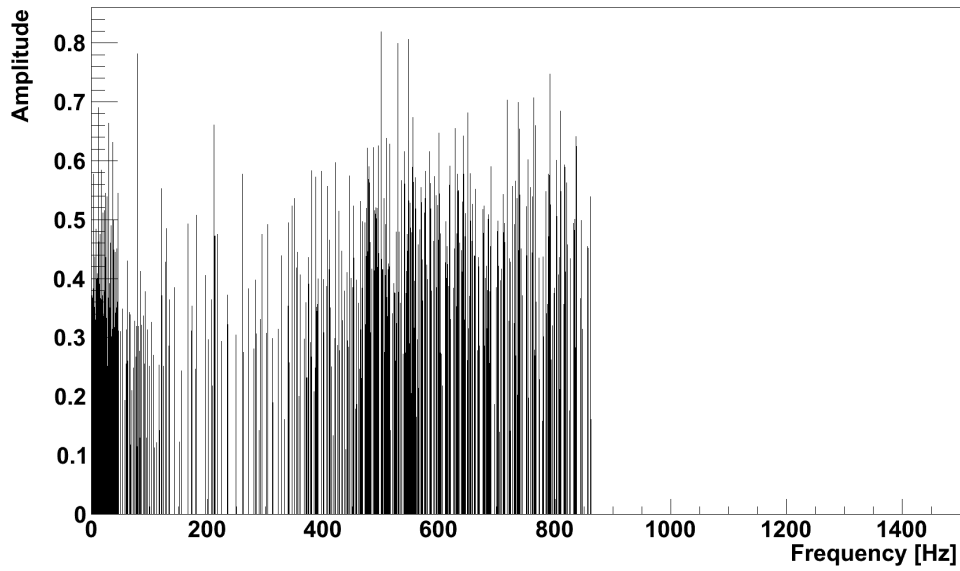


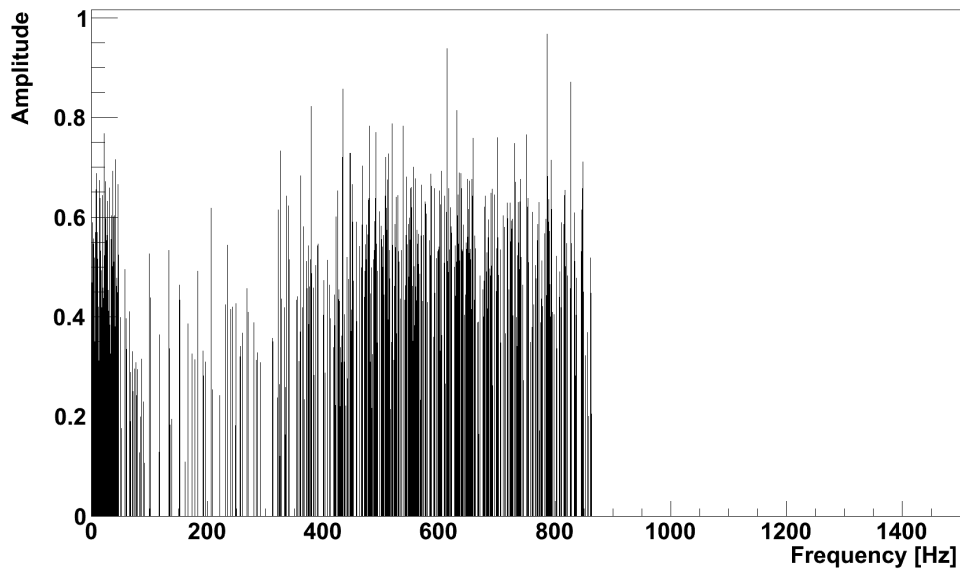
Figure D.19: Distance between the tracks which have been reconstructed by use of the reference planes hitting the MVD Prototype sensors and the indicated hits on these MVD Prototype sensors. The x-axis represents the time in which the beam spill is passing through the set-up as a function of the frame number, provided in μs .

Fast Fourier Transform

The fast Fourier transform is used to convert signals measured in a [time,value]-system into a [frequency, amplitude, phase]-system. During the conversion process, the interference of all potential modes are filtered and only multiple of the fundamental modes are taken into account. The formalism has been introduced by Cooley and Tukey [108].



(a) Possible frequencies in x-direction.



(b) Possible frequencies in y-direction.

Figure D.20: The result of the frequency analysis in x- (a) and in y-direction (b).

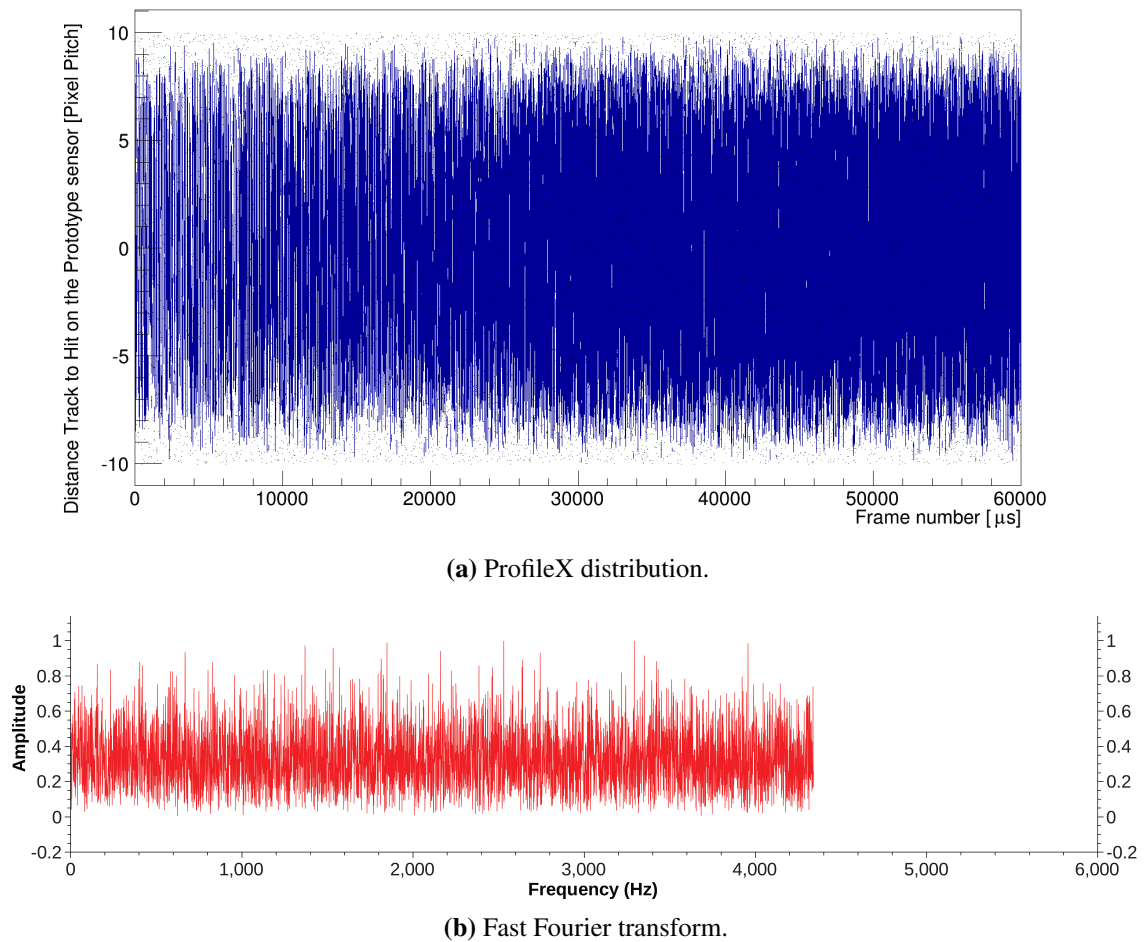


Figure D.21: The result of the vibration analysis. The result of the ROOT option “ProfileX” is shown in (a). In each bin, the mean value of the distance is calculated. The error appears as standard deviation. (b) shows the FFT of figure (a). A pronounced amplitude hinting at the appearance of possible vibrations cannot be found.

x-direction		y-direction	
Frequency [Hz]	Amplitude	Frequency [Hz]	Amplitude
40.22	0.295	40.03	0.209
40.31	0.107	40.40	0.261
40.63	0.150	40.59	0.305
40.68	0.444	40.65	0.194
40.82	0.396	40.87	0.140
40.87	0.271	40.91	0.380
40.91	0.204	40.96	0.249
41.05	0.197	41.05	0.137
41.33	0.209	41.15	0.309
41.42	0.183	41.38	0.287
41.70	0.164	41.42	0.716
41.79	0.307	41.70	0.146
41.84	0.136	41.80	0.123
41.89	0.341	41.89	0.359
42.07	0.173	42.07	0.320
42.26	0.196	42.26	0.458
42.35	0.323	42.35	0.311
42.40	0.284	42.44	0.217
42.81	0.351	42.63	0.116
42.91	0.265	42.82	0.220
43.09	0.316	42.91	0.461

Table D.9: *The extracted frequencies in the region of 40 to 43 Hz to ease their comparison to the frequency of the pump of the cooling system. The values have been rounded to the second digit for the frequencies and to the third digit for the amplitude.*

Thermal Expansion

Material	coefficient of thermal expansion [1/K]	Additional length [μm]	
		long side	short side
Sensors	5×10^{-7}	0.254	0.163
CVD diamond	1×10^{-6}	0.43	0.276
Glue	50×10^{-6}	21.5	13.8
	60×10^{-6}	25.8	16.6
Thermal interface area sensor to sensor carrier		21500	13800
Temperature difference	10 K		

Table D.10: *The coefficients of thermal expansion of the involved components of the MVD Prototype. The definition of the short and the long side of the MIMOSA-26 sensors is adopted from the sketch in Figure 5.3.*

Appendix E

Towards the MVD at SIS100



Figure E.1: The 1 : 1 mock-up of the proposed MVD geometry comprising all four MVD stations and their components. The components will be substituted with functioning elements bit by bit in the near future.

Bibliography

- [1] P. Senger et al. “Nuclear Matter Physics at SIS-100”. 2012. URL: <https://www-alt.gsi.de/documents/DOC-2011-Aug-29.html>.
- [2] A. Andronic et al. “Thermal hadron production in relativistic nuclear collisions: the hadron mass spectrum, the horn, and the QCD phase transition”. *Phys. Lett. B*, 673(2):142–145, 2009. doi:10.1016/j.physletb.2009.02.014.
- [3] K. Fukushima and T. Hatsuda. “The phase diagram of dense QCD”. *Rep. Prog. Phys.*, 74(1), 2011. doi:10.1088/0034-4885/74/1/014001.
- [4] The DOE/NSF Nuclear Science Advisory Committee. “The Frontiers of Nuclear Science, A Long Range Plan”. arXiv:0809.3137.
- [5] A. Andronic et al. “Hadron Production in Ultra-relativistic Nuclear Collisions: Quarkyonic Matter and a Triple Point in the Phase Diagram of QCD”. *Nuclear Physics A*, 837(1-2):65–86, 2010. doi:10.1016/j.nuclphysa.2010.02.005.
- [6] Z. Fodor and S. Katz. “Lattice determination of the critical point of QCD at finite T and μ ”. *JHEP*, 2002(014), 2002. doi:10.1088/1126-6708/2002/03/014.
- [7] B. Friman et al. “The CBM Physics Book - Compressed Baryonic Matter in Laboratory Experiments”. *Springer Verlag*, 2011. doi:10.1007/978-3-642-13293-3.
- [8] The ATLAS Collaboration. “ATLAS: A Toroidal LHC Apparatus”. *Nuclear Physics A*, 932:572–594, 2014. doi:10.1016/S0375-9474(14)00601-0.
- [9] The CMS Collaboration. “CMS: Compact Muon Solenoid”. *Nuclear Physics A*, 932:595–620, 2014. doi:10.1016/S0375-9474(14)00602-2.
- [10] The ALICE Collaboration. “ALICE: A Large Ion Collider Experiment”. *Nuclear Physics A*, 932:563–571, 2014. doi:10.1016/S0375-9474(14)00600-9.
- [11] The STAR Collaboration. “STAR: Solenoidal Tracker At RHIC”. *Nuclear Physics A*, 932:634–637, 2014. doi:10.1016/S0375-9474(14)00605-8.
- [12] A. Schmah et al. “Highlights of the Beam Energy Scan from STAR”. *Central European Journal of Physics*, 10:1238–1241, 2012. doi:10.2478/s11534-012-0149-1.

- [13] The NA61/SHINE Collaboration. “NA61/SHINE”. *Nuclear Physics A*, 904-905:1081c–1082c, 2013. doi:10.1016/j.nuclphysa.2013.02.196.
- [14] A. Andronic et al. “Hadron production in central nucleus-nucleus collisions at chemical freeze-out”. *Nuclear Physics A*, 772(3-4):167–199, 2006. doi:10.1016/j.nuclphysa.2006.03.012.
- [15] W. Cassing et al. “Open charm production in relativistic nucleus-nucleus collisions”. *Nucl.Phys. A*, 691:753–778, 2001. doi:10.1016/S0375-9474(01)00562-0.
- [16] S. Seddiki. “Contribution to the development of the Micro-Vertex Detector of the CBM experiment and feasibility study of open charm elliptic flow measurements”. *PhD thesis, Goethe-University, Frankfurt*, 2012.
- [17] J. Beringer et al. (Particle Data Group). “Particle Data Booklet”. *Phys. Rev.*, D86(010001), 2012.
- [18] T. Galatyuk et al. “Report of the PWG Dileptons”. *Talk, given 11.09.2014, CBM Collaboration Meeting, Krakow, Poland*.
- [19] T. Galatyuk. “Di-electron spectroscopy in HADES and CBM: from $p+p$ and $n+p$ collisions at GSI to $Au+Au$ collisions at FAIR”. *PhD thesis, Goethe-University, Frankfurt*, 2009.
- [20] J. Bouchet et al. “Heavy Flavor Tracker (HFT): A new inner tracking device at STAR”. *Nuclear Physics A*, pages 636–637, 2009. doi:10.1016/j.nuclphysa.2009.10.114.
- [21] The ALICE Collaboration. “Technical Design Report for the Upgrade of the ALICE Inner Tracking System”. *Journal of Physics G: Nuclear and Particle Physics*, 41(8), 2014. doi:10.1088/0954-3899/41/8/087002.
- [22] J. M. Heuser et al. “Technical Design Report for the CBM Silicon Tracking System (STS)”. (GSI-2013-05499), 2013. URL: <http://repository.gsi.de/record/54798>.
- [23] P. Akishin et al. “Technical Design Report for CBM - Superconducting Dipole Magnet”. 2014.
- [24] C. Höhne et al. “Technical Design Report for the CBM Ring Imaging Cherenkov Detector”. (GSI-2014-00528), 2013. URL: <http://repository.gsi.de/record/65526>.
- [25] V. Friese and C. Sturm (editors). “CBM Progress Report 2013”. 2013. URL: <https://www-alt.gsi.de/documents/DOC-2014-Mar-16-1.pdf>.
- [26] J. M. Heuser et al. “A High-Performance Silicon Tracker for the CBM Experiment at FAIR”. *AIP Conf. Proc.*, 842(1073), 2006. doi:10.1063/1.2220457.

-
- [27] I. Fröhlich et al. “Pluto: A Monte Carlo Simulation Tool for Hadronic Physics”. *Proceedings of Science*, ACAT2007:076. arXiv:0708.2382.
- [28] The CBM Collaboration. “Definition of the CBM Coordinate System and Basic Rules for Sub-detector Components Numbering”.
- [29] C. Trageser. “Systematische Untersuchung zur Auswirkung der Detektorgeometrie auf die Spurrekonstruktionseffizienz und Stoßparameterauflösung des CBM Mikro-Vertex-Detektor”. *Master thesis, Goethe-University, Frankfurt*, 2012.
- [30] N. Wermes. “Pixel Vertex Detectors”. arXiv:physics/0611075.
- [31] Erik Krebs. *private communication*.
- [32] M. Deveaux et al. “A first generation prototype for the CBM micro vertex detector”. *Nuclear Instruments and Methods A*, 718:305–306, 2013. doi:10.1016/j.nima.2012.10.013.
- [33] Anna Senger. *private communication*.
- [34] M. Al-Turany et al. “The FairRoot framework”. *Journal of Physics: Conference Series*, 396(2), 2012. doi:10.1088/1742-6596/396/2/022001.
- [35] I. Kisel. “Event reconstruction in the CBM experiment”. *Nuclear Instruments and Methods A*, 556(1):85–88, 2006. doi:10.1016/j.nima.2006.05.040.
- [36] C. Dritsa. “Design of the Micro Vertex Detector of the CBM experiment: Development of a detector response model and feasibility studies of open charm measurement”. *PhD thesis, Goethe-University, Frankfurt*, 2011.
- [37] C. Trageser. “Simulation der Multiplizitätsverteilung auf den Detektorstationen des MVD am CBM Experiment”. *Bachelor thesis, Goethe-University, Frankfurt*, 2008.
- [38] Philipp Sitzmann. *private communication*.
- [39] M. Koziel. “Development of radiation hardened pixel sensors for charged particle detection”. *PhD thesis, Université de Strasbourg*, 2011.
- [40] S. Amar-Youcef. “Design and performance studies of the Micro-Vertex-Detector for the CBM experiment at FAIR”. *PhD thesis, Goethe-University, Frankfurt*, 2012.
- [41] M. Deveaux et al. “Design considerations for the Micro Vertex Detector of the Compressed Baryonic Matter experiment”. *Proceedings of Science*, VERTEX 2008:028, 2008. arXiv:0906.1301.
- [42] M. Battaglia et al. “A Study of Monolithic CMOS Pixel Sensors Back-thinning and their Application for a Pixel Beam Telescope”. *Nuclear Instruments and Methods A*, 579(2):675–679, 2007. doi:10.1016/j.nima.2007.05.276.

- [43] G. Deptuch et al. “Simulation and measurements of charge collection in monolithic active pixel sensors”. *Nuclear Instruments and Methods A*, 465(1):92–100, 2001. doi:10.1016/S0168-9002(01)00361-8.
- [44] M. Winter et al. “Achievements and perspectives of CMOS pixel sensors for charged particle tracking”. *Nuclear Instruments and Methods A*, 623(1):192–194, 2010. doi:10.1016/j.nima.2010.02.192.
- [45] L. Greiner et al. “Experience from construction and operation of the STAR PXL detector”. *Talk, given 16.09.2014, CPIX 2014, Bonn, Germany*.
- [46] C. Hu-Guo et al. “First reticule size MAPS with digital output and integrated zero suppression for the EUDET-JRA1 beam telescope”. *Nuclear Instruments and Methods A*, 623:480–482, 2010. doi:10.1016/j.nima.2010.03.043.
- [47] M. Winter et al. “Status and Plans of the MVD-Sensor Developments”. *Talk, given 11.04.2013, CBM Collaboration Meeting, GSI, Darmstadt, Germany*.
- [48] M. Deveaux et al. “Radiation tolerance of a column parallel CMOS sensor with high resistivity epitaxial layer”. *Journal of Instrumentation*, 6, 2011. doi:10.1088/1748-0221/6/02/C02004.
- [49] D. Doering et al. “Pitch dependence of the tolerance of CMOS monolithic active pixel sensors to non-ionizing radiation”. *Nuclear Instruments and Methods A*, 2013. doi:10.1016/j.nima.2013.04.038.
- [50] D. Doering. “Untersuchungen zur Verbesserung der Strahlenhärte von CMOS-Sensoren zum Einsatz in Vertexdetektoren von Schwerionenexperimenten”. *PhD thesis, Goethe-University, Frankfurt, 2014*.
- [51] D. Doering et al. “Noise performance and ionizing radiation tolerance of CMOS Monolithic Active Pixel Sensors using the 0.18 μm CMOS process”. *Journal of Instrumentation*, 9(05):C0551, 2014. doi:10.1088/1748-0221/9/05/C05051.
- [52] S. Senyukov et al. “Charged particle detection performances of CMOS pixel sensors produced in a 0.18 μm process with a high resistivity epitaxial”. *Nuclear Instruments and Methods A*, 730:115–118, 2013. doi:10.1016/j.nima.2013.03.017.
- [53] G. Kretzschmar. “Vacuum operation of the CBM-MVD Prototype”. *Master thesis, Goethe-University, Frankfurt, in preparation*.
- [54] Christian Müntz. *private communication*.
- [55] Sergey Belogurov. *private communication*.
- [56] T. Tischler. “Untersuchungen zu Materialien und Haltestrukturen für den CBM MVD Demonstrator”. *Diploma thesis, Goethe-University, Frankfurt, 2010*.

- [57] Autodesk. *Autodesk Inventor Professional 2012 and 2013*. URL: <http://www.autodesk.com>.
- [58] S. Amar-Youcef et al. "Integration of the CBM MVD simulation model to the CBM-Root framework". *internal note*, 2013.
- [59] Michael Deveaux. *private communication*.
- [60] M. Winter et al. "Devt of CPS for the MVD: Status and Plans". *Talk, given 11.04.2014, CBM Collaboration Meeting, GSI, Darmstadt, Germany*.
- [61] M. Koziel et al. "A latch-up protected power supply for the CBM-MVD". *PHN-NQM-CBM-06, GSI Scientific Report*, 2011. URL: <http://www-alt.gsi.de/informationen/wti/library/scientificreport2011/PAPERS/PHN-NQM-CBM-06.pdf>.
- [62] M. Deveaux. "Development of fast and radiation hard Monolithic Active Pixel Sensors (MAPS) optimized for open charm meson detection with the CBM - vertex detector". *PhD thesis, Goethe-University, Frankfurt*, 2008.
- [63] Diamond Materials GmbH. *CVD diamond, data sheet*. URL: http://www.diamond-materials.com/downloads/cvd_diamond_booklet.pdf.
- [64] Momentive. *Thermal Pyrolytic Graphite, data sheet*. URL: <http://www.momentive.com>.
- [65] M. Koziel et al. "The Prototype of the Micro Vertex Detector of the CBM Experiment". *Nuclear Instruments and Methods A*, 2013. doi:10.1016/j.nima.2013.07.041.
- [66] Diamond Materials GmbH. *private communication*.
- [67] K. Arndt et al. "Mechanics for the CMS Upgrade Forward Pixel Detector". *Talk, given 20.06.2013, Forum on Tracking Detector Mechanics, Oxford, England*.
- [68] Stefan Gruenendahl. *private communication*.
- [69] P. Jasinski et al. "Construction of an Actively Cooled MAPS Device operated in vacuum near a storage ring beam". *Talk, given 01.07.2014, Forum on Tracking Detector Mechanics, DESY, Germany*.
- [70] Peter von Böckh and Thomas Wetzel. "Wärmeübertragung - Grundlagen und Praxis". *Springer Verlag*, 2011. doi:10.1007/978-3-642-15959-6.
- [71] Autodesk. *Autodesk Simulation CFD 2013 and 2014*. URL: <http://www.autodesk.com>.
- [72] Michal Koziel. *private communication*.

- [73] F. Morel et al. “MISTRAL & ASTRAL: two CMOS Pixel Sensor architectures suited to the Inner Tracking System of the ALICE experiment”. *Journal of Instrumentation*, 9, 2014. doi:10.1088/1748-0221/9/01/C01026.
- [74] Philipp Klaus. *private communication*.
- [75] M. Szelezniak et al. “Lessons learned from the STAR PXL detector”. *Talk, given 28.05.2014, HICforFAIR Workshop: Heavy flavor physics with CBM, FIAS, Frankfurt, Germany*.
- [76] T. Stockmanns. “STEP-to-ROOT – from CAD to Monte Carlo Simulation”. *J. Phys.: Conf. Ser.*, 396(2), 2012. doi:10.1088/1742-6596/396/2/022050.
- [77] B. Milanovic. “Development of the Readout Controller for the CBM Micro Vertex Detector”. *PhD thesis, Goethe-University, Frankfurt, 2015*.
- [78] Q. Li. “CBM-MVD prototype read-out”. *PhD thesis, Goethe-University, Frankfurt, in preparation*.
- [79] I. Rubinskiy et al. “An EUDET/AIDA Pixel Beam Telescope for Detector Development”. *Physics Procedia*, 37:923–931, 2012. doi:10.1016/j.phpro.2012.02.434.
- [80] R. De Masi et al. “Towards a 10 μ s, thin and high resolution pixelated CMOS sensor system for future vertex detectors”. *Nuclear Instruments and Methods A*, 628:296–299, 2011. doi:10.1016/j.nima.2010.06.339.
- [81] M. Winter et al. “Development of CMOS Pixel Sensors fully adapted to the ILD Vertex Detector Requirements”. arXiv:1203.3750.
- [82] M. Winter et al. “Development of Swift, High Resolution, Pixel Sensor Systems for a High Precision Vertex Detector suited to the ILC Running Conditions”. *DESY PRC RD Nr 01-04*, page 27.
- [83] Thorlabs GmbH. *Thorlabs, Torr Seal-10, glue, data sheet*. URL: <http://www.thorlabs.de>.
- [84] Epotecny. *Epotecny 505, glue, data sheet*. URL: <http://www.epotecny.com>.
- [85] Epotecny. *Epotecny NOA88, glue, data sheet*. URL: <http://www.epotecny.com>.
- [86] Epotecny. *Epotecny 501, glue, data sheet*. URL: <http://www.epotecny.com>.
- [87] Kroeplin Längenmesstechnik GmbH. *B220, data sheet*. URL: <http://www.kroeplin.com/Elektronische-Geraete.162.0.html?&L=jehqzqvxts>.
- [88] Keyence Deutschland GmbH. *VHX-600, digital microscope, data sheet*. URL: <http://www.keyence.de/products/microscope/microscope/microscope.php>.

- [89] C. Schrader et al. “Status of the CBM-MVD prototype readout”. *PHN-NQM-CBM-04, GSI Scientific Report*, 2011. URL: <http://www-alt.gsi.de/informationen/wti/library/scientificreport2011/PAPERS/PHN-NQM-CBM-04.pdf>.
- [90] Mech-El Industries Inc. *MEI 1204W, wire bonder*. URL: <http://mech-el.com/1204w.htm>.
- [91] Dow Corning GmbH. *Sylgard 186, bonding wire encapsulant, data sheet*. URL: <http://www.dowcorning.com/applications/search/products/default.aspx?R=118EN&country=DEU>.
- [92] Arctic Silver Incorporated. *Arctic Silver 5, heat conducting paste, data sheet*. URL: <http://www.arcticsilver.com/as5.htm>.
- [93] Kunze Folien GmbH. *Thermally conductive silicone film, KU-KC 15, data sheet*. URL: <http://www.heatmanagement.com/de/produkte/ku-kc>.
- [94] Peter Huber Kältemaschinenbau GmbH. *Cooling system CC-405, data sheet*. URL: http://www.huber-online.com/de/product_datasheet.aspx?no=2017.0001.01.
- [95] B. Neumann. “Entwicklung einer FPGA-basierten JTAG-Ansteuerung für die Sensoren des CBM-MVD”. *Master thesis, Goethe-University, Frankfurt*, 2013.
- [96] InfraTec GmbH. *VarioCAM hr, head 720, infrared camera, data sheet*. URL: <http://www.infratec.de>.
- [97] Jerome Baudot. *private communication*.
- [98] S. Amar-Youcef et al. “Note on the data analysis of the MVD Prototype beam time at CERN SPS in Nov. 2012”, 2014. URL: https://www-alt.gsi.de/documents/QCD_CBM-note-2014-001.html.
- [99] J. Michel et al. “The upgraded HADES trigger and data acquisition system”. *Journal of Instrumentation*, 6, 2011. doi:10.1088/1748-0221/6/12/C12056.
- [100] Q. Li et al. “Online data processing with the CBM-MVD prototype”. *PHN-NQM-EXP-14, GSI Scientific Report*, 2012. URL: <http://repository.gsi.de/record/51948/files/PHN-NQM-EXP-14.pdf>.
- [101] Rene Brun and Fons Rademakers. “ROOT - An Object Oriented Data Analysis Framework”. *Nuclear Instruments and Methods A*, 389:81–86, 1997. doi:10.1016/S0168-9002(97)00048-X.
- [102] L. Greiner et al. “STAR PXL Detector Progress Report”. *Talk, given July 2013, IPHC, Strasbourg, France*.

- [103] L. Musa et al. “Monolithic Pixel Detectors for high-precision tracking in HI experiments”. *Talk, given 14.10.2014, International Conference on Science and Technology for FAIR, Worms, Germany.*
- [104] engineering Fundamentals efunda. *Thermal conductivity of silicon and copper.* URL: <http://www.efunda.com/home.cfm>.
- [105] Ohaus Europe GmbH. *Ohaus Pioneer PA213C, precision scale, data sheet.* URL: <http://dmx.ohaus.com/WorkArea/showcontent.aspx?id=5206>.
- [106] VDI. “VDI-Wärmeatlas”. *Springer Verlag, 2006.* doi:10.1007/978-3-540-32218-4.
- [107] Swagelok Company. *Swagelok, tube fittings, flexible tubes.* URL: <http://www.swagelok.de/>.
- [108] James W. Cooley and John W. Tukey. “An Algorithm for the Machine Calculation of Complex Fourier Series”. *Mathematics of Computation*, 19(90):297–301, 1965. doi:10.1090/S0025-5718-1965-0178586-1.

Acknowledgment

The work presented in this thesis would not have been possible without the support of many people who I am indebted to.

First, I am very grateful to Prof. Dr. Joachim Stroth for giving me the opportunity to be part of his working group. I would like to express my gratitude for the possibility to contribute and continue, after finishing my diploma thesis, my work for the CBM Micro Vertex Detector in terms of a dissertation. I am, in particular, very appreciative for the opportunity to present the results of my work on specialized conferences and workshops as well as for the fact to be part of an international collaboration.

During my PhD studies I had the possibility to participate in the program of the Helmholtz Graduate School for Heavy Ion Research (HGS-HIRe) and the Helmholtz Research School for Quark Matter Studies (H-QM). I very much appreciated the lectures, talks, exercises and soft skill seminars. Therefore, I would like to thank Prof. Dr. Henner Büsching and the team of HGS-HIRe for their continuous commitment to provide these for all associated PhD students. In particular, I am very grateful for the opportunity to spend six weeks in the working group constructing the Heavy Flavor Tracker for the STAR experiment at the Lawrence Berkeley National Laboratory (LBNL, Berkeley, USA) and the financial support provided by the HGS-HIRe Abroad program.

I would like to thank Dr. Christian Müntz for many fruitful discussions on the details of my work and the MVD, for his support of the work which has been conducted in the context of this thesis as well as his proposed corrections to improve the structure and the content of my thesis.

Special thanks have to be attributed to Dr. Samir Amar-Youcef, Dr. Michal Koziel, in particular for his support related to the MVD Prototype project, and Dr. Jan Michel not only for proof-reading this thesis and proposing corrections but also for many interesting discussions. In addition, I would like to thank Dr. Christina Deveaux, Dr. Michael Deveaux, Dennis Doering, Philipp Klaus, Gisa Kretschmar, Qiyang Li, Dr. Manuel Lorenz, Philipp Sitzmann and Michael Wiebusch for the discussions and comments.

Last but not least, I want to express my gratitude to my family and, for her love, to Katharina.

Tobias Tischler

Curriculum Vitae

*Fichtenweg 1
63505 Langenselbold
Date of Birth: 20.01.1985
Place of Birth: Hagen*



Education

- 06/2004 **General qualification for university entrance (Abitur)**, *Kopernikusschule, Freigericht.*
- 2004–2010 **Diploma study of physics**, *Goethe University Frankfurt, Frankfurt am Main.*
- 5/2010–
present **PhD study of physics**, *Goethe University Frankfurt, Frankfurt am Main.*
- 5/2010–
present **Participant of the Helmholtz Research School for Quark Matter Studies in Heavy Ion Collisions (H-QM).**

Diploma thesis

- title *Untersuchungen zu Materialien und Haltestrukturen für den CBM MVD Demonstrator*
- supervisor Prof. Dr. J. Stroth
- diploma 05/2010
- grade Very good
- institute Institut für Kernphysik, *Goethe University Frankfurt, Frankfurt am Main.*

PhD thesis

- title *Mechanical Integration of the Micro Vertex Detector for the CBM experiment*
- supervisor Prof. Dr. J. Stroth
- institute Institut für Kernphysik, *Goethe University Frankfurt, Frankfurt am Main.*